Controls on Fault Network Evolution and Population Statistics - Insights from Field Studies and Numerical Modelling

Kathryn M. Hardacre B.A. (Oxon), M.Sc. (Dunelm)

Thesis submitted in fulfilment of
the requirements for the degree of
Doctor of Philosophy
to the
University of Edinburgh – 2000

I declare that this thesis has been composed by myself and it has not been submitted in any previous application for a degree. The work reported within was executed by myself, except where contributions have been stated and duly acknowledged.

Abstract

Faulting is the principal mechanism by which large strains are accommodated in the brittle lithosphere. Studies of continental fault populations have revealed many examples of power law fault size frequency distributions with a range of power law exponents, c. This observation prompts the following key questions. What do power law scaling relationships indicate about underlying physical processes? Do observed variations in c merely result from poor sampling of natural faults or do they have some geological significance? Can this scaling relationship be extrapolated to predict fault characteristics beyond the scale of observation? This study investigates the controls on fault development, and consequently size frequency distributions, using a combination of field studies and numerical modelling.

Previous workers have suggested that power law distributions can only develop when fault growth occurs predominantly by linkage. Moreover, when linkage dominates growth, c decreases as strain increases. This idea is inconsistent with my observations of the Chimney Rock Fault Array, Utah. Fault sizes in this array follow a power law with a low exponent (0.46 ± 0.03), but the orthorhombic geometry of the faults frustrates fault growth by linkage. Therefore, linkage cannot be the only mechanism for producing low-exponent power law fault size frequency distributions. Furthermore, analyses of fault sizes in two other orthorhombic arrays show that low-exponent power laws are not characteristic of all such arrays. In fact, fault sizes in these two arrays follow exponential, not power law, distributions. Clearly, then, a better understanding of the controls on fault size scaling is required.

This is the first study in which the effects of initial conditions (e.g. rheology and material properties), boundary conditions and fault growth properties on fault size scaling are explicitly considered. I use a 2D finite element code to generate kilometre-scale, conjugate, normal faults in cross-section under a range of boundary conditions. The deforming material is modelled with a strain-softening, non-healing, Von Mises rheology with Gaussian heterogeneity in yield strength distributed randomly throughout the mesh. Faults are not defined *a priori*. Consequently the evolution of geologically realistic structures in the model can be attributed to the physical principles involved, not to a pre-defined geometry.

Numerical modelling results indicate that initial conditions and boundary conditions control which growth processes dominate at a particular place and time. Thus, they also control fault size scaling. Both power law and non-power law distribution types emerged spontaneously, and the power law distributions showed a range of values of c between 0.53 and 1.27. In each simulation, the exponent c of the fault size cumulative frequency distribution was observed

to decrease with increasing extension; partly due to coalescence, but also because larger faults grew disproportionately faster than smaller ones. The dependence of c on total strain was weak and easily masked by other contributing factors. The exponent c systematically decreased as heterogeneity decreased and strength loss on failure increased. Most significantly, simulations with statistically identical material properties but different random heterogeneity in space gave power law distributions with as much variation in c as was observed in experiments with different material properties and different total strains. This result implies that extrapolating information about fault size scaling from one area to an adjacent area is inadvisable, even if the regions have the same lithologies and tectonic histories.

In each simulation, as strain increased, more small faults became inactive and more faults became constrained as their tips abutted other structures or intersected with the perimeter of the model. In combination, these processes caused a break in scaling between large and small fault sizes. The initial conditions and the boundary conditions controlled how fast strain localised onto the large structures and the size and shape of the deforming region influenced when the major faults became constrained. The breakdown in scaling occurs at larger strains, suggesting that extrapolating scaling relationships beyond the range of observation is more likely to give incorrect estimates in higher strain regions.

Preface

This Ph.D. study has included a period of suspension due to contract employment. The period from September until November 1998 was spent working in the Integrated Fields Section of Shell Research and Technical Services, Rijswijk, Holland in fulfilment of the obligations associated with my Shell Postgraduate Bursary.

Elements of the work contained in this thesis have been previously presented by myself in several oral and poster presentations. These were

- EUROROCK 99 - poster presentation
- Spring Meeting of the American Geophysical Union 1999 - oral presentation
- Shell Research and Technical Services, Rijswijk, Holland - invited talk
- GEOSCIENCE 98 - poster presentation
- Tectonic Studies Group of the Geological Society of London 1997 - poster presentation
- Geological Society of America Annual Meeting 1997 - poster presentation
- EAGE North Britain Student Group Annual Research Review - oral presentation

The numerical model used in this study was developed in France and consequently all comments within the code and documentation available at the start of this project were written in French. In addition to this thesis, I have produced an English version of the ADELI Users Guide, which is available on request.

Acknowledgements

I wish to thank my supervisors Patience Cowie, Ian Main and Bertrand Maillot for devising this project and asking the right questions from the very start. I thank Bertrand for setting me off on the right track and Ian for his injections of enthusiasm and for commenting on much of this thesis. Patience has been a constant source of sound scientific advice and encouragement; always believing that the results would come and that they would be worth waiting for. However, a Ph.D. tests one in ways non-scientific too, and in this respect the help, advice and support I received from Patience were invaluable.

This study would not have been possible without the help of many people in the Department of Geology and Geophysics. I would like to thank John Underhill and Nancye Dawers for their comments during the 6 month and 2 year review processes. Thanks also to Zoë Shipton, for sharing her views on faulting and her tent in Utah. She and my other sisters in arms - Ruth Gilpin and Ellen Wolfenden - were sources of support and inspiration throughout my time in Edinburgh. Special thanks must go to those who introduced me to the wondrous mysteries of UNIX, FORTRAN, LaTeX and GAWK - Mark Higgins and Jon Perry - and to Fernando Niño, who was a fine guide in the labyrinth that is ADELI. The computing officers Shane, Justin and Chis all provided help above and beyond the call of duty, with seemingly endless patience and wry humour.

This project was funded by a NERC scholarship and a Shell postgraduate bursary, for which I am grateful. When the money ran out, Colin and Norah Hardacre and John Braisby picked up the tab - many thanks.

The kindness of all my friends has also been greatly appreciated. In particular I would like to thank: Zoë Shipton, Ruth Gilpin and John Braisby for commenting on drafts of this thesis; Andy Hughes and Lynne Chambers for sharing the ups and downs of the first year with me; Andy Taylor and Solveigh Laß who knew little about faults but everything about the stresses and strains of their flatmate; and to Alix for many dinners, coffees and cakes, sage advice and countless laughs. Thanks to all those who persuaded me to go cycling, belly-dancing, rock-climbing and fireclub-swinging: you kept me sane.

I especially thank John B. for his unwavering love and understanding and for making the last twelve months happier than I had thought possible. Final thanks must go to my parents, who provided help and encouragement in this as in all things. Sorry you had to wait 26 years for your daughter to finish school.

Contents

List of Tables

List of Figures

Chapter 1

Introduction

The purpose of this chapter is to explain the concepts necessary to read this work, describe previous relevant studies and outline the aims of the project and the methods used.

1.1 Rationale

Strains in the brittle crust are primarily accommodated by faulting. Faults change the permeability of the rocks around them and they themselves may act as barriers or pathways for fluid flow. Surface faults affect present day drainage patterns, and faults active in the past influence the location of syn-rift sand bodies in modern hydrocarbon reservoirs. Fractures strongly influence the strength and deformability of rock masses. Additionally, active faults may be the site of potentially damaging earthquakes. Consequently, many aspects of natural resource development (oil and water prospecting), radioactive waste disposal, geomechanical engineering and seismic hazard assessment require a more complete understanding of faulting.

A fault population is a network of faults that developed in a single tectonic episode. Three observations of scaling relationships hold true in all populations regardless of their geological settings: larger faults have accumulated more displacement than smaller ones, there is a systematic distribution of fault sizes within arrays and faults are not homogeneously distributed in space. The principal aim of my project is to investigate how the physical mechanisms controlling fault evolution may be related to observed fault population systematics i.e. fault scaling relationships.

Many attempts have been made to link the observed relationship between displacement and length with a physical model for fault growth [e.g. Walsh & Watterson (1988) and Cowie & Scholz (1992*b*)]. By contrast, the physical basis of the fault size frequency distribution has received little attention until now. In particular, the importance of imposed boundary conditions (e.g. the magnitude and direction of far-field stresses) and initial conditions (e.g. the mechanical properties of the deforming region) as opposed to fault growth processes are widely ignored. My work addresses the combined effects of fault growth processes, initial conditions and boundary conditions on fault size frequency distributions.

1.2 Review of Previous Work and Current Understanding

1.2.1 Empirically-derived scaling relationships

Scaling laws describe how attributes (e.g. displacement, length) of differently-sized faults are related. A widely documented fault scaling relationship is that between displacement D and length L, which has the form

$$D = \gamma L^n, \tag{1.1}$$

where γ and n are constants (Walsh & Watterson 1988, Cowie & Scholz 1992*b*, Cowie & Scholz 1992*a*, Dawers, Anders & Scholz 1993, Schlische, Young, Ackermann & Gupta 1996). The numerous studies of this scaling law have led to the conclusion that γ is related to mechanical rock properties [primarily shear strength and rigidity, see Cowie & Scholz (1992*a*) and Cowie (1998a)]. Early studies (Marrett & Allmendinger 1992, Walsh & Watterson 1988) proposed that $n > 1$ but a weight of more recent evidence suggests that in most cases $n \approx 1$, which implies self-similar, fractal growth. Many studies have examined how this scaling relationship is affected by fault type (extensional, compressional or strike-slip: Wojtal (1994)), mechanical layering (Gross *et al.* 1997) and growth mechanism [isolated growth or linkage with other structures: Trudgill & Cartwright (1994), Cartwright, Trudgill & Mansfield (1995) and Dawers & Anders (1995)].

In contrast to the D-L relationship, the form of fault size frequency distributions in continental crust is still the subject of debate. Many authors argue that fault size frequency distributions are power law (Kakimi 1980, Gudmundsson 1987, Main, Meredith, Sammonds & Jones

1990, Villemin & Sunwoo 1987, Childs, Walsh & Watterson 1990, Yielding, Walsh & Watterson 1992, Davy 1993). That is, they can be described by an equation of the form

$$N_{\geq L} = aL^{-c}, \tag{1.2}$$

where $N_{\geq L}$ is the number of faults in the population that are larger than or equal to L, a is a constant, L is the length of a particular fault, and c is the power law exponent. Such functions form a straight line on logarithmic axes, with a gradient equal to c. Note that there is no characteristic length in equation 1.2 , it describes self-similar behaviour. The value of c is still contested. Some authors (Scholz 1997, Sornette & Davy 1991) maintain that there should be a universal value over the whole range of observable sizes , as is the case for the Gutenberg-Richter relation for earthquake magnitudes. Based on his study of faults on Venus, Scholz (1997) proposes that $c = 1$. Others [e.g. Cladouhos & Marrett (1996)] believe that it varies in some systematic way, depending on the mechanisms by which the faults are growing. Scholz & Cowie (1990) argue that c must be limited to a certain range of values because the total fault strain in a deforming region must be finite. According to these authors, for a population of faults with dimensions smaller than the thickness of the brittle crust, $c < 3.0$, whereas for faults larger than this size, $c < 2.0$.

Although a power law does describe many populations, there is still little understanding of the mechanism that gives rise to power law scaling and of the factors controlling the value of c. Alternatives to power law scaling for continental fault populations have also been proposed. Clarke, Cox & Laslett (1999) proposed fitting fault size cumulative frequency distributions with the Feller-Pareto distribution as it contains log-normal, Weibull and gamma distributions as special cases, as suggested by Rives, Razack, Petit & Rawnsley (1992) for joints, Clifton & Schlische (1997) for faults in clay models and Davy (1993) for the San Andreas fault system. Examples of continental fault populations with exponential size distributions also exist (Dawers (pers. com.) and also examples in Section 2.7.5). Characteristic lengths feature in all these distribution types so they are not scale invariant.

In contrast to continental fault populations, the cumulative size frequency distributions of fault length, scarp height and spacing for normal faults generated in oceanic crust are best described by exponential functions (Carbotte & Macdonald 1994, Cowie, Malinverno, Ryan & Edwards 1994). Exponential distributions have the form

$$N_{\geq L} = N_t e^{-\lambda L}, \tag{1.3}$$

where N_t is the total number of measurements and $\lambda = 1/ < L >$, where $< L >$ is the characteristic or mean value of L. Some effort has been made to explain this first-order difference between continental and oceanic fault populations. The appearance of exponential size scaling may be due to the narrow width of the active tectonic zone and Mid-Ocean Ridges and the thinness of the brittle, oceanic lithosphere (Cowie *et al.* 1994). These two factors limit the development of fault populations so that only a small number of faults, close to the axis, are active at any given time. Cowie *et al.* (1994) found that faults close to the ridge (the active population) had a power law size distribution and Bohnenstiehl & Klienrock (1999) found power law size scaling over a wider region adjacent to a faster spreading ridge.

In summary, the D-L relationship is relatively well understood in terms of physical processes. In contrast, there is little real understanding of the physical basis of the scaling relationship between size (L) and cumulative frequency (N). This is the the focus of this thesis.

1.2.2 Applications of scaling laws

Scaling laws for fault sizes have been used in several practical applications. Scholz & Cowie (1990), Marrett & Allmendinger (1991), Walsh, Watterson & Yielding (1991), Marrett & Allmendinger (1992) and Westaway (1994) used displacement length and size cumulative frequency relationships to estimate total extension due to faulting in various regions. These relationships were also used by Gauthier & Lake (1993) when developing a tool to assess the impact of faulting on hydrocarbon reservoir quality. Fault scaling laws were used by Golombek, Banerdt, Tanaka & Tralli (1992) to infer the mechanical behaviour of surface rocks on other planets. Underpinning every one of these uses of size frequency distributions is extrapolation from what can be measured to what cannot. This prompts the question "Are fault scaling laws reliable at predicting fault characteristics outside the observed range?" To answer this question empirically, previous studies have widened the range of fault sizes examined and considered fault populations in different tectonic settings and lithologies. However, this question can really only be answered by understanding the physical controls on fault scaling.

1.2.3 Measuring fault size

The validity of extrapolating scaling laws is still debated because of the difficulties of accurately measuring a wide range of fault sizes on a single image of a faulted region. Whereas the size range of faults in a single system may span up to eight orders of magnitude, the size range

observable from a single image is rarely greater than two orders of magnitude. We can more confidently extrapolate a relationship observed over eight orders of magnitude than over two. Faults on the Earth's surface have been imaged using satellites, aerial photographs and direct observation of outcrops. Faults in the sub-surface have been imaged using seismic reflection surveying, borehole imaging tools and by direct observation of core samples. The largest and smallest structures that can be resolved by each of these techniques vary greatly, but even so no single imaging technique permits the study of faults over more than three orders of magnitude.

The best measurements of fault size are total surface area and summed displacement across the fault surface (see Figure 1.1 for definition of other terms used to describe faults). However, an image of the fault in three dimensions is needed to make these measurements. Such fault images could be generated from 3D seismic data, but no such analysis of fault sizes has been published at present. In the field, it is not even possible to picture faults in this way, so alternative measures of size are used. These are commonly made on 1D line samples or 2D planar samples through the faulted rock volume. Fault sizes measured from 1D samples are displacements encountered along a transect across the earth's surface, along a single horizon on a seismic line or down a bore hole. The strict definition of displacement is the magnitude of the slip vector on the fault surface, but this is rarely reported. More commonly, only the vertical component of slip (the throw) is reported. This is a more convenient measure of fault movement where fault surfaces are not clearly exposed and for those who work with seismic data that has not been depth converted. Marrett & Allmendinger (1992), Walsh & Watterson (1992), Walsh, Watterson & Yielding (1994) and Needham, Yielding & Fox (1996) all give examples of line sampling. Two dimensional samples in map view comprise measurements of fault trace lengths and the maximum displacement measured on each fault trace. In cross sectional view the maximum displacement, not trace length, is the preferred measure (Fossen & Gabrielsen 1996, Ortega & Marrett 2000). Neither 1D or 2D measures of fault size are ideal and the two sampling methods yield different values of c. Although attempts have been made to reconcile the two (Marrett & Allmendinger 1991, Yielding, Needham & Jones 1996) the proposed relationships between c_{1d}, c_{2d} and c_{3d} assume that the distribution of faults in space is random and isotropic, which is rarely the case (Borgos, Cowie & Dawers 2000). It is, therefore, clearly best to compare like with like.

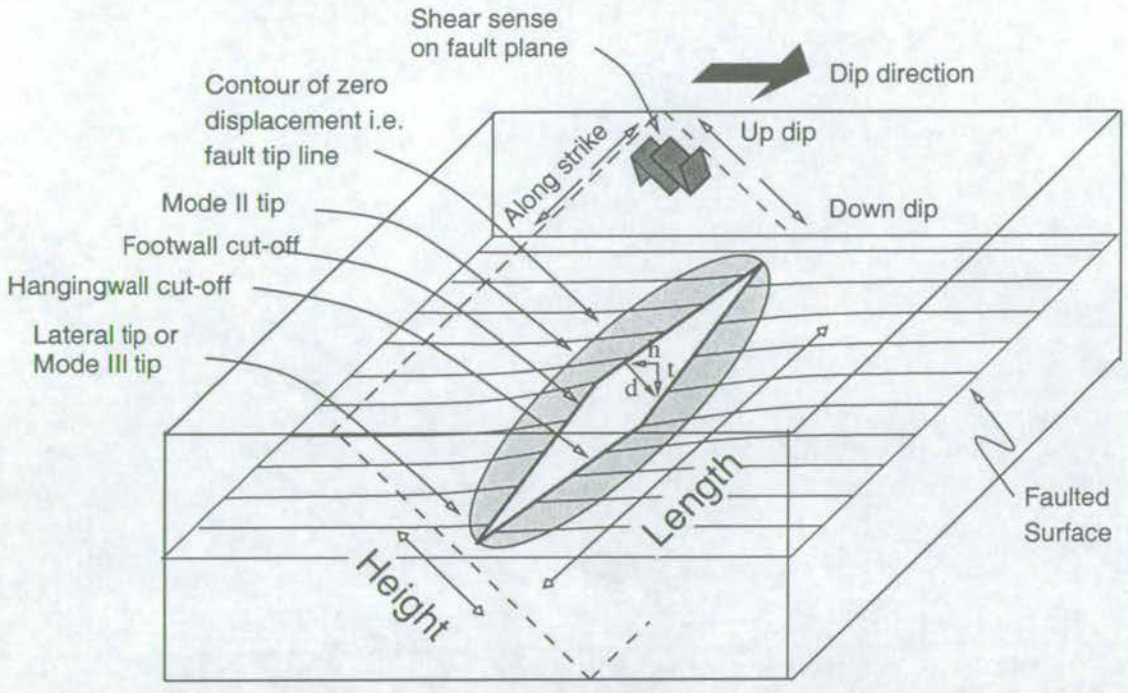

Figure 1.1. Anatomy of a simple fault, where d=displacement, h=heave, t=throw.

1.2.4 Difficulties in compiling size frequency statistics

All fault size data suffer from sampling artifacts, regardless of how the data were collected. Figures 1.2 and 1.3 illustrate the sampling issues associated with a common measure of fault size: trace length in map view.

If we idealise faults as ellipses (Barnett, Mortimer, Rippon, Walsh & Watterson 1987) randomly distributed throughout a volume, the measured trace length on a fault is generally not its maximum horizontal dimension, but depends upon where the measuring surface (map plane or plane of cross section) intersects the fault (Muraoka & Kamata 1983, Walsh & Watterson 1988). This problem is illustrated in Figure 1.2. However, Berkowitz & Adler (1998) concluded this effect alone would not mask the underlying power law distribution of fault sizes, i.e. trace lengths would also show power law scaling. The limited resolution of any imaging technique affects size frequency data in two ways (see Figure 1.3). Firstly, faults below the resolution threshold will not be imaged at all and the number of faults close to the resolution threshold may be underestimated. Secondly, large faults may also be absent from the sample if they lie outside the sample area. In both of these instances the scale range of the sample is less than that of the population. Pickering, Bull & Sanderson (1995) termed this bias *truncation*: the former left hand truncation, the latter right hand truncation. Displacement on an idealised fault is greatest at the centre and decreases linearly towards the tips [e.g. Scholz, Dawers, Yu,

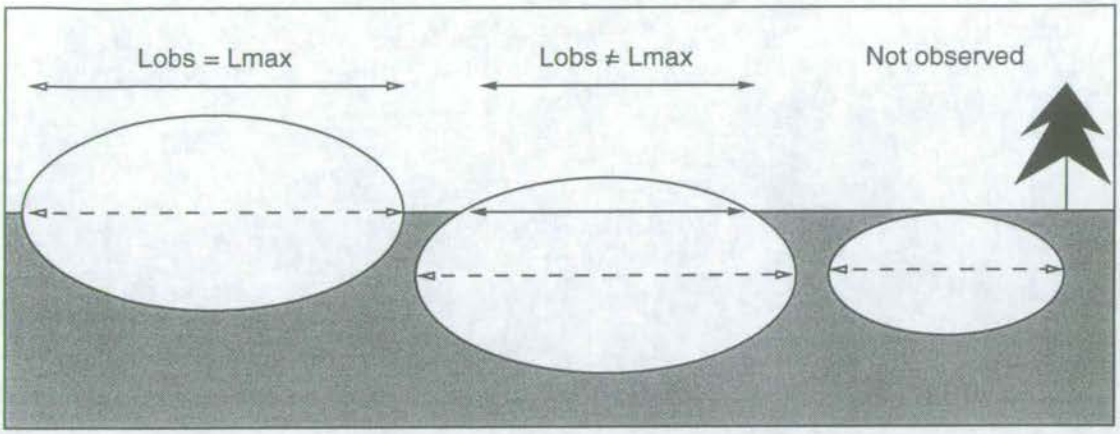

Figure 1.2. The problem of measuring fault trace length. Even for an idealised fault, observed trace length L_{obs} is not equal to the maximum trace length L_{max}. Berkowitz & Adler (1998) refer to this as the "chord" effect.

Anders & Cowie (1993) and Cowie & Shipton (1998)]. If the imaging technique can only resolve bed offsets (throws) above x, the portion of the fault near the tip where the offset is less than x will not be imaged, thus the fault trace length will be underestimated (Pickering, Peacock, Sanderson & Bull 1997). Underestimation of size is termed *censoring* and this systematic form of censoring was dubbed Type C by Pickering *et al.* (1995). Some of the faults in Figure 1.3 extend beyond the boundary of the study area: this is Type B censoring. Finally, as no fracture can have a measured length larger than that of the study area, the length of fractures spanning the entire study area will be underestimated: Pickering *et al.* (1995) dubbed this Type A censoring. Figure 1.3c illustrates the effect of these biases on a truly power law distribution of trace lengths: left hand truncation and censoring lead to shallow slopes at small length scales, whereas right hand truncation and censoring lead to steepening of the slope at large length scales. These deviations from the straight line in log-log space are sometimes referred to as "roll-overs" or "fall-offs". *In extremis*, a combination of these sampling biases may entirely obscure the power law nature of the distribution. This has led some authors to propose alternative functions for size cumulative frequency graphs (Bath (1981) provides a review of these suggestions in the field of earthquake size scaling).

Several authors (Yielding *et al.* 1996, Pickering *et al.* 1997) have proposed schemes whereby sampling biases may be corrected, but these corrections assume underlying power law distributions and linear displacement gradients on faults. Another approach to removing sampling artifacts is to calculate size cumulative frequency distributions from differently scaled images of the same fault population and combine the results. To combine the data at all scales the distributions are normalised, so that length is plotted against number per area. The small faults that are censored on a large scale map would be accurately imaged on a smaller scale

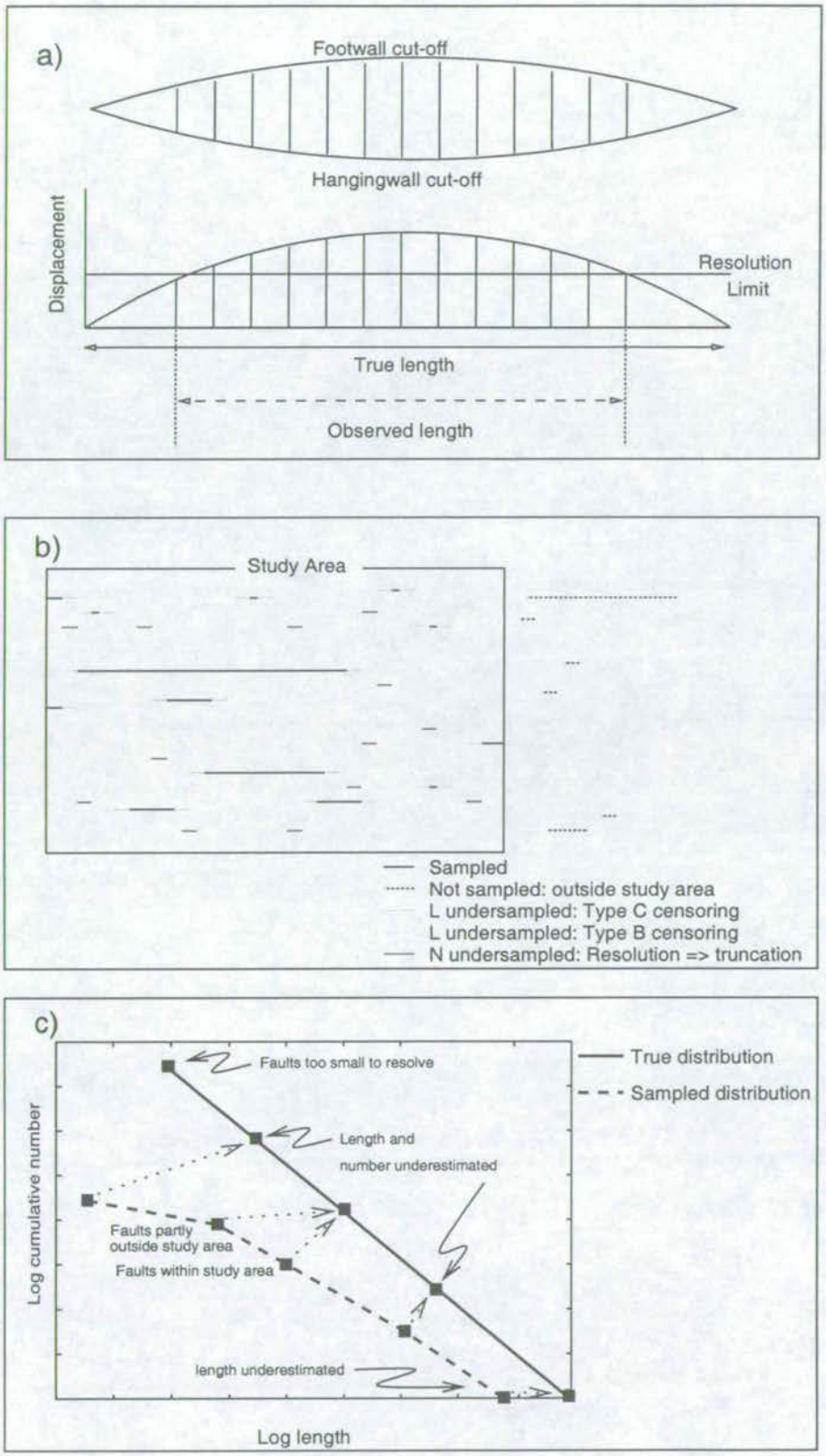

Figure 1.3. a) The effect of limited resolution on a single fault. b) The problems of limited resolution and sampling area dimensions in map view. c) The effect of different sampling biases on size cumulative frequency data.

map, however the large faults entirely within the area of the large scale map would suffer type A and B censoring on the smaller scale map. By combining distributions with overlapping scale ranges, accurate measurements of fault sizes across several orders of magnitude can be obtained. Using this approach Odling (1997) and Marrett (1999) inferred power law size scaling for fault trace lengths and displacements over four and five orders of magnitude, respectively. However, this approached has been criticised (Yielding *et al.* 1996) because, when choosing the sub-regions for small-scale mapping, the human eye is naturally attracted to areas with numerous faults or with complex fault geometries, so this technique may be biased and liable to overestimate the number of small faults.

1.2.5 Variations in power law exponents

Estimates of the power law exponent gathered from 1D transects lie between 0.40 and 1.32 (Nicol, Walsh, Watterson & Gillespie 1996). Yielding *et al.* (1996) report exponents varying between 0.96 and 1.48 when fault size is measured as the maximum displacement on a fault trace in map view. Ortega & Marrett (2000) report a power law exponent $c = 1.98$ for maximum displacement measured in cross-section. Published distributions of trace lengths on maps, summarised on Table 1.1, have values of c between 0.67 (Cladouhos & Marrett 1996) and 2.34 (Odling *et al.* 1999).

1.2.6 Deviations from power law size scaling

Several studies have found deviations from simple power law scaling, which question the significance of scaling relationships and the validity of extrapolating from them. For example, Fossen & Rørnes (1996) report different exponents for small and large faults in a single fault population measured at a single resolution. Ackermann & Schlische (1997) report similar findings. Hatton, Main & Meredith (1994) and Schultz & Fori (1996) relate breaks in slope on $\log faultsize$ versus $\log cumulativenumber$ plots with pre-existing mechanical discontinuities that affected the growth of faults above a certain size. Discontinuities have also been observed in combined datasets ($\log faultsize$ versus $\log numberperkm^2$) spanning several orders of magnitude. Nicol *et al.* (1996) observed that size frequency distributions for small-scale faults had lower power law exponents than those for large-scale faults. They postulated that differences in the power law exponent might reflect changing faulting mechanisms with scale. Castaing *et al.* (1996) and Ouillon, Castaing & Sornette (1996) found that different power law exponents best described size frequency distributions collected at different scales.

Name/location	Source	Size Range	c
Chimney Rock, Utah	Cladouhos & Marrett (1996) from map of Krantz (1988)	0.07-4.0km	0.67
Boso Peninsula, Japan	Kakimi (1980)	0.28-11.9km	0.97
Sinai	Knott *et al.* (1996)	0.31-0.93m	1.02
Corinth, Greece	Poulimenos (2000)	1.0-12km	1.37 1.05*
Laramide, Wyoming	Cladouhos & Marrett (1996) from map of Blackstone (1988)	3.2-240km	1.11
Yucca Mountain, USA	Cladouhos & Marrett (1996) from map of Scott & Castellanos (1984)	0.04-8.4km	1.21
Northern North Sea	Knott *et al.* (1996)	0.25-1.17km	1.29
Bishop Tuff, California	Scholz *et al.* (1993)	0.01-7.0km	1.30
Gulf of Mexico I	Cladouhos & Marrett (1996)	1.4-31.6km	1.66
Gulf of Mexico II	Cladouhos & Marrett (1996)	1.8-35.5km	1.67
Basin and Range	Cladouhos & Marrett (1996) from map of Stewart (1980)	5.0-126km	1.84
Mid-Atlantic Ridge	Bohnenstiehl & Klienrock (1999)	0.15-2.05km	1.64 1.92*
Venus	Scholz (1997)	0.9-42km	2.02
Gulf of Mexico	Cladouhos & Marrett (1996)	1.0-31.6km	2.07
Saudi Arabia	Odling *et al.* (1999)	0.001-1005km	2.34

Table 1.1. Published fault trace length datasets, showing a range of power law exponents. The * symbol denotes c values corrected for sampling biases using the method of Pickering *et al.* (1995).

Furthermore, they linked the lengths at which transitions from one law to the next occurred (so called characteristic lengths) with hierarchical mechanical layering in the crust (varying from bed thickness, to basin depth, to crustal thicknesses). Extrapolation implies a continuous distribution of fault sizes exists. However Koestler (1994) and Fossen & Hesthammer (2000) found faults of certain sizes to be absent in some populations.

1.2.7 Studying fault growth through time

It is often impossible to work out how a fault system evolved through time just by looking at its present day map pattern because repeated slip on faults often destroys or modifies evidence of earlier events. By examining the patterns of sedimentation, uplift and erosion around faults active at the Earth's surface, several authors (Suppe, Chou & Hook 1992, Leeder & Jackson 1993, Childs, Walsh & Watterson 1995, Jackson & Leeder 1994, Nicol, Walsh, Watterson & Underhill 1997, Morewood & Roberts 1999, Gupta, Underhill, Sharp & Gawthorpe 1999) have quantified rates of displacement accumulation and growth in some settings. However, most insights on the temporal development of fault patterns have come from models.

Physical and numerical models are the only ways to observe an entire fault array evolve from its inception on a human timescale. Although physical analogue models have been successfully used to study fault geometries (Kautz & Sclater 1988, McClay 1990, Dresden, Gwildis & Kluegel 1991, Higgins & Harris 1997, Brune & Ellis 1997), and fault population statistics (Davy, Hansen, Bonnet & Zhang 1995, Sornette, Davy & Sornette 1993, Mansfield 1996, Spyropoulos, Griffith, Scholz & Shaw 1999b, Ackermann, Withjack & Schlische 2000), they suffer from problems of reproducibility: no two boxes of sand are quite identical. Numerical models are not as complex as physical analogue models (numerical models typically have thousands of elements, compared with the millions of particles in sandbox experiments), but they offer more explicit control of initial and boundary conditions than physical analogue models and do not suffer from problems of reproducibility.

1.2.8 Numerical modelling

The first step in numerical modelling is to decide upon a conceptual framework that describes mathematically how we suppose rocks deform in response to applied loads. Brittle-elastic (Cowie, Vanneste & Sornette 1993, Maillot, Cowie & Lague 1998) and elasto-plastic (Poliakov, Herrman, Podlachikov & Roux 1994, McKinnon & Garrido de la Barra 1998) conceptual models are the most common. The deformation of elastic-plastic solids has many phenomenological similarities with the deformation of rocks seen in nature and in rock fracturing experiments. Firstly, deformation is permanent: when the deforming stress is released, the material does not recover its undeformed state. Secondly, the stresses required to give observed strains are reasonable tectonically (purely elastic models require unfeasibly large stresses to produce observed strains). Thirdly, deformation of rocks in the upper crust does seem to be a yield point phenomenon. Finally, plasticity theory predicts the localisation of strain into narrow zones, akin to faults. It should be noted that by modelling the deformation as that of a plastic solid on a macroscopic scale, we are not implying anything about the microscopic deformation mechanisms: ductile processes like intra-crystalline gliding or brittle processes like grain boundary sliding, fracturing and crushing may all result in apparently plastic behaviour at larger scales.

There are several computer-aided mathematical techniques for simulating the physics of faulting. They all provide approximate solutions to the equations that predict the response of a rock mass to external forces, but all are limited by computer power and so cannot wholly simulate the complexity of reality. Given this limitation, numerical models form a continuum between two basic approaches. At one end, all the possible physical influences

on faulting are included in the simulation but only simple geometries are considered. For example, the boundary element models of Martel (1997) and Martel (1999) give accurate solutions to the equations of linear elastic fracture mechanics but only a few faults can be modelled and fractures cannot propagate over time. At the opposite end of the spectrum are models which capture only the bare essentials of the physics of fracturing, but simulate realistically large numbers of faults and permit structures to develop over time. The cellular automaton of Wilson, Henderson & Main (1996) and the modified resistor network model of Cowie *et al.* (1993) are close to this end member. Between these extremes of approach lie finite difference (Maillot *et al.* 1998, Spyropoulos, Scholz & Shaw 1999), discrete element (Finch 1998, Aharonov 1999, Homberg, Hu, Angelier, Bergerat & Lacombe 1997) and finite element (Poliakov & Hermann 1994, Huc, Hassani & Chéry 1998, Gerbault, Poliakov & Daignieres 1998, McKinnon & Garrido de la Barra 1998, Dresden *et al.* 1991, Schultz-Ela & Jackson 1996) models. All methods produce errors associated with the discretisation of time and space. In this sense, no method is intrinsically better than another, but the nature of the scientific enquiry can dictate which is most appropriate. A finite element code was used in this study because, unlike some other schemes, boundary conditions are naturally incorporated in finite element models, rheologies are defined explicitly and large strains can be simulated. The code used here, ADELI, lies towards the "complexity of space, simplicity of physics" modelling end-member.

1.2.9 Why power law fault size scaling develops

Power law fault scaling relationships have been observed in extensional, compressional and strike-slip regimes in continental crust. These scaling relationships could not exist if faults at different scales develop independently or if faults in different tectonic regimes develop in fundamentally different ways. Their existence supports the hypothesis that the same mechanisms control fault populations, wherever they may be. Sornette, Davy & Sornette (1990*a*) and Sornette, Davy & Sornette (1990*b*) were the first to propose a theoretical framework for understanding the origin and evolution of fractal fault patterns. They suggested that fractal fault patterns with power law size scaling form in the brittle lithosphere as a consequence of the critical threshold nature of brittle failure and the failure-induced, far reaching stress perturbations predicted by the laws of elasticity. At fault tips and intersections, stresses are concentrated and enhanced (Seagall & Pollard 1980), but in the rocks adjacent to the fault walls, stress is relaxed [these areas are commonly referred to as stress shadows (Cowie, Sornette & Vanneste 1995, Willemse 1997, Harris 1998)]. Thus a combination of screening and enhancement effects spontaneously arise as strain is accommodated by brittle failure. Screening

and enhancement have been shown to be the essential ingredients for fractal pattern generation in many physical systems (Ball 1993).

1.2.10 Proposed controls on fault scaling

Proposed controlling mechanisms fall into three groups: initial conditions, boundary conditions and fault growth processes. Fault nucleation, growth by tip propagation, coalescence and interference all constitute growth processes. The initial conditions of the system are defined by the mechanical properties of the rock (rheology, heterogeneity and anisotropy) plus the size and shape of the deforming region. The boundary conditions are the stresses applied to the region plus any geometrical or kinematic constraints. Nucleation, tip propagation and linkage constitute fault growth processes. Inferences from theory, physical and numerical models form the basis of our current understanding of how these controls influence size scaling in natural fault systems.

1.2.11 Fault orientation

Fault orientations (dip and strike angles) are governed by the stress field and the rock type. However, pre-existing structures (e.g. joints) can also act as planes of failure even if they are not ideally oriented with respect to the stress field. For example, cooling joints in the Bishop Tuff, California, affect the orientation of fault segments in the population studied by Dawers *et al.* (1993), and Cartwright *et al.* (1995) showed that joints affected the development of later faults in the sandstones of the Canyonlands National Park, Utah.

Under conditions of plane strain, the faulting theory of Anderson (1951), predicts the formation of only two, conjugate fault sets. This has led to most cases of multiple fault sets being interpreted in terms of multiple deformation events. However, models proposed by Reches (1978) and Krantz (1988) show theoretically that irrotational three-dimensional strain results in the simultaneous development of four fault sets, arranged in orthorhombic symmetry (Figure 1.4). These models predict that faults will develop parallel to those planes most favourably oriented with respect to principal strain axes, i.e. those planes which require the minimum differential stress and energy dissipation to initiate slip.

These theoretical models are supported by experimental evidence and observations of natural faults. Oertel (1965) recognised the simultaneous development of four orthorhombic fault

a) 2d strain: Conjugate Faults b) 3D strain: Orthorhombic Faults

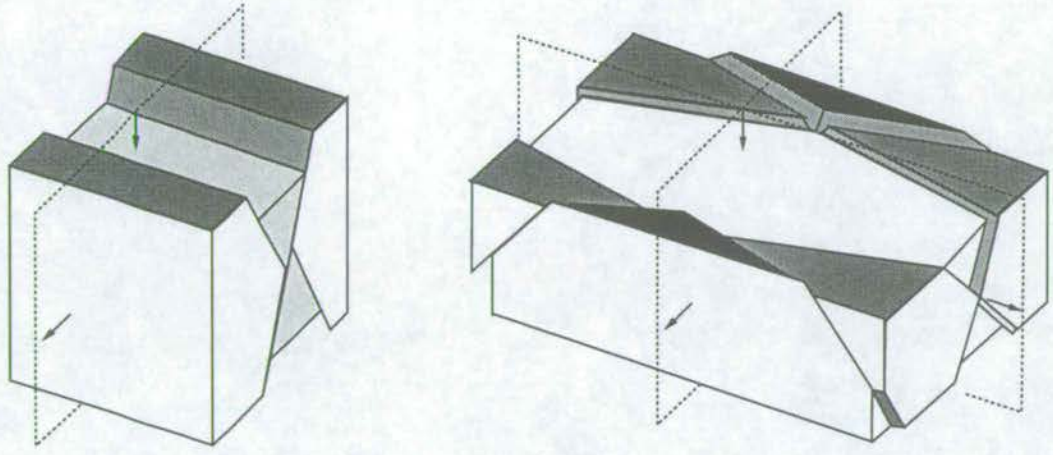

Figure 1.4. The nature of the stress field determines the number of fault sets. Arrows indicate non-zero principal stresses and dashed lines, principal planes of stress. In both scenarios, $\sigma_1 > \sigma_2 > \sigma_3$, but if $\sigma_2 = 0$, two conjugate sets arise, whereas if $\sigma_2 \neq 0$, four fault sets in orthorhombic symmetry result.

sets in analogue experiments, using cakes of clay subjected to three-dimensional deformation. Similar results were obtained by Kautz & Sclater (1988). Multiple fault sets were also seen by Withjack & Scheiner (1982) when they gently domed clay cakes already under uniaxial compression. Aydin & Reches (1982) and Reches & Deitrich (1983) showed that multiple fracture sets commonly develop in rock samples deformed in the laboratory under conditions of triaxial stress. Malone, Rothe & Smith (1975) used records of micro-seismic events in the Columbia River Basalt, Washington, to show that three non-coplanar faults could be active in a single stress field.

Orthorhombic fault sets are not uncommon in continental regions of the earth. Such fault arrays have been described from Texas (Yates & Thompson 1959); the East African Rift Valley (Walsch 1966); the Dixie Valley, Nevada (Thompson & Burke 1973, Krantz 1989); the Rhinegraben (Illies 1977); the Rio Grande Rift (Kelley 1979); the Matanuska Valley, Alaska (Bruhn & Pavlis 1981); Northern Mexico (Tibaldi 1988), Central Asia (Tibaldi & Grazioto 1997) and the Chugach Accretionary Complex, Alaska (Kusky, Bradley & Haeussler 1997). The clearest example, perhaps, being the Summer Lake Fault Array which offsets Tertiary tuffs in Oregon (Donath 1962).

1.2.12 Controls on fault patterns: growth processes

Here I present our current understanding of how fault growth processes affect the development of fault patterns. The processes of nucleation, growth and fault interaction are described in turn.

Nucleation: Nucleation is the formation of isolated cracks in intact rock and is controlled by the magnitude of the applied stress field and the distribution of mechanical weaknesses in a region. At the onset of deformation, failure will first occur where the rock is weakest. Orientations will be controlled by the regional stress, unless the rock has a pre-existing fabric, and most faults will be small.

Growth: Faults can increase in size either by propagation of the tip line or by linkage with other faults nearby. Here, I discuss tip propagation alone: linkage is discussed under the heading *interaction* below. The consensus view is that tip propagation is governed by the local stress field and the rock properties in the vicinity of the fault and within the fault zone itself but precisely how propagation occurs is still debated (Walsh & Watterson 1988, Cowie & Scholz 1992*b*, Marchal, Guiraud, Rives & van den Driessche 1998). As deformation proceeds, some faults may grow faster than others, for example if they encounter weaker rock at their tip line. Alternatively, different growth rates might occur if the deforming material has a strain-softening rheology, making the biggest faults the weakest faults and hence the most likely to slip. Layered brittle-ductile analogue models (Davy *et al.* 1995) have shown that rheological contrasts can also induce strain localisation.

Interaction: Growing faults perturb the stress field around them (Harris (1998) and references therein). Interaction occurs when the fault density is so large that the stress perturbations on nearby faults impinge. Growth by linkage involves an element of chance, related to the probability of finding suitably oriented nearby faults with which to link. However, because of stress shadow and enhancement effects, the availability of potential linkage partners is not random (Cowie 1998b). Indeed, Wu & Brun (1994) and Marchal *et al.* (1998) observed that small, coplanar faults commonly form ahead of propagating fault tips, enabling growth by hierarchical linkage.

Depending on the geometrical arrangement of the faults, interaction can either prevent the tips from advancing further or encourage them to propagate towards each other. When co-planar faults (faults with the same strike and dip) with some offset either along strike (Peacock & Sanderson 1991, Cartwright *et al.* 1995) or down-dip (Mansfield 1996, Childs, Nicol, Walsh

& Watterson 1996) interact, they can easily breach the region separating them producing a single fracture with only a slight dog-leg. If the faults are conjugate (same strike but opposite dip direction) and are separated along strike, linkage of their lateral tips is inhibited (Clifton, Schlische, Withjack & Ackermann 2000). However, small structures oblique to the main fault may develop in the region in between (Rosendahl 1975). These small structures are rarely parallel to the major faults nearby as their orientations are controlled by the local, not regional stress field.

Synchronous slip on non-coplanar intersecting faults is possible [interactions between conjugate structures in cross-section have been documented by Horsfield (1980) and Watterson, Nicol, Walsh & Meier (1998)] but only within certain geometrical/kinematic constraints. One such constraint is that faults cannot slip in ways that would cause fault blocks to overlap. Jackson & McKenzie (1983) argue that two intersecting faults can only be active if the slip vector of each fault lies within the plane of the other, such that continued slip does not generate voids at depth. King (1983) suggests slip is possible even when the slip vectors are not so conveniently aligned, but states that such slip requires pervasive fracturing of the surrounding fault blocks. He postulated that faults with a fractal size distribution could be generated in this way. Peacock & Sanderson (1991) were the first to observe that displacement profiles are affected by interaction between faults. Maerten, Willemse, Pollard & Rawnsley (1999) showed, using a numerical 3D model of cracks in an elastic medium, that interaction between faults at high angles modifies the local stress field and causes asymmetric/irregular slip distributions. Fault interaction and linkage in almost all geometries allows the development of small structures adjacent to the major faults in orientations not predicted/required by the regional stress field.

Localisation and Large Strain Phenomena: As total strain increases, Nicol *et al.* (1997) (natural faults), Ackermann *et al.* (2000) (clay model) and Cowie *et al.* (1993) (numerical model) report synchronous switching-off of small faults and localisation of strain onto the largest faults in the population. In the Cowie *et al.* (1993) model, this localisation arose through feedback between failure and re-loading of along-strike faults, but it is commonly related to strain-softening of the fault zone. Even without strain-softening, strain may localise onto the largest faults by the following mechanism. If the region is being deformed at a constant strain rate, at all times in the evolution of the array fault movement must accommodate the same amount of strain energy within a given interval of time. As faults grow, their surface areas increase, so rupturing the entire fault surface requires more energy. The population of growing faults can meet the imposed constant energy input in two ways: either all faults stay active (increasing surface area) but the time interval between successive slip events on each fault increases (decreasing displacement accumulation rate) or some faults switch off (which maintains or lowers slip surface

area) whilst others continue to accumulate displacement at a constant or even an increased rate. Syn-sedimentary faults arrays in several basins worldwide have been shown (Nicol *et al.* 1997) to exhibit this behaviour, with large faults having the same high displacement rate throughout their lives, but smaller faults having lower rates which decrease with time. There are, however, examples of the reverse happening at large strains: large faults becoming inactive and renewed activity of small faults coupled with nucleation of new structures. For instance, large tectonic rotation may inhibit movement on existing faults so that an entirely new set of faults must develop to accommodate the strain (Scotti, Nur & Estevez 1991, Jackson & McKenzie 1983).

1.2.13 Controls on fault patterns: initial and boundary conditions

Fault growth processes play an important part in the development of fault arrays but we should not underestimate the influence of initial conditions and boundary conditions.

Dealing first with boundary conditions, it is intuitive that the direction and magnitude of far field stresses will have some control on the orientation, size and number of faults which develop in a deforming region. Above, we noted that the geometry of faulting affects linkage opportunities: linkage is more likely in fault arrays with one fault set (co-planar arrays) rather than two (conjugate arrays) or more (e.g. orthorhombic arrays, with four fault sets) fault orientations. As the boundary conditions control the number of fault sets (Reches & Deitrich 1983), they should also control the likelihood of linkage. It has also been suggested that strain rate affects fault population development. In his discrete element numerical model, Tuckwell (2000*a*) observes that a minimum energy solution (localised deformation) is only reached if the rate at which the material is forced to change shape is comparable with the rate at which fault growth processes can accommodate the imposed shape change. If, however, the imposed strain rate outstrips faulting processes, disequilibrium (diffuse deformation) results. Deformation was more localised in slow strain rate analogue modelling experiments, which used a brittle layer of sand overlying a viscous layer (Davy *et al.* 1995). Strain rate-dependent localisation was also observed in a numerical model of failure in a viscoelastic material (Handge, Sokolov & Blumen 1997).

Coming to the initial conditions, the distribution of mechanical weaknesses in a deforming region initially controls nucleation and will influence subsequent growth, as described above. Davy *et al.* (1995) displayed the importance of rheological contrasts for the localisation of faulting using layered brittle-ductile analogue models. The rheology of fault zone rocks (whether they are strain-hardening or strain-softening) and whether stress is supported predominantly

at the tips or across the entire fault surface (Cowie & Shipton 1998) is also crucial to the spatial and temporal localisation of deformation.

It is also clear that basinal features such as width, depth to basement and basement structure will play a part in fault array evolution. The first two limit the size of the largest structure, whereas pre-existing basement structure may control the location of faults in space, at least initially (Fossen & Gabrielsen 1996, Kautz & Sclater 1988, Higgins & Harris 1997). Ackermann *et al.* (2000) showed that the thickness of a deforming layer also affects fault population evolution. He defined three types of behaviour in wet clay models: Stage I - Nucleation, Stage II - Transition and Stage III - Saturation. In Stage I, faults are free to grow in all directions (they are *unconstrained*) and typically have aspect ratios (length:height) of 2:1. In Stage II, large faults span the layer and can no longer grow up or down dip (in the terminology of Ackermann & Schlische (1997), they are *constrained*). Ackermann *et al.* (2000) find that faults accumulate displacement more slowly once they are constrained. This necessitates faster lengthening of existing faults and spatial infilling by new faults, which leads to higher fault aspect ratios. In Stage III, faults are regularly spaced as a function of mechanical layer thickness and spatial infilling stops. These criteria define saturation *sensu* Wu & Pollard (1995). Faults which span layers generally show flat-topped displacement profiles rather than the peaked distributions that characterise faults with free tip lines (Dawers *et al.* 1993). Faults can also be constrained at their lateral tips if they span the width of the deforming region. Gudmundsson (2000) discusses how constraining lateral tips may influence displacement-length scaling relationships, but to my knowledge no-one has studied the impact of different map dimensions/aspect ratios on fault population development and fault size frequency distributions.

1.2.14 How proposed controls affect fault scaling

To date, quantitative research on this topic has focused on the importance of different growth processes in fault array evolution and, with the exception of layer thickness, the influence of initial and boundary conditions on fault scaling has been relatively neglected. All studies of fault pattern evolution and fault scaling relationship development have one conclusion in common: the dominant processes change through time and so do the scaling parameters. For example, Sornette *et al.* (1993), Cowie *et al.* (1995), Cladouhos & Marrett (1996) and Ackermann *et al.* (2000) all report that c (the power law exponent of the fault size cumulative frequency distribution) decreases through time.

Displacement profiles and the displacement-length (D-L) scaling relationship have been used

to assess the relative importance of tip propagation versus linkage in particular fault arrays. A large scatter in the D/L ratio with many "under-displaced" faults showing irregular displacement profiles are thought to be indicative of linkage-dominant environments (Cartwright *et al.* 1995). Simpler profiles and less scattered D-L distributions are thought to characterise areas where linkage is inhibited. Ackermann & Schlische (1999) proposed that linear displacement length scaling breaks down when faults become constrained such that $n < 1$ in $D = \gamma L^n$.

Analogue models (both physical and numerical) have provided most of our information regarding the effect of growth processes, initial conditions and boundary conditions on fault size frequency distributions. Cladouhos & Marrett (1996) quantitatively evaluated the effects of nucleation, death, isolated growth and growth by linkage on the size frequency distributions of fault populations. They used a very simple, geometrical model of fault growth (vertical, parallel faults), in which interaction always led to linkage. Cladouhos & Marrett (1996) showed that, in their model, power law size scaling emerged spontaneously when faults began to link. They claimed that power law size scaling cannot develop or even be maintained by faults growing in isolation. Linkage decreases the total number of faults and increases the size of the largest faults and so lowers the slope of the size frequency distribution with time. Fault interaction which frustrates tip propagation does not affect size frequency distributions in such a predictable manner. There need be no effect on the size distribution if the faults previously propagating both lateral tips switch to propagating only one. Alternatively, if they become completely inactive, other faults in the system would be able to grow faster. If small faults gain the increased displacement rates, the slope of the distribution would go up, but if the increased displacement rates affected only large faults the slope of the distribution would go down. Interaction between faults producing small accommodation structures around the intersection would increase the slope of the size distribution. Yielding *et al.* (1996) interpreted power law size frequency distributions with large negative exponents in terms of this phenomenon.

As mechanical properties (heterogeneity, rheology and anisotropy) are difficult to reliably measure in the field (Katz, Reches, Lyakovsky & Baer 1999, Gross 1999) or control in analogue models, insights on the effects of these initial conditions on size frequency distributions have primarily come from numerical simulations. Sornette *et al.* (1990*a*, 1993) showed that heterogeneity in the brittle layer was a feature of all numerical and analogue models exhibiting fractal fault patterns and self-organised behaviour. In analogue models, heterogeneity takes the form of variability in the shape and size of sand grains (Sornette *et al.* 1990*a*). In numerical models, the heterogeneity may be prescribed [e.g. Cowie *et al.* (1993)] or enter via numerical noise [e.g. Poliakov *et al.* (1994)]. Cowie *et al.* (1993) demonstrated in a 2D numerical simulation that fractal fault patterns and power law scaling relationship develop

even when the undeformed material is randomly heterogeneous. This shows that organisation in fault populations is not inherited: fault arrays are self-organising systems. Tuckwell (2000*a*) concluded from a discrete element numerical model that increasing heterogeneity leads to increasingly localised deformation (although he does not explain what is meant by "increased heterogeneity": wider variation in elastic moduli, larger standard deviation of the strength distribution etc.). Cox & Paterson (1989, 1990) reached the opposite conclusion using a finite element model with heterogeneity in strength.

The effect of layer thickness on fault scaling statistics has been studied by Ackermann, Schlische & Withjack (1997). This analogue modelling study suggests that when the largest fault spans the entire thickness of the deforming region, power law size scaling breaks down, and faults begin to exhibit exponential size distributions. These authors note that the crust contains layering on different scales and that faults of different sizes will be affected by layering at different scales. They postulate that size frequency distributions may not be continuous as a result: small faults and large faults may show power law scaling with different exponents if they are unconstrained with respect to different mechanical layers. Alternatively, if small faults are unconstrained but large faults are constrained, the distribution will be a power law for small faults but exponential for large ones. Pacheco, Scholz & Sykes (1992), Davy (1993), Westaway (1994) and Scholz (1995) also suggest that changes in the power law exponent indicate different regimes of boundary conditions. They consequently conclude that changes in c at characteristic length scales could be a new and unique constraint on the geometry of critical mechanical elements in the brittle crust.

1.3 What's new about this approach?

The contribution of this work is novel for two reasons - the range of controls considered and the recognition of the importance of inactive as well as active structures. Several analogue and numerical models have been used to simulate the development of fault populations. Some have focused on the processes by which faults grow; namely nucleation, propagation and linkage. Others have considered the effects of heterogeneity in material properties, rheology, the dimensions of the deforming area or the boundary conditions. This is the first study in which all of the above are considered.

Though previous studies have reported faults becoming inactive, this is the first study to

explicitly monitor the separate contributions to fault size frequency distributions made by active and inactive structures.

1.4 Aims of the Project

The specific questions tackled by this study are:

- How do the proposed controls influence fault size frequency distributions?
- Is it appropriate to describe fault size frequency distributions with power laws?
- If so, is the power law exponent constant over the complete scale range? And if not, what can be deduced from the variations?
- Can a single power law exponent be used to describe all groups of faults, as is the case with the Gutenberg-Richter frequency magnitude relation for earthquake populations.
- What determines the pattern of activity and how does this affect size frequency distributions?

1.5 Thesis Organisation

There are two possible ways to tackle the problem of fault array evolution: field studies and modelling. In Chapter 2, I present a field study from an orthorhombic fault array and suggest how the fault size frequency distributions might be affected by the geometry of faulting and the mechanical layering of the faulted rock. Field studies are the only way to observe real fault patterns, but are limited in that they only reveal a snapshot of the deformation. Models are required to investigate the development of faults through time. In Chapter 3, I discuss the relative merits of numerical and physical modelling, before explaining my choice of a finite element model for this study. Numerical models of faulting require both a mechanical theory and a computational method: those employed in this study are described in Chapter 3. In Chapter 4, I describe how faults were defined in the model and how the output was processed to yield fault properties like dip, displacement and size, which are commonly measured in the field. The evolution of fault populations in two typical simulations is described in terms of these fault properties in Chapter 5. Here I also describe how changes in the fault size frequency distribution are related to changes in the proportion of faults that are active and

changes in fault growth mechanisms through time. The purpose of Chapter 6 is to show how the general relationships described in Chapter 5 are affected by changing the internal properties of the deforming medium, such as the spatial arrangement of weaknesses, the range of strengths present and the amount of strength-loss experienced at failure. In Chapter 7 I present experiments that show how the shape of the deforming region and its mechanical interaction with its surroundings (specifically, whether the deforming region rests on a rigid layer or a viscous fluid) affects fault behaviour. In Chapter 8, I present a synthesis of the results presented in previous chapters, state my conclusions and make some recommendations for future work.

Chapter 2

Fieldwork

Field studies are the only way to observe real fault patterns. This chapter focuses on fieldwork carried out in the Chimney Rock Fault Array, Utah. In addition to structural measurements I collected in the field, I also present fault size frequency distributions for this array. I discuss the problems associated with measuring the length of intersecting fault traces and present fault size frequency distributions for two other orthorhombic arrays. Structural data and fault size frequency distributions from the Chimney Rock Array illustrate the importance of kinematic constraints as well as fault growth processes in controlling fault array evolution.

2.1 Fieldwork Motivation

The fieldwork element of this project was motivated by the question "When examining the patterns made by a population of faults, how much of what we see is a response to regional boundary conditions and how much is caused by more local influences?" Smaller faults in a population are central to this question. If the regional scale is the dominant influence, nucleation generally occurs at the onset of deformation. In this case, small faults are simply old faults that were abandoned early on, as strain localised onto the largest structures. Their orientations and slip senses are dictated by the regional stress field. If the remaining active faults grow by linkage, we expect the exponent of the size frequency distribution (c) to decrease through time. However, if local conditions generate new faults, for example to accommodate interaction between, and continued movement on, older, larger faults, then nucleation can continue throughout the active life of the population. Small structures so produced are not

necessarily oriented favourably with respect to the regional stress field. If local conditions require continued nucleation, c need not decrease as strain increases.

The relative numbers of old, abandoned small faults versus those formed as accommodation structures will depend on fault geometry and how far the system has evolved. In arrays of coplanar faults, we might expect most small faults to belong to the first group i.e. old, abandoned structures. In arrays with more than one strike direction, and hence more interactions between non-coplanar faults, we would expect to see relatively more accommodation structures. Geometry has a further effect. In arrays where all faults have the same dip and strike, it is quite probable that a growing fault will find at its tip a fault with which it can link, but this is less likely in conjugate arrays and less likely still in arrays with multiple strike directions.

The field study of Chimney Rock Fault Array, Utah was motivated by two seemingly inconsistent observations. Faults in the array have orthorhombic symmetry and so we would expect there to be many small accommodation structures and few examples of faults linking, and hence a high c value. However, Cladouhos & Marrett (1996) calculated a c value for this array equal to 0.67: a low value compared with the other datasets in their study (see Figure 2.1). These observations may be reconciled if all four fault sets were not simultaneously active, if the reported value of c is incorrect or if the low value of c was produced by a mechanism other than fault linkage. These ideas were investigated in the field.

2.2 Previous Work in the Field Area and Fieldwork Aims

The Chimney Rock Array has featured in three previous studies. Krantz (1988) concluded that the Chimney Rock faults constitute an orthorhombic array formed at depth under conditions of triaxial stress, after mapping their outcrops and recording displacements and slip senses. His map of the area was used by Cladouhos & Marrett (1996) to create a fault size cumulative frequency distribution for this array (See Figure 2.1). Shipton (1999) used the faults of the Chimney Rock Array in her investigation of the relationships between displacement, length and the zone of damage surrounding a fault.

My fieldwork in the Chimney Rock Array had three aims:

1. To verify the claim (Krantz 1988) that all four fault sets were simultaneously active and

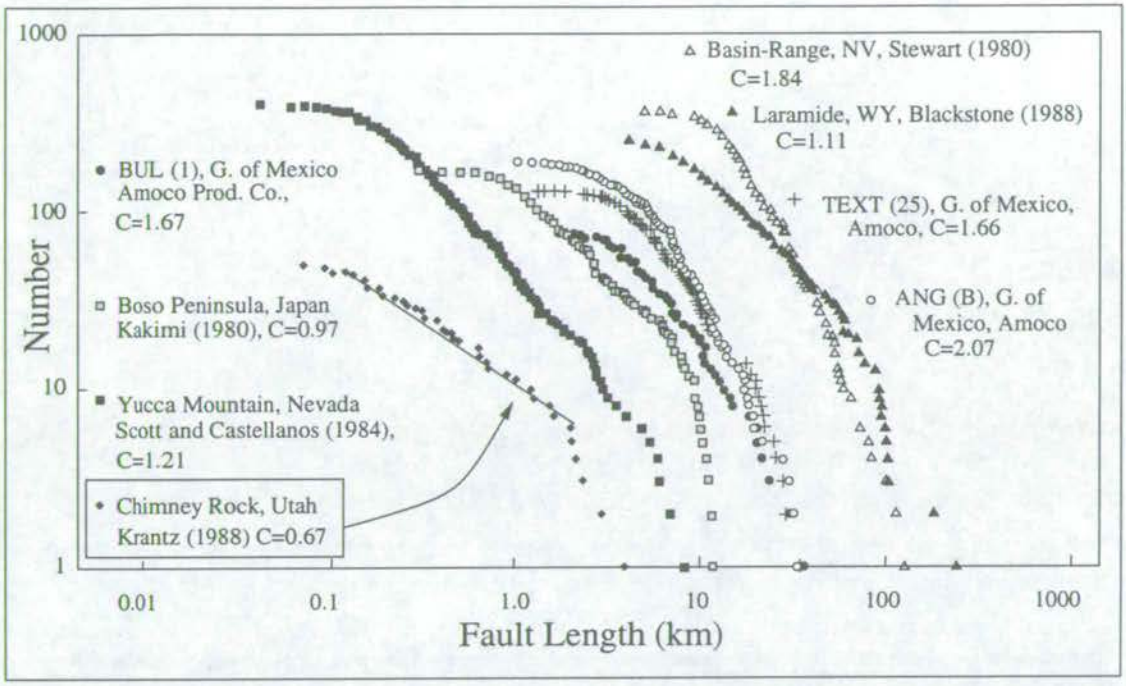

Figure 2.1. Size cumulative frequency plot (on logarithmic axes) of several datasets including the Chimney Rock Array. Note the comparatively low slope of the Chimney Rock distribution. After Cladouhos & Marrett 1996.

to record the orientation and slip senses of small scale structures, particularly near fault intersections.

2. To determine whether intersecting faults continued to slip or locked up, as this could influence the array's size frequency distribution.

3. To determine if the fault sizes in the array really do follow a power law with a low value of c. In order to do this I had to test the validity of the statistical analysis used by Cladouhos & Marrett (1996) and test the accuracy of the map made by Krantz (1988) on which their analysis was based.

2.3 The Field Area

The Chimney Rock Fault Array (CRFA) is located in the San Rafael Swell, East Central Utah (Figure 2.2), and has wonderful 3D exposure of faults in deep, winding canyons. The Swell is a broad asymmetric, NE-trending upwarp approximately 120km long and 50km wide. The strata on the western flank dip $2-6^{o}$ to the west whereas those on the eastern edge dip between 45 and 85^{o} in the opposite direction. In the region of Chimney Rock, which is near the crest of

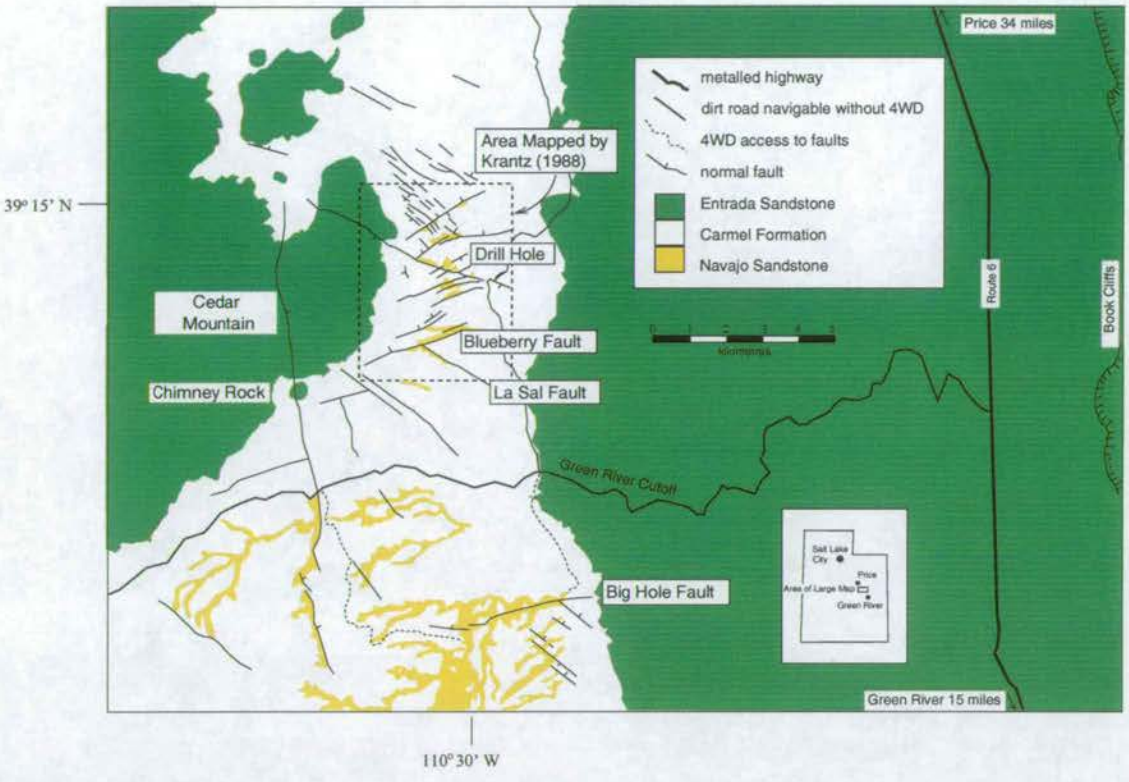

Figure 2.2. The location of the field area, after Shipton 1999, based on maps produced by the United States Geological Survey (USGS).

the fold, bedding dips gently 4^o to the southeast. The swell is one of many structural highs thought to have formed during the Laramide Orogeny, 80 – 54 million years ago. NE-SW compression activated old basement structures as thrusts, generating monoclines or drape folds in the overlying units (Kelley 1955, Davis 1978). The CRFA outcrops in the Lower Jurassic Navajo and Middle Jurassic Carmel Formations. The Navajo Formation is a fine-grained, well-sorted, high porosity [> 24%, (Aydin & Johnson 1978)] sandstone with large aeolian cross beds interspersed with massive planar beds. It lies below the Carmel Formation, which consists of interbedded marine limestones and shaley marls. The marine incursion which separates the two is marked by palaeotopography and a unit full of slump structures at the top of the Navajo. The thickness of the massive sandstone of the Navajo Formation in the region of the CRFA has been estimated at 115m (Krantz (1986), p.51). Bedding within the Carmel Formation is laterally continuous and is an ideal marker with which to constrain fault throw.

Within the Navajo, the faults are not simple slip planes but wide zones of densely packed deformation bands which anastamose up dip, down dip and along strike. Deformation bands form due to the rolling and crushing of quartz grains during deformation (Aydin & Reches 1982, Mair 1997, Mair, Main & Elphick 2000). They are more resistant to weathering than their

surroundings (Figure 2.3) and stand proud of weathered surfaces. Slip surfaces within bundles of deformation bands are polished and striated but by no means planar, having undulations parallel to the slip direction on scales from centimetres to metres. The zone of deformation bands surrounding a slip surface is sometimes referred to as a damage zone (Shipton 1999). This expression of deformation is characteristic of high porosity sandstones. The faults of the Chimney Rock Array vary in length from 100m to 6km, have displacements in the range 1m to 29m and are typically steeply dipping ($65 - 85^0$). The array consists of four fault sets arranged in orthorhombic symmetry, as shown by Figure 2.4. The depth at which the CRFA formed is not known.

2.4 Fieldwork Strategy

The fieldwork comprised a preliminary survey of the whole area and more detailed surveys of two specific regions where non-coplanar faults intersect. These areas are shown highlighted in Figure 2.4 and are hereafter referred to as the La Sal and Drillhole Intersections. Maps of these areas were constructed using a Topcon laser theodolite, which gives the x, y and z coordinates of a reflector with a precision of ±5mm over distances up to 1.8km. In each region, the top of the Navajo Formation, several distinctive beds within the Carmel Formation and fault slip surfaces were surveyed. Throw profiles for each fault could then be obtained by measuring the vertical separation between the hangingwall and footwall outcrops of each bed. Measurements were made of the orientation of striae and slip surfaces within fault zones and these measurement locations were also surveyed.

2.5 Aim I: Do All Chimney Rock Structures Fit the Orthorhombic Model?

The preliminary survey revealed that mutually cross-cutting relationships exist between faults on all scales in the four predicted orientations. For example, among the major faults (Figure 2.4), the NW-striking Glass fault truncates the NE-striking North Fault whilst the NE-striking Blueberry Fault truncates the NW-striking La Sal Fault. This observation forces us to reject the hypothesis that the Chimney Rock faults formed by the superposition of two conjugate fault sets. Slickenlines on fault surfaces were predominantly dip-slip, as reported by (Krantz 1988). The small degree of variability in measured slip direction could be accounted

Figure 2.3. Typical morphology of faults in the high porosity Navajo sandstone. Hammer for scale.

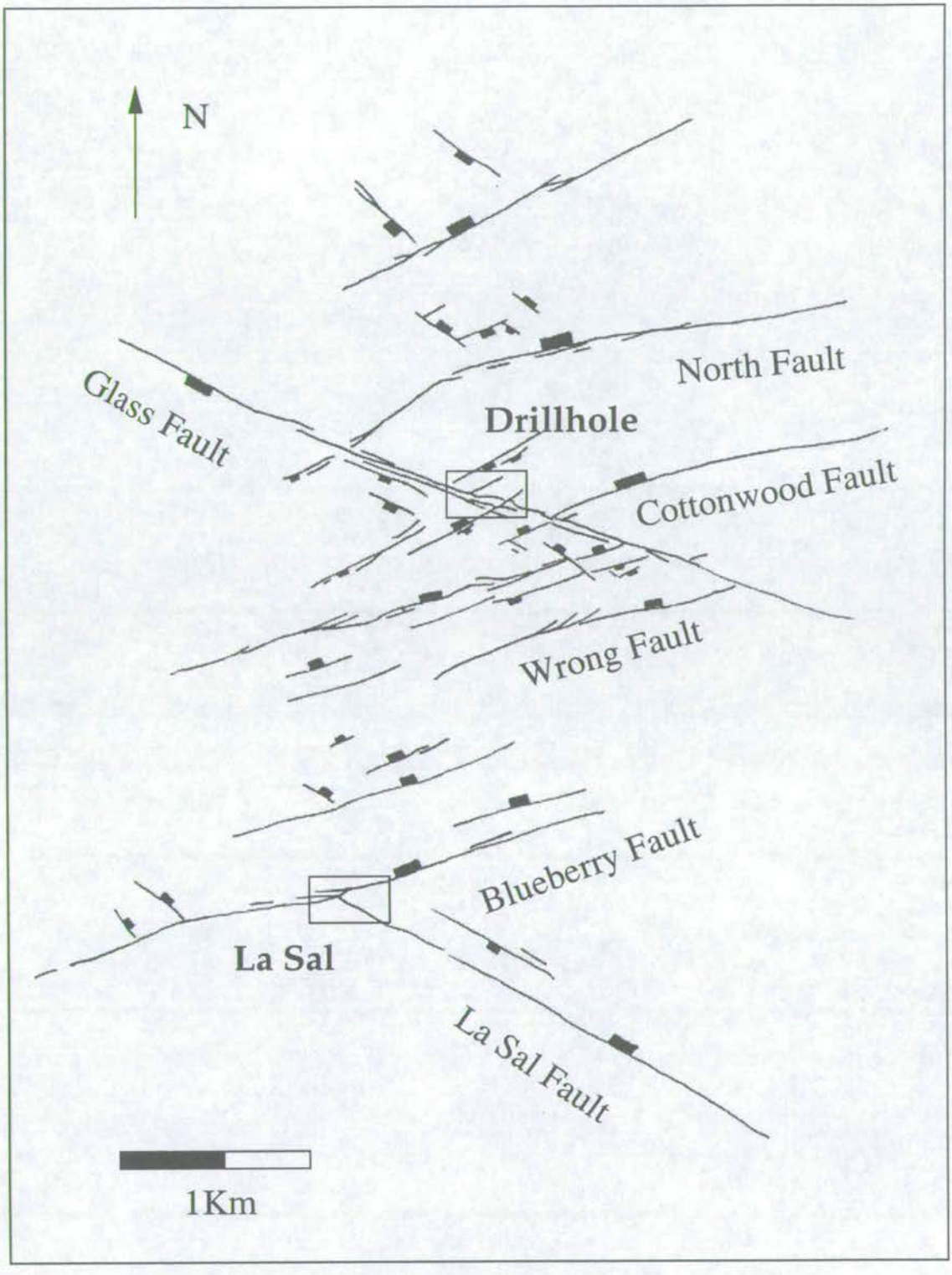

Figure 2.4. The orthorhombic faults of the Chimney Rock Array, after Krantz(1988).

for by changes in fault shape or differences in frictional anisotropy along the fault, as suggested by Pollard, Saltzer & Rubin (1993) and Wojtal (1996). My investigation of the orientations, slip directions and cross-cutting relationships displayed by the Chimney Rock faults support the theory (Krantz 1986, 1988, 1989) that these structures formed as a coeval, orthorhombic array in a triaxial stress field.

Krantz's map (Krantz 1986) adequately represents the large scale structure of the array, but is inadequate in small regions where several faults intersect, such as the study areas. Figures 2.5 and 2.6 show maps of the La Sal and Drillhole Intersections. Structural data for the two areas are shown on lower hemispherical, equal area projections in Figure 2.7, with data from Krantz (1988) for comparison. To aid descriptions of deviations from the orthorhombic model, I introduce the term "co-pitch": the angle measured on a fault plane between a striation and the dip direction. Dip-slip striae have a co-pitch of 0^o, strike-slip striae, a co-pitch of 90^o.

In both areas, it is apparent that there are significant departures from the ideal model of orthorhombic faults with pure dip-slip. Most importantly, both maps and stereonets reveal faults in unpredicted orientations with oblique striations. The poles to planes and the slip vectors plotted on Figure 2.7b and *c* do not define four clusters, unlike the data collected by Krantz (1988) (Figure 2.7a), and certainly do not fall within the 95% confidence limits of his data.

Figure 2.8 illustrates another way to compare the fault system at the intersections with the predictions of the orthorhombic model. Pairs of fault plane and slip direction measurements are rotated so that the three principal strains are vertical, N-S and E-W. The fault poles are then reflected into the NE quadrant of the stereonet, following the rules of orthorhombic symmetry. The fault pole and slip measurement that make up each pair undergo the same reflection. Krantz (1989) states that, after this transformation, the faults in his dataset have a mean dip and dip direction of 72° to 204. The theory of orthorhombic faulting (see Chapter 1) predicts dip-slip on this surface, i.e. striae plunging at 72° to 204. The striae on Figure 2.8a [data from Krantz (1989)] are clearly better clustered about the predicted slip direction than are the striae on Figure 2.8b, which were collected by myself at the La Sal and Drillhole intersections. It would appear that the fault system viewed as a whole fits the orthorhombic model better than the fault systems at the intersections.

The structures at the intersections exhibit another deviation from the ideal model. In the ideal model, faults are freely-slipping planar features, but at the Drillhole the fault forms a breccia 14 m thick at its widest point. Finally, Krantz's model (Krantz 1988) assumes all strain is

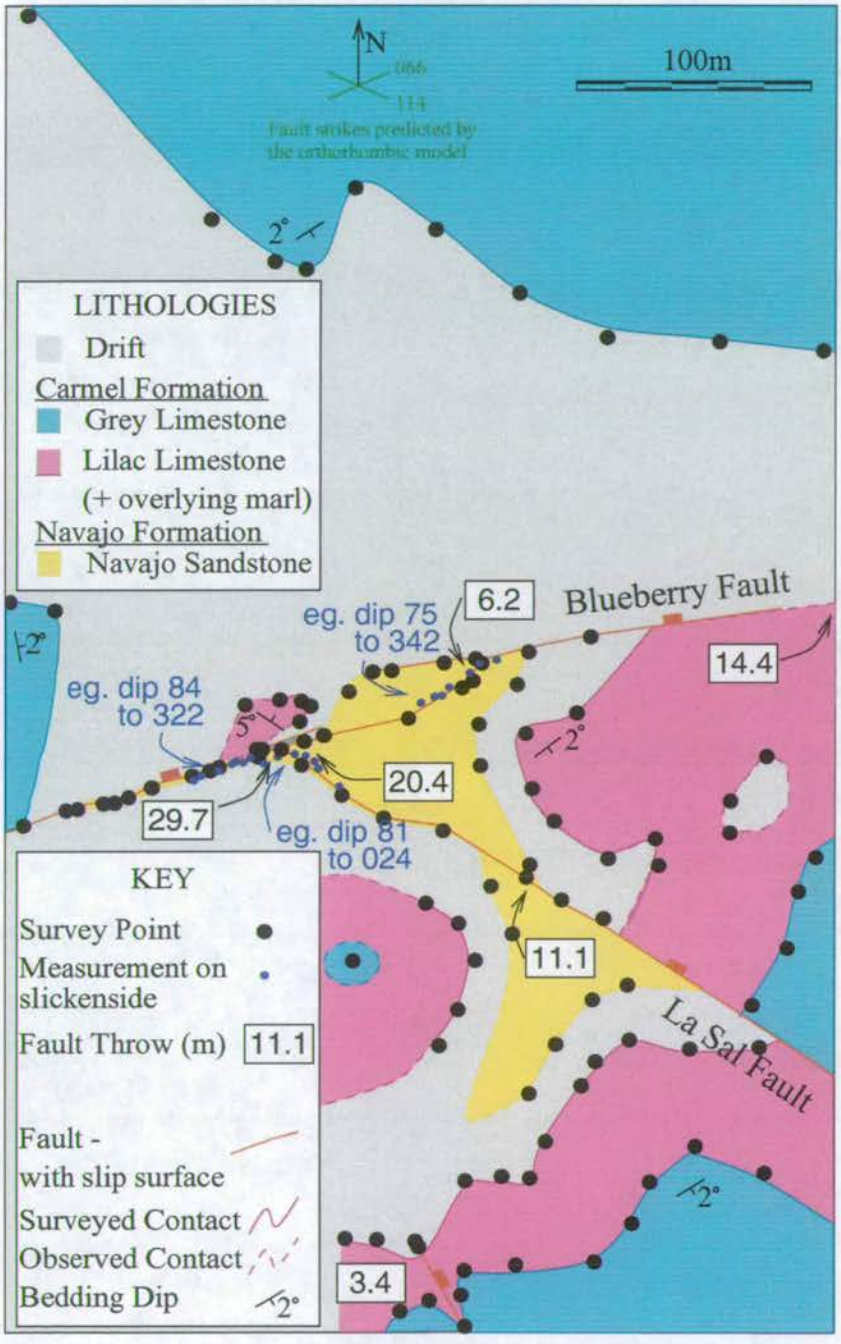

Figure 2.5. Map of the La Sal Intersection.

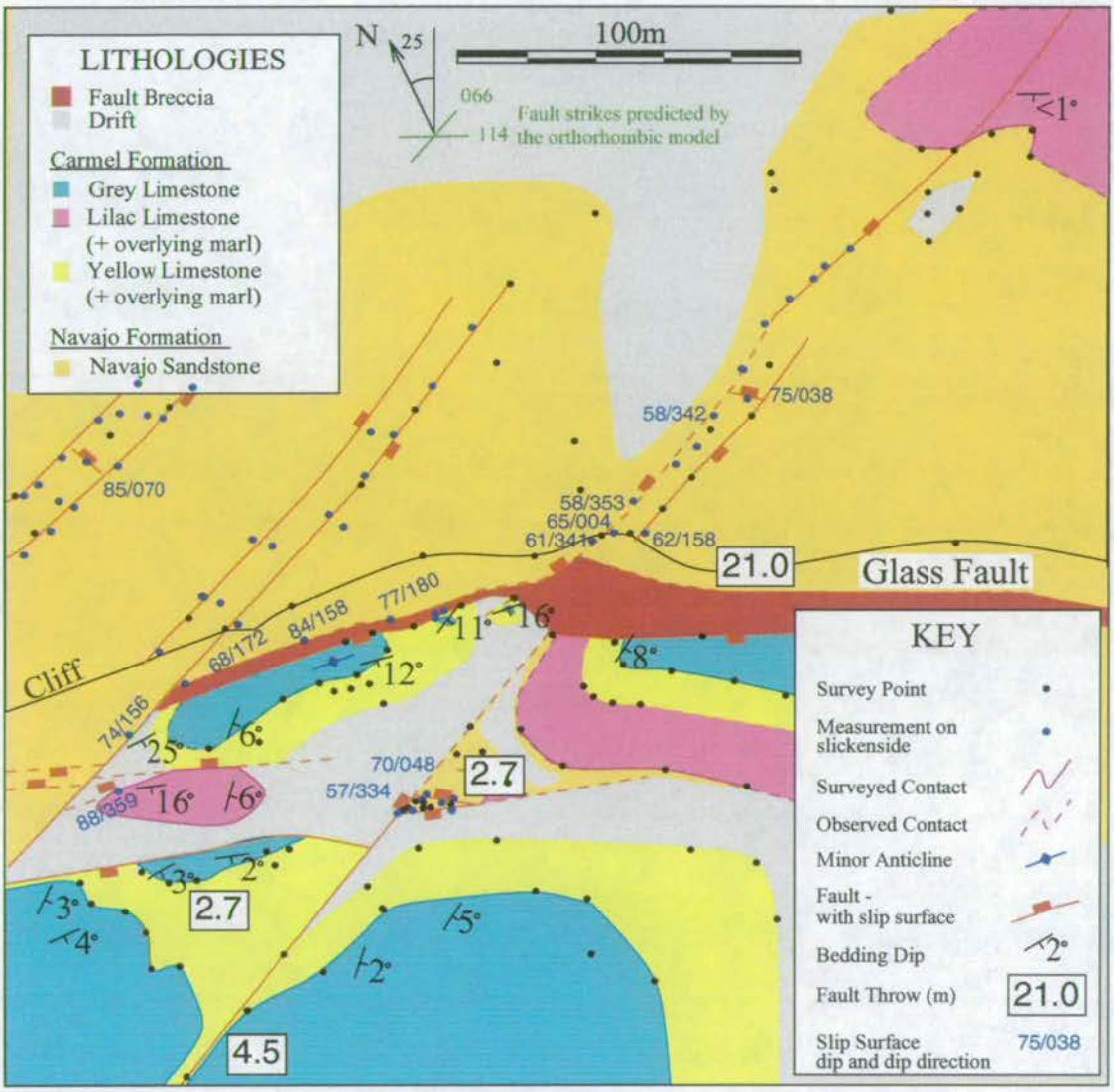

Figure 2.6. Map of the Drillhole Intersection.

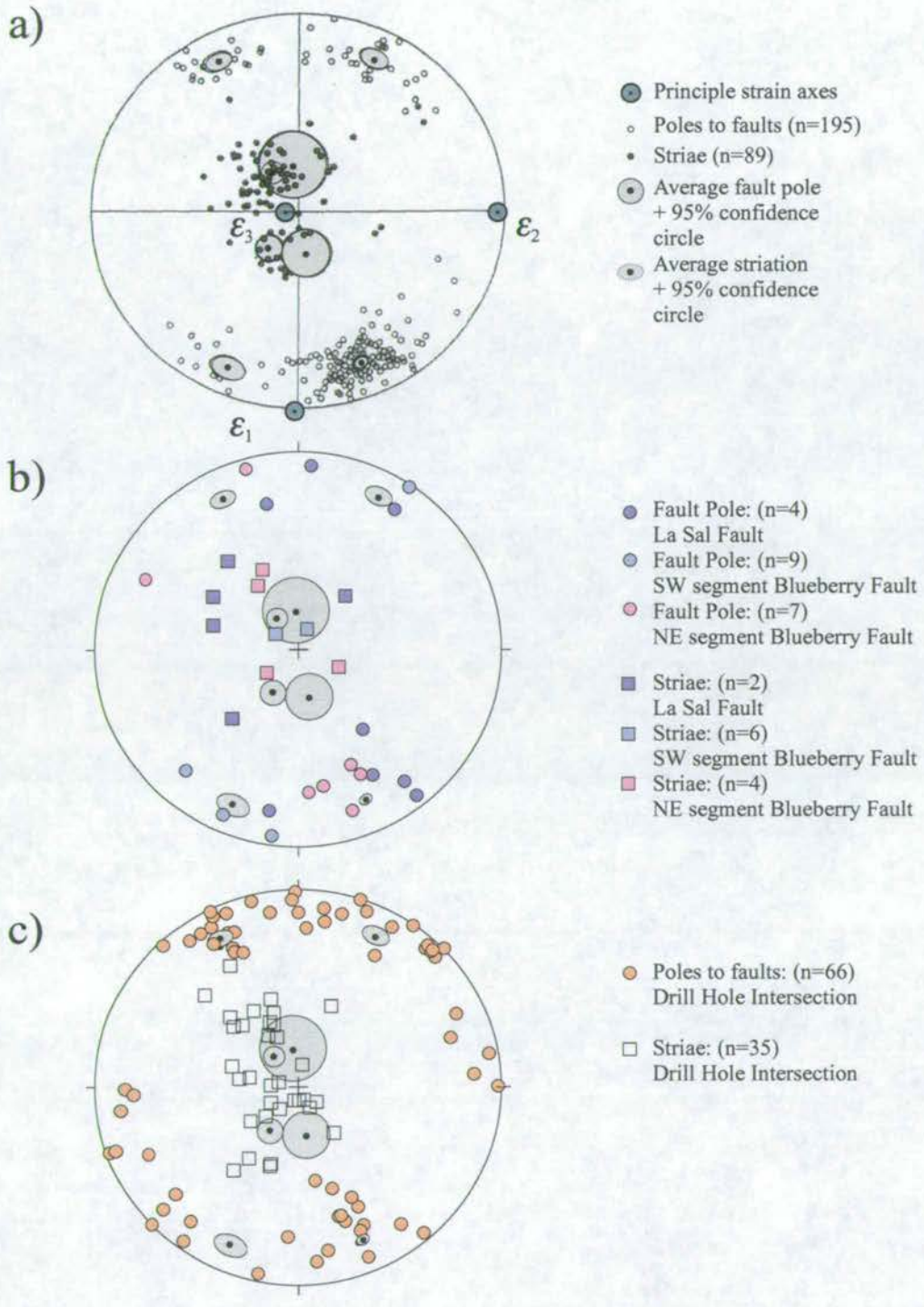

Figure 2.7. Equal-area projection of poles to fault planes and striations. a) Data collected by Krantz throughout the Chimney Rock Array (Krantz 1988). Fisher mean orientations with 95% confidence circles determined for each cluster. Principal strain axes determined by the odd axis method of Krantz (1988). b) Data collected at the La Sal Intersection, with mean orientations from Krantz (1988) for comparison. c) Data collected at the Drillhole Intersection, with mean orientations from Krantz (1988) for comparison.

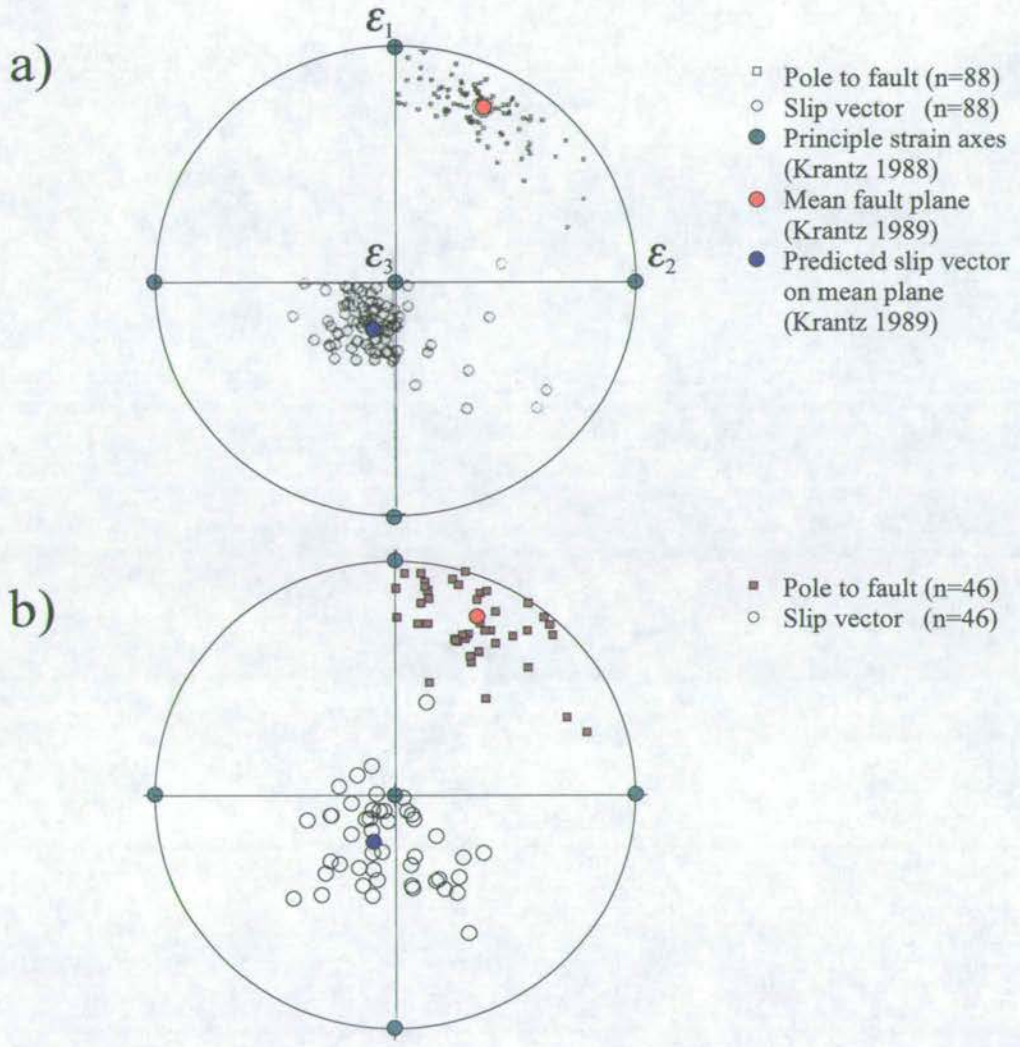

Figure 2.8. Stereonet plot of Chimney Rock Fault Array data, after rotation of principal strains and reflection of fault poles and slip vectors. a) Data collected by Krantz (Krantz 1989) throughout the Chimney Rock Array. Also shown are the average reflected fault pole for this dataset and the slip vector predicted for that fault. The observed slip vectors are tightly clustered about the predicted orientation. b) Data collected at the intersections. Slip vectors for this dataset are not so well clustered about the predicted value.

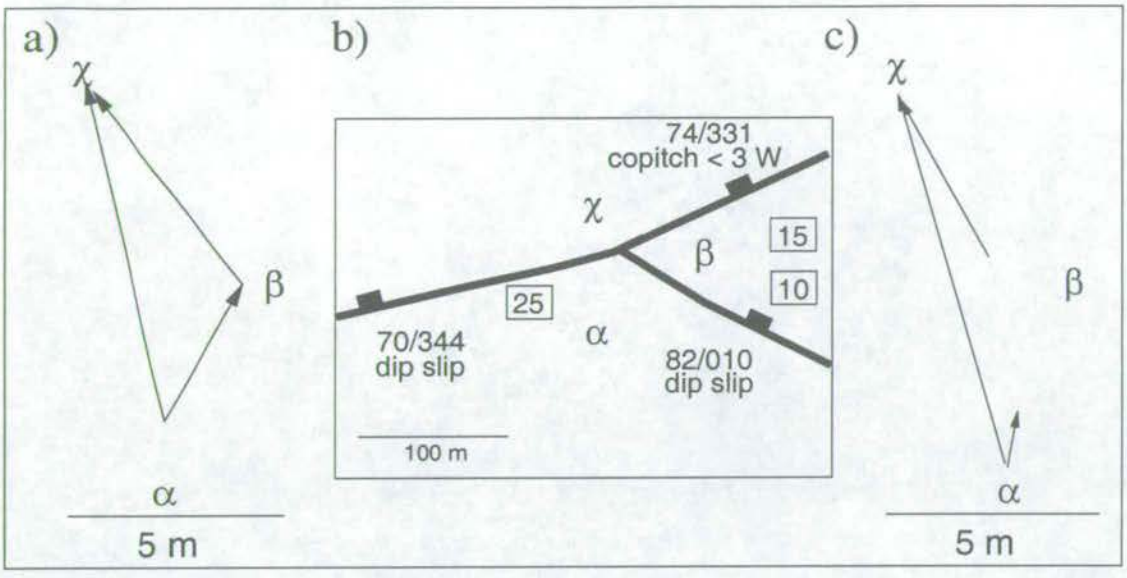

Figure 2.9. a)Vector diagrams showing heaves on the major faults at the La Sal Intersection. Fault blocks are labelled α, β and χ. Redrawn from Figure 35 of Krantz (1986). b) Fault throws, dips, dip directions and slip directions at the intersection, from Krantz (1986). c) Vector diagrams of heaves using the information in b).

accommodated by brittle failure, but a hangingwall anticline in the Carmel Formation at the Drillhole suggest that this may not be the case. However, I draw this final conclusion cautiously because these structures may not have a tectonic origin and may simply have formed as the limestones collapsed due to preferential erosion of the softer underlying marls.

Krantz (1989) recognised some deviations from the ideal model; for example, he noted at the La Sal Intersection that slickenlines on the La Sal Fault and the southwest segment of the Blueberry Fault were dip-slip, but those on the northeast segment deviated from dip-slip by several degrees, with slip to the southwest. He constructed a vector diagram (Figure 2.9a) of fault heaves at the intersection, concluding from the neat closure of the loop that the three fault-bounded blocks behaved rigidly at the intersection point and moved contemporaneously. My work confirms that the three faults were moving at the same time. However, using Krantz's (1986) map, reproduced in Figure 2.9b, I was unable to recreate the closed circuit of fault displacement vectors (Figure 2.9c). This suggests that the fault blocks themselves deformed; most likely, by compaction of the high-porosity Navajo. Moreover, I observed slickenlines on all three faults which were consistently oblique-slip not pure dip-slip as predicted by the orthorhombic theory. Those on the Blueberry Fault southwest of the La Sal Intersection (dark blue on Figure 2.7a) showed the largest deviations from dip-slip. Krantz (1989) also noted more significant deviations from the simple orthorhombic model. He reports angular differences between predicted and observed fault slip vectors of up to 49.4^o and claims an average misfit

of 10.8° for the whole population (Figure 2.10a). I performed an identical analysis of the fault slip vector data I collected at the Drillhole and La Sal Intersections (Figure 2.10b). Although the range of my co-pitch values ($0-57°$) is similar to those recorded throughout the population ($0-49.4°$), the mean value (14.13°) is significantly higher. This reflects the fact that, at the intersections, there are fewer examples of dip-slip and more examples of oblique-slip.

2.6 Aim II: Do Faults Link or Arrest at Intersections?

The question of whether faults link or arrest at intersections can be addressed by examining the pattern of displacement on the faults themselves and the damage around the faults. At the La Sal Intersection, the same three marker horizons outcrop in every fault block, so the displacement patterns on the faults could be measured. This was not the case at the Drillhole Intersection and so fault displacement profiles could not be constructed for this area. In order to create displacement profiles for the La Sal and Blueberry Faults, a best-fit surface was fitted to the surveyed data points on each stratigraphic horizon in each fault block. This was achieved by using the Generic Mapping Tools Software (Wessel & Smith 1998). In general, the best fitting surfaces agreed with bedding measurements made in the field (Figure 2.11). However, this was not the case for the Grey Limestone in the hangingwall of the La Sal Fault, where the almost linear arrangement of the data points poorly constrained on the dip and strike of the surface. To generate a surface for this horizon in the La Sal hangingwall block, I assumed that the Grey Limestone has the same orientation as the underlying Lilac Limestone and that the vertical separation of these two horizons, which is nearly constant in the La Sal footwall block, is also constant in the hangingwall block. The mean distance from the surveyed points on the Grey Limestone to the Lilac Limestone surface below was 8.54m so this value was chosen for the separation of the Grey and Lilac Limestone surfaces in the La Sal hangingwall. Estimates of displacement based on the Top Navajo surface are considered unreliable unless close to surveyed points, because of decimetre-scale undulations on this surface. Finally, the small splay of the Blueberry Fault is clearly controlling the orientation of Lilac Limestone outcrop in the hangingwall of the Blueberry Fault right next to the fault. Therefore, the surface fitted to this outcrop can only be considered reliable near to the surveyed points.

After surface fitting, intersections between the horizons and the fault surfaces were calculated, in order to generate stratigraphic separation diagrams (Figures 2.12 and 2.13). The offset between equivalent horizons in the footwall and hangingwall gives the vertical component of fault slip or displacement. In some instances, the data used to define the best fitting surface lie

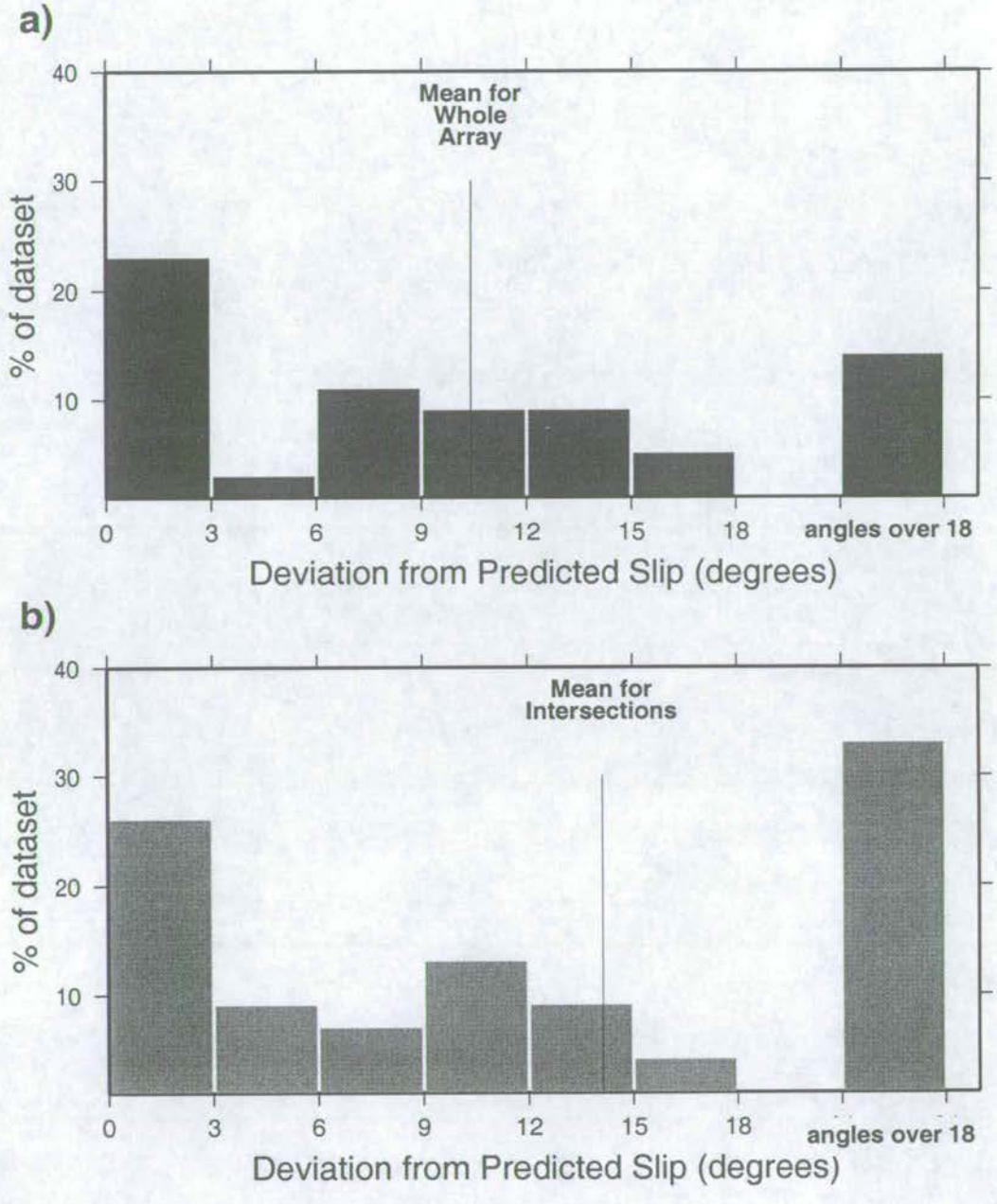

Figure 2.10. Histogram of co-pitches or deviation angles between predicted and observed slip vectors for individual faults in the Chimney Rock Array. a) Data collected by Krantz(1989), at unspecified locations b) Data collected at the intersections, this study.

some distance from the fault. This is the case with the Grey Limestone in the hangingwall of the Blueberry Fault, for instance (see Figure 2.11). Figure 2.14 illustrates how extrapolation from distant outcrops can lead to underestimation of fault throw, if fault drag occurs. Poor throw estimates can also result if the marker horizons have experienced vertical movement not associated with faulting. This may occur if the soft marls underlying the limestones have begun to erode, for example, close to a cliff edge. If the Grey Limestone in the hangingwall of the Blueberry Fault has slumped in response to erosion of the underlying marl, this would lead to an overestimation of the throw on the Blueberry Fault.

The displacements on the faults at the La Sal Intersection show that they were active simultaneously. The trace of the La Sal Fault is truncated by the Blueberry Fault and the displacement on the La Sal Fault is not zero at the intersection point (Figure 2.13). If the faults were not growing simultaneously, this implies that the La Sal Fault formed before the Blueberry Fault and previously extended to the northwest of the present day intersection. Therefore, there ought to be another part of the La Sal Fault in the hangingwall of the Blueberry fault. As the throw on the Blueberry Fault (20.4m) is very much less than the height of the La Sal Fault (Nicol *et al.* (1996) state that typically fault height=length/2.5; the La Sal Fault fault has a truncated length of 2.67km, and so it should be hundreds of metres high.), the portion of the La Sal Fault downthrown in the hangingwall of the Blueberry Fault should be visible. There is no evidence for an extension of the La Sal Fault in this location. Therefore, the La Sal Fault must have accumulated some displacement since finding itself in the footwall of the Blueberry Fault. The asymmetry of the La Sal Fault's displacement profile (Figure 2.13c) also supports the idea that the La Sal and Blueberry Faults were simultaneously active. Asymmetric slip distributions displayed by overlapping normal faults elsewhere have been attributed to interaction between the stress fields of the structures (Willemse, Pollard & Aydin 1996, Dawers *et al.* 1993, Peacock & Sanderson 1991).

Faults with significant displacement (> 1cm) in the Navajo Sandstone are expressed as a slip surface surrounded by a zone of deformation bands. The deformation bands in this zone have a similar orientation to the adjacent slip surfaces. If the interaction of two faults prevents one of them from growing, the damage associated with the dead fault will be overprinted by structures forming around the still-active fault. I did not observe this pattern at either intersection, and so I cannot conclude that interaction between non-coplanar faults caused any of the interacting structures to arrest their growth completely. It is tempting to conclude from the large amount of damage (not surveyed) surrounding the intersections that such non-coplanar intersections frustrate fault movement. However, elsewhere in the array (e.g. towards the western tip of the Big Hole Fault) increases in off-fault damage have been observed even where the intersecting

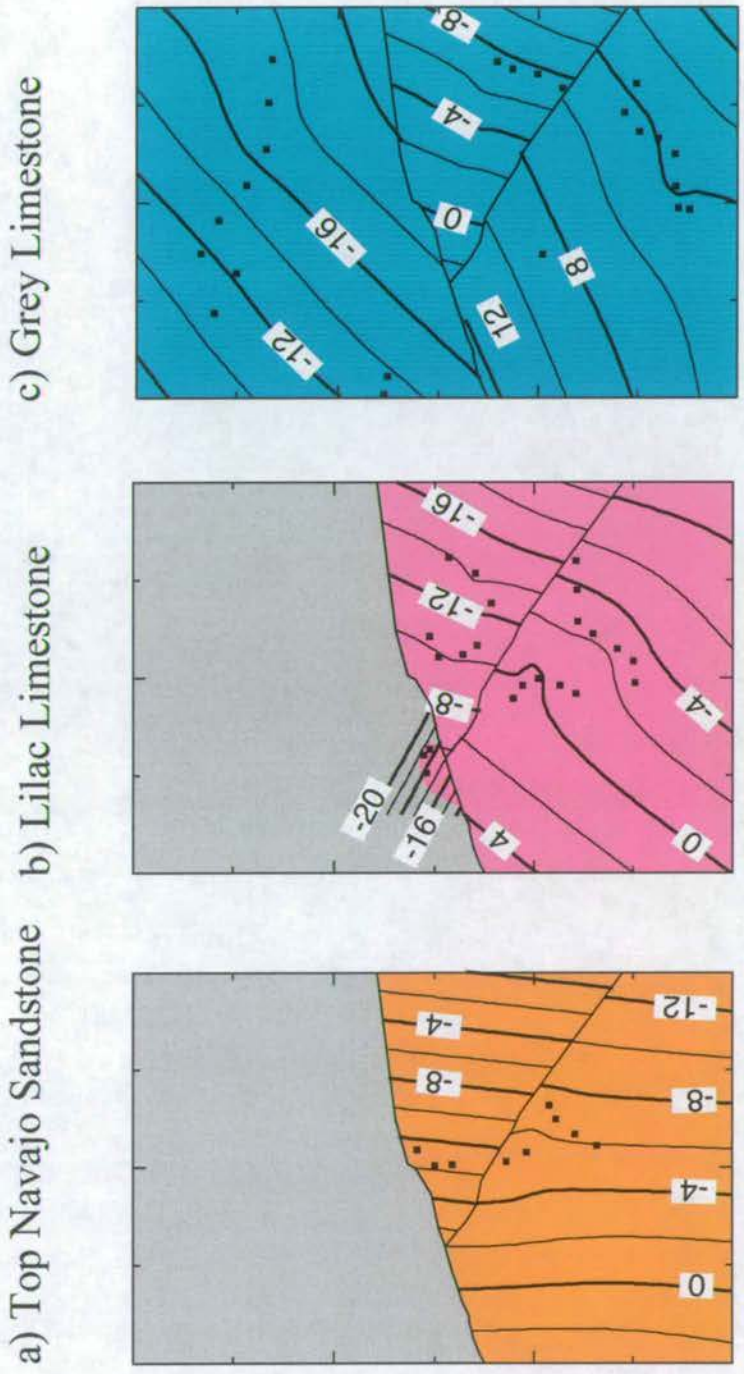

Figure 2.11. Best fit surfaces to marker horizons in the three fault blocks at the La Sal Intersection. The elevations are contoured in metres. Dots indicate the survey points through which surfaces have been fitted.

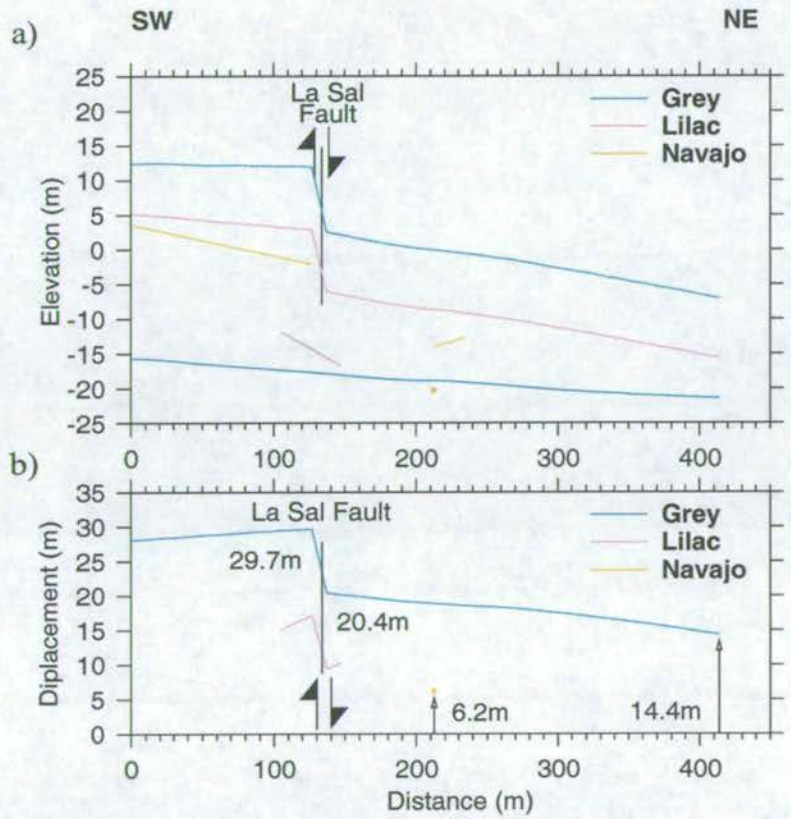

Figure 2.12. a) Stratigraphic separation diagram and b) displacement profile for the Blueberry Fault. Horizons in the footwall are shown in lighter shades, horizons in the hangingwall in darker shades. Poorly fitting surfaces are only shown where there are nearby control points.

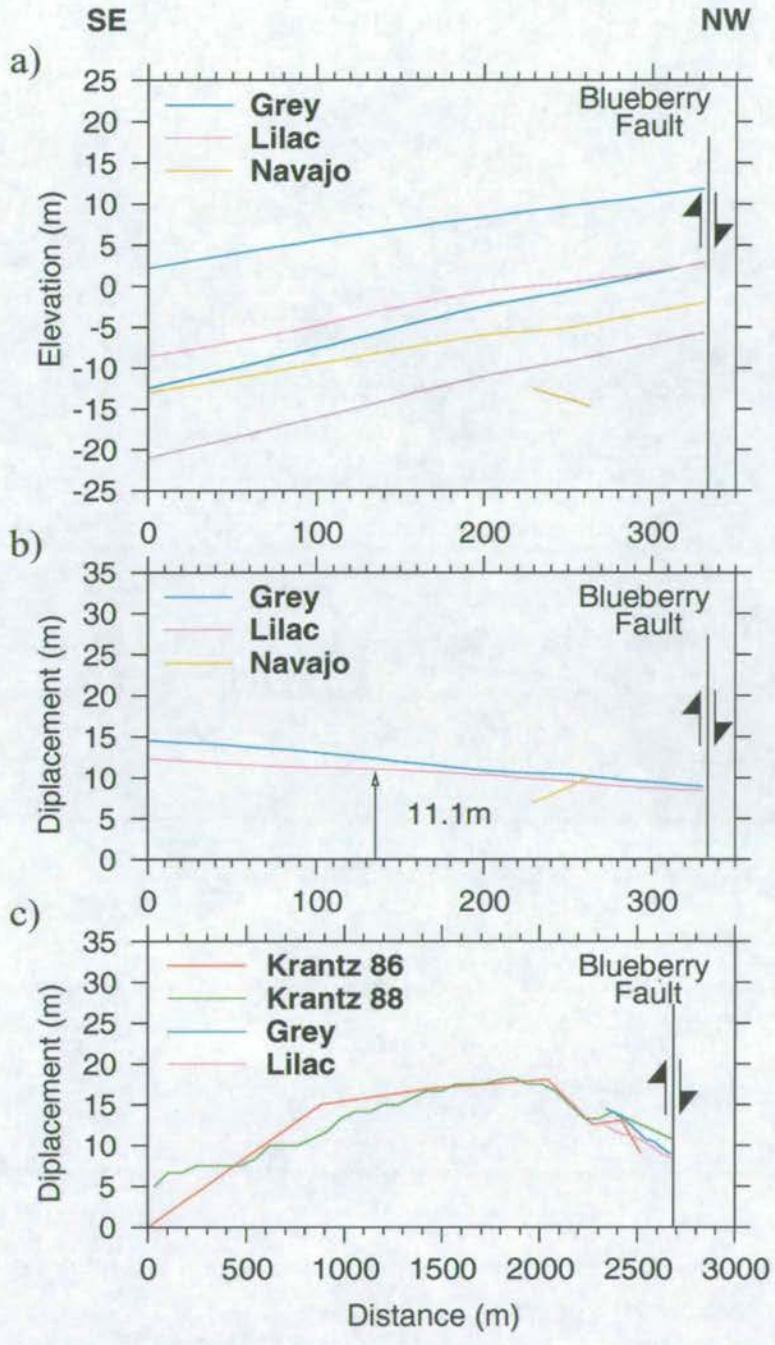

Figure 2.13. a) Stratigraphic separation diagram and b) displacement profile for the La Sal Fault. Horizons in the footwall are shown in lighter shades, horizons in the hangingwall in darker shades. Poorly fitting surfaces are only shown where there are nearby control points. c) Displacement profiles constructed from Figure 28 of Krantz (1986) and Figure 13 of Krantz (1988) shown with the data from b) for comparison.

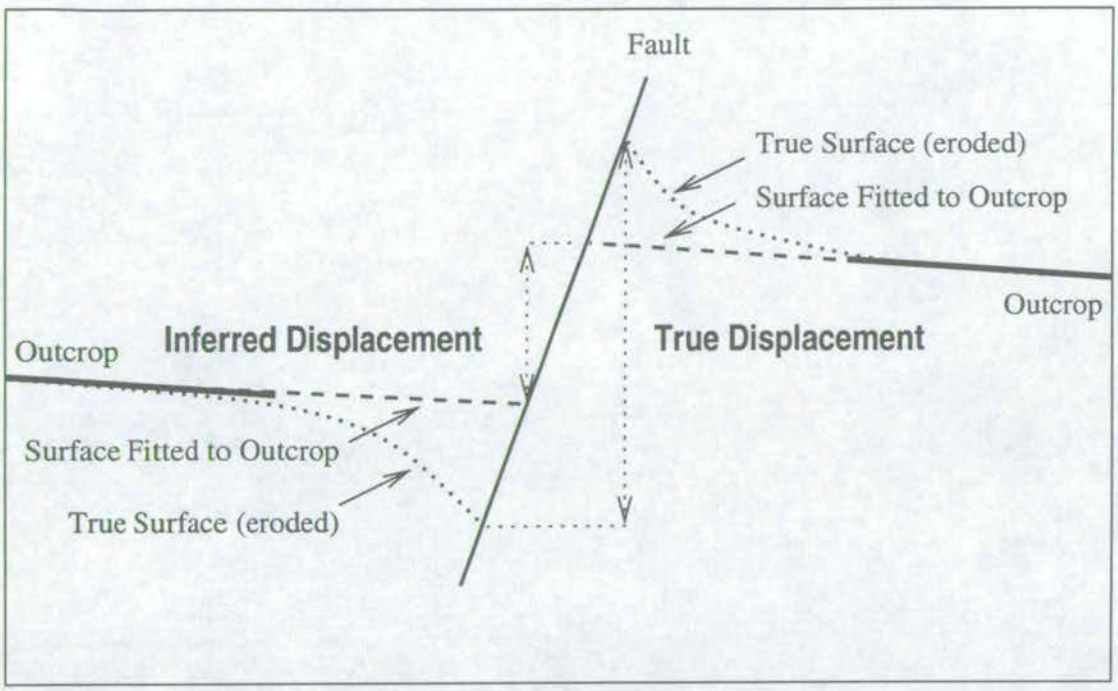

Figure 2.14. Underestimates and overestimates of displacement can result from failure to sample close to faults, if fault drag occurs.

structures are coplanar (Shipton 1999). Unfortunately, it was not possible in the time available to make a quantitative comparison between these two localities. As a consequence, whilst we can conclude that intersecting faults expend more energy damaging the rock around them than isolated faults, we cannot say conclusively that non-coplanar intersections frustrate growth more than coplanar intersections.

2.7 Aim III: Does the Chimney Rock Array Size Frequency Distribution Follow a Low Exponent Power Law?

2.7.1 Approach

To check that the array does indeed have a low power law exponent, I first examined the accuracy of the map on which Cladouhos & Marrett (1996) based their analysis. I then considered their assumptions, sampling methodology and interpretations. Finally, I compared

the c value for the Chimney Rock Array with the c values I calculated for two other orthorhombic arrays and published values.

2.7.2 The accuracy of the map

The map (Krantz 1986) used by Cladouhos & Marrett (1996) is generally accurate, but has some problems. It does not show where outcrops are obscured by surface erosional features or wind-blown sand. Hence, faults may terminate on the map some way from the actual fault tip. Thus, fault trace length statistics calculated from this map would not accurately represent the true structure. Cladouhos & Marrett (1996) made no correction for this effect whereas I assumed that points on the map where faults terminate in free space coincide with fault tips, but added an appropriate length to fault traces obviously cut short by erosion (e.g. faults which still have metres of displacement at their apparent tip). For larger faults, the position of the obscured tip was estimated by linearly extrapolating the displacement gradient measured on the exposed portion of the fault. This requires the assumption that fault displacement gradients are linear at the tips, which is consistent with the observations of Dawers *et al.* (1993) and Shipton (1999). For shorter faults with few displacement measurements on Krantz's (1986) map this was not possible. In this situation, I assigned the fault a trace length equal to twice that from the observed tip to the point of maximum measured displacement. This assumes that Krantz accurately determined the positions of the point of maximum displacement and the tip and also assumes that the displacement profile is symmetrical. If the structure was interacting with nearby faults, this final assumption may not be valid.

The structures I observed at the intersections that do not have one of the four fault orientations predicted by Krantz (1988) are too small to appear on the map produced by Krantz (1986). Therefore any frequency distribution based on this map will not be affected by them. The USGS map of the Chimney Rock area (see Figure 2.2) shows faults that are as large as the structures that appear on Krantz's map (Krantz 1986) but are outside his map area. They show a similar range of orientations and sizes as the faults studied by Krantz (1986) and they occur at the same stratigraphic level. It is thus reasonable to suppose that they were produced in the same deformation episode. Consequently, the size frequency distribution based on Krantz's map (Krantz 1986) represents only a subset of the whole population.

2.7.3 The sampling method and statistical analysis

Clarke *et al.* (1999) have shown that a given fault size frequency distribution can yield several values of c depending on the technique used to fit the data to a power law (see Section 4.4). Cladouhos & Marrett (1996) do not describe how they calculated a value for c in the Chimney Rock Array but it is likely that they followed common practice: that is, they performed a log-log transform on the data, and then estimated c using least squares regression on the straight line section of the distribution. In order to compare my analysis with theirs, I too adopted this technique, despite the fact it has been shown to give unreliable estimates of c (Clarke *et al.* 1999). Figure 1 of Cladouhos & Marrett (1996) suggests that regression was performed on fault lengths between 100m and 2km and I used this range in my analysis also to aid comparison. It is hard to attach a valid standard error to the estimate of the slope using the linear regression technique (Clarke *et al.* 1999) and Cladouhos & Marrett (1996) do not report an error on their estimate of c. I used a Student's T-test [p1267, Kreysig (1993)] to estimate the uncertainty, even though this requires the assumption that measurements are independent and the random variable (y, if regressing y on x) is normal.

The sampling methodology used for constructing the distribution in Cladouhos & Marrett (1996) is not described explicitly. In personal communication, the authors stated that "the lengths in our database are fault-parallel trace lengths, not corrected in any way to account for branches. We used map-view continuity, fault orientation and throw values to decide which is the main fault at branches." Unfortunately, this does not describe a unique sampling strategy, and the choice of sampling strategy has a large impact on the size frequency distribution. Hence, I elected to produced three different fault trace length frequency distributions from Krantz's map (Krantz 1986) using three different sampling strategies which meet this description. This was an effort to reproduce their results and test the robustness of their estimate of c for the Chimney Rock Array.

2.7.4 Results

In the first analysis (Figure 2.15a, b, c), I only included faults with two free tips (e.g. the Blueberry Fault) and did not include faults which terminate at intersections (e.g. the La Sal Fault). This sampling methodology could yield a size frequency distribution unrepresentative of the whole population. The size of the longest fault (4.17 km) and the total number of faults (45) in the population I obtained using this technique are comparable with those reported by Cladouhos and Marrett (3.9 km and 49, respectively). However, my distribution has a much

larger power law exponent than theirs- $c = 0.816 \pm 0.061$, compared with 0.67 - and far fewer faults longer than 1km.

The second sampling method groups faults together so that, where two or more faults intersect, the size of the structure is taken to be the sum of the trace lengths of the intersecting faults. Only faults intersecting at a low angle (arbitrarily set at 15°) in map view were clustered together as a single structure. Clustering all intersecting fault segments, whatever their angle of intersection, would be a closer analogue to the method used by Cowie *et al.* (1993) to extract size frequency distributions from numerical models of fault populations (see Section 4.1). This approach can be useful as it facilitates comparisons between distributions from computer-generated and natural fault arrays. However, Cladouhos and Marrett's (1996) description of their sampling technique does not seem to be compatible with joining faults which have distinctly different orientations. Clustering faults meeting at low angle intersections lowers the number of small faults and increases the number of large ones. As a consequence, the power law exponent of this distribution (Figure 2.15d, e, f) - $c = 0.636 \pm 0.029$ - is understandably a little lower than that of the distribution in Figure 2.15a. It is also better constrained.

The final sampling method considers every point where a fault ends on Krantz's map to be a fault tip: whether it terminates at an intersection with another fault or in free space. This method increases the number of small faults and decreases the number of large ones. The power law exponent of this distribution (Figure 2.15 g, h, i), $c = 0.831 \pm 0.023$ is consequently higher than that of the other two distributions. The results of all three sampling methods are summarised in Table 2.1 and Figure 2.16. The second of the sampling strategies gives results that are most consistent with those of Cladouhos & Marrett (1996).

Method	c	N	Lmax (km)
C&M 96	0.67	49	3.9
Free Tips	0.816 ± 0.061	45	4.17
Clustered	0.636 ± 0.029	55	3.92
Segments	0.831 ± 0.023	88	2.92

Table 2.1. The essential properties of the four size frequency distributions for the Chimney Rock Array.

2.7.5 Comparing the value of c from Chimney Rock with other arrays

This exercise has shown that the result obtained by Cladouhos & Marrett (1996) for the value of c is reproducible, but that the exponent of the fault size frequency distribution can be very strongly dependent on the sampling technique employed (Figure 2.16). Even if a sampling

technique which increases the value of c is employed, the exponent for the Chimney Rock Fault Array is still lower than 1 (Figure 2.17 and low in comparison with published c values for other fault populations. Table 1.1 shows c values from fault length cumulative frequency distributions, produced by 2D sampling of continental fault populations. All but two, the Boso Peninsula and the Chimney Rock datasets, have power law distributions with $c \geq 1$. All published fault size cumulative frequency distributions come from arrays of parallel or conjugate faults. This prompts the question, are low exponent power laws characteristic of orthorhombic arrays?

In order to compare the Chimney Rock data with other orthorhombic arrays, fault length cumulative frequency distributions were also calculated for the Summer Lake and Michoacan areas using the maps of Donath (1962) and Tibaldi (1988). Sections of these two maps are reproduced in Figure 2.18. Unfortunately, I was not able to ground-truth the accuracy of these maps in the field in the way I could at Chimney Rock. In the Michoacan area, some faults may be obscured by the lake. Workers in Summer Lake area (Crider and Pollard 1996a, b) comment (Crider, pers. com.) that Donath's map (Donath 1962) is generally consistent with aerial photos but it does not accurately represent the segment boundaries she observed in the field. Unfortunately, some faults extend beyond the map boundaries in both regions. Yielding *et al.* (1996) advise that, where fault traces extend out of the sample area, it is better to include the part lengths than to discard them. Partial trace lengths were included in size frequency distributions for both the Michoacan and Summer Lake areas. I used the last of the sampling methods described in Section 2.7.3 above (taking each segment to be an individual fault) to aid comparison between the datasets.

It is clear from Figure 2.19 that the Chimney Rock data are quite different from the Summer Lake and Michoacan datasets. Figure 2.19a shows the three datasets on log-log axes, with both power law and exponential best-fit curves. The power law fit seems most appropriate for the Chimney Rock data, but the Summer Lake and Michoacan datasets more closely resemble exponential size distributions. The characteristic lengths ($1/\lambda$) of the best fitting exponential curves (0.327 km at Chimney Rock, 0.773 km at Summer Lake and 3.39 km at Michoacan), reflect the different scales at which the faults were observed. For all three populations, mean lengths were calculated by summing the measured lengths and dividing by the number of faults measured. In each population, the mean fault length (0.455 km at Chimney Rock, 0.933 km at Summer Lake and 5.18 km at Michoacan) is higher than the characteristic length. If the faults sizes in these three areas really do have exponential frequency distributions, this suggests that the very smallest faults in the population are not being observed. If instead we assume that the underlying distributions are power law, both the Summer Lake and Michoacan datasets show serious truncation bias: underestimation of the numbers of small faults producing a "roll-over"

in the cumulative frequency distribution towards smaller fault lengths. Power law exponents were calculated by taking logarithms and performing linear regression of cumulative frequency on size over the straight-line part of the curve (determined by eye). The power law exponent which best fits the Chimney Rock data (0.83) is considerably lower than the exponents for the Summer Lake (2.35) and Michoacan (3.00) datasets. This study shows that low power law exponents are, therefore, not a feature of all orthorhombic arrays.

Geological differences between the areas might be the cause of the differences in the size frequency distributions of the three fault arrays. Firstly there are lithological differences between the sites that undoubtably have rheological consequences: the faults at Chimney Rock formed in high porosity sandstone but faults in the other areas cut volcanic tuffs and ash flows. Fossen & Hesthammer (1997) show another example of a fault populations in a high porosity sandstone that shows a size cumulative frequency distribution with a low power law exponent. Steen & Andresen (1999) also report variations in power law exponent related to host lithology. Secondly there is a difference in the boundary conditions of deformation: the faults at Chimney Rock grew at depth, whereas faults in the other two areas formed in a layer with one free surface. Finally it is possible that the areas have experienced different amounts of strain and consequently different amounts of fault interaction. Without displacement data for the faults mapped by Donath (1962) and Tibaldi (1988), the strains in the areas cannot be measured. However, we can infer from the map patterns that the faults at Summer Lake experienced the most interaction: there are proportionally fewer faults with free tips in the Summer Lake Array than in the Chimney Rock and Michoacan arrays.

2.8 Discussion

In the Chimney Rock Fault Array, structures at the intersections of non-coplanar faults deviate in two ways from the model proposed by Krantz (1988), which described faults in orthorhombic symmetry moving by pure dip-slip. Firstly, slip on the major faults becomes oblique in proximity to the intersections. Secondly, smaller faults around the intersections show a range of orientations and slip directions. Changes in slip surface orientations and slip directions could be caused either by changes in the state of stress in the vicinity of the intersection, by the action of local kinematic constraints, or by a combination of both. These ideas are discussed more fully in Section 1.2.12, but a simple kinematic constraint is that faults cannot slip if, by slipping, they open up significant voids at depth. The faults at Chimney Rock formed far from a free surface, and so it is likely that they experienced this constant volume constraint.

The length cumulative frequency distribution of the Chimney Rock Fault Array has a low value of c: low compared with published values and with other orthorhombic arrays. This low value cannot be solely attributed to sampling bias. Low c values have elsewhere been interpreted as indicating linkage-dominated growth (Cladouhos & Marrett 1996), but linkage in this array could well be inhibited by fault geometry. These observations can only be reconciled if another mechanism for lowering c was operating as these faults developed. Krantz (1986) notes that major faults striking in the same direction are consistently spaced approximately 110 m apart, and that this length scale is comparable with the thickness of the Navajo Sandstone [115m - Krantz (1986)]. If the thickness of the deforming layer controls the spacing of the faults, might it not also influence the size frequency distribution? For example, if faults cease to grow once they span the thickness of the deforming layer, additional strain energy cannot be dissipated by slip on the biggest faults, but must be accommodated by smaller faults in the array. Figure 2.20 shows schematically how size cumulative frequency distributions with a low slope might be generated in this way, as the total number of faults remains constant, but the number of faults of maximum size increases. Analyses of the fault sizes in the Summer Lake and Michoacan areas suggest that power law distributions with low exponents are not characteristic of all orthorhombic arrays. Indeed, these analyses suggest that exponential relationships, and not power laws, may best describe fault sizes in some continental areas.

2.9 How Field Observations Motivated Modelling

The fieldwork suggests that the distribution of strain between the processes of nucleation, growth and linkage of fractures depends on whether fault growth is constrained by geometry, kinematics and layer thickness. Put simply, these constraints will determine how strain is accommodated by faults of different sizes. This in turn controls the form and parameters that describe the fault size frequency distribution.

The numerical modelling was motivated by these questions, which arose as a consequence of this fieldwork:

1. How are fault size frequency distributions affected by geometric or kinematic constraints on fault movement?
2. How are fault size frequency distributions affected by finite layer thickness?
3. Under what conditions do faults show power law size scaling?

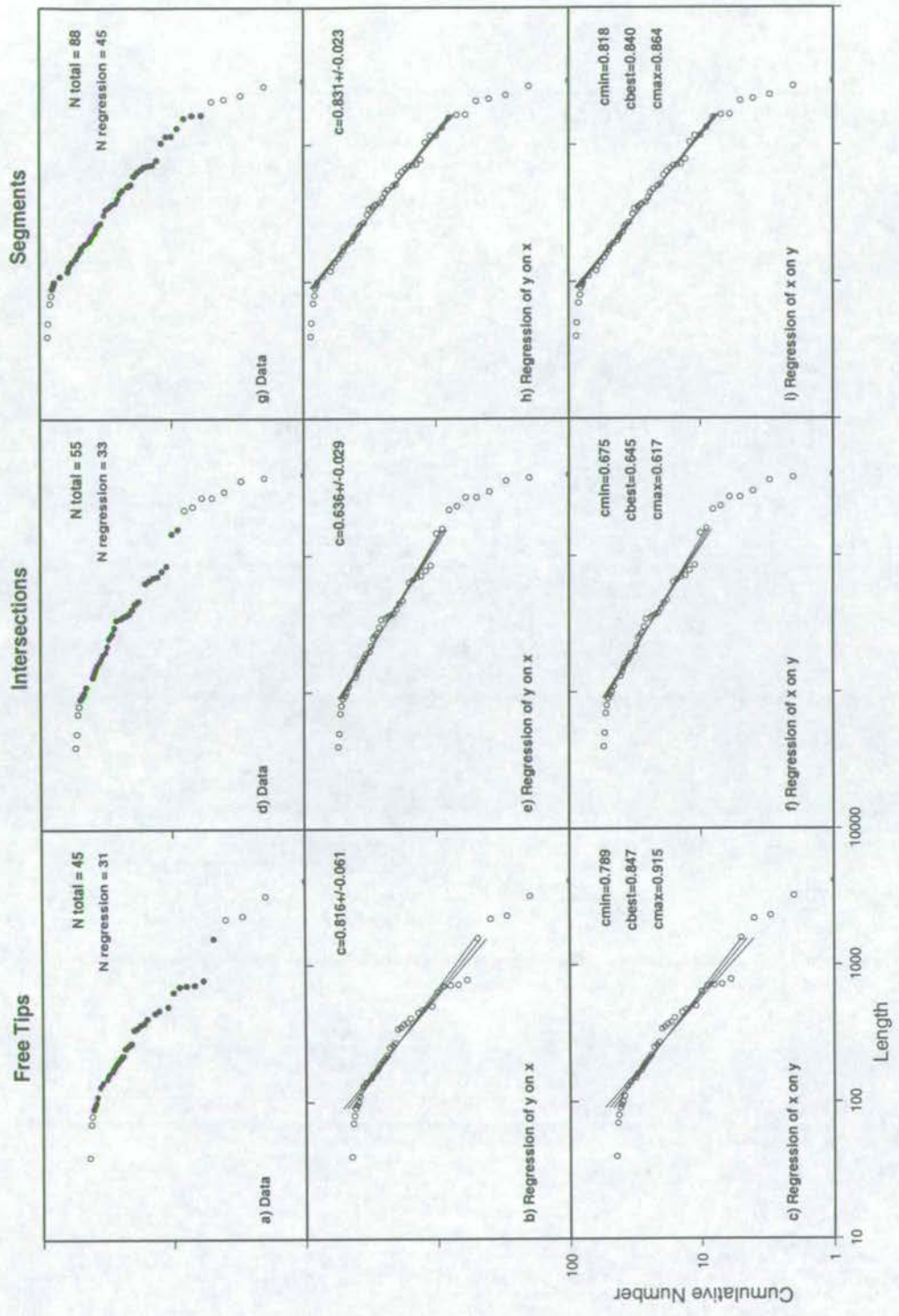

Figure 2.15. Fault trace length frequency distributions of the CRFA. All graphs have the same axes as plot c)
a-c: compiled using only faults with two free tips,
d-f: compiled by clustering intersecting faults together,
g-i: compiled by measuring each segment as a separate fault.

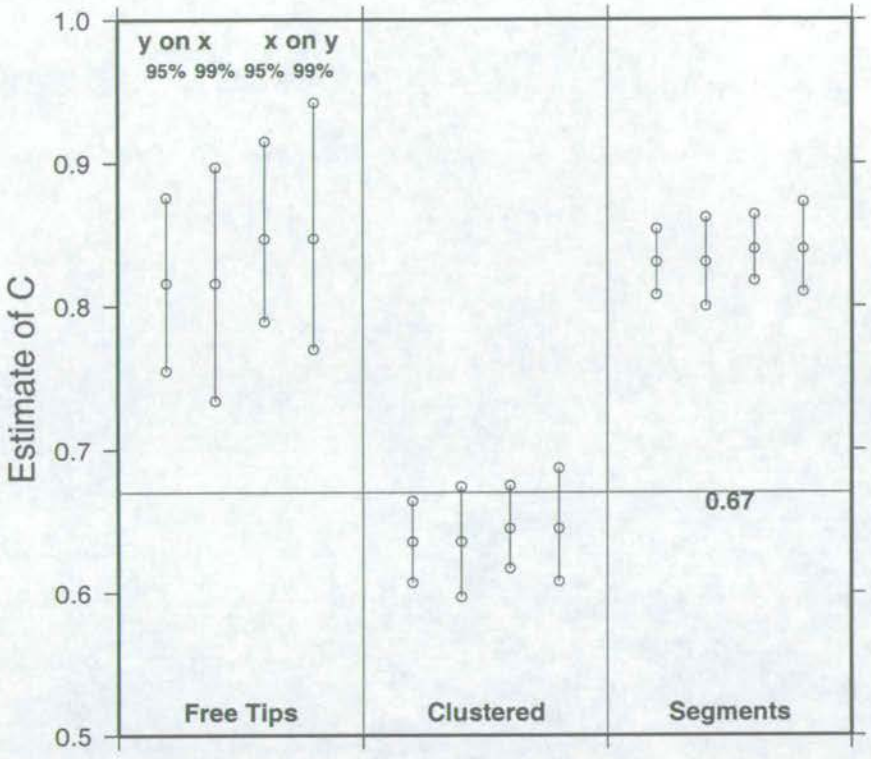

Figure 2.16. Various estimates of the power law exponent for the Chimney Rock Array, with Cladouhos and Marrett's value 0.67 for comparison.

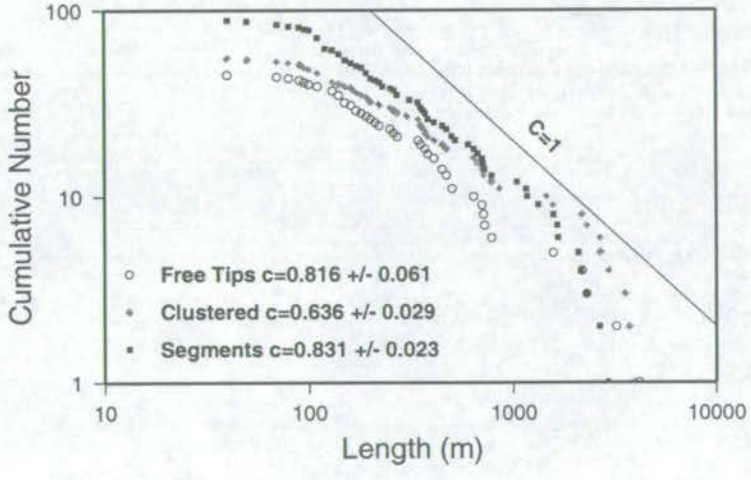

Figure 2.17. Size cumulative frequency distributions of the Chimney Rock Array using different sampling techniques. Note, all distributions have a lower slope - power law exponent, c - than the reference line, for which $c = 1$.

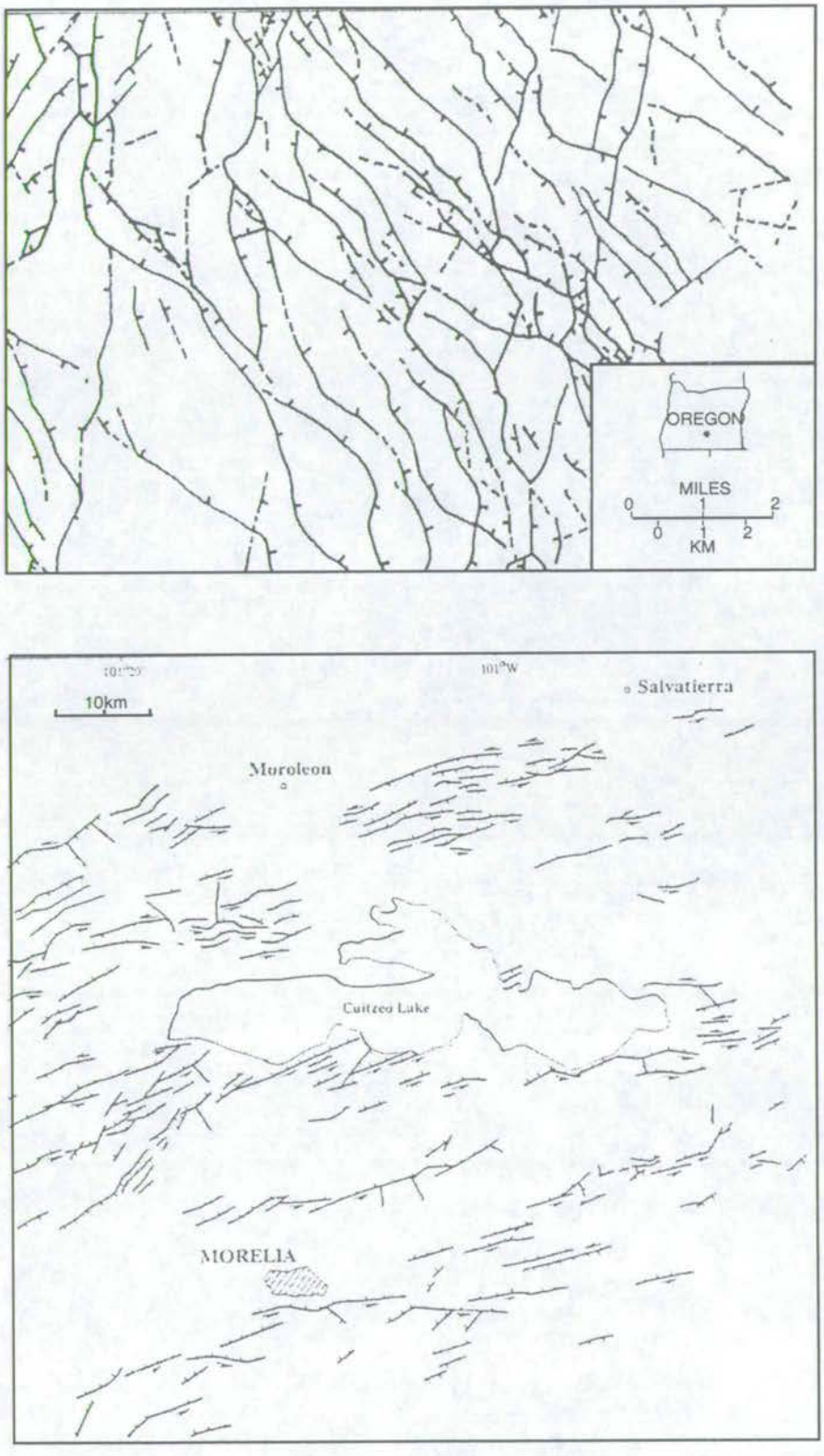

Figure 2.18. Extracts from the maps of the Summer Lake and Michoacan areas, produced by Donath (1962) and Tibaldi(1988). Ticks on downthrown side of faults. Arrows show faults with oblique motion.

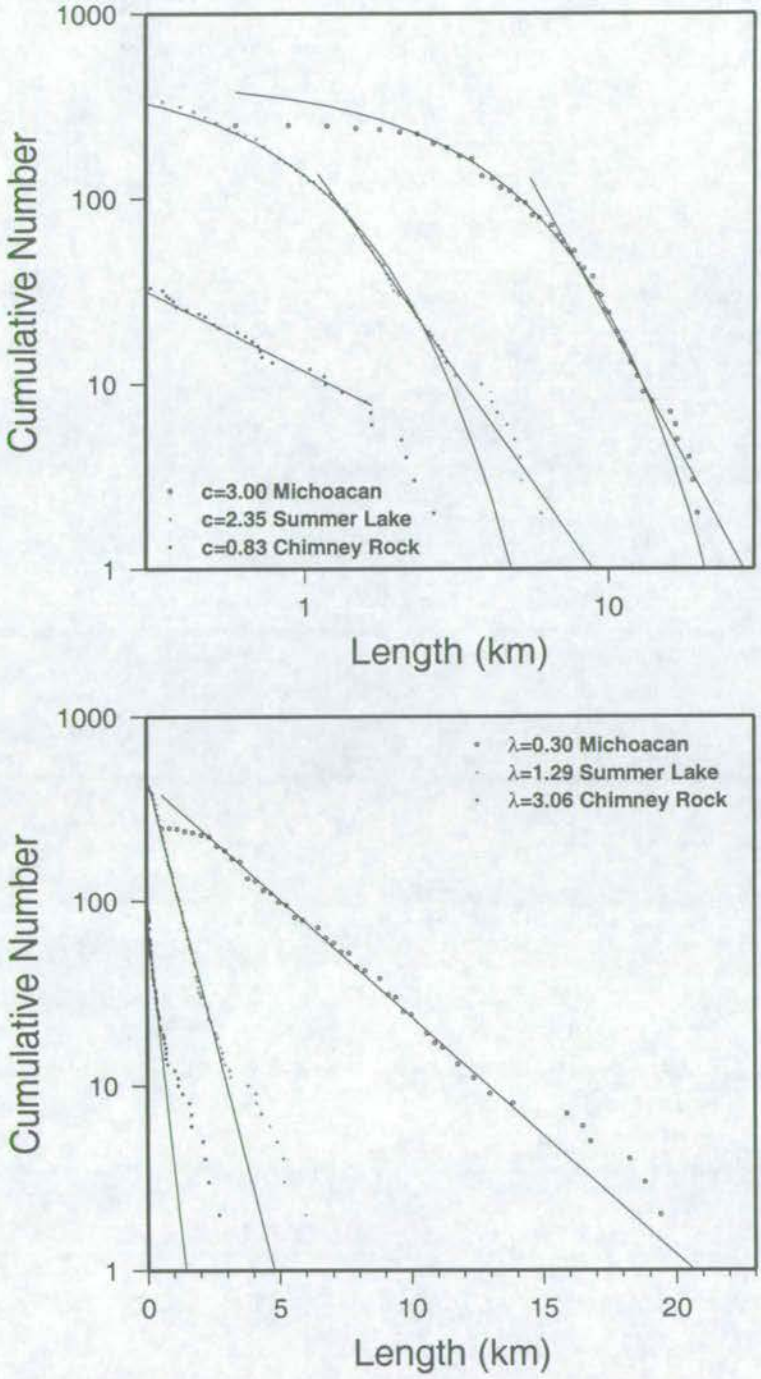

Figure 2.19. Comparing the Chimney Rock data with fault size cumulative frequency distributions from two other orthorhombic arrays. a) Distributions on log-log axes with both exponential best-fit curves and power law best-fit lines. b) Distributions on log-linear axes, with exponential best-fit lines. Discounting sampling bias, the Chimney Rock data are best fit with a power law, exponential distributions give a better fit to the other two orthorhombic fault arrays.

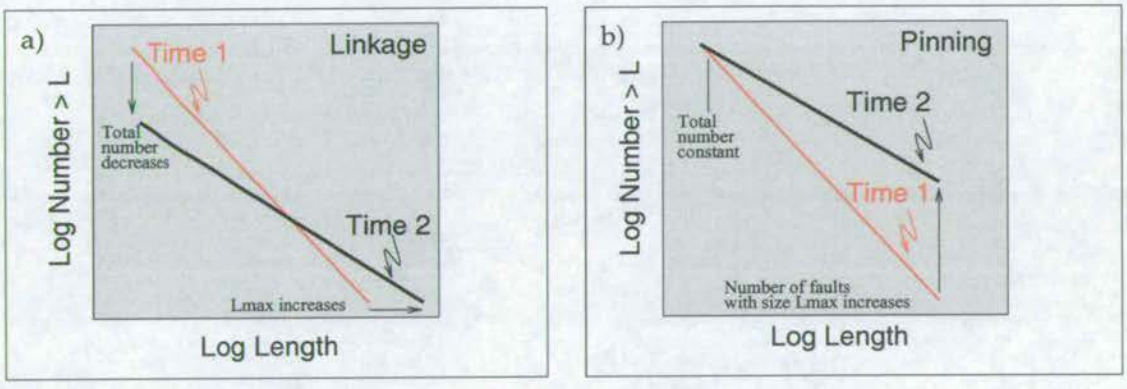

Figure 2.20. Cartoon log-log plots showing a decrease in the power law exponent of fault size cumulative frequency distribution caused a) by linkage, b) by "pinning" the size of the biggest faults.

Chapter 3

Numerical Modelling using ADELI

The field study of the Chimney Rock Array suggests that the development of fault populations and their size frequency distributions will be affected if faults are confined within a single layer and if interactions between non-coplanar faults are common. In this chapter I introduce a numerical model which can simulate the growth of conjugate structures within a finite region. The model takes into account both elastic and inelastic rheologies and the tensorial nature of deformation. I discuss the theory underlying the model and how this is implemented numerically. I go on to discuss the various tests used to validate this model and check that it is "fit-for-purpose" before presenting the limitations of the model.

3.1 Why Use Numerical Models?

There are three possible ways to tackle the problem of fault array evolution: field studies, analogue modelling and numerical modelling. Field studies are of great importance because they yield information about natural faults. Unfortunately, they cannot tell the whole story, being limited by lack of exposure and the fact that they only show a snapshot of deformation. Although necessarily simpler than geological reality, models let us study how fault populations develop through time. Numerical models are more flexible than analogue models using sand, clay etc. in terms of the range of rheologies and boundary conditions they can incorporate. Analogue models also suffer from problems of reproducibility: no two boxes of sand are ever

the same. However, the supreme strength of numerical models is that values of stress, strain and displacement can be found at any location in the deforming region at any point in time.

3.2 Theory

3.2.1 The conceptual framework

Models of faulting must refer to a mechanical theory which comprises the governing equations of stress equilibrium, a failure criterion defining the peak stresses the rock can withstand, constitutive laws (stress-strain relationships) that characterise the behaviour of the material before and after failure and the boundary conditions (the conditions imposed on the boundaries of a body in terms of stress or velocity, and throughout it as distributed sources, such as the force of gravity). Fault models must be capable of accounting for the observed characteristics of fault genesis, orientation and operation.

In this study, the mechanical theory describing the behaviour of an elastic-plastic continuum subjected to 2-D plane strain has been used to investigate faulting in cross-section on the kilometre scale over thousands of years. Figure 3.1 illustrates the essential features of a generic elastic-plastic material undergoing axial compression. If a stress lower than σ_y is applied to the material, recoverable, elastic deformation results. If the stress is increased, there comes a point when the system starts to undergo permanent changes in response to the applied stress; this is the yield point. If stress has to increase for deformation to continue, as in the illustration, the material is described as strain hardening. The system then reaches a peak stress σ_p before entering a regime where continued deformation requires a lower and lower stress; behaviour termed strain softening. Eventually the material softens no more and can continue to accumulate strain provided a limiting stress equal to its residual strength σ_r is applied. If the stress is removed entirely, only the elastic strain is recovered and a permanent strain remains.

3.2.2 The physical framework

As dynamic rupture is not the focus of this investigation, we can consider the deformation of crustal material as a quasi-static phenomenon. That means that there are no accelerations in the system and the equations of motion reduce to stress equilibrium equations written in terms

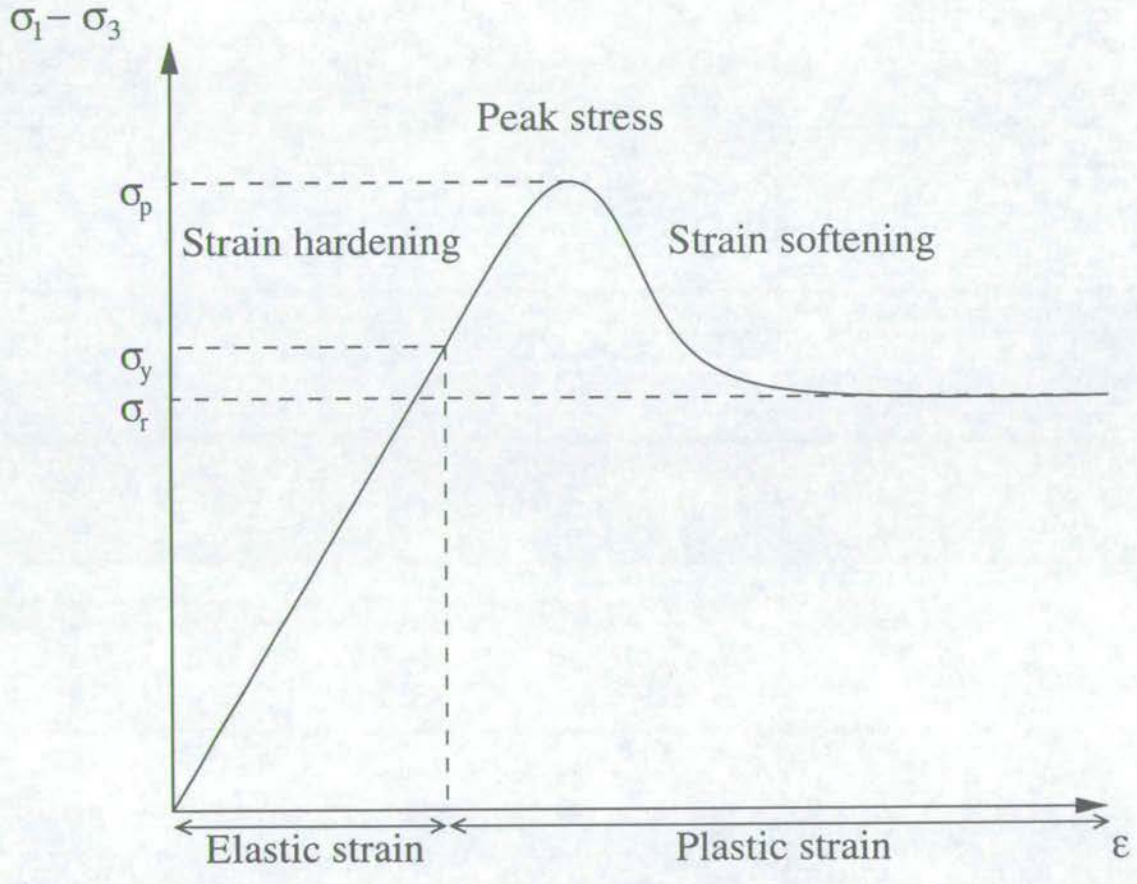

Figure 3.1. Stress-strain curve for a generic elastic-plastic material in a uniaxial compression experiment. σ_1, the maximum compressive stress, acts along the axis of the sample, σ_3 is the confining pressure and ϵ is the axial strain.

of surface forces and body forces

$$\begin{aligned} \frac{\partial \sigma_{11}}{\partial x_1} + \frac{\partial \sigma_{21}}{\partial x_2} + \frac{\partial \sigma_{31}}{\partial x_3} + \rho X_1 &= 0, \\ \frac{\partial \sigma_{12}}{\partial x_1} + \frac{\partial \sigma_{22}}{\partial x_2} + \frac{\partial \sigma_{32}}{\partial x_3} + \rho X_2 &= 0, \\ \frac{\partial \sigma_{13}}{\partial x_1} + \frac{\partial \sigma_{23}}{\partial x_2} + \frac{\partial \sigma_{33}}{\partial x_3} + \rho X_3 &= 0, \end{aligned} \tag{3.1}$$

where σ_{13} is the traction in the x_1 direction on a plane normal to the x_3 direction and $X_{1,2,3}$ are the components of body force (gravity) in the three coordinate directions.

To write the stress balance equations in terms of strain, a constitutive law of the form

$$\sigma_{ij} = f(\epsilon_{kl}) \tag{3.2}$$

is needed. In elasto-plastic materials, there are two constitutive regimes (elastic and plastic) separated by a yield criterion. Jaeger & Cook (1968) define a yield criterion as "a relationship between the principal stresses such that, if it is satisfied, the material will flow". If a plastic material is strain hardening or softening, however, whether or not the material can flow will be determined by a softening/hardening parameter as well as the stress state. This softening/hardening parameter, κ, relates to ϵ_p, the plastic strain already experienced. Thus, yield criteria in general can be expressed as

$$F(\sigma, \kappa) < 0 \quad \text{elastic regime} \qquad F(\sigma, \kappa) \geq 0 \quad \text{plastic regime} \tag{3.3}$$

Stress-strain relationships for elasto-plastic solids are described further in Sections 3.2.3 and 3.2.4.

As boundary conditions are normally given in terms of displacements, not strains, it is useful to replace strains with displacements in the equations to be solved. This is done using the

definition of strain,

$$\begin{pmatrix} \sigma_{11} & \sigma_{12} & \sigma_{13} \\ \sigma_{21} & \sigma_{22} & \sigma_{23} \\ \sigma_{31} & \sigma_{32} & \sigma_{33} \end{pmatrix} = \begin{pmatrix} \frac{\partial u_1}{\partial x_1} & \frac{1}{2}[\frac{\partial u_1}{\partial x_2} + \frac{\partial u_2}{\partial x_1}] & \frac{1}{2}[\frac{\partial u_1}{\partial x_3} + \frac{\partial u_3}{\partial x_1}] \\ \frac{1}{2}[\frac{\partial u_1}{\partial x_2} + \frac{\partial u_2}{\partial x_1}] & \frac{\partial u_2}{\partial x_2} & \frac{1}{2}[\frac{\partial u_2}{\partial x_3} + \frac{\partial u_3}{\partial x_2}] \\ \frac{1}{2}[\frac{\partial u_1}{\partial x_3} + \frac{\partial u_3}{\partial x_1}] & \frac{1}{2}[\frac{\partial u_2}{\partial x_3} + \frac{\partial u_3}{\partial x_2}] & \frac{\partial u_3}{\partial x_3} \end{pmatrix} \tag{3.4}$$

where $u_{1,2,3}$ are the components of the displacement vector in the three principal coordinate directions.

3.2.3 Constitutive laws: Elasticity

Within the mechanical theory of elasto-plasticity as used in this study, the pre-yield behaviour of the deforming material is linearly elastic. That is, it follows Hooke's Law of linear elasticity, which has the general form

$$\sigma_{ij} = c_{ijkl}\epsilon_{kl}. \tag{3.5}$$

where σ_{ij} is the stress tensor, ϵ_{kl} the strain tensor and c_{ijkl} the tensor of elastic moduli. In the pre-yield regime, the material is homogeneous and isotropic so

$$c_{ijkl} = \lambda\delta_{ij}\delta_{kl} + \mu(\delta_{ik}\delta_{jl} + \delta_{il}\delta_{jk}). \tag{3.6}$$

where δ_{ij} is the Kronecker delta ($\delta_{ij} = 1$ if $i = j$, $\delta_{ij} = 0$ otherwise) and μ and λ are the Lamé parameters. The arguably more familiar elastic moduli Young's modulus E and Poisson's ratio v are related to the Lamé parameters by

$$E = \frac{\mu(3\lambda + 2\mu)}{(\lambda + \mu)} \tag{3.7}$$

$$v = \frac{\lambda}{2(\lambda + \mu)}\ . \tag{3.8}$$

3.2.4 Constitutive laws: Plasticity

The constitutive equations for post-yield plastic behaviour do not link stress with strain but rather with strain rate. They take the general form

$$\dot{\epsilon_{ij}} = \lambda_p \frac{\delta G(\sigma, \kappa)}{\delta \sigma_{ij}} \tag{3.9}$$

where a dot denotes a derivative with respect to time, λ_p is simply a constant of proportionality and G is a function of σ and κ termed a *plastic potential function.* For the particular case where $G = F$, the plastic flow law is termed *associated*, whereas the term *non-associated flow law* relates to the general case $G \neq F$. Physically speaking, associated laws are preferable because the flow laws that relate the post-yield stresses and incremental strains are derived from the yield function. This is equivalent to saying that the material can only deform in ways which maintain the yield stress. However, most associated laws have a drawback: they predict that any increment of plastic shearing will be accompanied by a proportional increase in volume of the sheared material. In contrast, non-associated flow laws allow volume constancy during deformation. Laboratory rock deformation tests show that some rocks do dilate during deformation, but that dilation is significant only at small strains under low confining pressures (Brace, Paulding & Scholz 1966). Which type of flow law is best, then, is determined by the scale of the tectonic problem being addressed. Associated and non-associated flow laws are most easily compared on a plot (Figure 3.2) using the same coordinate axes for normal stresses (σ_n) and plastic normal strains (ϵ_n^p), shear stresses (σ_s) and plastic shear strains (ϵ_s^p). The Mohr circle on Figure 3.2 a) illustrates a stress state at the point of yield. Limiting stress states can be represented in two ways (see the inset of Figure 3.2 a): by the Coulomb line, which makes a tangent to all critical stress circles at points corresponding to incipient slip planes; by the shear strength line, which passes through all critical stress circles at the point of maximum shear stress. The angles of inclination for the two lines, ϕ and χ respectively, are linked by the relation

$$sin\phi = tan\chi \tag{3.10}$$

We can define vectors for incremental plastic strain ($\overrightarrow{\delta\epsilon^p}$) and stress ($\overrightarrow{\sigma}$) in this shear/normal stress/strain space. Their spatial association is motivated by the fact that the dot product of these two vectors is the increment of plastically dissipated mechanical work. The normal component of $\overrightarrow{\delta\epsilon^p}$ is $\frac{\delta V}{V}$, the sum of the normal strains, also termed the volumetric strain or

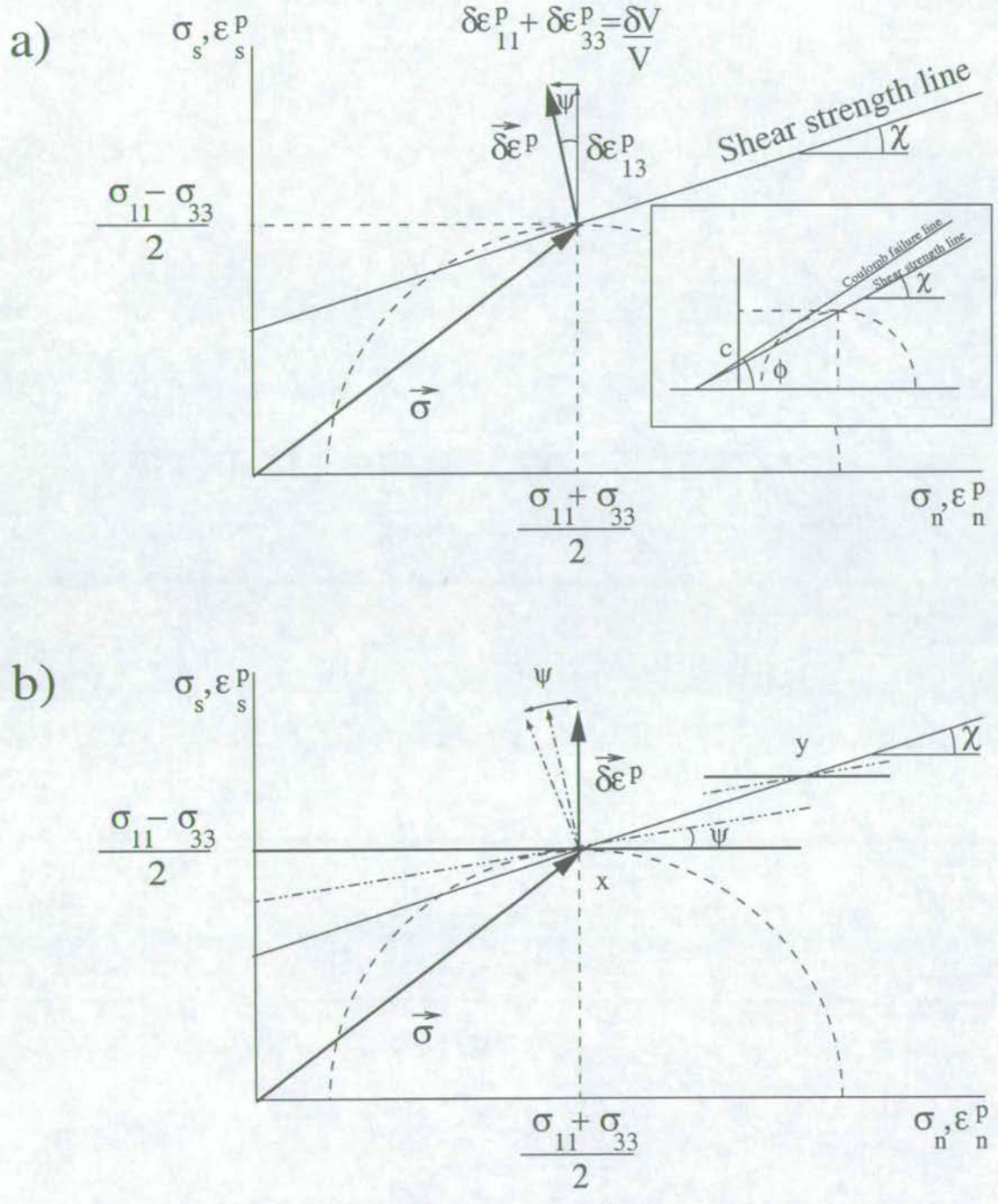

Figure 3.2. Relating dilatancy, limit stress and plastic strain increments in the combined stress/plastic strain plane. After Mandl (1993).

dilation. ψ is known as the dilation angle. For associated flow laws, $\chi = \psi$ and the incremental plastic strain vector is perpendicular to the shear strength line. Unless $\chi = 0$, this *condition of normality* means associated plastic flow laws predict dilation under shearing. For non-associated flow laws, the incremental plastic strain is not normal to the shear strength line but to the plastic potential function. Non-associated laws allow us to model materials with pressure dependent yield functions ($\chi > 0$) but without dilatant plastic flow ($\psi = 0$). Plastic potential functions do not form continuous lines on diagrams like Figure 3.2: they must be redrawn at every critical state of stress, indicated on b) by the thick horizontal lines at x and y. Of course, plastic potential functions with $\psi \neq 0$, $\psi \neq \chi$ can be chosen (short dash-dot lines on Figure 3.2b) but they also suffer from the problem of predicting that any increment of plastic shearing will be accompanied by a proportional increase in volume, which is not the observed behaviour of crustal rocks over length scales of kilometres. In this study, the same pressure independent relationship was chosen for the yield function F and plastic potential function G, and so consequently the associated plastic flow law did not have the drawback of dilation.

3.2.5 Yield and the scalar invariants of stress

Elastic behaviour breaks down when the rock begins to permanently deform or yield. A mathematical framework for describing the conditions at yield is required. Pressure alone does not cause rock failure, so all yield criteria must include deviatoric stress terms. A further property of yield criteria is that they must be independent of the choice of coordinate axes, so can be expressed in terms of the invariants of the stress tensor. If we consider a compressional stress state

$$\sigma_{ij} = \begin{pmatrix} \sigma_1 & 0 & 0 \\ 0 & \sigma_2 & 0 \\ 0 & 0 & \sigma_3 \end{pmatrix} \tag{3.11}$$

with $\sigma_1 > \sigma_2 > \sigma_3 > 0$, we can visualise the state of stress as an ellipsoid in stress space with principal axes of length σ_1, σ_2 and σ_3. The invariants are then three independent measures of the size and shape of the ellipsoid. The first invariant is the trace of the matrix and the sum of the lengths of the principal axes of the ellipsoid:

$$I_\sigma = \sigma_1 + \sigma_2 + \sigma_3 \tag{3.12}$$

$$I_\sigma = 3\sigma_m \tag{3.13}$$

where σ_m is the mean normal stress or pressure. The second invariant of the matrix relates to the sum of the areas of the ellipses that lie in the principal planes of the ellipsoid:

$$II_\sigma = -(\sigma_2\sigma_3 + \sigma_3\sigma_1 + \sigma_1\sigma_2). \tag{3.14}$$

The third invariant is the determinant of the matrix, which relates to the volume of the ellipsoid as it is the product of the lengths of the ellipsoid's principal axes:

$$III_\sigma = \sigma_1\sigma_2\sigma_3. \tag{3.15}$$

For coordinate systems not aligned with the principal stress axes

$$\sigma_{ij} = \begin{pmatrix} \sigma_{11} & \sigma_{12} & \sigma_{13} \\ \sigma_{12} & \sigma_{22} & \sigma_{23} \\ \sigma_{13} & \sigma_{23} & \sigma_{33} \end{pmatrix} \tag{3.16}$$

the invariants are:

$$I_\sigma = \sigma_{11} + \sigma_{22} + \sigma_{33} \tag{3.17}$$

$$II_\sigma = -(\sigma_{22}\sigma_{33} + \sigma_{33}\sigma_{11} + \sigma_{11}\sigma_{22}) + \sigma_{23}^2 + \sigma_{13}^2 + \sigma_{12}^2 \tag{3.18}$$

$$III_\sigma = \sigma_{11}\sigma_{22}\sigma_{33} + 2\sigma_{23}\sigma_{13}\sigma_{12} - \sigma_{11}\sigma_{23}^2 - \sigma_{22}\sigma_{13}^2 - \sigma_{33}\sigma_{12}^2 \tag{3.19}$$

In the case of plane strain ($\sigma_{21} = \sigma_{22} = \sigma_{23} = 0$), only two independent measures of the stress state exist

$$I_\sigma = \sigma_{11} + \sigma_{33} \tag{3.20}$$

$$II_\sigma = -\sigma_{33}\sigma_{11} + \sigma_{13}^2 \tag{3.21}$$

The stress tensor is often split into a pressure tensor, σ_m, and a deviatoric stress tensor, $\sigma_{ij}^{'}$ so that

$$\sigma_{ij} = \sigma_m + \sigma_{ij}^{'}. \tag{3.22}$$

For the plane strain case where principal stresses coincide with coordinate axes, we have

$$\begin{pmatrix} \sigma_1 & 0 \\ 0 & \sigma_3 \end{pmatrix} = \begin{pmatrix} \frac{\sigma_1+\sigma_3}{2} & 0 \\ 0 & \frac{\sigma_1+\sigma_3}{2} \end{pmatrix} + \begin{pmatrix} \sigma_1 - \frac{\sigma_1+\sigma_3}{2} & 0 \\ 0 & \sigma_3 - \frac{\sigma_1+\sigma_3}{2} \end{pmatrix}. \tag{3.23}$$

$$= \begin{pmatrix} \frac{\sigma_1+\sigma_3}{2} & 0 \\ 0 & \frac{\sigma_1+\sigma_3}{2} \end{pmatrix} + \begin{pmatrix} \frac{\sigma_1-\sigma_3}{2} & 0 \\ 0 & \frac{\sigma_1-\sigma_3}{2} \end{pmatrix}, \tag{3.24}$$

and for the plane strain case in a generic coordinate system

$$\begin{pmatrix} \sigma_{11} & \sigma_{13} \\ \sigma_{13} & \sigma_{33} \end{pmatrix} = \begin{pmatrix} \frac{\sigma_{11}+\sigma_{33}}{2} & 0 \\ 0 & \frac{\sigma_{11}+\sigma_{33}}{2} \end{pmatrix} + \begin{pmatrix} \sigma_{11} - \frac{\sigma_{11}+\sigma_{33}}{2} & \sigma_{13} \\ \sigma_{13} & \sigma_{33} - \frac{\sigma_{11}+\sigma_{33}}{2} \end{pmatrix} \tag{3.25}$$

$$= \begin{pmatrix} \frac{\sigma_{11}+\sigma_{33}}{2} & 0 \\ 0 & \frac{\sigma_{11}+\sigma_{33}}{2} \end{pmatrix} + \begin{pmatrix} \frac{\sigma_{11}-\sigma_{33}}{2} & \sigma_{13} \\ \sigma_{13} & \frac{\sigma_{33}-\sigma_{11}}{2} \end{pmatrix}. \tag{3.26}$$

Failure criteria can also be expressed in terms of the invariants of these two parts of the stress tensor: I of σ_m, and II of $\sigma_{ij}^{'}$:

$$I_{\sigma_m} = \sigma_{11} + \sigma_{33} \tag{3.27}$$

$$II_{\sigma'} = |\sigma'_{ij}| = -(\frac{\sigma_{11} - \sigma_{33}}{2})^2 - \sigma_{13}^2 \tag{3.28}$$

$$I_{\sigma_m} = \sigma_1 + \sigma_3 \tag{3.29}$$

$$II_{\sigma'} = |\sigma'_{ij}| = -(\frac{\sigma_1 - \sigma_3}{2})^2 \tag{3.30}$$

On a Mohr diagram, these invariants correspond to the centre and the square of the radius of the stress circle (See Figure 3.3). In three dimensions, it is also useful to consider the invariants of the isotropic and anisotropic parts of the stress tensor separately.

$$I_{\sigma_{ij}} = \sigma_1 + \sigma_2 + \sigma_3 = 3\sigma_m \tag{3.31}$$

$$I_{\sigma'_{ij}} = \sigma'_1 + \sigma'_2 + \sigma'_3 = (\sigma_1 - \sigma_m) + (\sigma_2 - \sigma_m) + (\sigma_3 - \sigma_m) = 0 \tag{3.32}$$

$$II_{\sigma'_{ij}} = -(\sigma'_2\sigma'_3 + \sigma'_3\sigma'_1 + \sigma'_1\sigma'_2) \tag{3.33}$$

Putting 3.32 in 3.33 we have

$$II_{\sigma'_{ij}} = \frac{1}{2}(\sigma'^2_1 + \sigma'^2_2 + \sigma'^2_3) \tag{3.34}$$

3.2.6 Yield criteria I: The Von Mises law

Having developed a mathematical framework for discussing the phenomena of yielding, we can now examine all the criteria that have been proposed to describe rock failure. The simplest of these is the criterion proposed by Von Mises. This yield criterion (Figure 3.4) describes the failure of a purely cohesive, non-frictional solid. It does not include a mean stress term because

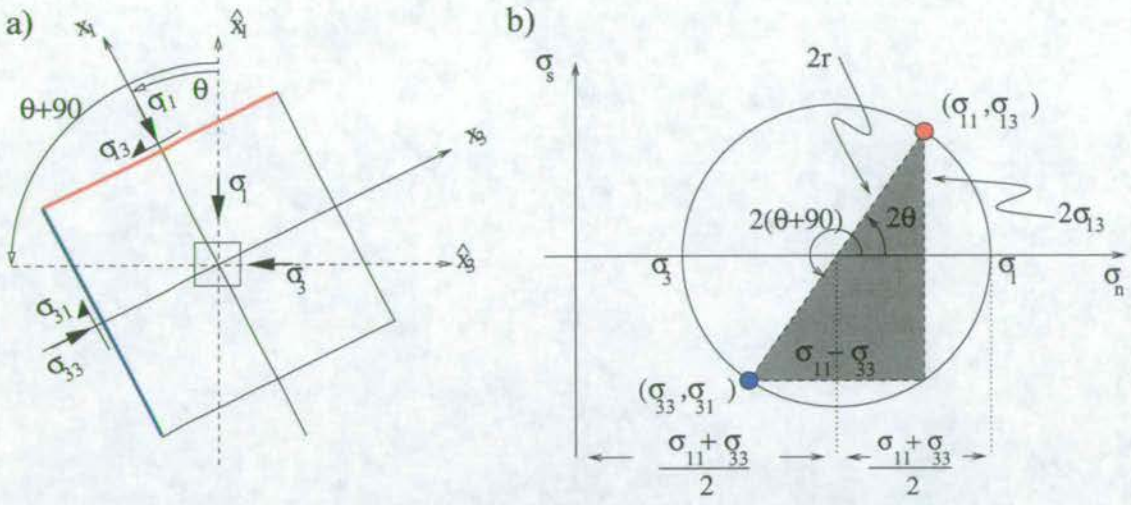

Figure 3.3. a) The stress state at a point described both on Cartesian axes, $x_{1,3}$, and principal axes $\hat{x}_{1,3}$. b) The same stress state on the Mohr circle. Applying Pythagoras' theorem to the shaded triangle we have: $(2r)^2 = (\sigma_{11} - \sigma_{33})^2 + (2\sigma_{13})^2$, or $r = (\frac{1}{4}\ (\sigma_{11} - \sigma_{33})^2 + \sigma_{13}^2)^{1/2}$.

the shear strength of such a material would be unaffected by a change in the mean effective normal stress. It states that failure occurs when the deviatoric stress meets the condition

$$II_{\sigma'} = \frac{\sigma_o^2}{3}\ , \tag{3.35}$$

or (using 3.34)

$$(\sigma_1^{'2} + \sigma_2^{'2} + \sigma_3^{'2}) = \frac{2\sigma_o^2}{3}\ , \tag{3.36}$$

where σ_o is a material constant, as illustrated in Figure 3.4 c).

In the plane strain case (Figure 3.4 a and b) we can write:

$$(\frac{\sigma_1 - \sigma_3}{2}\ )^2 = K^2 \tag{3.37}$$

In strain hardening or softening, σ_o is not constant but varies as the accumulated plastic strain, κ, varies between 0 and a critical value κ_c (Figure 3.4 d). The yield/plastic potential function is then

$$F(\sigma, \kappa) \equiv G(\sigma, \kappa) = \sigma_{eff} - \sigma_y = \sqrt{\frac{3}{2}\ (\sigma_1^{'2} + \sigma_2^{'2} + \sigma_3^{'2})} - \sigma_y \tag{3.38}$$

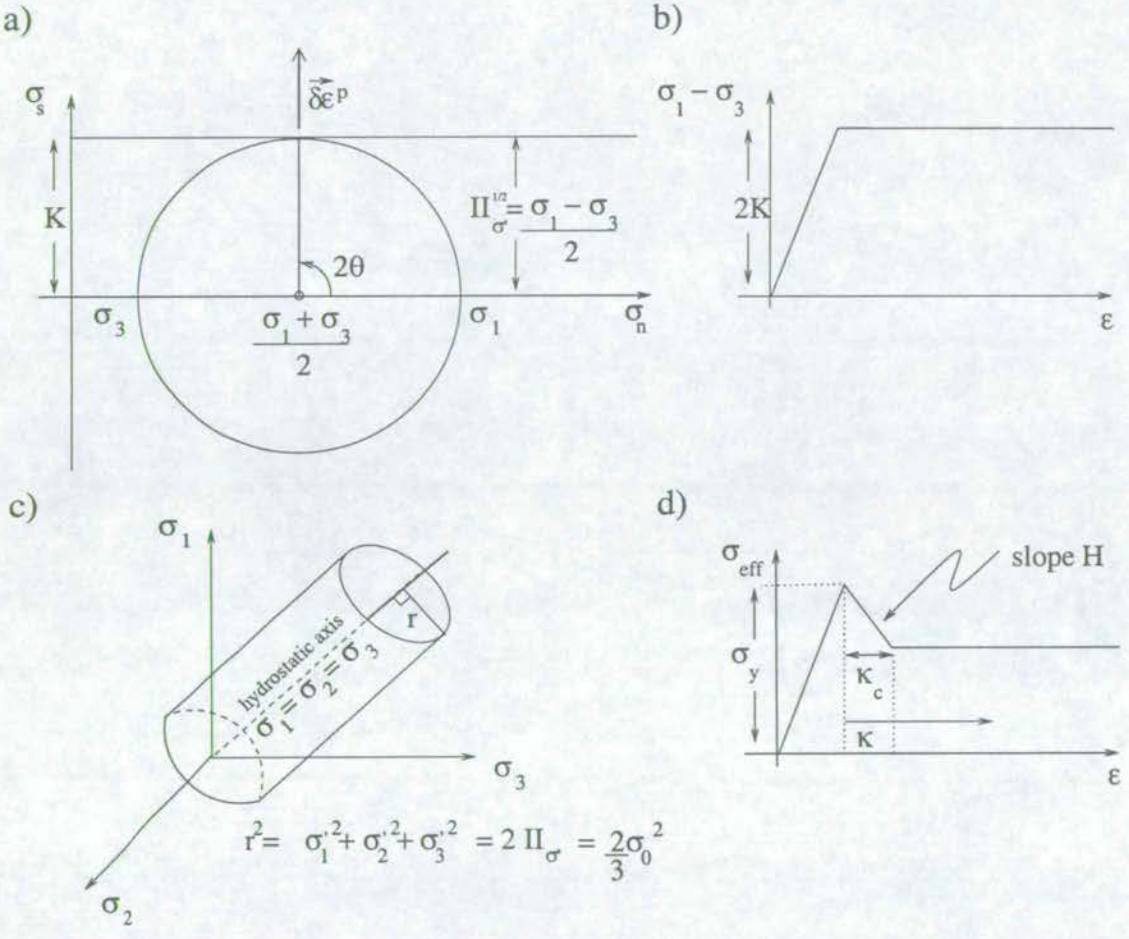

Figure 3.4. Several ways to visualise the Von Mises yield criterion: a) Normal stress/shear stress space. The relationship between the yield function and the Mohr circle. b) Stress/strain curve for uniaxial compression. c) The yield surface in principal stress space. d) Stress/strain curve for a strain softening Von Mises material in uniaxial compression.

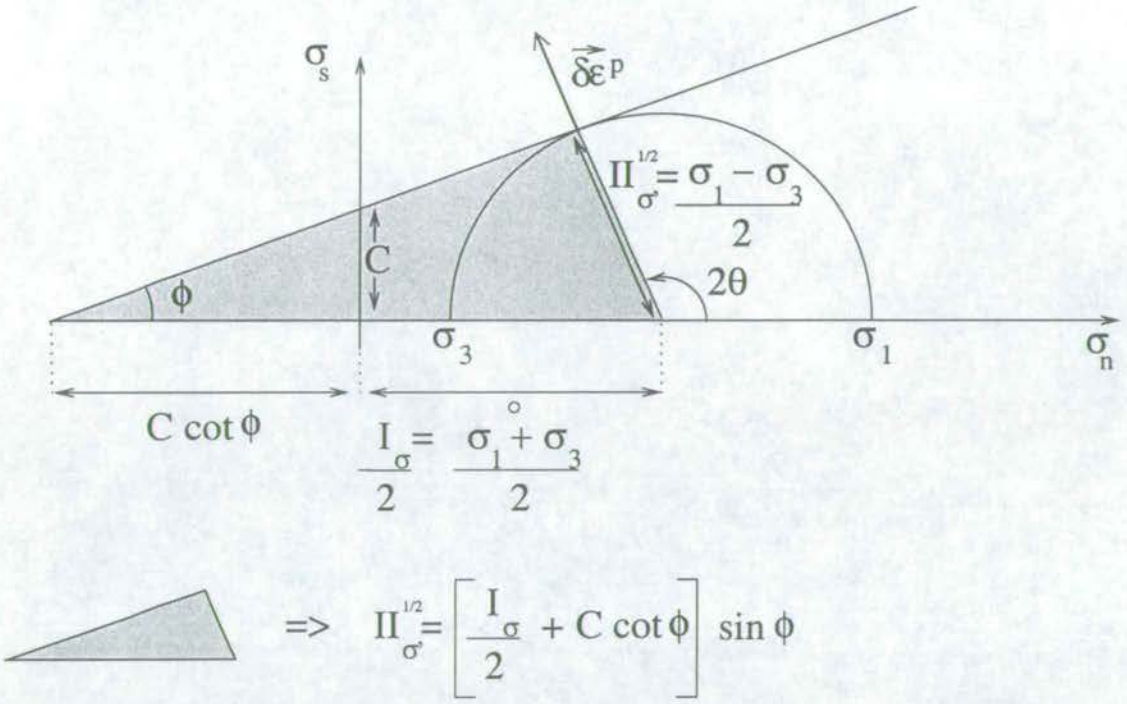

Figure 3.5. The Mohr-Coulomb failure criterion in normal stress/shear stress space. Simple trigonometry on the shaded triangle gives the yield criterion in terms of the invariants of the stress tensor, rather than σ_n and σ_s.

$$\sigma_y = \begin{cases} \sigma_o + H\kappa, & \kappa < \kappa_c \\ \sigma_o + H\kappa_c, & \kappa \geq \kappa_c \end{cases} \tag{3.39}$$

3.2.7 Yield criteria II: The Mohr-Coulomb law

The Mohr-Coulomb criterion (equation 3.40) is more realistic for frictional materials like rock. In contrast to the Von Mises criterion, the yield strength is not independent of mean effective normal stress. It states that failure will occur on a plane when the combination of shear stress (σ_s) and effective normal stress (σ_n) exceeds a critical value C:

$$|\sigma_s| - \sigma_n tan\phi = C \tag{3.40}$$

The critical value C is the cohesive shear strength and ϕ the angle of internal friction, as illustrated by Figure 3.5. Expressing 3.40 in terms of the invariants of the stress tensor, for the

plane strain case, we have

$$(II_{\sigma'})^{1/2} = \frac{I}{2}\ sin\phi + Ccos\phi. \tag{3.41}$$

In terms of principal stresses, the Mohr-Coulomb plastic yield function reads

$$F(\sigma_{ij}) = \sigma_1 - \sigma_3 - (\sigma_1 + \sigma_3)sin\phi - 2cos\phi = 0 \tag{3.42}$$

and the plastic potential function is

$$G(\sigma_{ij}) = \sigma_1 - \sigma_3 - (\sigma_1 + \sigma_3)sin\psi + constant \tag{3.43}$$

which generates an associated flow law if $\psi = \phi$.

The failure envelope in principal stress space is an hexagonal cone (see Mandl (1993), p.334 for a derivation of this result). In a space where the coordinate axes are defined by the directions of the principal stresses (and principal strains, as we assume they are coaxial), the strain rate vector must be normal to the surface defined by the plastic potential function. A unique normal can be defined for a plane but not for a line; only one normal exists for each face of an hexagonal pyramid, but any number of lines can be drawn which are 90^0 to the edges where the faces meet. For this reason, it is unwise to use the Mohr-Coulomb law as a plastic potential function for numerical simulations, at least.

3.2.8 Yield criteria III: The Drucker-Prager law

The yield criterion developed by Drucker & Prager (1952) is another model for failure of pressure-sensitive materials. The advantage of this law over the Mohr-Coulomb law is that it forms a smooth yield surface (see Figure 3.6) in principal stress space and so unique normals to the yield surface can always be found. Hassani, Jongmans & Chéry (1997) define the Drucker-Prager yield function as

$$F(\sigma) = \sqrt{3}II_{\sigma'_{ij}}^{1/2} + \frac{\alpha}{3}\ I_{\sigma_{ij}} - \alpha P_o \tag{3.44}$$

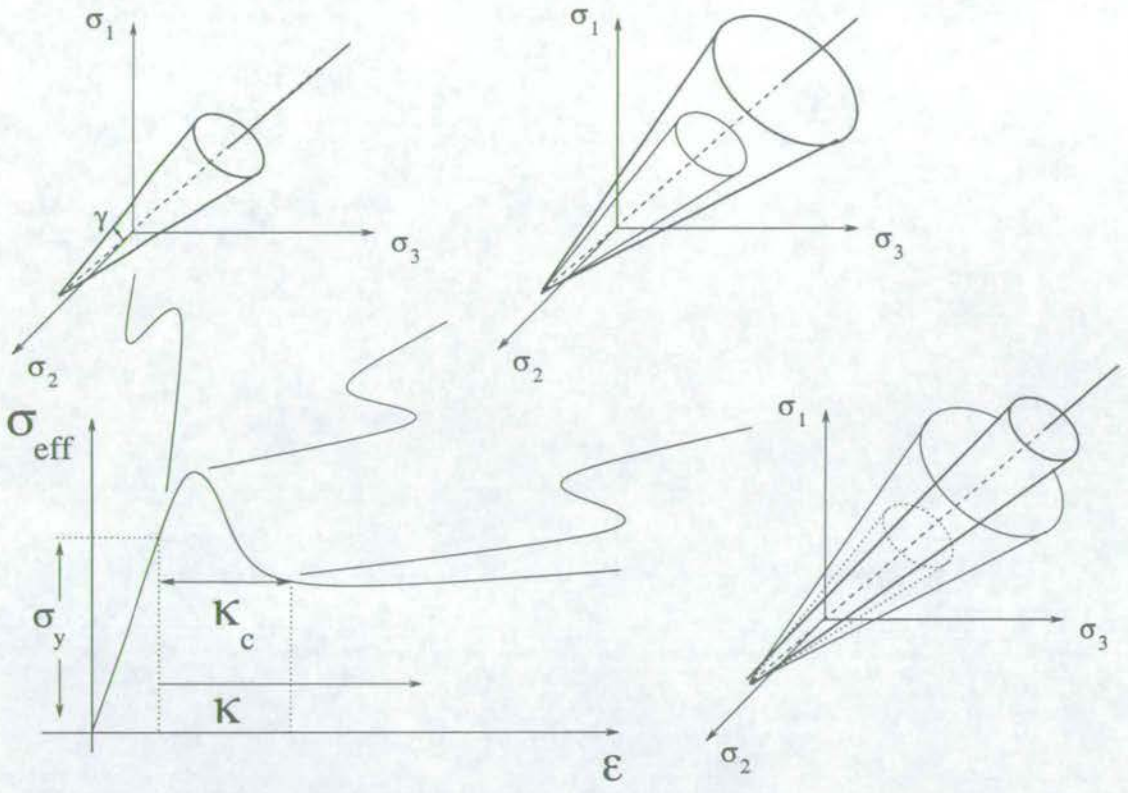

Figure 3.6. Relating the stress-strain curve for a strain hardening and softening Drucker-Prager material with the yield surface in principal stress space. For a cone inscribed inside the Mohr-Coulomb pyramid, the apex lies in the tensile octant at a distance $Ccot\phi$ from the origin. The half-apex angle, γ is related to the internal friction angle by $tan\gamma = \sqrt{3}sin\phi(3+sin^2\phi)^{-1/2}$.

where α and P_o are simply parameters of the Mohr envelope that depend on the angle of internal friction ϕ and the cohesion C

$$\alpha = \frac{6sin\phi}{3 - sin\phi}\ , P_o = Ccot\phi \tag{3.45}$$

Explicitly:

$$F(\sigma) = \left(\frac{3}{2}\left(\sigma_1^{'2} + \sigma_2^{'2} + \sigma_3^{'2}\right)\right)^{1/2} + \frac{6sin\phi}{3 - sin\phi}\ \frac{\sigma_1 + \sigma_2 + \sigma_3}{3} - \frac{6sin\phi}{3 - sin\phi}\ \frac{Ccos\phi}{sin\phi} \tag{3.46}$$

The Drucker-Prager yield function can be modified to incorporate strain softening and hardening by introducing a dependence on κ, the accumulated plastic strain.

$$F(\sigma, \kappa) = \sigma_{eff}(I_{\sigma_{ij}}, II_{\sigma'_{ij}}, \kappa) - \sigma_y(\kappa) = 0 \tag{3.47}$$

In the Von Mises case, hardening or softening was achieved by making the cohesion vary with κ. In the Drucker-Prager case, the yield strength could be varied by making either the cohesion, or the angle of internal friction, or both, strain-dependent. Mandl (1993) states "Since virtually nothing is known about the strain dependence of the cohesive strength, one might as well disregard such changes and maintain a constant value instead". In the formulation of Niño (1997) cohesion is constant and ϕ varies with strain in the manner proposed by Leroy & Ortiz (1989)

$$sin\phi(\kappa) = sin\phi_i + 2(sin\phi_f - sin\phi_i)\frac{\sqrt{\kappa_c \kappa}}{\kappa + \kappa_c} \tag{3.48}$$

in which ϕ_i is the initial angle of internal friction and ϕ_f the friction angle attained after the cumulative plastic deformation has acquired the value κ_c. σ_{eff} and σ_y in equation 3.47 are then

$$\sigma_{eff} = \left(\frac{3}{2}\left(\sigma_1^{'2} + \sigma_2^{'2} + \sigma_3^{'2}\right)\right)^{1/2} + \alpha(\kappa)\frac{\sigma_1 + \sigma_2 + \sigma_3}{3} \tag{3.49}$$

$$\sigma_y = \alpha(\kappa) C cot\phi(\kappa) \tag{3.50}$$

and

$$\alpha(\kappa) = \frac{6sin\phi(\kappa)}{3 - sin\phi(\kappa)} \tag{3.51}$$

The plastic potential function is given by

$$G(\sigma_{ij}) = \left(\frac{3}{2}\left(\sigma_1^{'2} + \sigma_2^{'2} + \sigma_3^{'2}\right)\right)^{1/2} + \frac{6sin\psi}{3 - sin\psi}\ \frac{\sigma_1 + \sigma_2 + \sigma_3}{3} \tag{3.52}$$

3.2.9 Yield criteria IV: The Van Eekelen law

Barnichon & Charlier (1996) advocate the use of the yield criterion developed by Van Eekelen

(1980):

$$F(\sigma_{ij}) = aI_{\sigma_{ij}}(1 - bsin3\beta)^n - \sqrt{II_{\sigma'_{ij}}}. \tag{3.53}$$

In addition to pressure and deviatoric stress, this yield criterion introduces a dependence on the third invariant of the stress tensor by including a term β, the Lode angle.

$$\beta = \frac{1}{3}\, sin^{-1}\left(\frac{3\sqrt{3}III_{\sigma'_{ij}}}{2II^{3/2}_{\sigma'_{ij}}}\right) \tag{3.54}$$

or Hill (1950)

$$\beta = tan^{-1}\left(\frac{-1}{\sqrt{3}}\,\frac{2\sigma_3 - \sigma_1 - \sigma_2}{\sigma_1 - \sigma_2}\right). \tag{3.55}$$

Looking down the hydrostatic axis (Figure 3.7), β is the angle between the pure shear line and the line defining the state of stress. This criterion also allows for different angles of internal friction in compression ϕ_c and tension ϕ_e, via the coefficients a and b.

$$b = \frac{\left(\frac{r_c}{r_e}\right)^{1/n} - 1}{\left(\frac{r_c}{r_e}\right)^{1/n} + 1}, a = \frac{r_c}{(1+b)^n} \tag{3.56}$$

where

$$r_c = \frac{1}{\sqrt{3}}\,\frac{2sin\phi_c}{3 - sin\phi_c}, r_e = \frac{1}{\sqrt{3}}\,\frac{2sin\phi_e}{3 + sin\phi_e}. \tag{3.57}$$

The Van Eekelen criterion is a clearly a better approximation to the Mohr-Coulomb criterion than the Drucker-Prager cone but, like the Drucker-Prager cone, it forms a smooth surface in principal stress space. This means that unique normals can be defined all across the yield surface, making it suitable for use in numerical models (see Section 3.2.7).

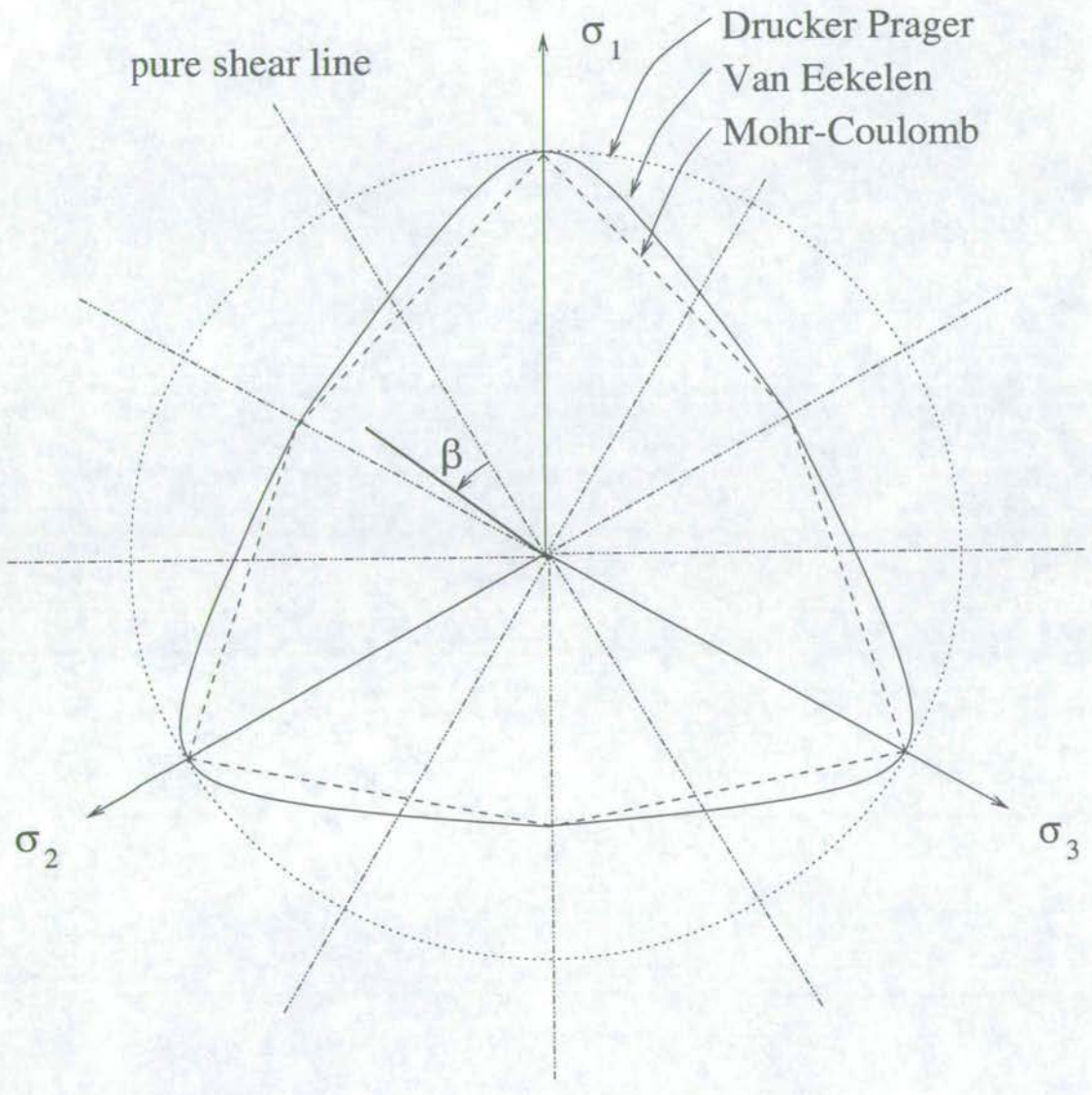

Figure 3.7. Limit surfaces for Mohr-Coulomb, Drucker-Prager and Van Eekelen models, looking down the hydrostatic axis in principal stress space.

3.2.10 Choosing an appropriate yield criterion for this study

Yield criteria appropriate to this study must meet several conditions. Firstly, they must be suited to solution by numerical methods. The Mohr-Coulomb law was rejected for this study because calculating the strain rate from the stress fields involves finding a normal to the yield surface and, for this law, unique normals do not always exist. To be suitable for this study, the theory must also include a description of post-yield strain softening. The Van Eekelen criteria was ruled out on this basis, as I was able to find no reference to the use of this law with strain-dependent friction angles (i.e. softening). Finally, the plastic law should allow the initial yield strength, peak strength and residual shear strength to be controlled precisely and independently. In the Drucker-Prager case these attributes of the stress-strain curve are not independent and are controlled indirectly by the parameters ϕ_i, ϕ_f and ψ. For this reason, the Drucker-Prager criterion was not used in this study. The only criterion which proved to be acceptable in terms of the criteria above is that of Von Mises. It is far from ideal, however, as it fails to properly describe two observations related to faulting in rock, namely the increase in yield strength with mean stress and the inclination of faults with respect to the maximum compressive principal stress (in nature, the angle is always $< 45^o$, but Von Mises law predicts failure at 45^o exactly).

3.3 Numerical Implementation of the Theory: ADELI

3.3.1 Contributions to the evolution of the code

Numerical models are most effective if designed and used for simulating a specific physical system. However, writing a code from scratch to address the issues specific to this study was not feasible given the time constraints on this project. For that reason, I chose to use a pre-existing code; ADELI. I had access to other numerical modelling software, but I chose ADELI because it can model large strains (up to 5% extension) and a wide range of boundary conditions, making it particularly suitable for this study. Although not a commercial code, ADELI uses several sophisticated techniques to improve efficiency and its use in modelling geological problems is well established (see below). However, as ADELI was not written with this study in mind, and consequently some modifications had to be made, I took the precaution of performing some tests to verify that it was "fit-for-purpose" (Section 3.5).

The ADELI code solves two-dimensional geodynamic problems in viscous and elasto-plastic

rheologies under quasi-static conditions. Spatial discretisation is accomplishes using the finite element method. Temporal discretisation is done using the finite difference method. The boundary conditions create plane strain in a body which is finite in two directions but infinite in the third, so while the stress field is three dimensional, strains in the third direction cannot occur. The essential elements of the code are covered below but more detailed descriptions can be found in Hassani (1994) and Niño (1997).

ADELI was written by Riad Hassani and Jean Chéry, and owes much to the FLAC code of Cundall (1989), in terms of the methods used to solve the governing equations. Fernando Niño developed the re-meshing algorithms and Francis Lucazeau added routines for erosion and sedimentation, not used here. In various implementations, ADELI has been used to investigate:

- earthquake nucleation and propagation in terms of changes in crustal strength or fault rheology (Huc *et al.* 1998),
- plate deformation and stress in subduction processes (Hassani *et al.* 1997),
- the topography generated by crustal-scale normal faults (Hassani & Chéry 1996),
- the propagation of a blind thrust through overlying sediments (Niño, Philip & Chéry 1998), and interactions between faults, erosion and sedimentation in compressional basins (Niño, Chéry & Gratier 1998).

Previous studies using ADELI have modelled only a few faults in layers composed of homogeneous materials. They have incorporated faults as frictional surfaces, whose location and geometrical arrangement was defined by the user. In some studies, strain localised in regions up-dip or down-dip from the pre-defined fault as a response to movement on the surface, but fault growth and interaction have only been studied in this limited sense. By contrast, in this study faults are not defined *a priori* but develop spontaneously as bands of localised shearing. I modified the code to incorporate heterogeneity so that the initial location and orientation of shear bands would be controlled simply by the location of weaknesses and the prevailing stress field.

3.3.2 The finite element method

The finite element method relies on the postulate that a complex whole can be broken down into a finite number of smaller pieces, the behaviour of each of which is known or can be supposed. To apply the finite element method to geodynamic problems, the deforming region

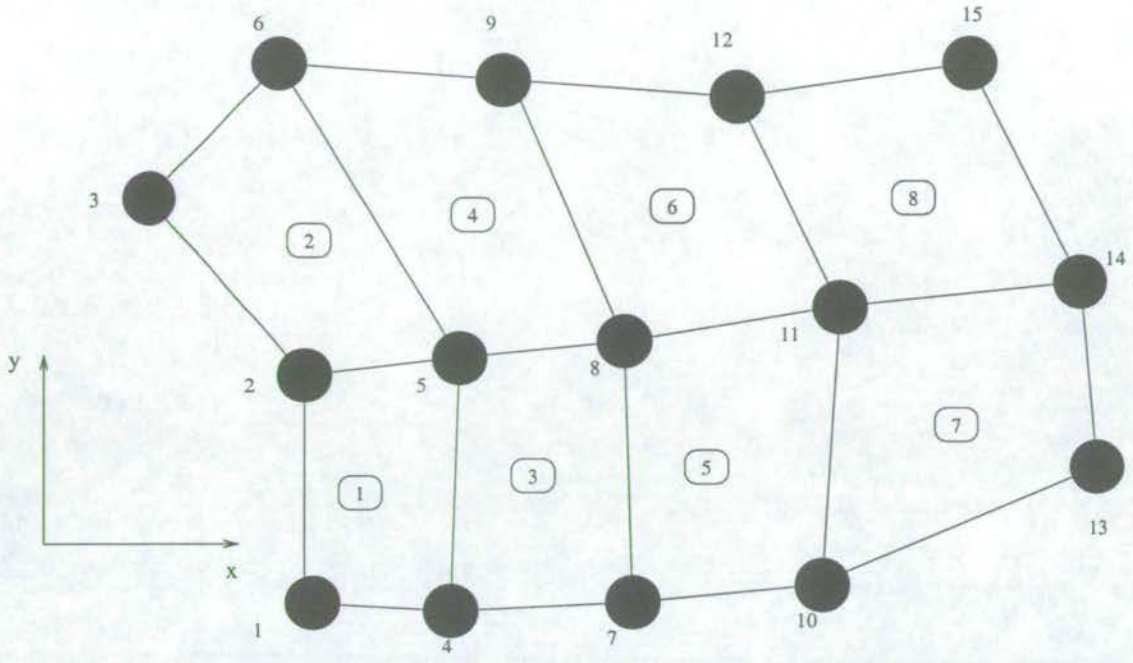

Figure 3.8. Finite element mesh terminology, filled circles represent nodes, open boxes elements.

is discretised into a mesh of elements joined by nodes and the governing equations are solved for displacement and velocity at each node. The values of these quantities at every point in space can then be found by interpolating between the values at the nodes of each element. Figure 3.8 illustrates the terminology of the finite element mesh. The physical domain is broken down into 8 elements. The shapes of the elements are determined by the positions of the 15 nodes. When the domain is loaded, the nodes can move. In the two-dimensional case illustrated, all possible movements of a node can be described by a combination of translation in the x direction (u) and translation in the y direction (v), so each node is said to have two degrees of freedom. The entire model illustrated would then have 15x2=30 degrees of freedom. At each point in space the mechanics of the system at equilibrium is described by

$$F_{ext} + F_{int} = M\ddot{u}, \tag{3.58}$$

where M is the mass matrix, $\ddot{u}$ is the nodal acceleration vector, F_{ext} and F_{int} are vectors of the external and internal nodal forces. In quasi-static equilibrium, there are negligible accelerations so the expression reduces to

$$F_{ext} + F_{int} = 0. \tag{3.59}$$

3.3.3 The fictional mass approach

For a system in quasi-static balance, the traditional formulation of finite elements leads us to solve an equation of the form [see for example Zienkiewickz (1977)]:

$$F = Ku \tag{3.60}$$

where K is called the stiffness matrix. In a 2D formulation the force at each node i can be resolved into two components, X_i and Y_i, and the displacement into u_i and v_i. For a domain described by just four nodes, equation 3.60 expands to

$$\begin{pmatrix} X_1 \\ Y_1 \\ X_2 \\ Y_2 \\ X_3 \\ Y_3 \\ X_4 \\ Y_4 \end{pmatrix} = \begin{pmatrix} k_{11} & k_{12} & k_{13} & k_{14} & k_{15} & k_{16} & k_{17} & k_{18} \\ k_{21} & k_{22} & k_{23} & k_{24} & k_{25} & k_{26} & k_{27} & k_{28} \\ k_{31} & k_{32} & k_{33} & k_{34} & k_{35} & k_{36} & k_{37} & k_{38} \\ k_{41} & k_{42} & k_{43} & k_{44} & k_{45} & k_{46} & k_{47} & k_{48} \\ k_{51} & k_{52} & k_{53} & k_{54} & k_{55} & k_{56} & k_{57} & k_{58} \\ k_{61} & k_{62} & k_{63} & k_{64} & k_{65} & k_{66} & k_{67} & k_{68} \\ k_{71} & k_{72} & k_{73} & k_{74} & k_{75} & k_{76} & k_{77} & k_{78} \\ k_{81} & k_{82} & k_{83} & k_{84} & k_{85} & k_{86} & k_{87} & k_{88} \end{pmatrix} \begin{pmatrix} u_1 \\ v_1 \\ u_2 \\ v_2 \\ u_3 \\ v_3 \\ u_4 \\ v_4 \end{pmatrix} \tag{3.61}$$

In a realisation with *nnodes* nodes, the stiffness matrix would have $4nnodes^2$ elements and so, in all but trivial problems, finding the displacements by solving this equation requires the inversion of a large, sparse matrix. Although efficient algorithms exist for just this task, the problem of storing and inverting a large matrix can be avoided entirely by the use of the fictional mass approach. The static solution has no reliance on accelerations, but for numerical efficacy, we can add a fictitious acceleration provided that we also add a damping term to remain in the quasi-static regime. Equation 3.59 then becomes

$$F_{ext} + F_{int} = M\ddot{u} + C\dot{u} = 0, \tag{3.62}$$

and the displacement vector u can be found by direct integration from the acceleration. Poliakov (unpubl.) expressed concerns over the effect of a velocity dependent damping term since localisation occurs as a discontinuity in velocity gradient (Odé 1960, Rudnicki & Rice 1975, Rudnicki 1977) and this term is governed by velocity. Cundall & Board (1988) recommend

the use of a damping term based on the magnitude of the unbalanced force instead,

$$F_{damp} = -a\ sgn(\dot{u})|F_{ext} + F_{int}|. \tag{3.63}$$

where a is the damping coefficient and $sgn(\dot{u})$ the sign (-ve or +ve) of $\dot{u}$. Should the damping term become too large, the quasi-static assumption will be invalid so the damping coefficient must be carefully chosen (a value of 0.8 was used in this study) and relative size of the unbalanced forces must be negligible. This is the case if

$$\frac{|F_{int} + F_{ext}|}{|F_{int}| + |F_{ext}|} << 1 \tag{3.64}$$

3.3.4 Fixing the time step

ADELI has an intrinsic time step Δt chosen to be sufficiently small so that elastic waves propagate only a fraction of the length of one element, ensuring numerical stability of the FE scheme. If the smallest elemental length is Δl_{min} and compressional elastic waves propagate at v_p, then

$$\Delta t = \frac{\Delta l_{min}}{v_p} \tag{3.65}$$

The wave velocity is related to material properties by

$$v_p^2 = \frac{1}{\rho}\ [K + \frac{4}{3}\ \mu], \tag{3.66}$$

where K is the bulk or incompressibility modulus and μ the shear modulus. Rewriting, we find an expression for density in terms of two physical parameters (the elastic moduli) and two numerical parameters (the time step and length scale of spatial discretisation)

$$\rho = (\frac{\Delta t}{\Delta l_{min}}\ )^2[K + \frac{4}{3}\ \mu]. \tag{3.67}$$

By increasing the fictitious density by a factor of 10, we increase the time step by a factor of 100 and so by increasing the fictitious mass, we can examine deformation over longer time intervals without increasing the time-step (which degrades the numerical solution) or increasing the run

time of the simulation (which is computationally expensive). The mass of an element is found using this density and the area of the element. The mass of a node (the elements of the mass matrix M of equation 3.63) is taken to be the mean of the masses of the elements to which it is attached.

Typical runs contained thousands of calculation time steps, and it was not possible to write to disk the displacements, velocities stresses and strains of all elements in the mesh at each time step. Consequently in addition to the calculation time step, a write time step or snapshot interval had to be defined. This was chosen to be a multiple of the calculation time step such that between 20 and 40 snapshots were recorded in each simulation.

3.3.5 Solution algorithm

A general solution algorithm is presented here, for iteration number n. For completeness, steps involving contact forces on frictional surfaces have been included, however this aspect of the code was not used in this study. For all elements

1. Calculate the external forces (explicit finite element scheme)
2. Calculate the unbalanced force
3. Calculate the acceleration
4. Calculate the unbalanced velocities and displacements (via finite differences)
5. Calculate the contact forces
6. Correct the velocities and displacements (via finite differences)
7. Update the node coordinates with calculated displacements
8. Recalculate the stress field and the internal forces (via implicit finite element scheme)
9. Return to 1, with n=n+1

3.4 Model Parameters

As with all experiments, decisions have to be made about the design of the model. Choices in the physical system include the size of the model, the boundary conditions and the mechanical

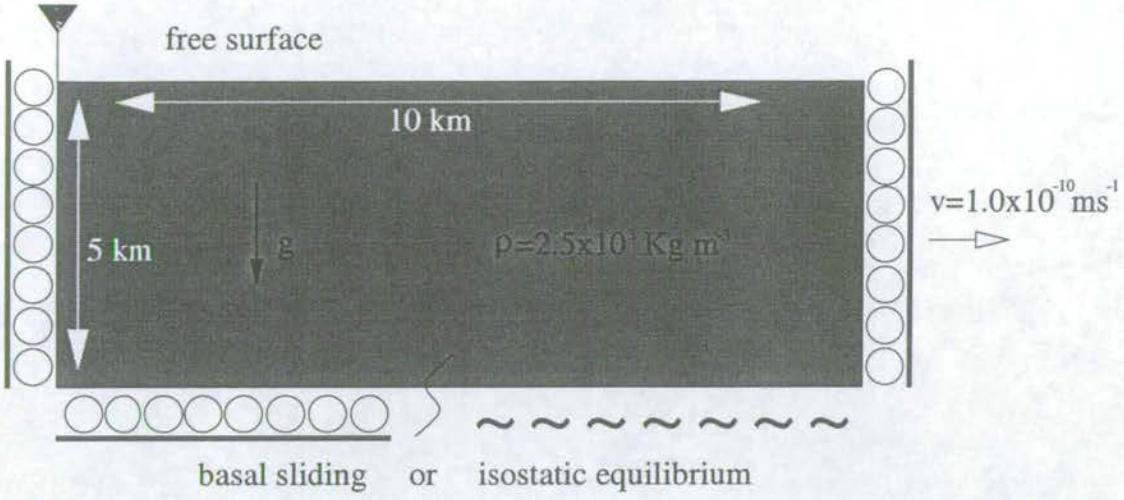

Figure 3.9. The geometry and boundary conditions of the standard model: 5000 quadrilateral elements representing an elasto-plastic Von Mises solid. The left hand wall is pinned, the right hand wall moves at a constant velocity.

properties of the deforming material. In the numerical system, variables include the number, shape and size of the elements. Ideally, the effect of variations in all parameters should be investigated. A more practical approach, however, is to use a benchmark design wherein all the parameters are fixed except those of particular interest, which are varied one at a time. The standard model or benchmark is illustrated in Figure 3.9, and its numerical and physical parameters described below.

3.4.1 Numerical parameters in the standard model

Both computational and physical considerations influence the choice of element shape and mesh geometry. T3 elements (three node elements which ideally form equilateral triangles) are the simplest for FE calculations but they are not necessarily the best. Niño (1997) provides a detailed assessment of different element shapes and mesh geometries within ADELI. He found meshes composed of Q4 elements (four node elements composed of two overlayed pairs of triangles) gave the closest approximation to the analytical solution for a rigid block indenting a perfectly plastic half space, given by Prandtl (1920). Consequently, meshes made of Q4 elements have been used throughout this study.

McKinnon & Garrido de la Barra (1998) found that the shear bands in their numerical experiments were biased towards an alignment parallel with the axes of the grid. They claim that such grid dependent effects can be reduced by the use of slightly irregular meshes, which are generated by taking a regular grid and randomly "nudging" each node a small distance.

The axes of the Q4 grids used in this study were vertical and horizontal and the boundary conditions were chosen to produce conjugate structures with equal angles of dip. Therefore, unlike in McKinnon's experiment, neither fault set was closer to parallelism with the grid than the other, so no bias could occur. Also, by forming the quadrilateral elements from two pairs of triangles overlayed rather than a single pair, there was no preferred orientation in the mesh associated with the diagonal line joining the two triangular sub-elements. Consequently, I did not deem it necessary to use irregular grids in these simulations.

There are also physical and numerical considerations when choosing the number of elements in a simulation. The maximum number of elements which can be modelled is limited by available computing resources. More elements improve the resolution of the simulation but result in unacceptably long run times. The physical problem addressed by the simulation dictates a lower limit on the number of elements we should consider modelling. To say anything statistically meaningful about fault size frequency distributions, the size range in the population must span over two orders of magnitude. The number of elements in the mesh should therefore certainly be more than the number of structures required for the population to cover the desired two orders of magnitude range of sizes. Assuming size frequency distributions follow a power law we have

$$N_{\geq Lmin} = aL_{min}^{-c} \tag{3.68}$$

$$N_{\geq Lmax} = 1 = aL_{max}^{-c} \tag{3.69}$$

$$\frac{N_{\geq Lmin}}{1} = \left(\frac{L_{min}}{L_{max}}\right)^{-c} = \left(\frac{1}{100}\right)^{-c} = 100^{c} \tag{3.70}$$

so for values of c between 1 and 1.5, between 100 and 1000 structures would be needed to cover the desired scale range. Based on this analysis, the standard model was divided into 5000 initially square Q4 elements.

3.4.2 Physical parameters in the standard model

The standard model measures 10km across and 5km deep. This model was not designed to correspond exactly with any particular geological scenario, but simply to include the essential features of physical reality which may influence faulting in general: the selected dimensions are large enough so that the forces of gravity and applied extension (see below) are comparable. Also, by modelling only a relatively thin region, we can avoid complexities like rheological variation with depth due to increasing temperatures. Each of the 5000 elements in the standard model measures 100 m x 100 m. The influence of the size and shape of the deforming region on fault patterns and fault population statistics is presented in Section 7.2.

The boundary conditions on the side walls of standard model are given in terms of velocities normal and tangential to the surface. In the simulation illustrated by Figure 3.9, the normal velocity of nodes on the left hand wall is zero, but the rollers indicate that nodes are free to slide parallel to the surface. Nodes on the opposite wall may also move up or down but they are additionally constrained to move with a velocity of $1.0\text{x}10^{-10} ms^{-1}$ normal to the surface. These boundary conditions prevent rotation of the whole deforming region. Given the length of the model, the applied velocity translates to an extensional strain rate of $10^{-14} s^{-1}$, which lies within the range of expected geological strain rates (between $10^{-12} s^{-1}$ and $10^{-15} s^{-1}$, Twiss & Moores (1992) p.382). The standard run time is $4.0\text{x}10^{12} s$ (approximately 127 thousand years) so the total extensional strain is 4%.

In all experiments there is a free upper boundary, but the lower surface is constrained in one of two ways. In some realisations (Section 7.1), nodes at the base of the model are free to move in the x direction but not in the z direction, resulting in basal sliding. This boundary condition is commonly employed in analogue modelling studies, but is rare in nature. In most realisations (Chapters 5 and 6), the base of the model rests on an inviscid fluid in a state of isostatic equilibrium. Again, this boundary condition is quite removed from reality; the natural situation it most closely resembles, perhaps, being the special case of sediments deforming above a thick layer of salt. However, this this sort of boundary condition is frequently used in analogue modelling studies and is closer to reality than the basal sliding model.

The material properties of the deforming material, listed in Table 3.1, were chosen to mimic those of the Darley Dale sandstone modelled as a strain softening Von Mises solid, Figure 3.4. They were chosen with reference to Niño (1997) who compiled average values for the elastic and plastic parameter of sandstones by fitting the stress-strain curves determined experimentally by Jones & Murrell (1989), Touloukian, Judd & Roy (1981), Baidyuk (1967) and Mestat (1993). In

Property	Value	Units
Young's modulus	$1.36\text{x}10^{10}$	Pa
Poisson's ratio	0.30	*none*
Density	$2.5\text{x}10^{3}$	Kg/m^3
Yield strength	$275\text{x}10^{6}$	Pa
Post-yield strength drop	$75\text{x}10^{6}$	Pa
Critical plastic Strain κ_c	0.02	*none*

Table 3.1. Mechanical and rheological properties of the deforming material in the standard model.

simulations where the basal boundary was in isostatic equilibrium, a density of $2.8\text{x}10^{3}Kg/m^3$ was used for the inviscid fluid underlying the deforming material.

3.4.3 Heterogeneity of the medium

As well as the overall lithology of the lithosphere, heterogeneity has been shown to be a key element in the development of fault networks [e.g. Cowie *et al.* (1993)]. In a heterogeneous crust subjected to deformation, faults and fractures nucleate at those points with the lowest failure strength. Variations in composition, grain size and texture constitute heterogeneities in real rocks. In analogue models, heterogeneity enters the system via microscopic variations in the sand grains, clay or gypsum used to represent the brittle crust. In both these cases, quantitative descriptions of heterogeneity in material properties are impossible. This poses a question for the numerical modelling of fault growth, "What is an appropriate way to include heterogeneity of material properties in numerical simulations of faulting?" In some numerical models (Schultz-Ela & Jackson 1996, Poliakov *et al.* 1994, Poliakov & Hermann 1994, Gerbault *et al.* 1998, Barnichon & Charlier 1996), heterogeneity enters the system via numerical "noise": round-off errors in floating point arithmetic. In others (Belytschko, Chiang & Plaskacz 1994, Leroy & Ortiz 1989), a single imperfection is introduced as a seed in an otherwise uniform mesh. These imperfections vary in size from an individual element to several 10's of elements, often taking the form of a reduction in yield strength. Non-uniform failure can also be induced by creating geometrical instabilities in the mesh e.g. by fixing one node to create a displacement discontinuity (Dresden *et al.* 1991) or by cutting a notch in the mesh perimeter (Davis & Fletcher 1990). Most commonly, prescribed heterogeneity appears as a range of material properties distributed in some way throughout the deforming region. A value for each mesh element is drawn from a probability distribution, either randomly or in some systematic way which gives spatial correlation of material properties. Various studies are summarised in Figure 3.10 in terms of the material properties they have considered to be

heterogeneous, the form of the probability distributions (uniform, Gaussian) and the nature of spatial heterogeneity (random, fractal).

I rejected numerical round-off as a source of heterogeneity because the amplitude of the noise can neither be measured nor controlled: it is entirely dependent on machine architecture. This is undesirable when trying to run a suite of experiments where you wish to vary one parameter but keep all others (including heterogeneity) fixed. Also, independent researchers may find it difficult to reproduce experimental results if they are dependent on machine architecture. As natural materials typically exhibit a range of material properties, I considered it more realistic to incorporate heterogeneity via a distribution of material properties rather than use a single imperfection to trigger nucleation.

In this study, yield strength was chosen as the heterogeneous property. Strength was assumed to follow a Gaussian probability distribution with a constant mean and a variety of distributions with different standard deviations have been modelled (see Section 6.3). The spatial arrangement of properties was achieved thus (See Figure 3.11):

1. A discrete approximation to a Gaussian distribution, with the desired mean and standard deviation, was generated. The range of strengths, from $\mu - 3\sigma$ to $\mu + 3\sigma$, was divided into 100 possible values. The relative frequency of each strength value was then calculated before being scaled so that the frequency of the most extreme value was one. This required 3300 materials in total.

2. Elements in the mesh were dealt with sequentially from top left to bottom right. For each element, a random number was generated between 0 and 1, using the algorithm *ran*1 by Press, Teukolsky, Vetterling & Flannery (1996).

3. This number was scaled to be a random integer lying between 1 and 3300, and the element assigned the corresponding material number.

The end result should be a mesh with a Gaussian distribution of strengths, randomly arranged in space. This does not necessarily guarantee that weaknesses will be uniformly distributed throughout the mesh, just that there will be no spatial correlation between them. In order to create several meshes with statistically the same properties but different spatial distributions (see Section 6.2), the generator was given different seeds, but allowed to select materials from the same strength distribution.

Author	Frequency Distribution	Spatial distribution
Heimpel & Olson (1996)	Initial seed fault plus heterogeneity in strength. Gaussian distribution with $\sigma=0.1\mu$	Random.
Cowie et al. (1993)	Heterogeneity in elastic modulus or yield strength. Uniform distribution.	Random.
Spyropoulos et al (1999)	Heterogeneity in yield strength. Form of distribution undisclosed, but has variance O(10) to O(1) with respect to unity.	Random.
McKinnon & Garrido de la Barra (1998)	Heterogeneity in Young's modulus. Triangular distribution with maximum deviation from μ=20 MPa	Random.
Wilson et al (1996)	Heterogeneity in elastic modulus or yield strength. i)Uniform ii)Gaussian ii)Fractal (Weibull) iv)Gaussian	 i)Random ii)Random ii)Non-fractal iv)Fractal

Figure 3.10. Heterogeneity in published numerical modelling experiments.

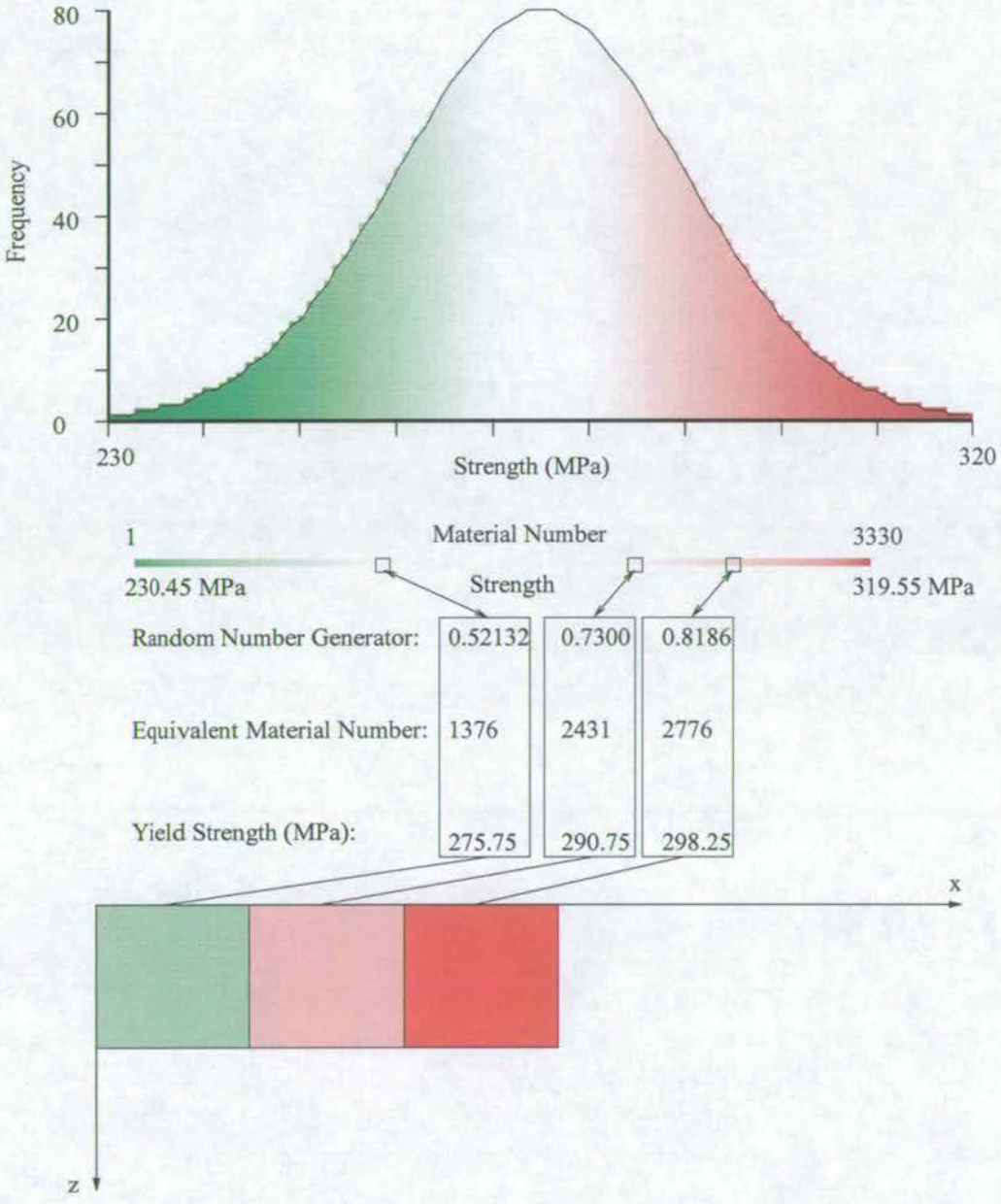

Figure 3.11. To prescribe heterogeneity, i) a Gaussian strength distribution with a population of 3330 materials is created. ii) A random number generator picks one of 3330 materials. iii) The strength of that material is then assigned to an element of the mesh.

3.5 Testing ADELI

3.5.1 Mesh effects

The outcome of a finite element experiment depends both on features of the model that have a basis in reality (e.g. boundary conditions, material properties and the constitutive model) and those that do not, which are known collectively as mesh effects. These include the fineness of the mesh, the shape of elements and their alignment with respect to the boundaries of the material and also forces on those boundaries.

3.5.2 Calculation order dependence

To answer the question, "Does the numerical solution depend on the order in which the elements are considered?" a very simple experiment was performed. The benchmark mesh (100 elements wide x 50 elements deep) was deformed by applying a constant velocity to the right hand side. A solution was found considering the elements in order 1–100, 101–200 etc. A physically identical experiment was then performed, but the order of solution changed to 100–1, 200–101 etc. The following outputs of the two simulations were compared:

1. The coordinates of nodes on the perimeter of the deforming region at the end of the experiment (Figure 3.12).
2. The map of broken elements after 60% and 100% of run time (Figure 3.13).
3. The size frequency distributions after 60% and 100% of run time (Figure 3.14). Section 4.3 provides a detailed description of how size frequency distributions are calculated in this study.

Although there are differences, due to the order in which calculations are performed in ADELI, the differences are so small that they do not alter the conclusions drawn from the the size frequency distributions. The same test was also performed for a model which differed from the benchmark in just one respect. Instead of a normal distribution of yield strengths, only one strength was used for all of the elements: the mean strength of the benchmark mesh, 275 MPa. This test showed a much stronger calculation order dependence (Figures 3.15, 3.16, 3.17).

This is unsurprising because in these simulations, numerical round-off error in calculation of stresses is the only noise in the system, it controls where the shear zones nucleate but is very

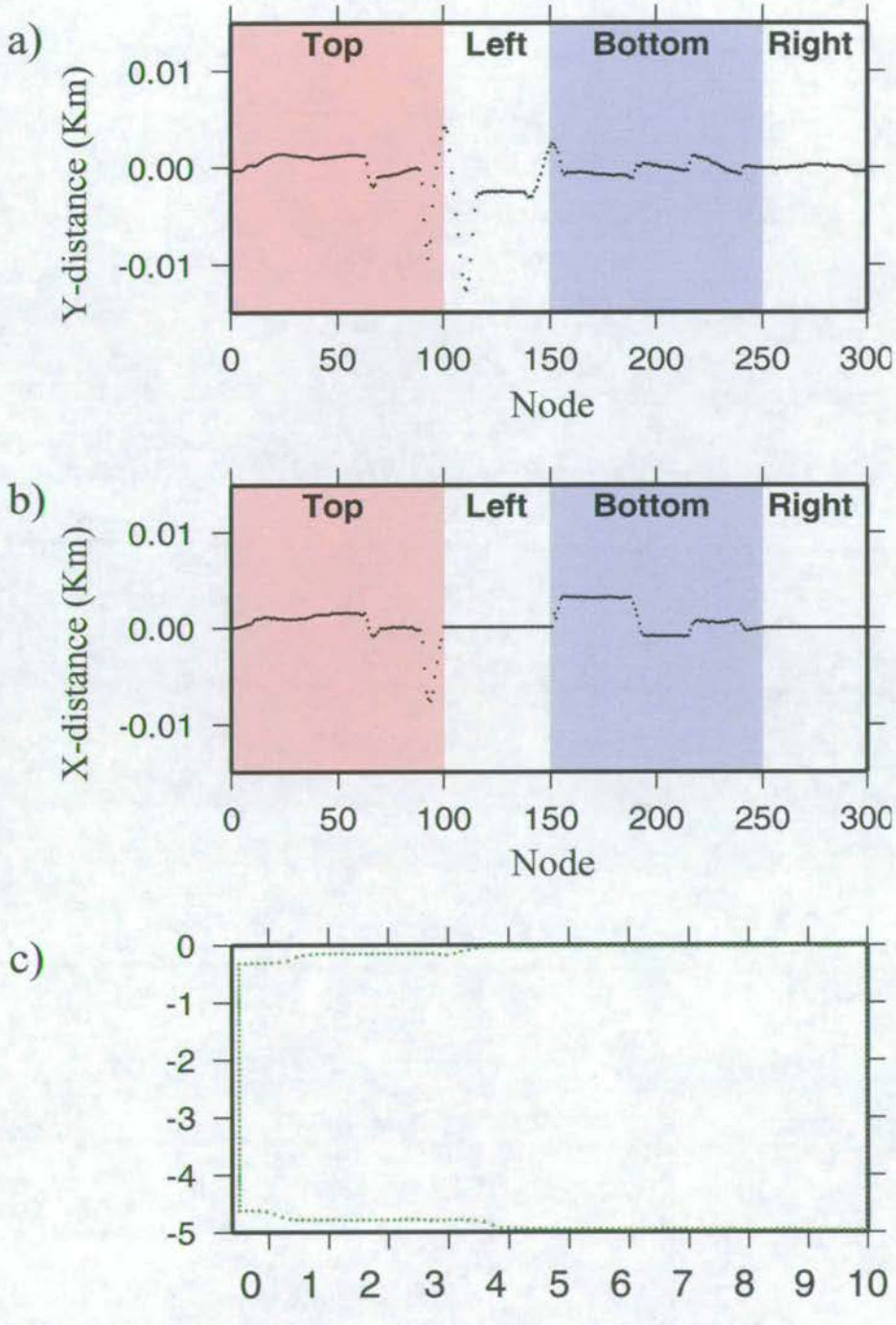

Figure 3.12. Calculation order dependence of node coordinates in the benchmark mesh after the total run time (4% extension). a) Mismatch in y versus node number. b) Mismatch in x versus node number. c) Node locations when the calculation is done in the normal order (red) and reverse order (green). Nodes along the perimeter are numbered clockwise, starting in the top right corner of the model.

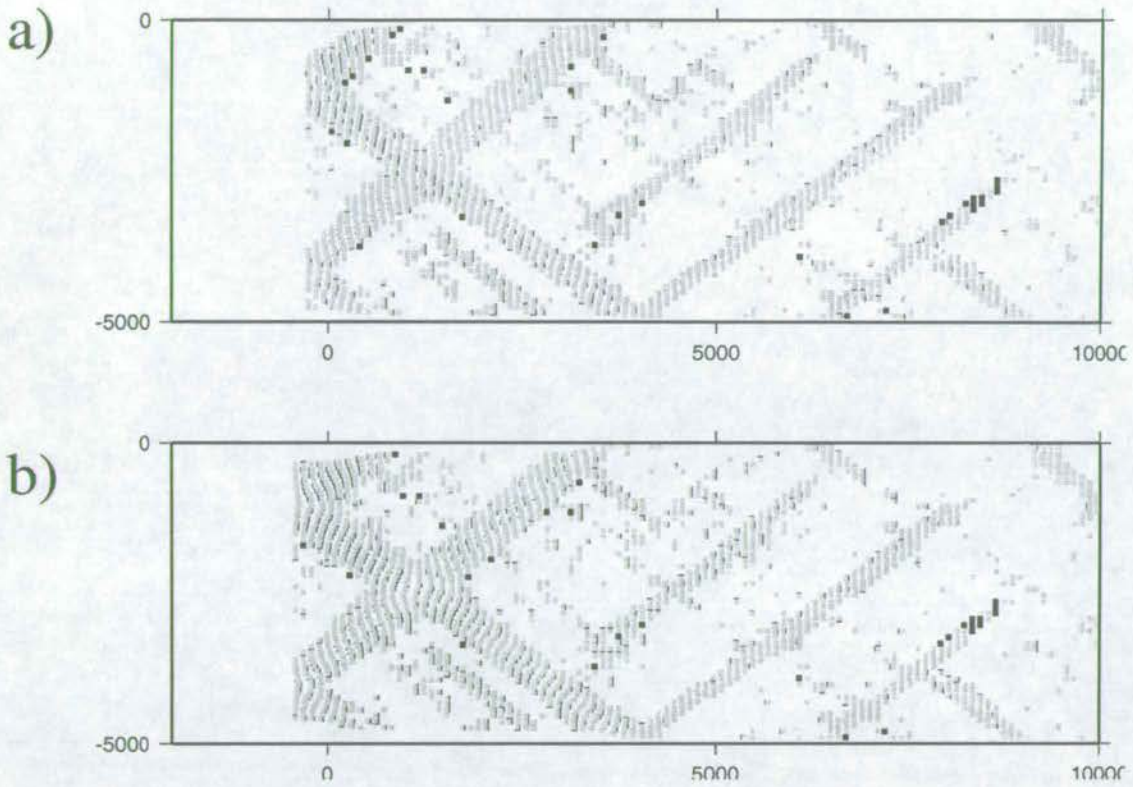

Figure 3.13. Calculation order dependence in the benchmark mesh determined using broken element maps a) after 60% of run, b) after 100% of run. Broken elements from the run with normal calculation order are plotted first in black. Those from the reverse calculation order run are overlayed and plotted in grey.

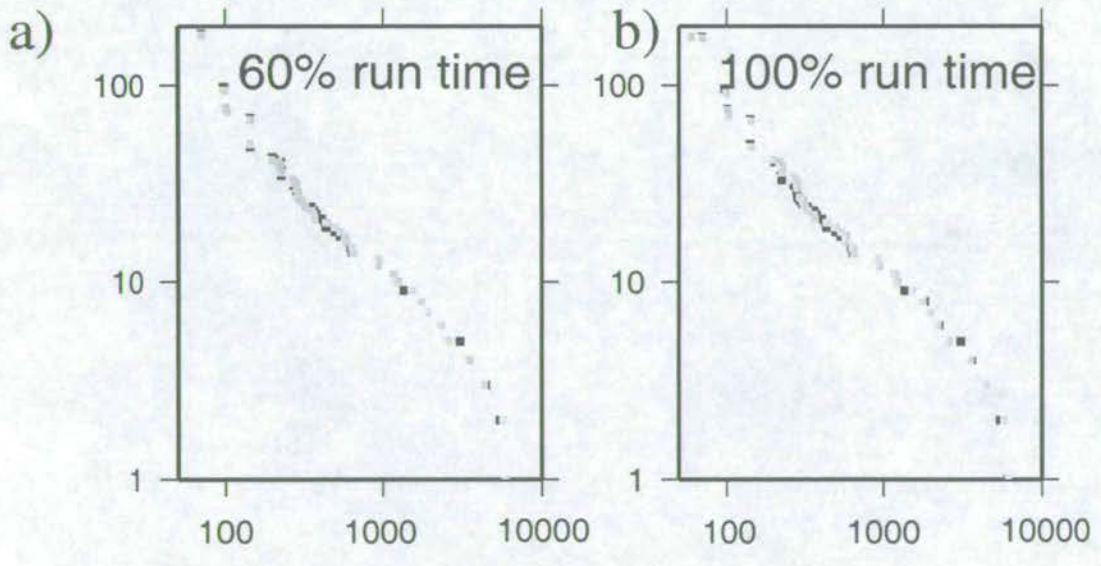

Figure 3.14. Calculation order dependence in the benchmark mesh illustrated by size frequency distributions. Plot order and colour coding as in Figure 3.13.

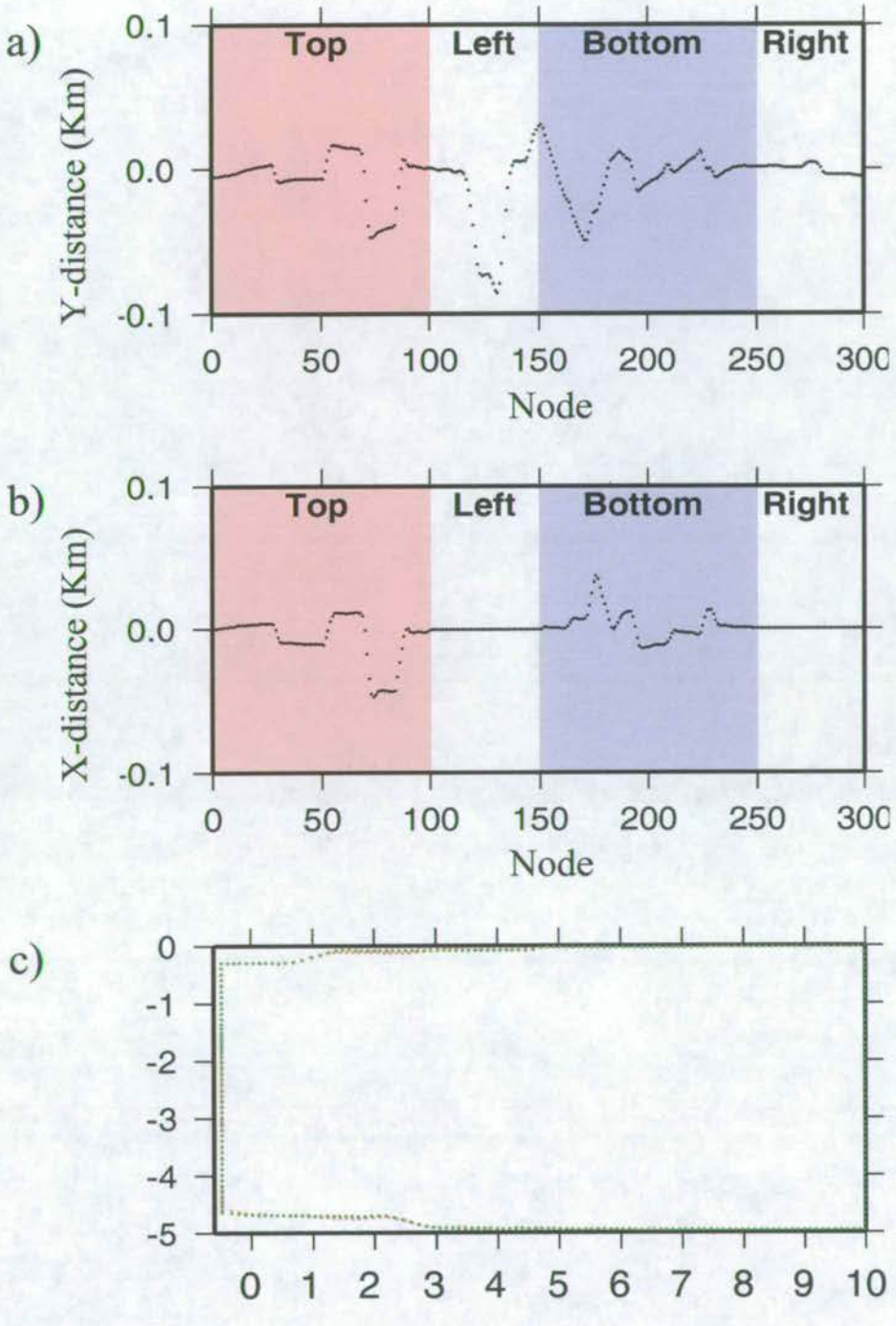

Figure 3.15. Calculation order dependence of node coordinates in a homogeneous mesh after the total run time (4% extension). a) Mismatch in y versus node number. b) Mismatch in x versus node number. c) Node locations when the calculation is done in the normal order (red) and reverse order (green). Nodes along the perimeter are numbered clockwise, starting in the top right corner of the model.

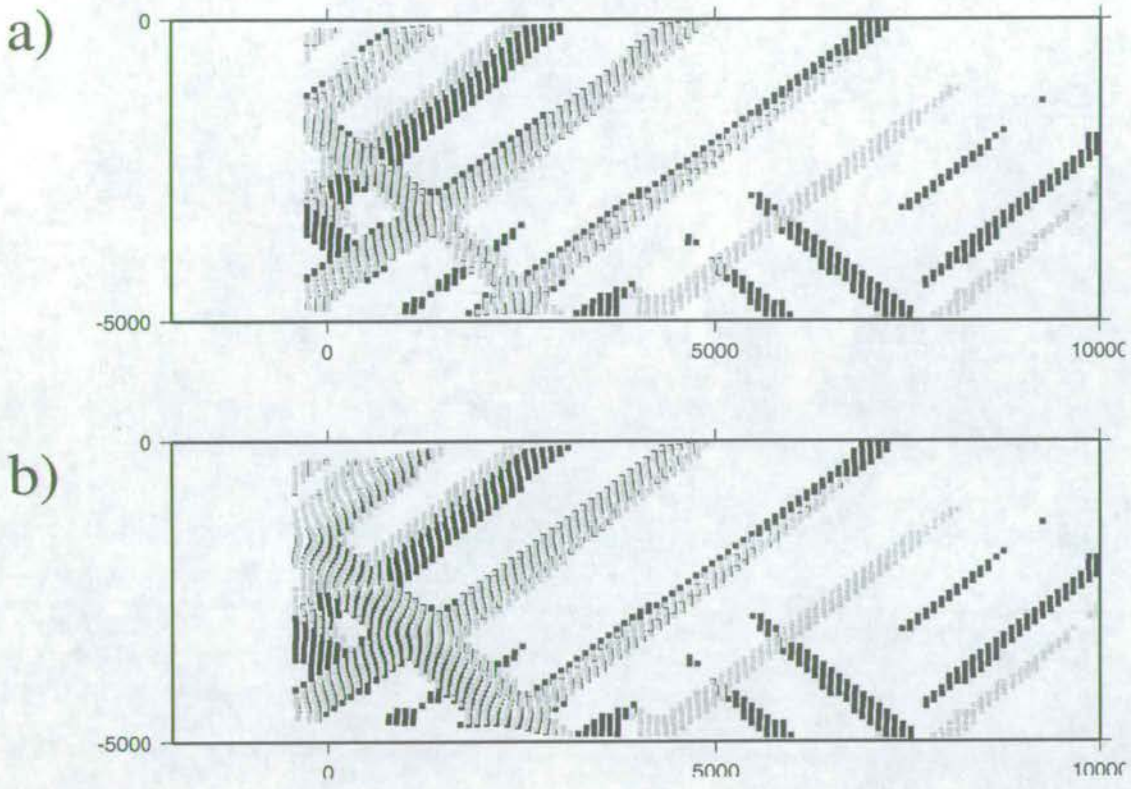

Figure 3.16. Calculation order dependence in the homogeneous mesh determined using broken element maps a) after 60% of run b) after 100% of run.

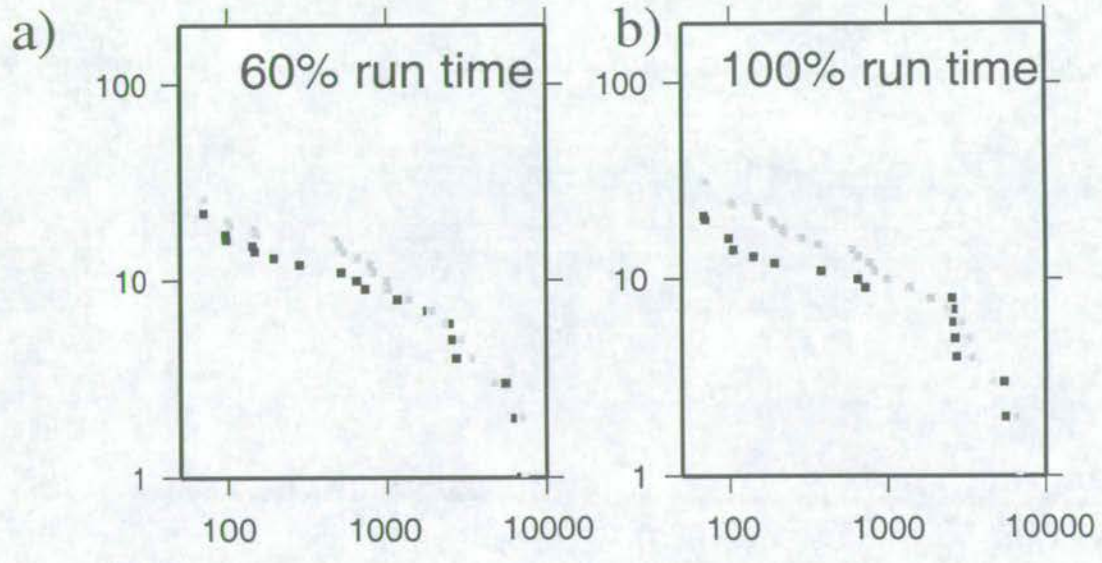

Figure 3.17. Calculation order dependence in the homogeneous mesh illustrated by size frequency distributions.

sensitive to the order in which the calculation is performed. These simulations suggest that runs with strong heterogeneity (large standard deviations in yield strength) are advisable because they are less troubled by numerical artifacts like calculation order dependence.

3.5.3 Heterogeneity

The method for prescribing heterogeneity was tested for: i) agreement between the strength distribution of the mesh and the desired Gaussian distribution and ii) randomness of the random number generator. The strength distribution of several meshes are presented superimposed on their target Gaussian distribution in Figure 3.18. There is scatter but no systematic bias. This is the best we can expect from a method with a random element. As a crude test of the randomness of the random number generator, the frequency of each of the 3300 materials was measured and compared. An unbiased generator should produce a uniform distribution in a sufficiently large population. Figure 3.19 below shows the frequency distribution for materials in four 5000 element meshes. Although the distribution is not uniform, there does not appear to be a systematic bias.

To ensure that material properties were spatially uncorrelated, the seeds and parameters of the random number generator were chosen carefully to give exceedingly long lists of random numbers without repetition. Press *et al.* (1996) claim this generator should not suffer from period exhaustion if called less than 10^8 times which is more than adequate for even the biggest ADELI meshes.

3.6 Limitations of ADELI

The most obvious limitation of this code is that it cannot deal with three-dimensional problems. Also, deformation as modelled by this code is quasi-static, so the effects of dynamic rupture cannot be taken into account and brittle-elastic rheologies cannot be studied. By using an elastic-plastic model for material behaviour, time-dependent phenomena like stress relaxation through creep are excluded from the simulation. This reduces the realism of crustal-scale simulations run over 10,000 years. Fault behaviour observed in analogue models such as large structures locking-up, subsequent reactivation of dead structures and de-localisation of strain also cannot be achieved with a strain-softening elasto-plastic constitutive law. We know that rocks are heterogeneous, but little work has been done to quantify heterogeneity in rock strength at the kilometre scale, though Katz *et al.* (1999) and Gross (1999) have characterised

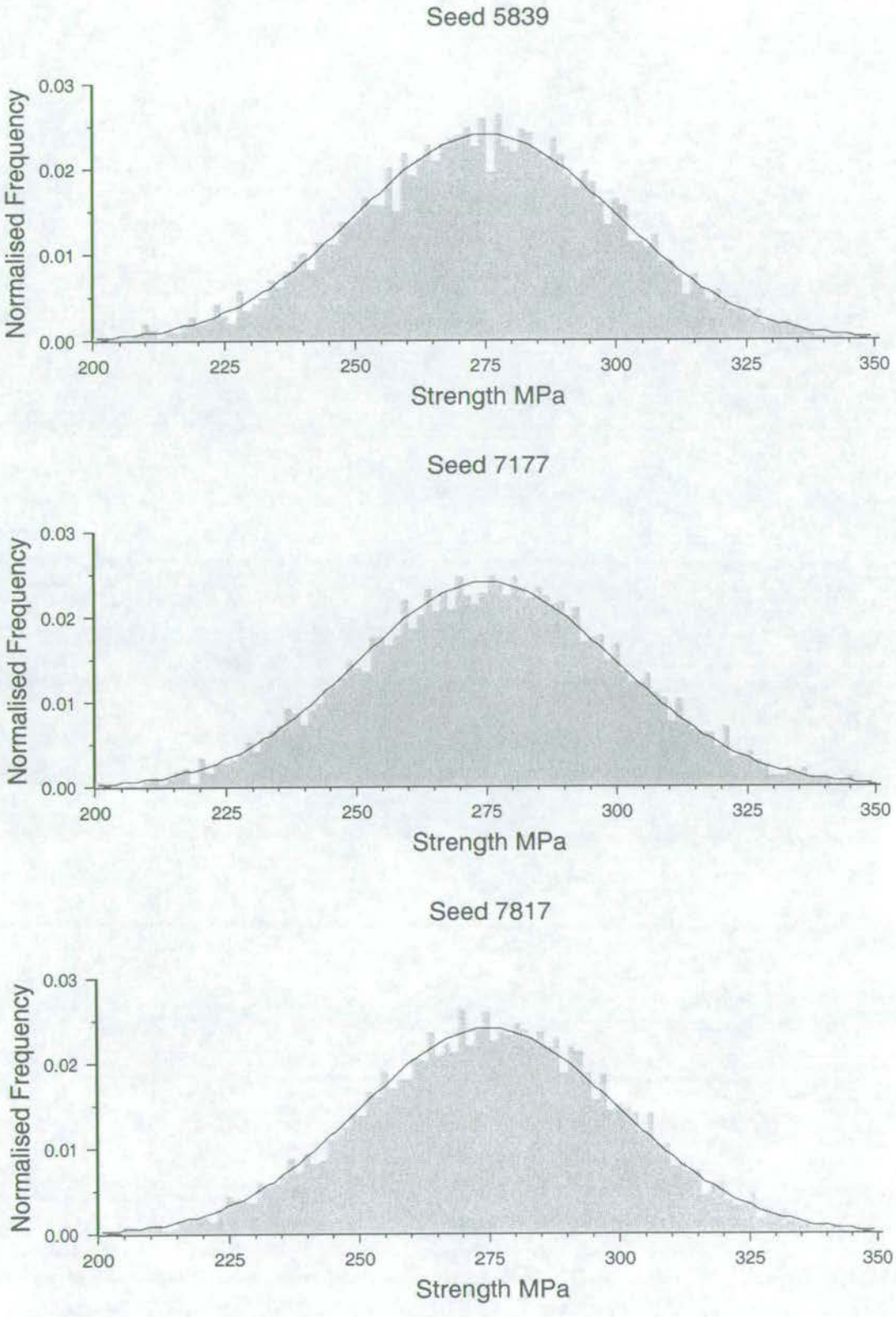

Figure 3.18. Strength distribution of several meshes (filled polygon) and target Gaussian distributions (solid lines).

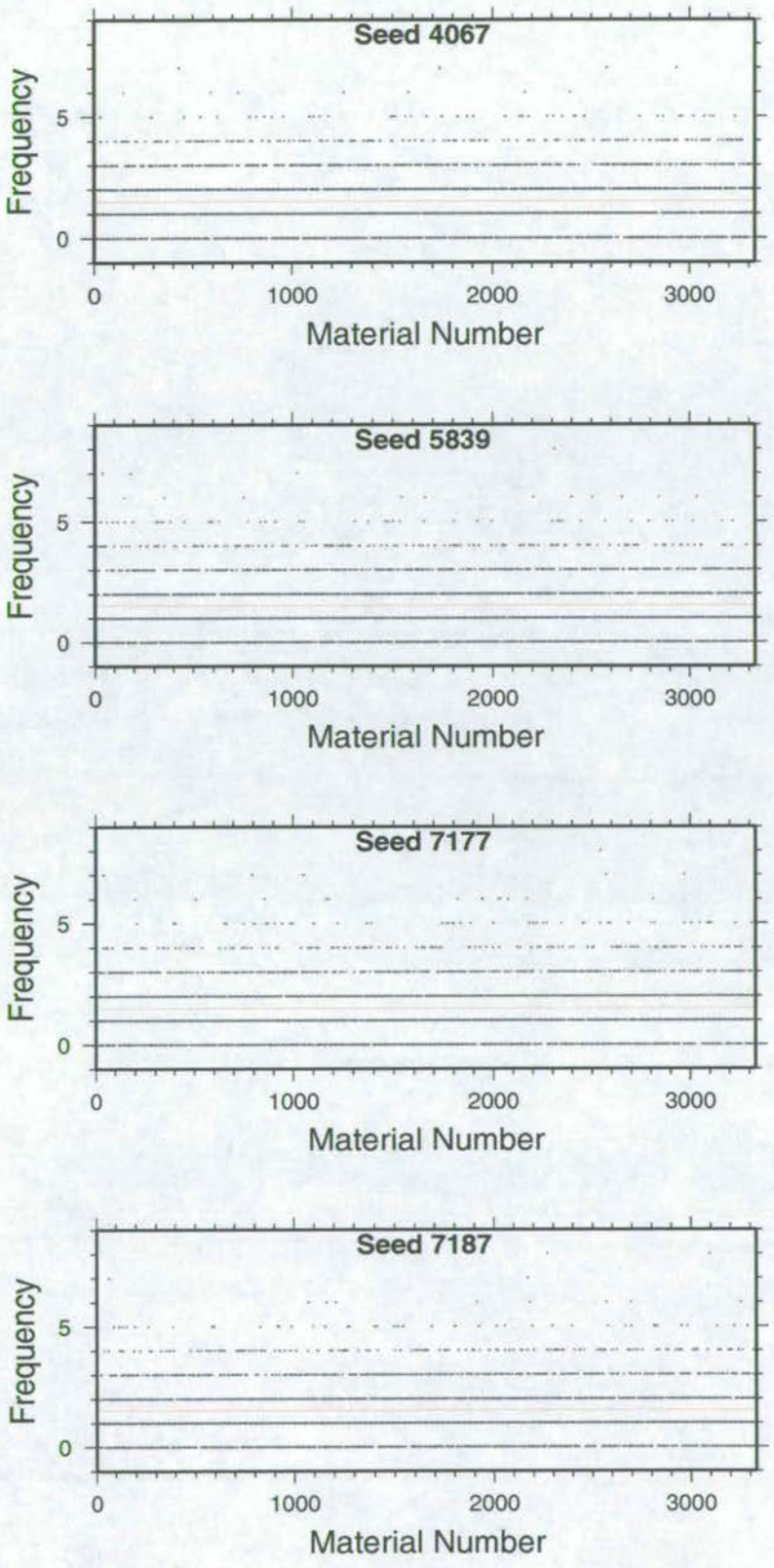

Figure 3.19. Frequency of each of the possible 3330 material numbers in four meshes created by using four different seeds in the random number generator. A uniform distribution would give a theoretical frequency of 1.501 (shown as a red line).

local variation in rock strength. Consequently, the model of heterogeneity used in this or any numerical simulation of faulting may not be a true reflection of strength variation in the Earth. Thermal and fluid effects are totally neglected.

As with any computer-based study, the complexity achievable in a single simulation (for example the number of mesh elements) and the total number of simulations possible in a given time are limited by available computing resources. The results of finite element modelling are always strongly dependent on the fineness of the mesh, but runs with exceedingly fine meshes (say with 1,000,000 elements rather than the 5000 elements used in this work) were untenable given available computing resources. Only a certain amount of experimental work is possible in the course of a Ph.D. Consequently, no runs were performed varying the numerical parameters such as the time-step and damping coefficient. Time constraints also meant that the effect on fault population evolution of some physical parameters, such as mean strength, strain rate and aspect ratio (independent of layer thickness), could not be investigated.

3.7 Summary

An existing numerical model for solving geodynamic problems in two dimensions has been adapted to include heterogeneity of yield strengths. A simple yield criterion that is independent of mean stress and dependent only on deviatoric stress has been chosen for this study. Heterogeneity takes the form of a Gaussian distribution of yield strengths randomly distributed in space. The model has been tested for calculation order dependence and found to be least sensitive to changes in the order of calculation when the deforming material is strongly heterogeneous i.e. contains a wide range of yield strengths. The standard boundary conditions (unilateral extension above a ductile substrate) generate conjugate, normal faults in cross-section.

Chapter 4

Extracting Fault Properties from Model Output

The large volumes of data produced by models like ADELI are both a benefit and a drawback of the numerical method. The model provides data for stress, strain, velocity and displacement at thousands of points in space at hundreds of points in time: a wealth of data not available to those studying faults in the field or even in analogue experiments. However, extracting useful information from these data in order to examine the processes governing faulting and the attributes of the faults themselves is quite a challenge. In this chapter I describe how I have processed the data output by ADELI so that it can be compared with observations of natural fault populations such as displacement and length. Specifically, I describe how faults are defined in the model and how the properties calculated at each mesh node (e.g. x and y coordinates) are converted into fault attributes (e.g. displacement). The various analysis techniques are illustrated throughout this chapter by applying them to standard ADELI runs.

4.1 Defining Faults in Model Output

The raw output from ADELI provides data about the elements and nodes of the finite element mesh, not faults. We therefore need an objective, ideally automated, way to convert data on elements into meaningful information (e.g. size, orientation) on faults. Previous studies (Cowie *et al.* 1993, Poliakov & Hermann 1994) have used a two-step algorithm for clustering failed elements into faults. With two-step algorithms, each element is first tested against a failure

criterion to define whether it is broken or unbroken. Then, broken elements are tested against some geometrical criteria to assess whether or not they should be joined with adjacent broken elements to form a cluster or fault. For rectangular grids, two possible geometrical criteria are "only join broken elements if they share a common edge" or "join broken elements if they share a common edge or corner". Two-step algorithms work very effectively where structures are largely parallel. However, such schemes would treat intersecting conjugate structures as a single fault. The scheme I have developed is an improvement on two-step algorithms in that it can separate synthetic and antithetic structures. This is a more geologically realistic approach to clustering, but is more systematic than clustering "by hand". The importance of measuring faults systematically is discussed in Chapter 2.7.4.

Figure 4.1 shows each step of my clustering algorithm. My three step scheme works by first applying a failure criterion to assess which elements are broken (Figure 4.1a). If an element has experienced finite plastic strain, it is considered to be broken. The scheme then examines the gradients in the strain field around each broken element. If the NW-SE gradients are smaller than the NE-SW gradients, the element is flagged as belonging to a right-dipping fault. If the opposite is the case, the element is flagged as belonging to a left-dipping fault (Figure 4.1b). The third step of the scheme is to apply geometrical criteria to join adjacent elements only if they are broken and have the same flag (Figure 4.1c). Figure 4.2 shows the result of applying my clustering algorithm at five times during a standard ADELI run (with isostasy at the base, extended from the right hand side to a total extension of 2.5%). This shows that the automatic clustering works well in general but can be refined manually, in circumstances when it makes geological sense to do so. For example, most geologists would say that the region highlighted in Figure 4.2b contains three left-dipping faults, but the clustering algorithm considers them to be a single structure (Figure 4.2c). After clustering, useful information such as displacement, orientation and length, can be gathered for each fault.

4.2 The Variation of Displacement Along Individual Structures

For consistency with the published literature [e.g. (Childs *et al.* 1990), (Gillespie, Walsh & Watterson 1992), (Dawers *et al.* 1993)] throughout this study I use the term displacement to mean the throw on a structure. How displacement varies along a chord across the surface of an isolated fault will be determined by rock properties (Bürgmann, Pollard & Martel 1994, Cowie & Scholz 1992*b*), fault shape (Willemse *et al.* 1996) and whether the fault is confined within a layer

Figure 4.1. The three-step clustering algorithm. a) Elements with strains above a certain threshold (in colour) meet the failure criterion and are considered broken. Failed elements with low strains are shown in purple and blue, higher strains in red and yellow. b) Elements with 'right-dipping' shear sense in green, 'left-dipping' shear sense in blue. Grey elements are not broken. c) Points belonging to the same cluster are shown in the same colour. Solid lines are the best fitting straight line through each cluster.

(Dawers *et al.* 1993, Gross, Gutierrez-Alonso, Bai, Wacker, Collinsworth & Behl 1997). Most importantly from the perspective of identifying the factors controlling faulting, displacement profiles are also affected by fault interaction, from the point where just their stress fields interact (Peacock & Sanderson 1991, Willemse *et al.* 1996) through to the point where their surfaces intersect (Horsfield 1980, Odonne & Massonat 1992, Nicol, Walsh, Watterson & Bretan 1995, Watterson *et al.* 1998, Maerten *et al.* 1999). To create a displacement profile, one needs measurements of fault slip at several points along a chord across the fault's surface. In nature, exposure permitting, slip can be measured at any point along the fault trace. In finite element models, measurements can only be made between offset elements. Therefore the location and number of measurements possible are controlled by the discretisation of the grid. In effect, this means that displacement profiles can only be generated for the larger structures.

The method I use for generating a displacement profile for non-intersecting modelled structures (see Figure 4.3a) is as follows. The clustering algorithm is used to define which elements belong to the structure. The nodes which define these elements are then assigned to rows (Figure 4.3a): at the start of the experiment, all the nodes belonging to the same row would have had the same y coordinate. For each row in the cluster, the y coordinates of the node furthest right (n1) and the node furthest left (n2) are extracted. The displacement (throw) at n2 is taken to be the difference in these two values. I consider displacement to be positive if $y_{n_2} - y_{n_1} > 0$. This means that structures which dip to the right have positive displacements. For experiments where the moving wall is on the right hand side, faults with positive displacements are synthetic (as defined by Stewart & Argent (2000) Figure 2b) to the overall deformation.

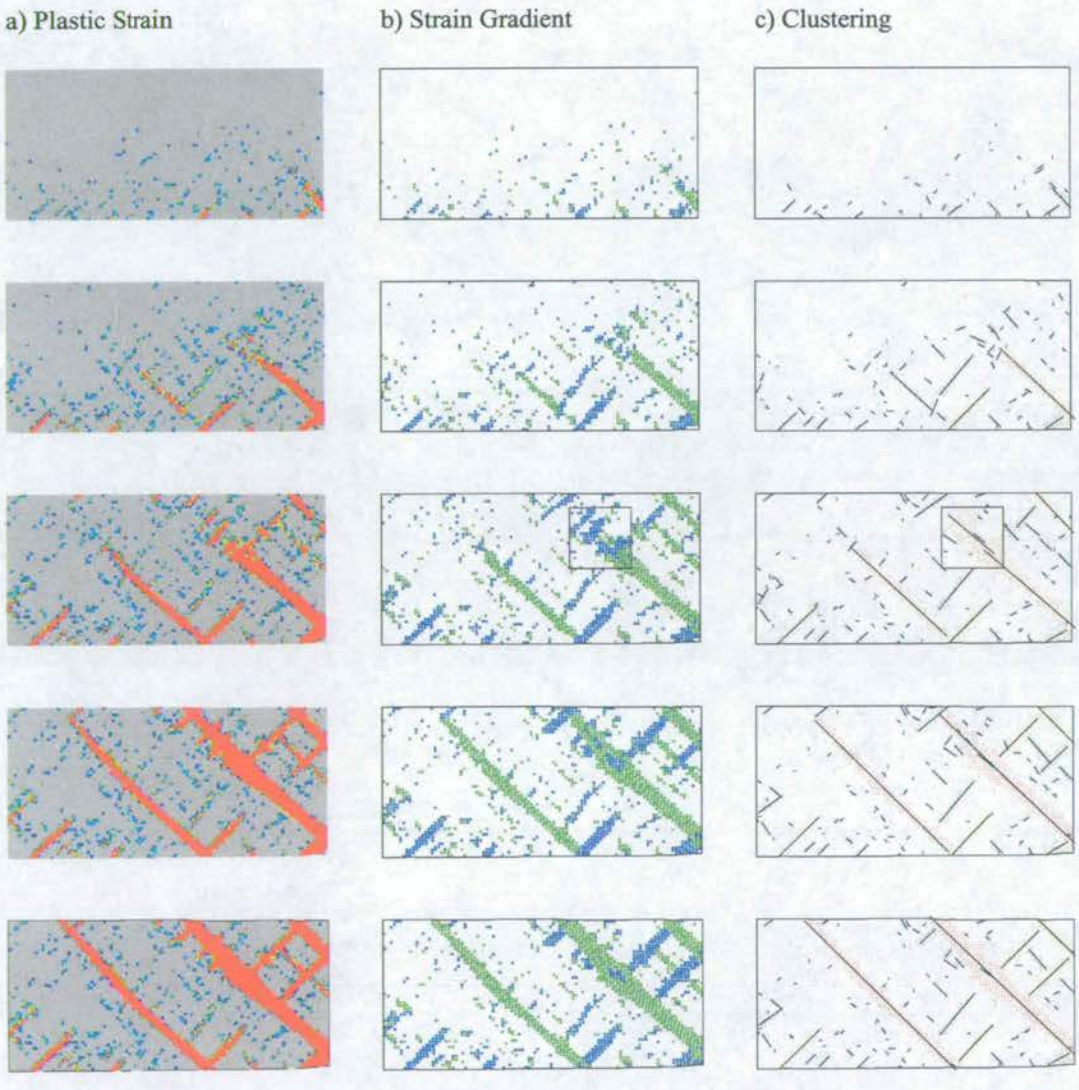

Figure 4.2. The three-step clustering algorithm applied to ADELI output. Same colour scheme as Figure 4.1. The box highlights an area where the clustering algorithm might be refined manually.

Where faults intersect other structures, a slightly different approach is taken, illustrated by Figure 4.3b. Each fault in the conjugate pair is treated separately. In the case of Fault 1 on Figure 4.3b, the displacement for the first eight rows would be calculated as above. Rows 9 and 10 are defined by extending the trend of the fault throughout the intersection. This can result in some nodes being used to construct displacement profiles for both of the intersecting faults. After defining the rows, displacement is calculated as above. The same procedure is then applied to Fault 2. Fault displacement profiles are presented in Section 5.2.2 where they are used to illustrate fault growth, down-dip linkage and the development of conjugate intersections.

4.3 Size Frequency Distributions

As discussed in Chapter 1, the form of fault size frequency distributions and their evolution through time is affected by fault development: specifically, whether faults are growing in isolation or linking up, how strain is distributed between faults of different sizes and whether or not faults are confined within a layer. In this section, I consider several possible ways to measure the size of structures in ADELI, and propose a favoured measurement.

The measure of fault size applied to the structure simulated by ADELI should ideally meet the following criteria. Firstly, the measure should be comparable with the measures used in studies of natural faults (e.g. length, displacement). Secondly, modelled faults measured in this way should have sizes spanning more than one order of magnitude; size frequency distributions of questionable significance could result otherwise. Finally, the measure should be equally applicable to the smallest and the largest faults, at all stages in the evolution of the population. As discussed in Section 1.2.1, several different fault properties have been used as measures of fault size. In cross section, the possible measures of fault size are length and displacement. Length is the distance measured from the upper tip to the lower tip along the trace of the fault [sometimes also termed height e.g. Finch (1998), Ortega & Marrett (2000)]. Displacement has been defined (Yielding *et al.* 1996) both as the amount a fault offsets a particular horizon, and the maximum offset of any horizon observed anywhere along the fault trace. I adopt this second definition of displacement.

The most common measure of size for natural faults seen in cross section is displacement. However, as described in Section 4.2 above, this measure cannot be applied to many of the smaller structures in ADELI models. Fault length can easily be measured and Finch (1998)

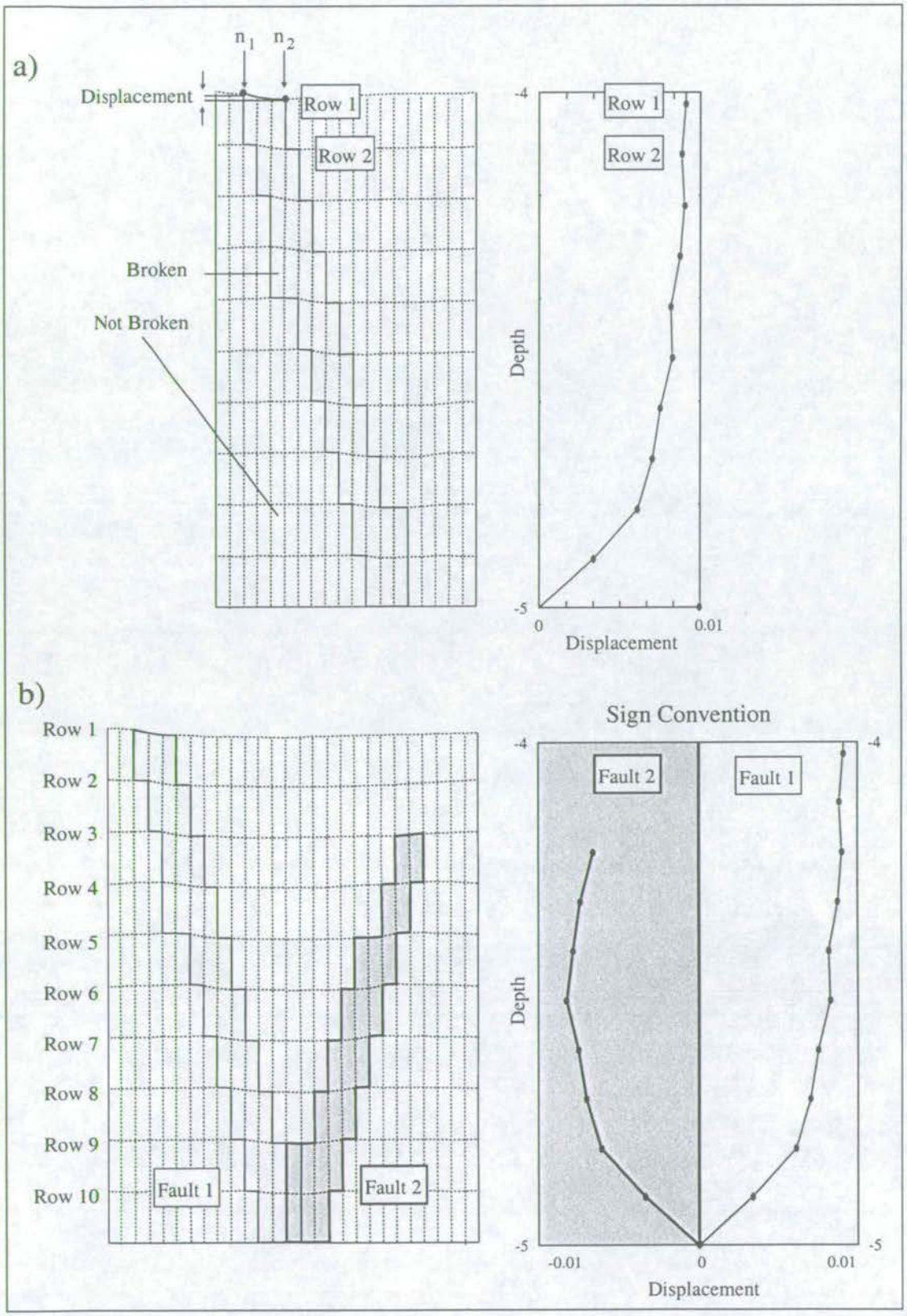

Figure 4.3. Calculating displacement profiles from ADELI output. a) Cartoon profile for a single shear zones. b) Cartoon profiles for intersecting shear zones.

used this measure of fault size in her study of faulting in cross section using a discrete element model. This measure is not ideal, however, because fault length ceases to increase once the fault span the entire thickness of the layer. Consequently, fault length is a poor measure of size for the large faults that develop in ADELI runs at high strains. There is also the problem of assigning a length to structures that contain only one element. Ideally, a measure needs to be found that scales with displacement (which can be measured throughout the experiment, but only on the largest faults) and also with length (which can be measured at all size scales, but only up to the time at which faults span the layer thickness).

The precedent set by other numerical modelling studies (Cowie *et al.* 1993, Poliakov & Hermann 1994) is to use the number of elements in the structure as a measure of fault size. This is an attractive measure for the size of faults in ADELI too because the number of elements in a cluster continues to increase, even after it spans the layer thickness. However, using number of elements as a measure of fault size also has its problems. Figure 4.4 shows a size frequency distribution, where size is measured as the number of elements, for structures in an ADELI run. The fault sizes cover more than one order of magnitude, but because the number of elements in a cluster must be an integer, there are only 12 different fault sizes in the distribution (12 points on the graph). This equates to binning the data and introduces a resolution problem for the smallest structures. When fitting a power law to this distribution by linear regression after taking logs, 77% of the faults are represented by only 2 points in the regression. This amounts to biasing the data to emphasise the importance of the larger structures.

The measure of fault size preferred by this study is total plastic strain. For a single element, the plastic strain is calculated by finding the perpendicular distance in principal strain space from the yield surface to the point that represents the strain state of the element. The total plastic strain of the cluster is simply the sum of the plastic strains of its constituent elements. This measure of size can be applied equally well to the largest and the smallest structures alike. Sizes measured in this way cover more than one order of magnitude and this measure produces size frequency distributions defined by hundreds of points. However, as this measure does not directly relate to a measure commonly used in studies of natural faults, it must be calibrated against length and displacement data.

The procedure for measuring the length of structures composed of finite elements (illustrated in Figure 4.5) is as follows. For structures containing more than one element, the two elements in the cluster which are farthest apart are found. The length of the cluster is taken to be the distance between the centres of these two elements. The phrase "tip-to-tip" will be used hereafter to describe this method of calculating fault length. For faults containing just one

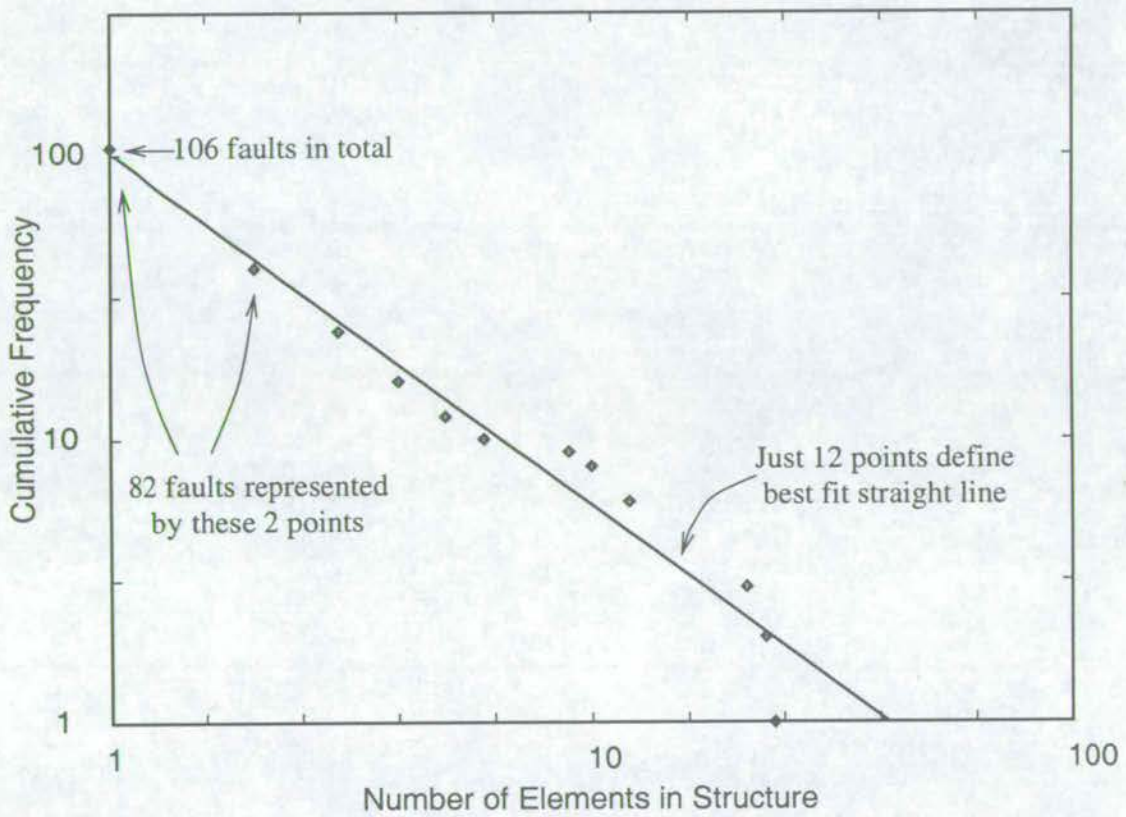

Figure 4.4. Fault size frequency distribution, using number of elements as a measure of fault size.

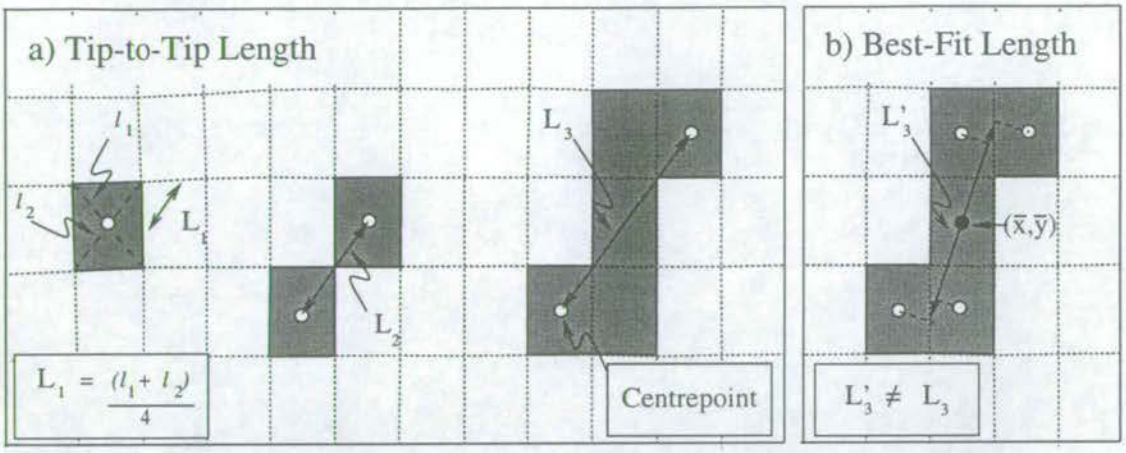

Figure 4.5. a) Within ADELI, fault length (synonymous with height in this study) is defined as the distance between the centre points of the two most distant quadrilateral elements in the structure. b) Illustrates what is meant by "tip-to-tip" length and "best-fit" length.

element, the fault length is calculated by summing the length of the lines that diagonally join the nodes of the element (l_1 and l_2 on Figure 4.5) and dividing by four. In this way, single element faults have roughly half the length of faults made of two elements joined diagonally (on Figure 4.5, $L_1 \approx \frac{1}{2}L_2$). Note that in large structures with several elements in each row, the dip of the line connecting the elements that are furthest apart may differ from the dip of the overall structure by several degrees. For this reason, the length of the best-fitting line through the structure was also calculated. This was achieved by finding the best-fit line using the reduced major axis method (see Davis (1986), p.200), projecting the centre points of each element along a perpendicular onto the best fit line and then measuring the distance between the two most distant points on the line. For structures with just one element, the "best-fit length" was calculated in the same way as the "tip-to-tip length", described above.

We would expect that structures containing the same number of elements arranged in similar geometries would display a narrow range of fault lengths, but a wider range of total plastic strains. For this reason, we would not expect a 1:1 correlation of total plastic strain with fault length, especially for the structures with few elements. Thus, calibration cannot be achieved by simply plotting length versus total plastic strain. To determine the usefulness of total plastic strain as a measure of fault size, it is better to take several datasets, calculate fault sizes in the two different ways and compare the resulting size frequency distributions. This was done and the results are shown in Figure 4.6.

Figure 4.6 shows fault size frequency distributions for a single ADELI run at 5 different times. Fault sizes were calculated in three different ways: using the number of elements in the structure, its tip-to-tip length and its total plastic strain. All three measures give distributions

that plot as straight lines in log-log space, and the slope of the line decreases with time. The total plastic strain distribution shows the same features as the length frequency distribution; the size frequency distribution that uses the number of elements as a measure of size compares less favourably. For example, at time 8, a break in the slope of the length frequency distribution appears. This feature also appears in the total plastic strain frequency distribution at the same time, but it is not apparent in the 'number of elements' frequency distribution. This break in slope occurs when the largest faults just spans the entire layer thickness, and its physical significance is discussed in Section 5.3.3. Total plastic strain has a further advantage over the other measures of size: far more data-points define the total plastic strain distribution and so the bias towards large faults during power law fitting by linear regression (see Figure 4.4) is reduced. However, there is a disadvantage to using total plastic strain as a measure of fault size. On Figure 4.6 the "number of elements" and "tip-to-tip length" distributions contain 250 faults, spanning 3 orders of magnitude. The total plastic strain distribution contains the same number of faults but spans 4 orders of magnitude. This means that the "number of elements" and "tip-to-tip length" distributions will have similar power law exponents, but the exponent for the total plastic strain distribution will necessarily be lower. In conclusion, total plastic strain can be considered a useful measure because size frequency distributions produced using this measure show the same features as length-frequency distributions. However, the power law exponent relating total plastic strain to frequency will be lower than the power law exponent that relates length to frequency.

Having compared total plastic strain with fault height, I now examine its relationship to displacement. Displacement is defined for each row of nodes in a structure, whereas total plastic strain is a property of each element. Therefore the first step must be to calculate values of total plastic strain at the node locations. This was achieved by averaging the values of the four elements adjoining each node. A total plastic strain for each row of nodes was then calculated, and profiles of displacement and total plastic strain were constructed for each fault (see Figure 4.7). Displacements calculated at conjugate intersections were not included, because the opposite sense of shear on the two structures means that the displacements "cancel out". In many cases, the two profiles have very similar shapes: total plastic strain generally varies along a fault in the same way as displacement. This point is emphasised by Figure 4.8 which shows the pairs of displacement and total plastic strain values calculated for each row of each fault. Although there is some scatter, there is a clear linear relationship between displacement and total plastic strain, measured row by row. For each of the structures highlighted in Figure 4.7, the total plastic strain for the entire structure and the sum of the displacement measurements were calculated. Figure 4.9 shows a linear relationship between the two, suggesting that

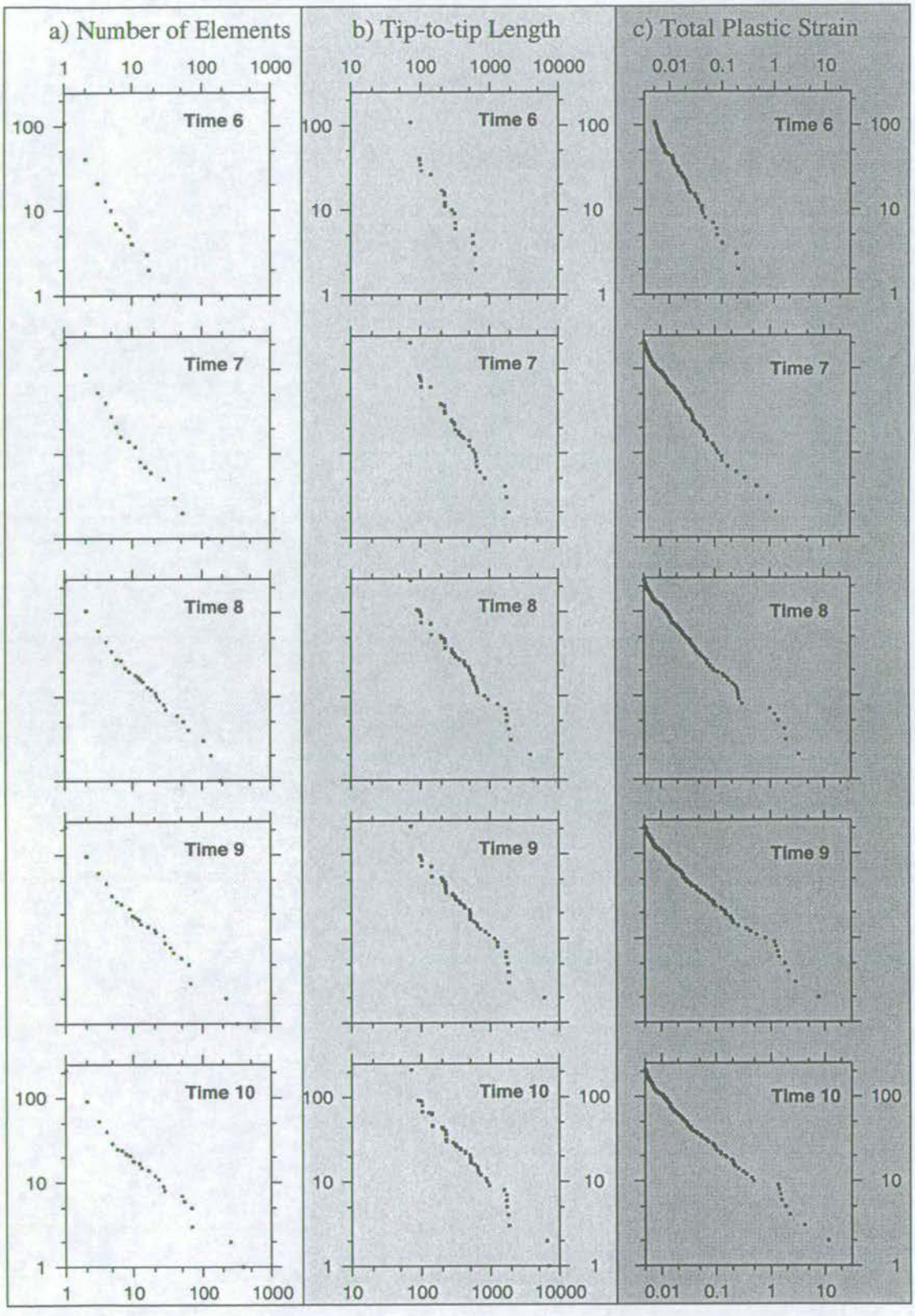

Figure 4.6. Size frequency distributions generated using three different measures of size. a) Number of elements b) Tip-to-tip length c) Total plastic strain. Size measure on the x axis, cumulative frequency on the y axis.

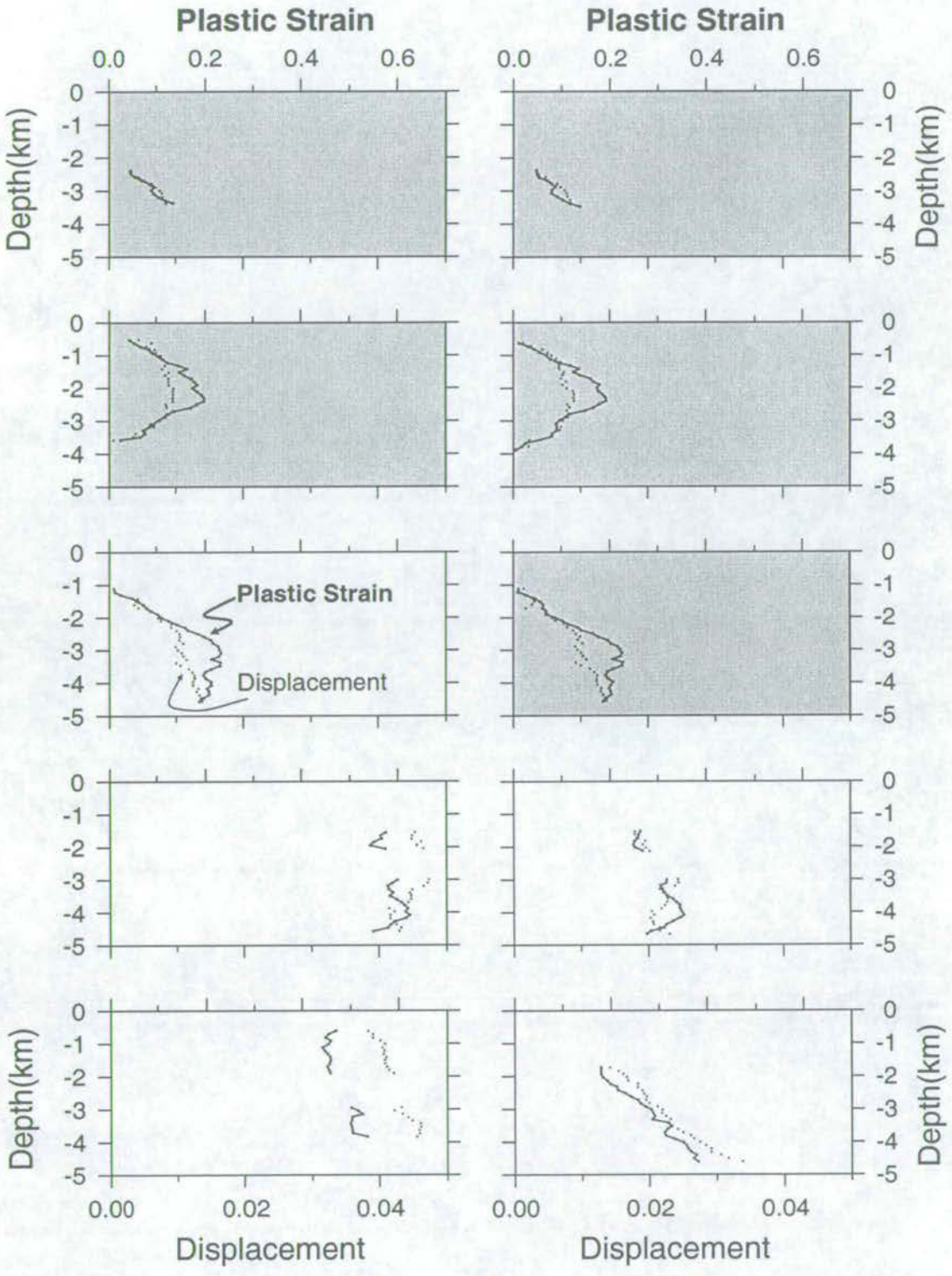

Figure 4.7. Profiles of total plastic strain (bold line) and displacement (thin line) along 10 structures from runs of the standard model with isostatic conditions at the base. There are gaps where the structure being profiled intersects other faults (see text). Highlighted structures have no intersections, and were used to create Figure 4.9

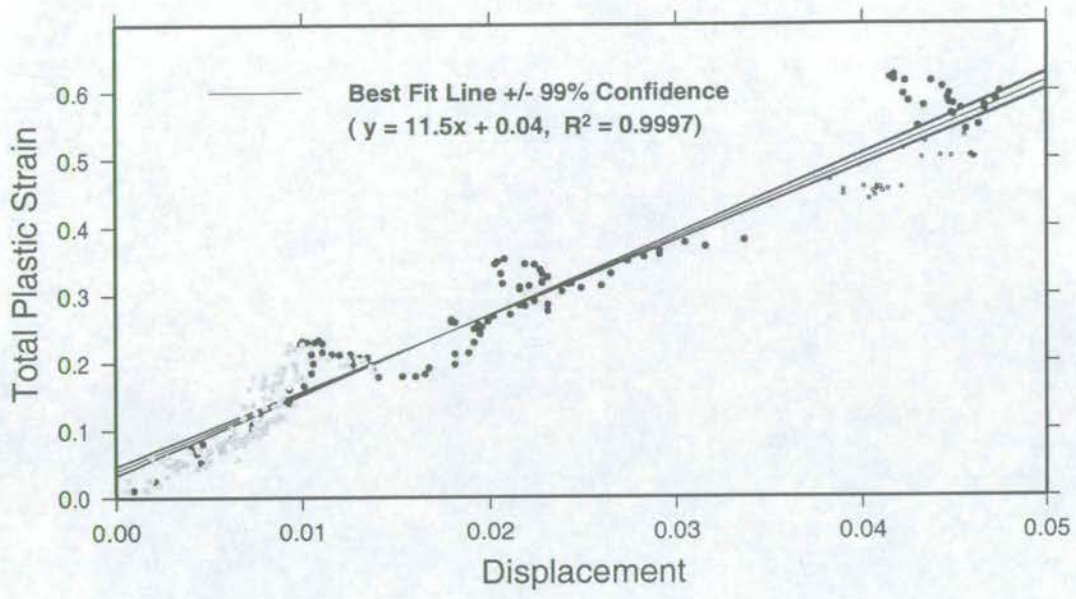

Figure 4.8. Displacement versus total plastic strain. Each data point is a single row in one of the 10 structures profiled in Figure 4.7. Best fit lines for regression of strain on displacement, with 99% confidence limits. Highlighted points are from the structures used to generate Figure 4.9.

measuring total plastic strain for a structure in ADELI is equivalent to measuring the area under a displacement profile for a natural fault. Scholz *et al.* (1993) state that the area under a displacement profile is a more stable measure of fault size than maximum displacement, based on field observations of faults described by Dawers *et al.* (1993).

In conclusion, total plastic strain is a robust measure of fault size. It compares well with displacement and length, two measures which are commonly used to describe the size of natural faults. I have shown that total strain frequency distributions show the same features as length frequency distributions for structures present at low strains in ADELI simulations. This measure of size also scales with displacement at higher strains, making it an appropriate measure for structures of all sizes at any strain.

4.4 Determining the Exponent of Power Law Distributions

There are three commonly used definitions of a power law distribution. Barton & Zoback (1992) describe power law distributed fracture apertures in terms of the discrete frequency

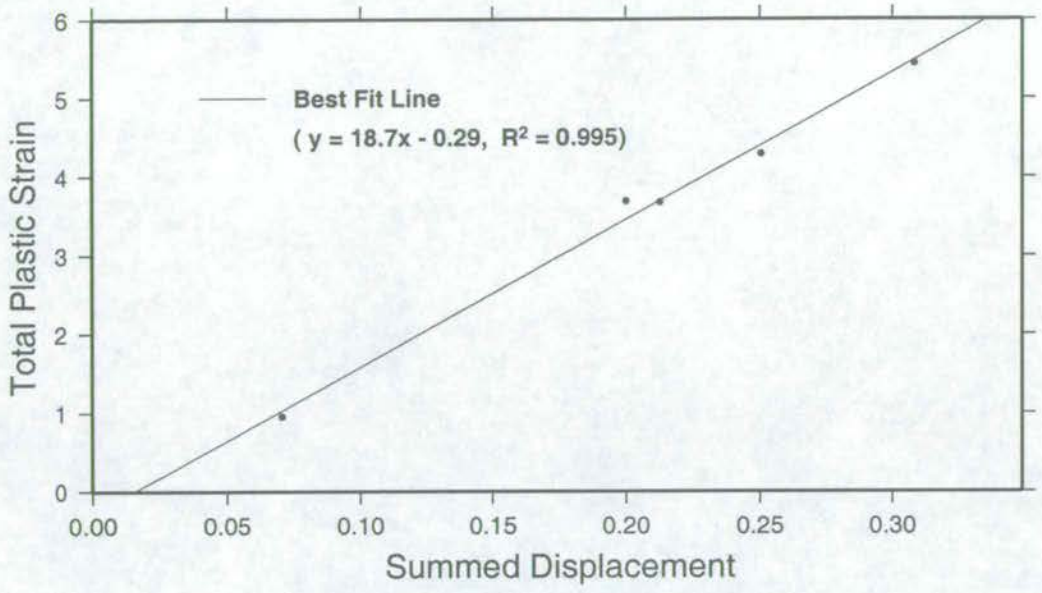

Figure 4.9. Summed displacement versus total plastic strain for 5 structures which do not intersect with other structures nor the perimeter of the deforming block.

distribution:

$$n = a_1 x^{-c_1} \tag{4.1}$$

where x is the size of the aperture and n is the number of aperture values in an interval $x \pm \delta x$. An alternative definition of power law size scaling is based on the discrete frequency of $\log x$ (hereafter referred to as the log-interval distribution):

$$\log n = a_2 - c_2 \log x \tag{4.2}$$

where n is the number of structures in an interval $logx \pm \delta(\log x)$. This definition is most commonly used in earthquake studies. In fault population studies it is most usual to see power law relationships written in terms of the cumulative distribution:

$$N = a_3 x^{-c_3} \tag{4.3}$$

where x is fault length and N the number of faults of size x or larger (the cumulative frequency).

All three definitions are compatible, and Pickering *et al.* (1995) show that c_2 and c_3 are theoretically identical. However, for data affected by sampling bias, the different power law definitions lead to different estimates of the exponent. Pickering *et al.* (1995) do not recommend the use of discrete frequency distributions. They calculated c_1 for representative samples of a power law distributed population and found it to be an inaccurate estimate of the exponent of the underlying population. The value of c_2 is affected by the choice of interval, $\delta(\log x)$ and so Equation 4.3 has become the method of choice for estimating power law exponents for the vast majority of geologists studying fault populations. However, determining power law exponents from cumulative frequency distributions is not without its problems. Even in the absence of sampling bias, cumulative frequency distributions show a "roll-over" towards large magnitudes due to what Pickering *et al.* (1995) termed the finite-range effect.

To calculate the power law exponent from a distribution, we need a fitting procedure. To be useful, a fitting procedure should yield (i) estimates of the parameters a_* and c_* ($* = 1, 2$ or 3) , (ii) error estimates on these parameters and (iii) a statistical measure of goodness-of-fit. In fault population studies, exponents are normally found by taking logs of the fault sizes and frequencies before fitting a straight line through the transformed data using linear regression. Taking logs of the cumulative frequency distribution (Equation 4.3 above) gives

$$\log(N) = log(a_3) - c_3 \log(x) \tag{4.4}$$

and so c_3 may be estimated from least squares regression of $Y = \log(N)$ on $X = \log(x)$, giving c_{LR}:

$$c_{LR} = \frac{\Sigma(X_i - \overline{X})(Y_i - \overline{Y})}{\Sigma(X_i - \overline{X})^2}. \tag{4.5}$$

A Student's T-test [p1267, Kreysig (1993)] can be used to estimate the uncertainty on the slope, assuming that the measurements are independent and the random variable ($log(N)$) is normal. The goodness-of-fit can be measured using the r^2 statistic, given by

$$r^2 = \frac{\sum_{i=1}^{n}(\hat{Y}_i - \bar{Y})^2}{\sum_{i=1}^{n}(Y_i - \bar{Y})^2} \tag{4.6}$$

where $\bar{Y}$ is the mean $\log(N)$ and $\hat{Y}_i$ the values predicted by the regression line at each X_i.

The linear regression method assumes that the residuals of the dependent variable (the

difference between measured Y_i and predicted $\hat{Y}_i$) are independent and random. As N must be an integer, this is not the case. Clarke *et al.* (1999) criticise the least squares method for this very reason and propose a more statistically rigorous approach instead. They formulate the problem thus: if $S(x)$ is the proportion of faults with lengths greater than or equal to x, then

$$S(x) = \left(\frac{x}{\lambda}\right)^{-\alpha} \tag{4.7}$$

where λ is the size of the smallest structure. The maximum likelihood (ML) estimator of α is

$$\alpha_{ML} = \frac{n}{\Sigma Y_i} \tag{4.8}$$

where n is the number of faults in the population and $Y_i = \ln\left(\frac{X_i}{\lambda}\right)$. The minimum variance unbiased estimator of the power law exponent (α_{MVUE}) is

$$\alpha_{MVUE} = \frac{n-1}{\Sigma Y_i} \tag{4.9}$$

and 95% confidence limits for α_{MVUE} are

$$\alpha_{lower} = \frac{\chi^2_{2n,97.5}}{2\Sigma Y_i}, \qquad \alpha_{upper} = \frac{\chi^2_{2n,2.5}}{2\Sigma Y_i} \tag{4.10}$$

where $\chi^2_{v,c}$ is the c percent point of the χ^2 distribution on v degrees of freedom. Clarke *et al.* (1999) do not suggest a goodness-of-fit statistic for the maximum likelihood method. The maximum likelihood estimator is known to be biased, but has been shown by Clarke *et al.* (1999) to yield more reliable estimates of the power law exponent and more realistic error bounds than linear regression.

Having selected a distribution (discrete, log-interval or cumulative) and a fitting method (linear regression or maximum likelihood), the only question remaining is which points in the distribution should be fitted? Because of the problems of sampling bias, data from the extremes of the distribution are often removed before fitting the power law [see, for example, Ackermann *et al.* (2000)]. Usually this is simply done by "eye-balling": points at either end of the distribution are excluded if they do not describe a straight line in log-log space. More objective methods are based on maximising the goodness-of-fit statistic (Ortega & Marrett

2000). Size distributions produced by ADELI have very obvious breaks in slope (see Figure 4.6), so r^2 maximisation was deemed unnecessary and straight line sections were chosen by eye.

This study is driven by the observations of fault size frequency distributions and their power law exponents reported in published literature. Consequently, for consistency with published studies, it is desirable to adopt the most commonly used approach: linear regression of cumulative frequency data in log-log space. However, to gauge how much variation in c might be due to the curve fitting algorithm, I analysed 10 cumulative frequency distributions (shown previously in Figure 4.6 b and c) using the both the linear regression method and the maximum likelihood method. I also determined c for both datasets using the log-interval method with linear regression.

Figure 4.10 shows the cumulative frequency distributions of Figure 4.6 with best fit power laws determined using the maximum likelihood and linear regression methods. α_{MVUE} is the power law exponent calculated using the maximum likelihood method; c_{LR} is the exponent calculated using linear regression of $\log N_i$ on $\log x_i$. The maximum likelihood estimator method gives a poor "eyeball fit" when applied to the length frequency data (left column, Figure 4.10), but provides a rather better fit to the total plastic strain frequency data (right column, Figure 4.10). For the length data at times 6 and 7, $\alpha_{MVUE} > 2$, which is not consistent with the dimensionality of the experiment (a 2D sample of fault trace lengths should have an exponent less than 2).

I have noted previously (Section 4.3) that length frequency distributions for structures in ADELI suffer from problems of binning due to mesh discretisation and that linear regression estimates of c can be unreliable as a consequence. Estimates of c using the maximum likelihood method are more strongly affected by binning because this method aims to fit the majority of the data-points, and in this case the measurements which are most strongly affected by mesh discretisation (small faults with 1 to 4 elements) constitute most of the data-points. To illustrate this problem, I removed faults with just one element from the dataset of tip-to-tip lengths and used the maximum likelihood method to re-estimate the power law exponent. The results are shown by the curves labelled $\alpha_{MVUE'}$ on Figures 4.10 and 4.11. The difference between $\alpha_{MVUE'}$ and α_{MVUE} varies between 0.97 and 1.82. As the maximum likelihood estimator is so sensitive to discretisation problems, I conclude that it is inappropriate to use this method to estimate power law exponents with length frequency data. The length data are already binned, due to the mesh discretisation. This caused difficulties with the log-interval method as the interval size had to be made quite large (0.2) to avoid empty bins. Unfortunately, increasing the bin width decreases the number of bins, and thus the number of data-points controlling the best-fit line. This in turn increases the uncertainty on the estimate of the power law exponent. For

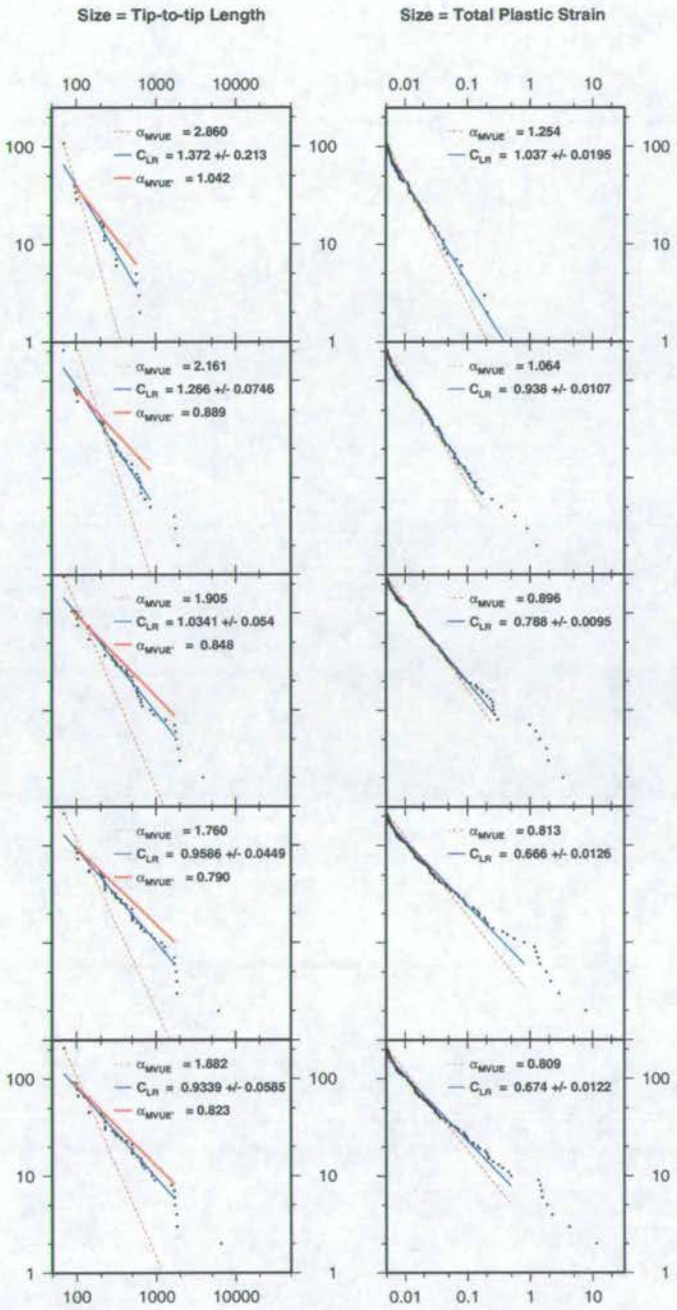

Figure 4.10. The size distributions of Figure 4.6 with best fit power laws determined using the maximum likelihood estimator (α_{MVUE}) and linear regression (C_{LR}). Best fit lines are only plotted in the interval over which they were calculated.

the length frequency dataset presented above, the 95% confidence limits on estimate of c were as large as the value of c itself, so no meaningful conclusions can be drawn from this analysis.

It seems that the choice of method used to estimate the power law exponent is less critical when the total plastic strain data are considered (Figure 4.10, right hand panel). This point is highlighted by Figure 4.11, which shows estimates of the exponent for both datasets using the different estimation methods. For the size frequency distributions with size measured as length (Figure 4.11a), the discrepancy between α_{MVUE} and c_{LR} is large and the curves do not have the same trend. The discrepancy between $\alpha_{MVUE'}$ and c_{LR} is smaller, but the curves still do not have the same form. In contrast, the exponents calculated for the total plastic strain data (Figure 4.11b and Figure 4.12) agree within 95% confidence limits and, most importantly, change in the same way through time. I therefore conclude that the *value* of c is relatively insensitive to the curve fitting method employed for total plastic strain frequency distributions but not for length frequency distributions. It is, however, worth noting that the *uncertainty* on c is rather more sensitive to the the parameter fitting method chosen. Figure 4.12 suggests that the technique most commonly used by geologists (linear regression in log-log space) underestimates the uncertainty on c. Having evaluated the merits of the different parameter methods, I henceforth use the least squares method.

4.5 Summary

I have developed a new algorithm for automatically assigning elements to structures, which is capable of discriminating between synthetic and antithetic structures. I have also shown how displacement profiles for such structures may be generated. I demonstrate that the total plastic strain scales with displacement summed over the entire the structure and that total plastic strain is more useful than tip-to-tip length as a measure of fault size in cross section. I describe several methods for fitting power laws to size frequency distributions, and show that it is appropriate to use linear regression to determine the power law exponent for data where size is measured as total plastic strain. However, I recognise the fact that this method underestimates the uncertainty on c.

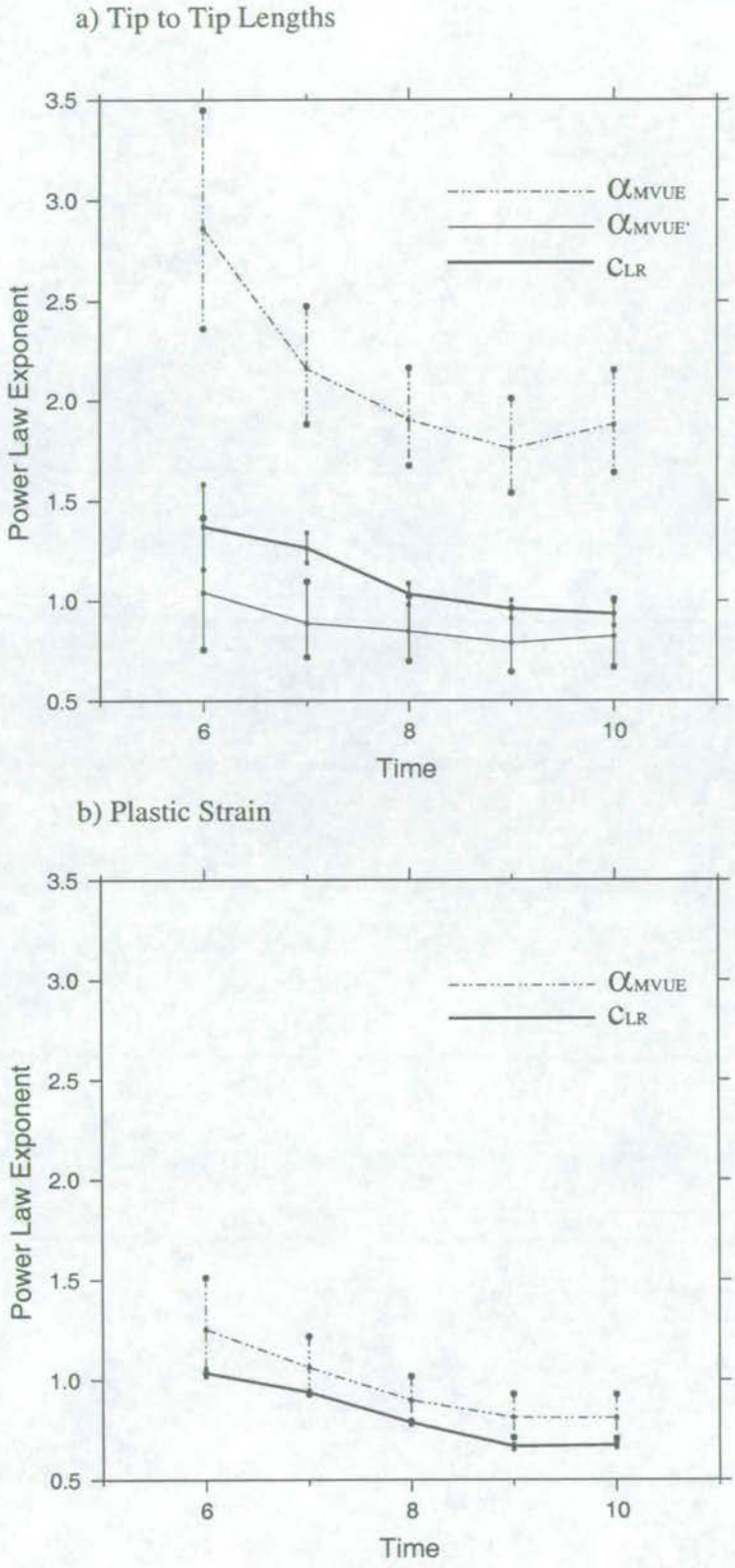

Figure 4.11. Power law exponent (plus error bars) versus time for the distributions of Figure 4.6. a) Length cumulative frequency distributions b) Total plastic strain cumulative frequency distributions.

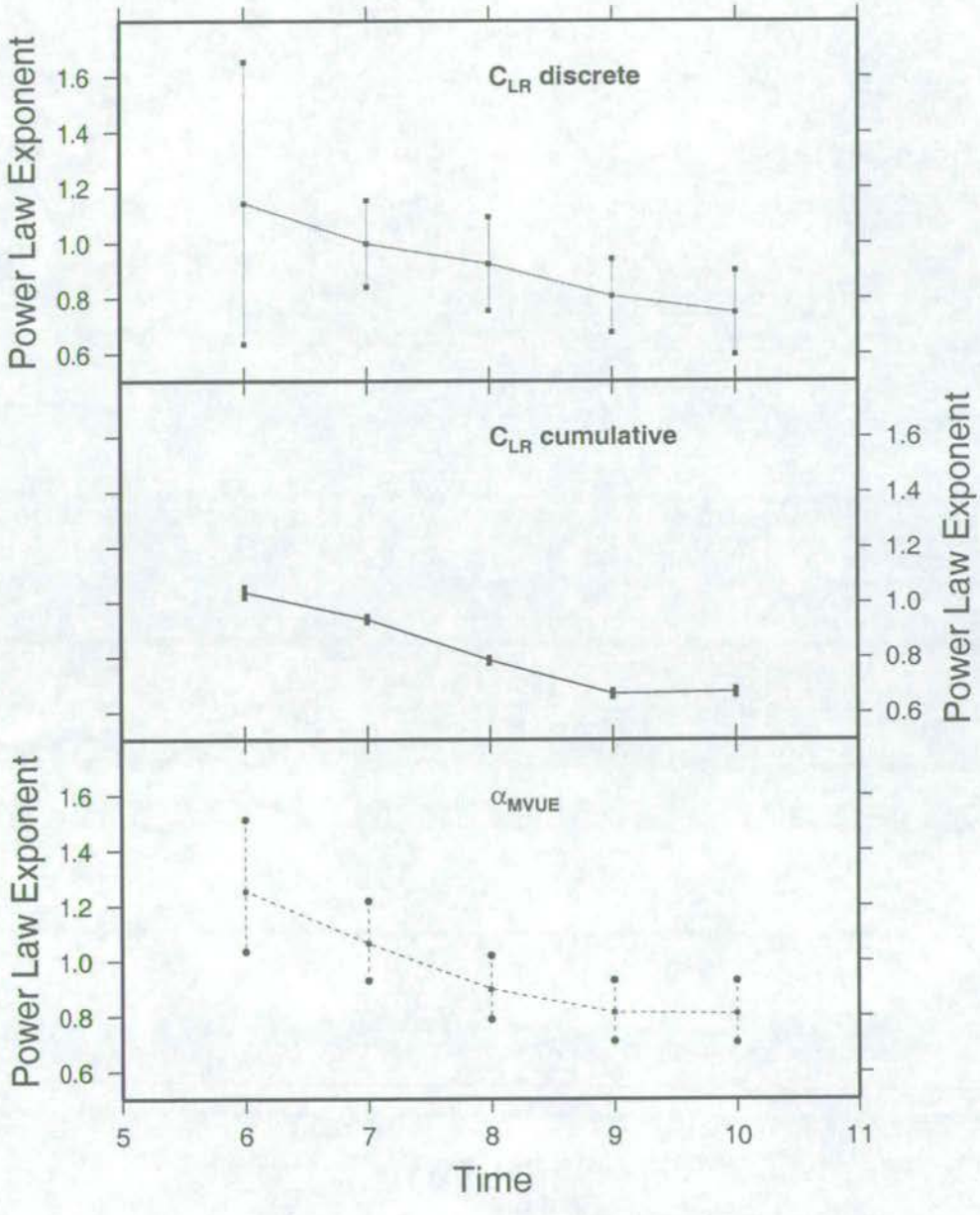

Figure 4.12. Power law exponents (plus error bars) versus time for total plastic strain data. Top: exponent estimated using linear regression on discrete frequency distribution. Middle: exponent estimated using linear regression on cumulative frequency distribution. Bottom: exponent estimated using maximum likelihood method.

Chapter 5

The Evolution of Structures in the Numerical Model

The purpose of this chapter is to describe in detail the behaviour of structures in the numerical model, compare faults in the model with natural structures and explain observed behaviour in terms of properties of the whole system. I show how the chosen material properties (a strain-softening Von Mises rheology with heterogeneity in yield strength) influence fault nucleation, orientation, growth and activity. I also discuss how the geometry of faulting affects the mechanical response of the system as a whole. Finally, I relate observed fault size cumulative frequency distributions (which vary from power law at low strains to a combination of power law and exponential at higher strains) to the temporal changes in the proportion of faults that are active and the growth mechanisms of active faults.

5.1 Approach

The experiments presented below are two realisations of the standard model (see Section 3.4 for details of the standard model), with normally distributed yield strengths with a mean of 275 MPa and standard deviation of 25 MPa. The yield strengths are randomly arranged in space and the same spatial distribution is used in both experiments. Isostasy operates at the basal boundary. The only difference between the two simulations is this: in Experiment A, the region is deformed by moving the left wall; in Experiment B, the right wall is moved.

The structures that develop in the two experiments are described in terms of their arrangement in space, their orientations and their displacement profiles. Natural faults are commonly described in these terms, so comparisons can easily be made between natural faults and modelled structures. The structures are also described in terms of their modes of growth, stress fields and activity in order to understand why the faults behave as they do. The understanding thus gained is used to explain particular features of the size frequency distribution displayed by the modelled fault population.

5.2 Deformation Development Through Time

5.2.1 Nucleation

Fault patterns for the two runs are shown in Figure 5.1. In both runs, failure initiates at the base of the deforming region. This is because I use a yield criterion that depends on deviatoric stress alone (the Von Mises criterion, see Chapter 3), and the deviatoric stress is largest at the base of the model.

Initially elements fail all across the model, not just near to the moving wall. A nucleation front then propagates upwards and across the model (clearest on Figure 5.3). Nucleation causes an increase in the number of faults and an increase in the total number of broken elements (Figure 5.2). The zones of failure are fairly evenly spaced. Ord (1990) links the formation of shear bands at particular spacings in a mesh to variations in the computed stress field. She explains that the governing equations of deformation have a periodic solution, but that the analytic solution does not prescribe wavelengths. However, in the numerical solution, the two inherent length scales, the element height (d) and the model height (L), induce wavenumber selection. She concludes that the periodicity of the bands is determined by the ratio d/L. The formation of shear bands at particular spacings could be considered to be an artifact of the numerical method alternatively, we could equate d and L to meaningful geological length scales, for example grain size and layer thickness. In addition to the stress field, another factor determines whether or not a particular element at the base will fail: the yield strength of the element. Figure 5.4 shows how nucleation is linked to yield strength variations. In both experiments, the very weakest elements in each row are always broken. At 0.9% total model extension, Experiment A and Experiment B are very similar: they posses 111 and 115 broken elements respectively, and of these, 90 broken elements are identical. This shows that the yield

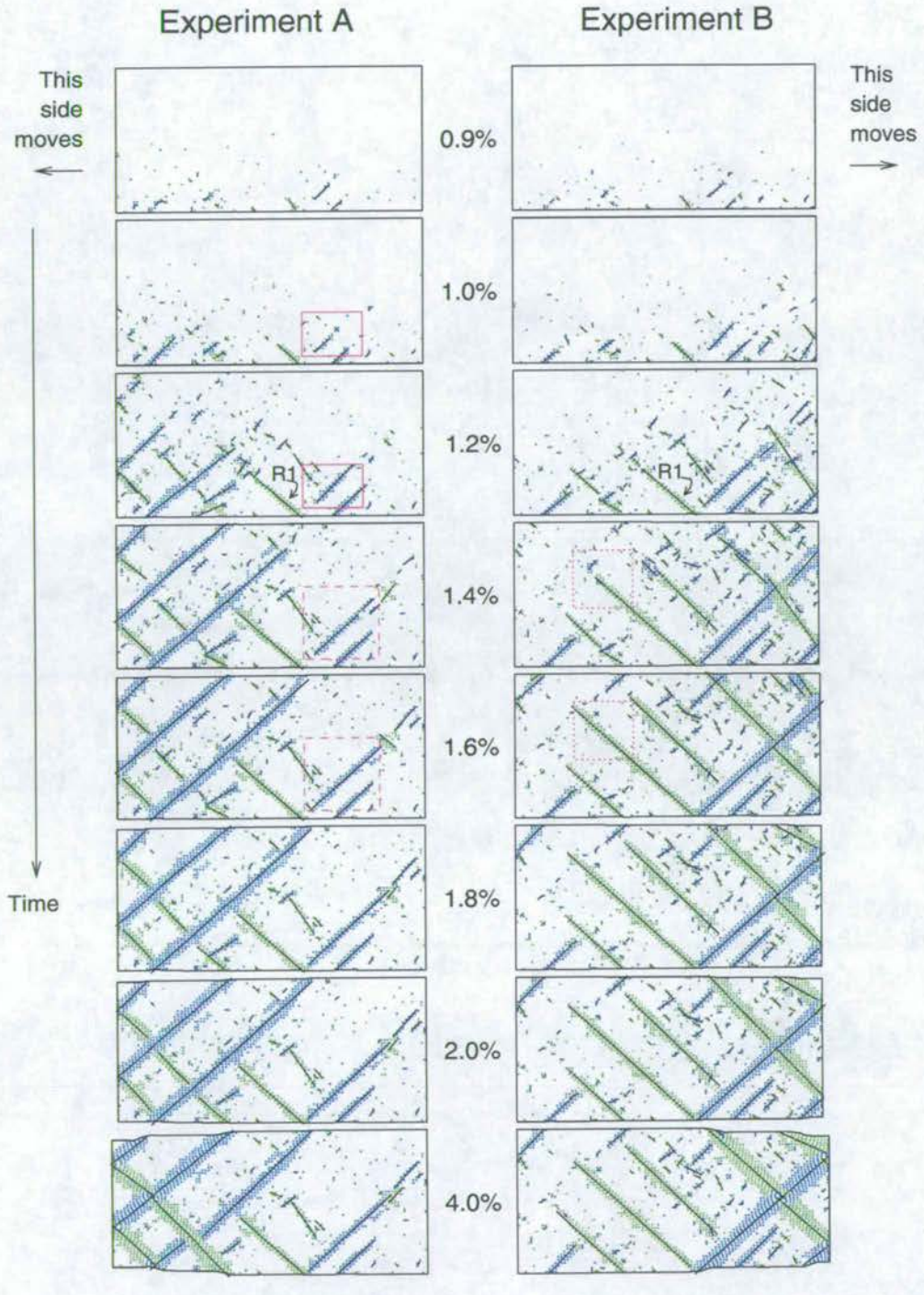

Figure 5.1. Snapshots of two models showing the evolution of fault patterns with time; Experiment A on the left, B on the right. Elements in right-dipping faults are coloured green; elements in left-dipping faults are coloured blue. Black lines show the best-fitting straight line through the elements in each fault. The areas highlighted in magenta boxes are referred to in Section 5.2.2. The extension of the whole model at the time of the snapshot is shown between the two panels.

strength distribution is the most important factor controlling where deformation nucleates in these simulations.

Left-dipping and right-dipping structures form in both experiments, as predicted by the faulting theory of Anderson (1951). Initially, the number of broken elements in synthetic and antithetic structures are almost identical(Figure 5.5). Studying the map at 1% extension, it is clear that very weak elements that form the nuclei of left-dipping structures in Experiment A also form the nuclei of left-dipping structures in Experiment B. The same is true of right dipping structures. I thus conclude that it is the local variation in yield strengths that determines whether a broken element will initiate as a right-dipping or left-dipping structure. The low dip of the modelled structures (around 45°, Figure 5.6) compared with natural faults [typically~60° - Knipe, Jones & Fisher (1998), although active faults with dips as low as 45° have been reported (Jackson & McKenzie 1983)] is again a consequence of modelling the deforming material as a Von Mises solid. New structures continue to emerge until 1.8% extension.

5.2.2 Growth

As the model is extended, faults grow upwards by tip propagation (see the solid box on Figure 5.1), down-dip linkage with synthetic structures (dashed box on Figure 5.1) and by the assimilation of small, antithetic structures (dotted box on Figure 5.1).

In the nucleation phase, fault development is largely controlled by the distribution of yield strengths. During the growth phase, the dominant controls on fault development are the boundary conditions and the interaction with other structures. The boundary conditions concentrate strain near to the moving wall, accelerating the growth of structures in this area (Figure 5.7). In Experiment A, structures in the left-hand half of the model develop fastest but in Experiment B, strain is concentrated on structures in the right-hand half of the model. As strain is increasingly localised near to the moving wall, more small faults become inactive (Figure 5.3). The boundary conditions also favour the growth of faults on the basis of their orientations. As extension proceeds, the proportion of broken elements in synthetic structures increases in both models (Figure 5.5).

To illustrate how the development of a particular structure may be influenced by other structures nearby, let us consider fault R1 on Figure 5.1. At 1.2% strain in both experiments, this fault is roughly the same size, the yield strengths of the elements surrounding this structure are identical and, being almost exactly half way between the two side walls, the loading is

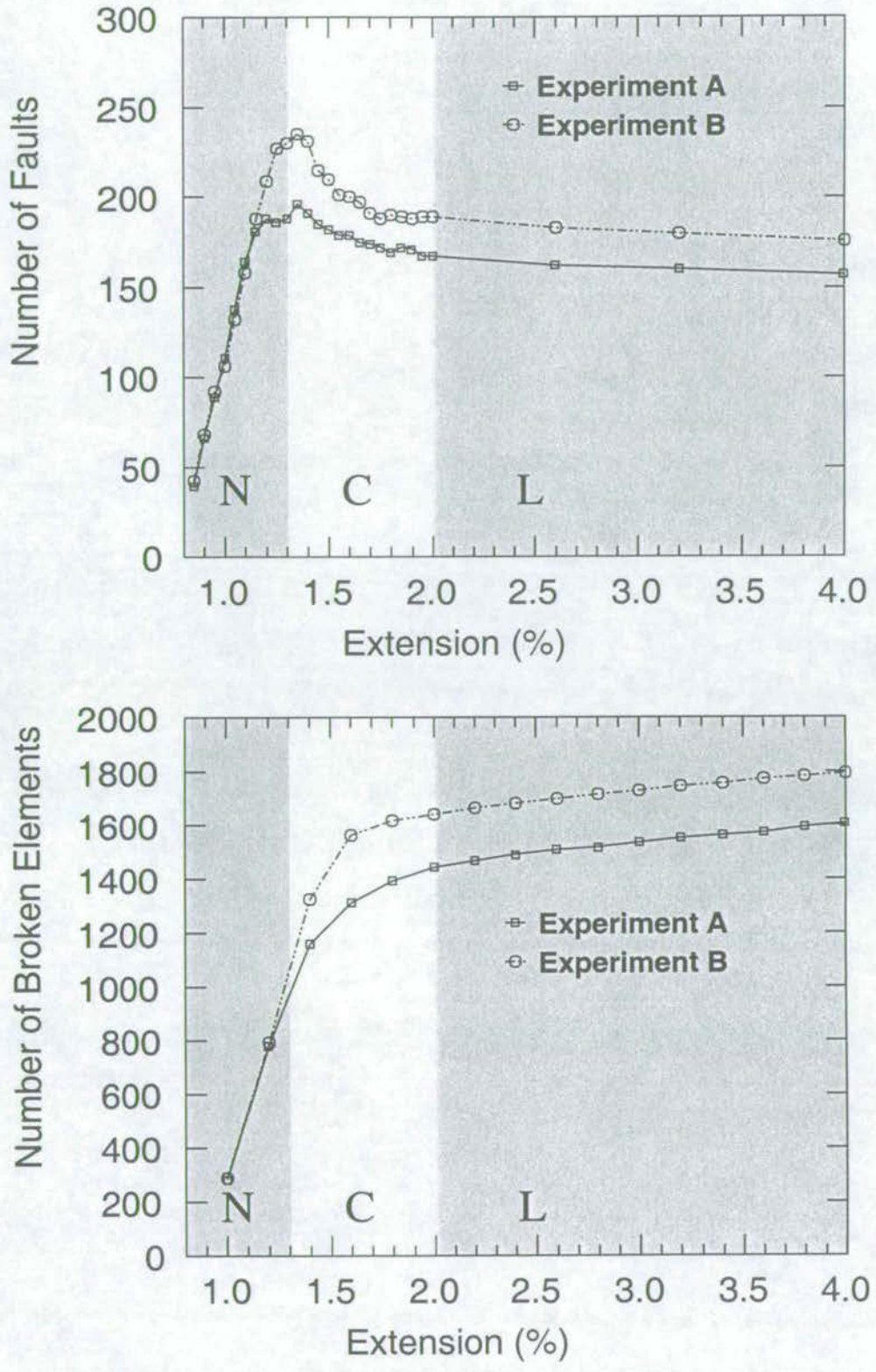

Figure 5.2. Number of faults and broken elements versus time. Shaded bars highlight time periods when fault nucleation (N), coalescence (C) and localisation (L) are the dominant processes for accommodating imposed deformation. Boundaries between different regimes determined from activity maps (Figure 5.3).

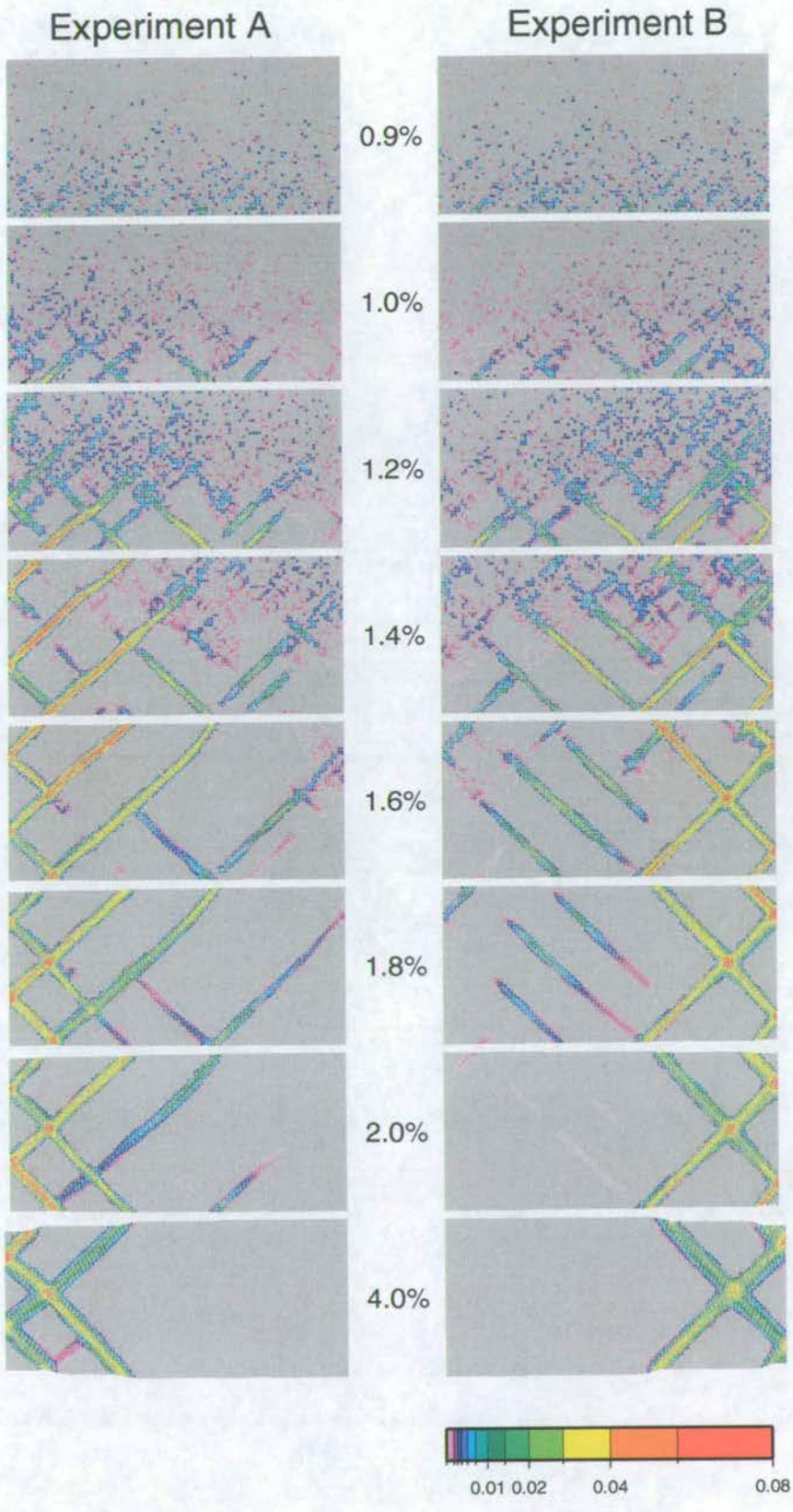

Figure 5.3. Activity maps for the two experiments. Each plot shows the increase in plastic strain in the last 0.1% (top two plots) or 0.2% (other plots) extension.

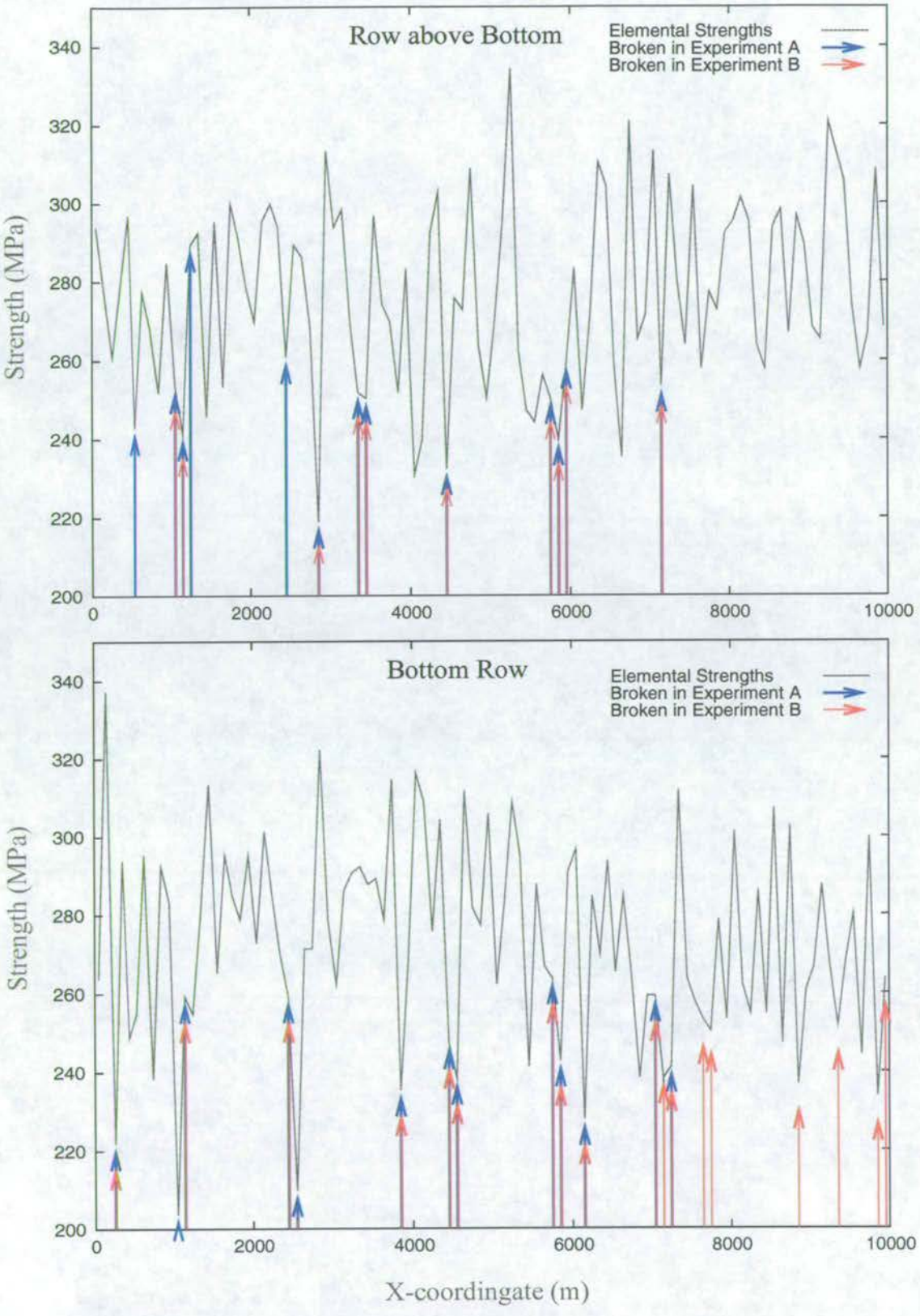

Figure 5.4. Yield strengths and broken elements in the two lower-most rows of the two simulations.

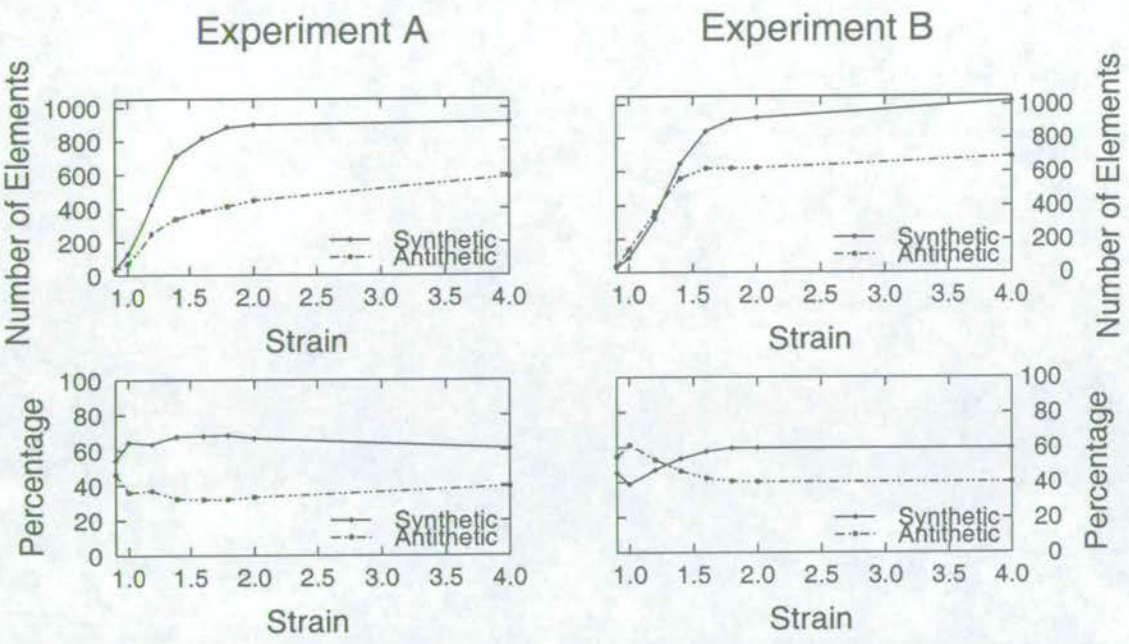

Figure 5.5. Number (upper plots) and percentage (lower plots) of broken elements belonging to either synthetic or antithetic structures in Experiments A and B.

comparable. In Experiment A, its upward propagation is frustrated by a large left-dipping structure, whereas in Experiment B, its growth is unhindered. Although R1 continues to accumulate displacement in both experiments (Figure 5.8), in A the shape of the profile does not change, whereas in B, the most active part of the fault (the portion of the structure that accumulates the most displacement between time increments) moves upwards through time. In both experiments, up to 1.4% extension, the maximum displacement (Dmax) occurs at the lowest point on the fault. This is because the fault nucleated at the base and propagated upwards; Dmax is at the base not because this part of the fault has a higher displacement rate, but because this part of the fault has been active for longer. At later times, the displacement at the base decreases due to interaction with a conjugate structure (see Section 5.2.3).

Figure 5.9 illustrates another way in which the failure of some elements affects the loading in others. At the onset of deformation, the deviatoric stress increases with depth due to the overburden - this deviatoric stress gradient is caused by the overburden. The deviatoric stress also increases towards the moving wall - this stress gradient results from the applied load. At higher strains, deviations from the lithostatic line emerge. Higher than lithostatic stresses result when the failure of one element enhances the load on a neighbour. Lower than lithostatic stresses occur in elements that have failed and in elements that have been unloaded by the failure of others. Although elements at all depths have failed, the range of deviatoric stresses in a single row of elements increases with depth.

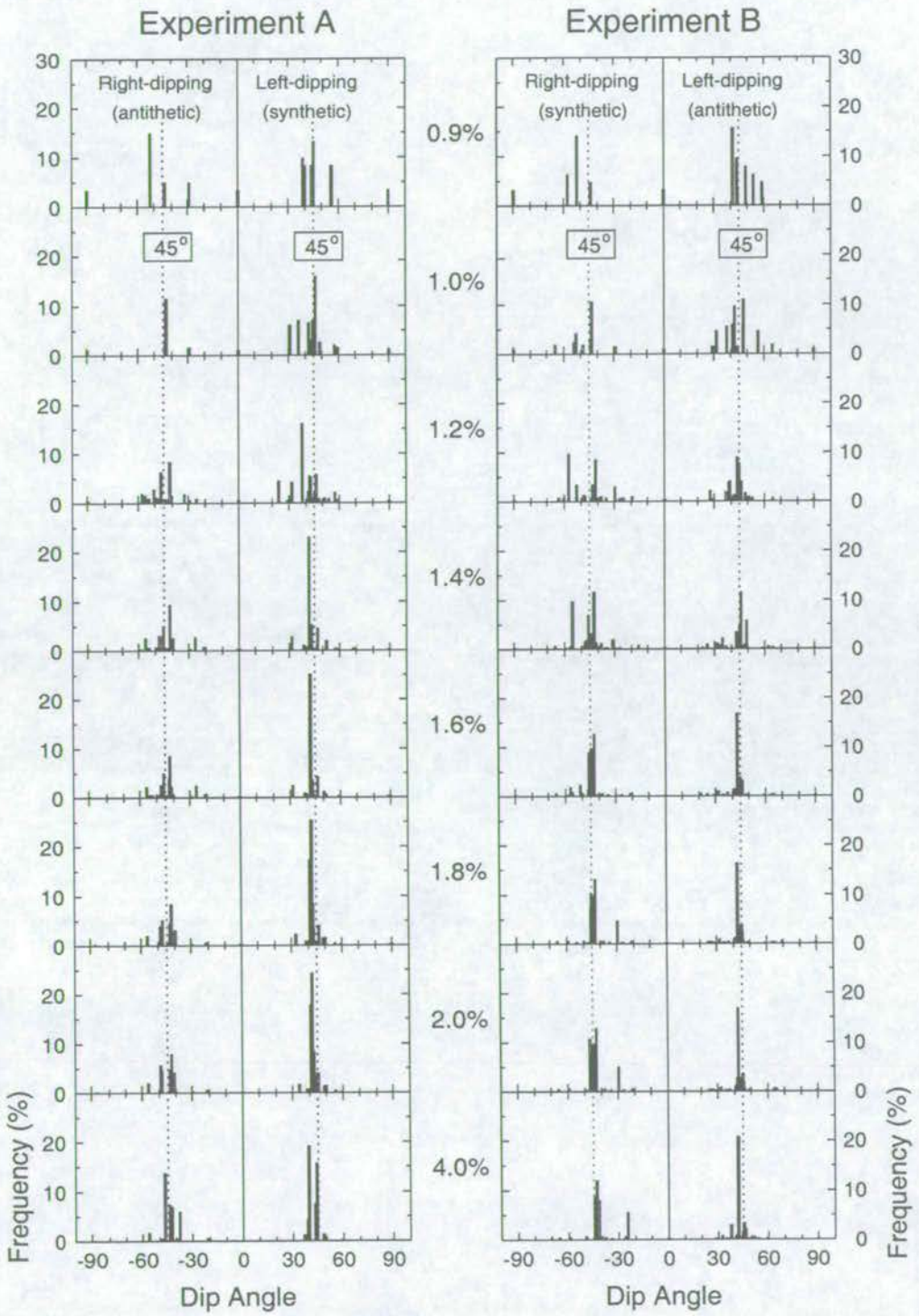

Figure 5.6. a) Experiment A (moving left wall), b) Experiment B (moving right wall). Dip distributions for two model runs, showing the proportion of broken elements in structures of a given dip. The regional extension at the time of each snapshot is shown between to two columns.

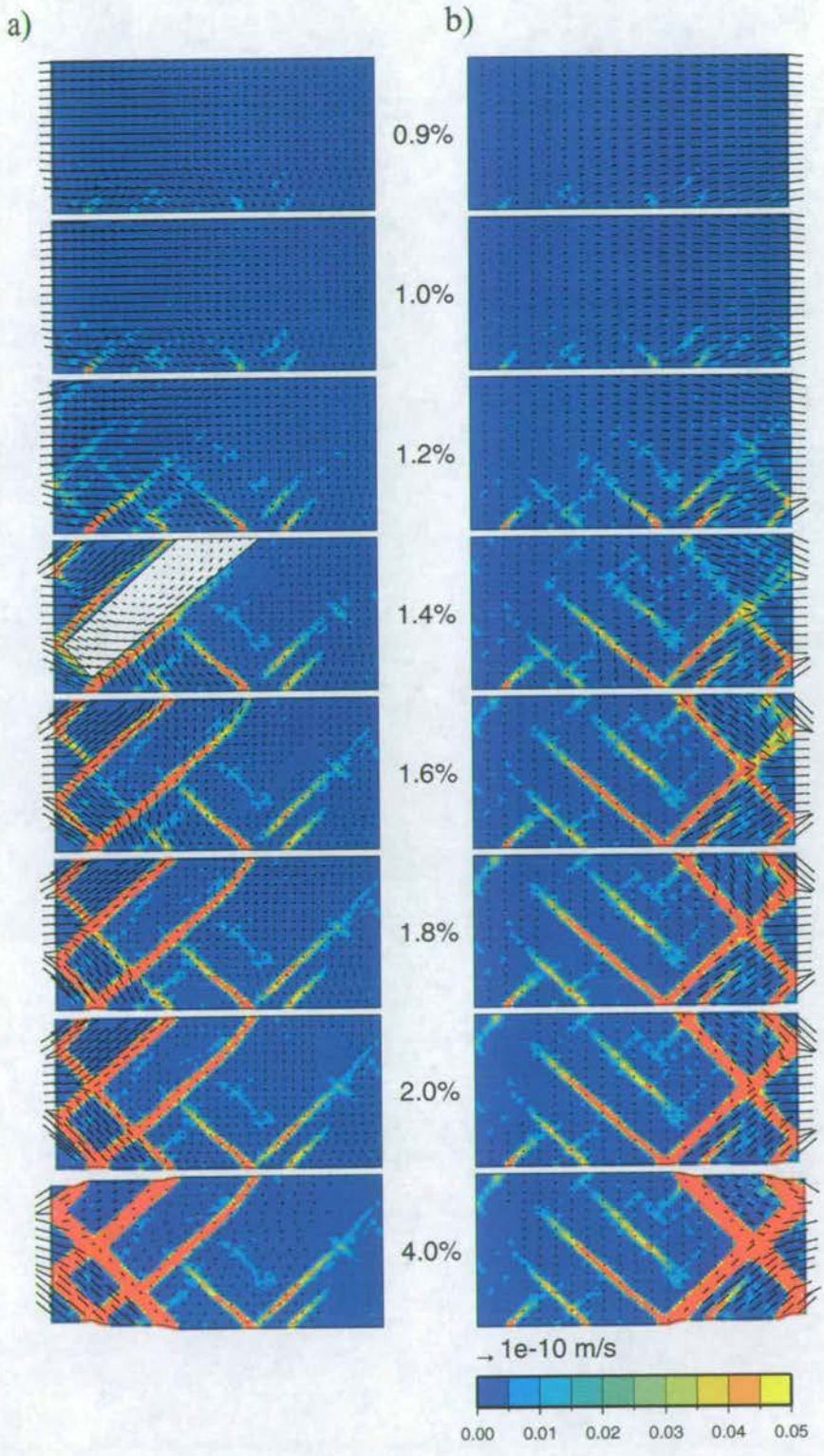

Figure 5.7. Snapshots of two simulations showing the evolution of plastic strain (colour-filled contours) with time a) in Experiment A, b) in Experiment B. Red areas have strains above 0.05. Arrows are instantaneous velocity vectors. Regional extension at the time of each snapshot is shown between the two panels. Rotation within a fault block is highlighted by the white box.

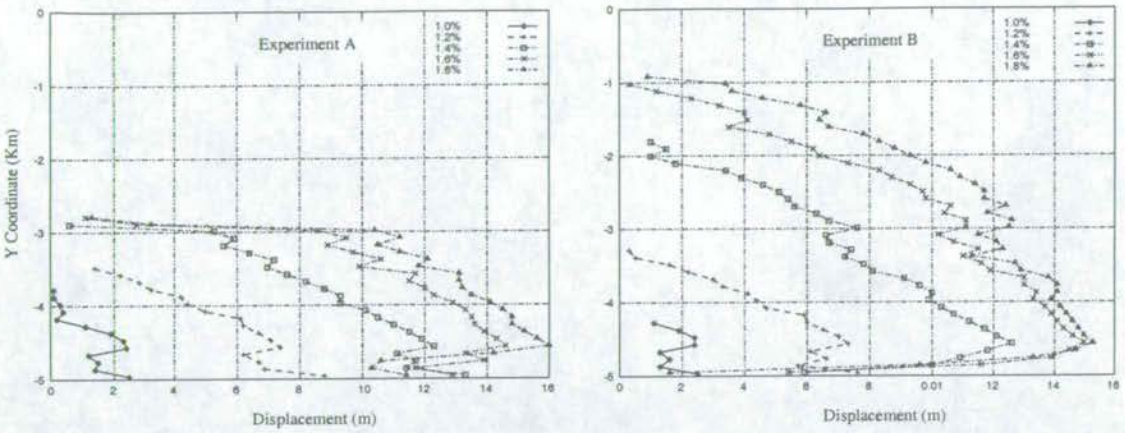

Figure 5.8. Displacement profiles for fault R1 in Experiments A and B. In Experiment A, a large antithetic fault prevents the upward propagation of this structure.

Figure 5.10 shows how the growth of R1 in Experiment B affects the deviatoric stress and the principal stress directions in the surrounding region. The zone ahead of the propagating structure experiences enhanced loading (red), whereas those areas to either side of the structure are unloaded (green). Enhanced loading will only cause failure if the yield strength of the element is exceeded, so even elements with the greatest increase in deviatoric stress are not necessarily broken. The most important point to realise is that we cannot infer the pattern of enhanced loading at 0.9% extension (top plot, Figure 5.10) from the pattern of failure at 1.0% extension (bottom plot, Figure 5.10). If these were stress maps through a section of the earth's crust, we would anticipate minor structures at different locations from the patterns at 0.9% extension and 1.0% extension. Consequently, it would be inappropriate to use the later map to predict the pattern of minor structures that developed as the major structure was growing.

During the growth phase, elements thin and extend in response to the thinning and lengthening of the whole model. This reduces the dip of both synthetic and antithetic structures (Figure 5.6). Rotation of the material between sets of parallel structures (box on Figure 5.7) changes the dip of some structures within fault bounded blocks: synchronously increasing the dip of one set of faults while decreasing the dip of the conjugate set.

5.2.3 Intersections and coalescence

This section is not entitled "linkage" because the joining of similar sized structures (what is often meant by the term "linkage") is rare in the simulations presented here. The commonest form of fault joining is the assimilation of small structures by large ones. By 1.4% strain, faults can be divided into those that define blocks and those that are contained within blocks. Structures

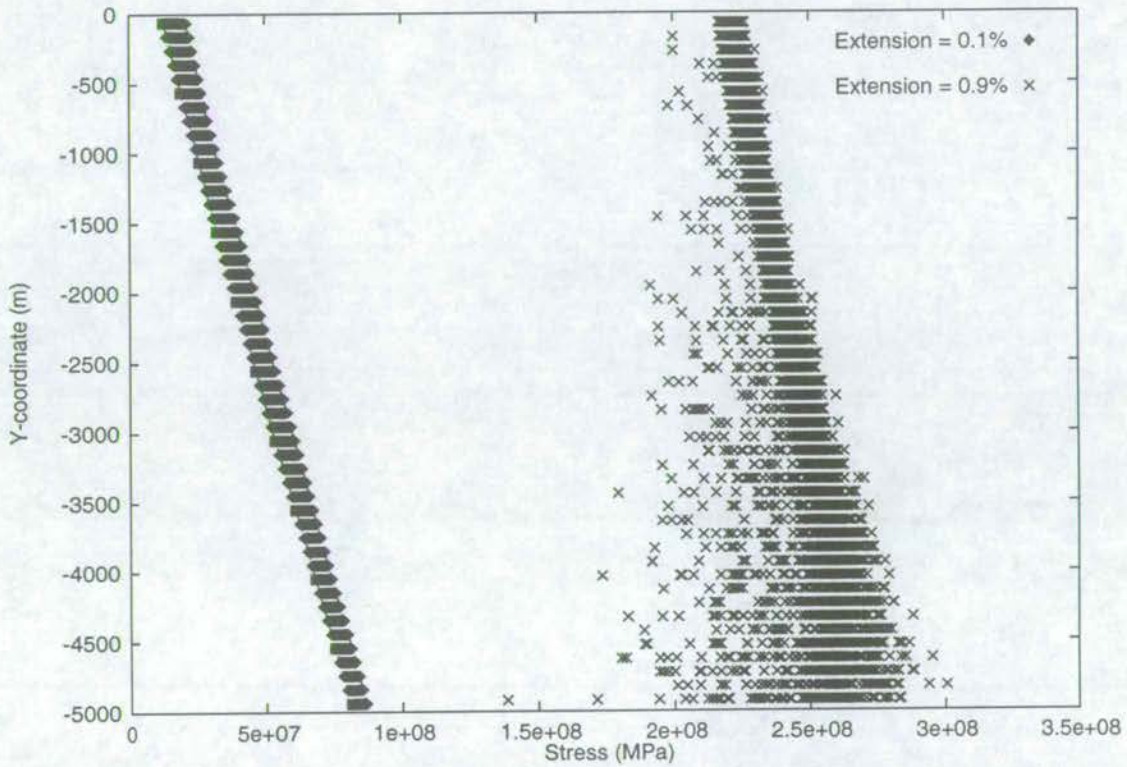

Figure 5.9. Deviatoric stress versus depth for elements at different stages of extension. At the onset of deformation, the trend is dominated by the effects of the overburden and the applied extensional stress. After 0.9% extension, when less than 1% of the elements are broken, the trend is disrupted by the softening of broken elements and the associated loading of their neighbours (see text).

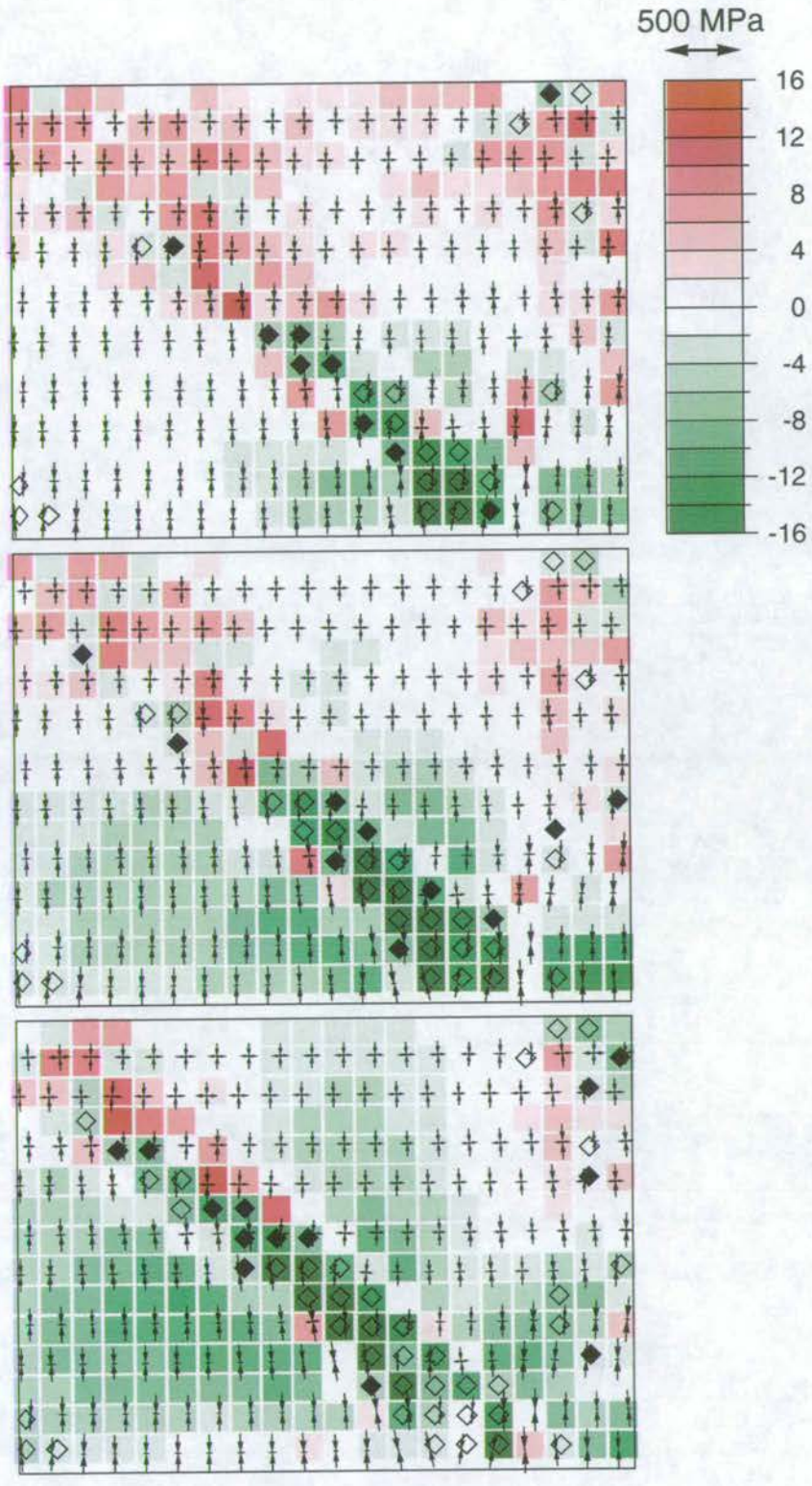

Figure 5.10. Loading and unloading of elements near to a propagating fault at 0.9% (top), 0.95% (middle) and 1.0% (bottom) total extension. Colours show changes in deviatoric stress during the last time increment. Arrows show the direction and magnitude of principal stresses, scaled to the double arrow shown above the scale bar. Broken elements are marked with a diamond. Elements that have just broken in the last time increment have filled diamonds.

inside small blocks (particularly near the moving wall) are more likely to be assimilated into the major block-bounding structures than structures within larger blocks. Large blocks therefore preserve a sub-population of minor, inactive faults that formed early in the deformation. As size frequency distributions include both active and inactive structures, the presence of such sub-populations can alter the form of size distributions. Large blocks containing many small structures can be seen towards the right hand side of Experiment A. The spatial arrangement of the major faults is important in another way. As noted previously, activity tends to concentrate near to the moving wall as the model is extended. If several large and intermediate-sized structures are present in this area, structures with a range of sizes continue to be active. However, if only a few large faults occur near the moving wall their growth becomes much faster than other faults in the population. On the size cumulative frequency distribution plotted in log-log space, this can cause a break in slope between the largest structures and the rest of the population - a phenomenon discussed further in Section 5.2.6.

Although rare, there are occasional instances of synthetic faults of comparable size (within one order of magnitude) linking in a down-dip direction (dashed box on Figure 5.1). Displacement profiles for the coalescing structures are shown in Figure 5.11. Although at 1.4% extension no unbroken elements separate the two structures, the linkage zone is still clearly visible as a local minimum on the displacement profile at this time. By 1.5% extension, however, there is no trace of a local minimum in the displacement profile at the former linkage site. The point where synthetic structures link is not permanently recorded by displacement profiles in these simulations. However, low displacements persist at points where antithetic structures have been assimilated (highlighted on Figure 5.11). On both structures, the displacement gradient in the linkage zone steepens with increasing interaction (1.2% to 1.4% extension). The deviatoric stress in the region between the two structures prior to linkage is high (see Figure 5.12), although not significantly higher than that found at a nearby free tip.

As well as interacting with other synthetic structures, faults in these simulations commonly interact with antithetic structures. In finite element simulations, shear zones often "reflect" at the boundaries of the deforming region (Davis & Fletcher 1990, Hobbs, Mülhaus & Ord 1990, McKinnon & Garrido de la Barra 1998). This leads to V-shaped fault intersections and simple grabens. Structures that intersect with the upper and lower boundaries continue to accumulate displacement and the resultant thinning is compensated isostatically. Faults that intersect with but do not reflect at the bottom boundary have their displacement maximum at their lowermost tip (e.g. Fault L2 on Figure 5.13). This pattern of displacement was explained in Section 5.2.2. Faults that intersect with a conjugate at the base of the deforming region do not have Dmax at their lower-most tip (Faults L1 and R1 on Figure 5.13), even though

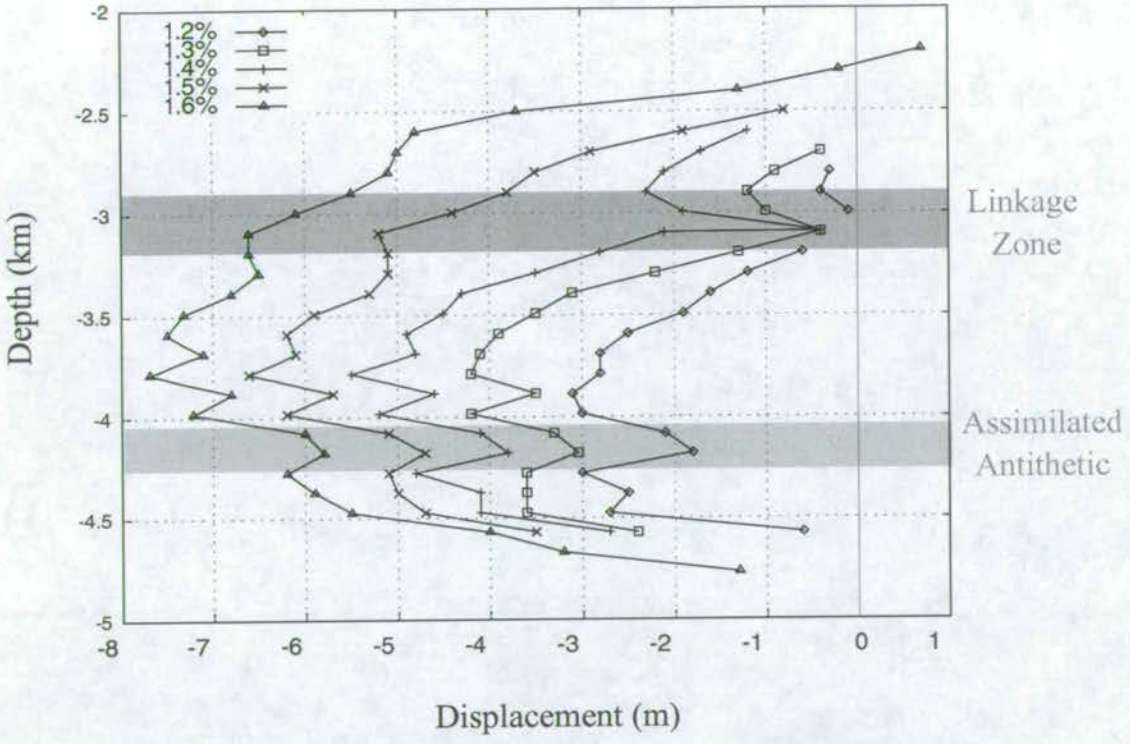

Figure 5.11. Displacement profiles on faults linking down-dip (these structures are highlighted in the dashed box on Figure 5.1. The numbers in the key refer to the total extension of the model at the time of the snapshot.

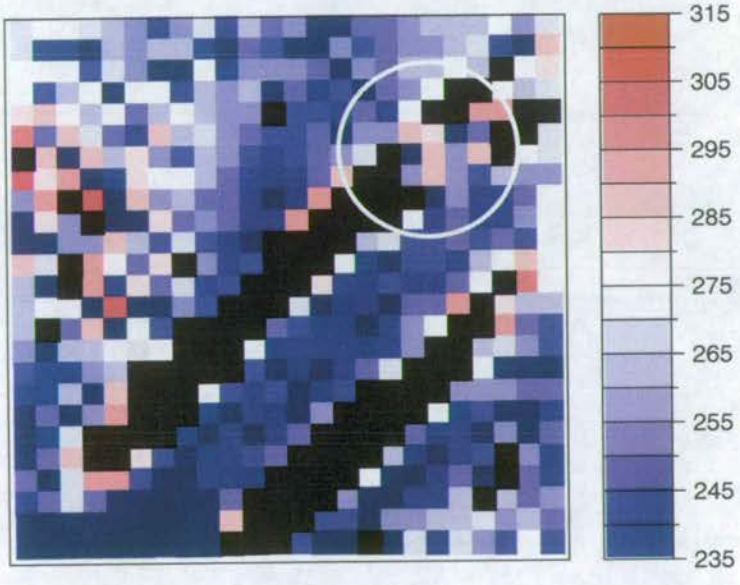

Figure 5.12. Deviatoric stress in the region surrounding two faults (the same structures as in Figure 5.11) linking down-dip at 1.3% total extension . The white circle highlights the region between the two interacting structures. Although the stress is high in this region, stresses of similar magnitude are present elsewhere in the area shown, for example at nearby fault tips.

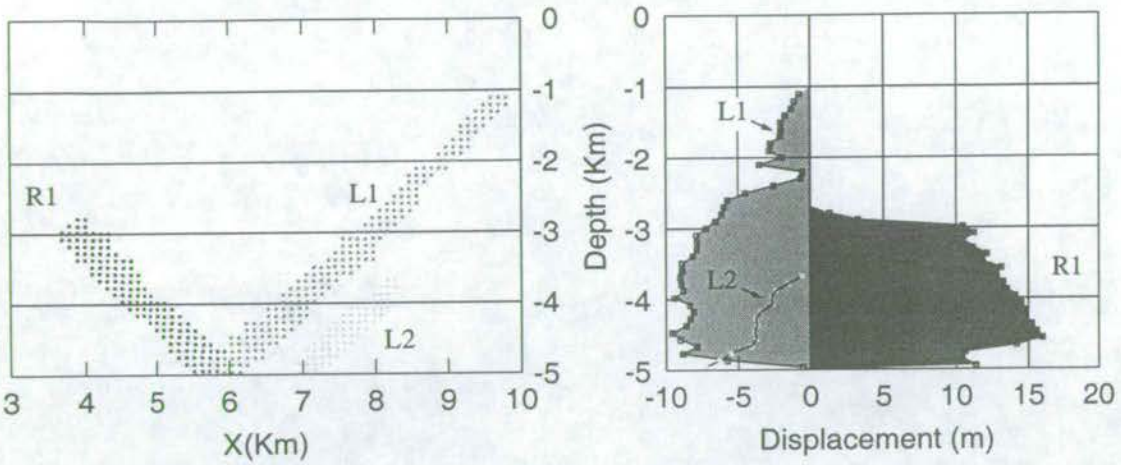

Figure 5.13. Displacement on faults intersecting with the base of the model (snapshot from Experiment B at 1.8% total extension). Map pattern on the left, displacement profiles on the right. Fault L1 is shown earlier in its development in Figures 5.11 and 5.12.

they too nucleated at the base of the model. This is because the displacements on the two oppositely-dipping structures "cancel-out".

The presence of two sets of faults in the models also leads to another form of interaction: X-shaped intersections or "hour-glasses" in the terminology of Nicol *et al.* (1995). In ADELI, structures in this geometry do not "lock-up", but continue to accumulate displacement (Figure 5.14) as the whole model is extended. This is consistent with contemporaneous movement on conjugate fault zones in sand-box models observed by Horsfield (1980). Displacement profiles for X-shaped intersections in the model compare well with those measured on natural faults in similar geometries for example Figure 5.15 [after Watterson *et al.* (1998)]. Displacement gradients on fault surfaces cause strain in the surrounding rock volume (Barnett *et al.* 1987). High displacement gradients at the point of intersection can be accommodated either by horizontal extension or by volume loss in the rocks close to the intersection (Nicol *et al.* 1995). Odonne & Massonat (1992) present an example of an X-shaped intersection in a layered carbonate sequence and show two possible restorations of the undeformed geometry (reproduced in Figure 5.16). In their first restoration, faults blocks were considered to be rigid and voids remained along the fracture surfaces. In the other, they allowed strain within the layers, which produced voids along bedding planes, implying volume loss in the fault blocks (either by compaction or solution) during fault slip. Porosity loss associated with compaction at X-shaped fault intersections has been documented in chalk (Koestler & Ehrmann 1991) and sandstones (Gabrielsen & Koestler 1987). The pattern of volumetric strain around an X-shaped intersection in an ADELI simulation is shown in Figure 5.17. To correct for compaction, the area of each element was normalised to the mean area of elements in its row. The relative velocities of

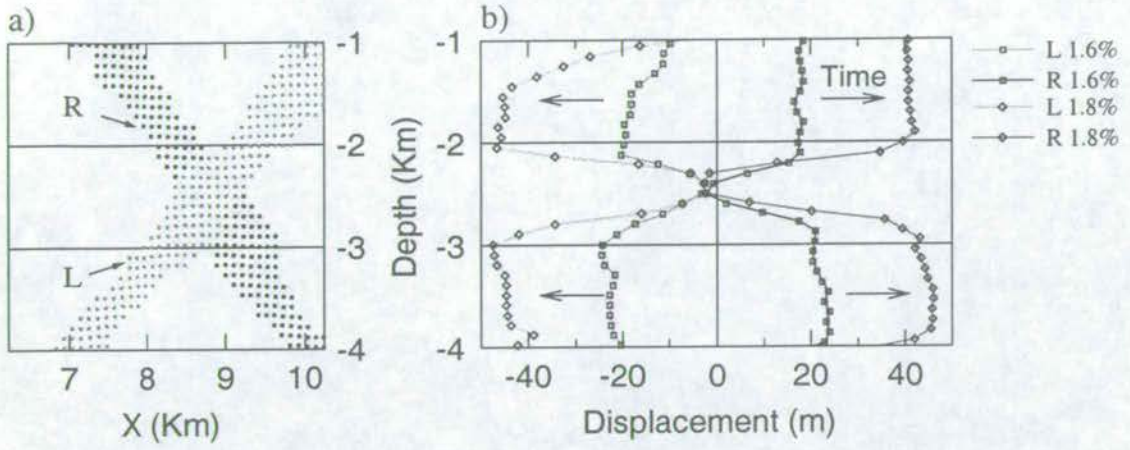

Figure 5.14. Displacement on faults intersecting in the middle of the deforming layer. a) Snapshot of the map pattern at 1.6% total extension in Experiment B, adjacent to the moving right-hand wall. b) Displacement profiles on R and L at 1.6% and 1.8% extension.

the blocks surrounding the intersection have the same pattern as those inferred by Odonne & Massonat (1992) from their second restoration (Figure 5.18). However, in my simulation, the zones that experienced the largest relative area loss near to the X-shaped intersection do not occur in the fault blocks but in the fault zones themselves. This suggests that, in nature, low porosity blocks will not necessarily be found near an X-shaped fault intersection if there is a mechanism for transporting material from the fault zone itself.

5.2.4 Saturation

At 1.6% extension, continuous faults first span the entire thickness of the layer and the system achieves a saturated state [sensu Wu & Pollard (1995)]. After this point, fault blocks largely cease to rotate and instead move by translation (Figure 5.7). Faults in the two experiments begin to behave differently after this time. In Experiment B, there are no more nucleation or linkage events, but faults with a range of sizes remain active (see right-hand panel of Figure 5.3). In Experiment A, a large, new, right-dipping structure emerges by linking several small faults, and only the very largest structures remain active (see left-hand panel of Figure 5.3).

This difference in behaviour rests upon the fault geometries in the two experiments. The moving wall is required to remain vertical, and so the movement on the active faults must be kinematically compatible with this imposed boundary condition. The isostatic boundary condition at the base concentrates deformation onto faults adjacent to the moving wall as time goes on. In Experiment B, a pair of conjugate faults, compatible with the imposed irrotational side wall, formed adjacent to the moving wall. In Experiment A, a synthetic array of faults

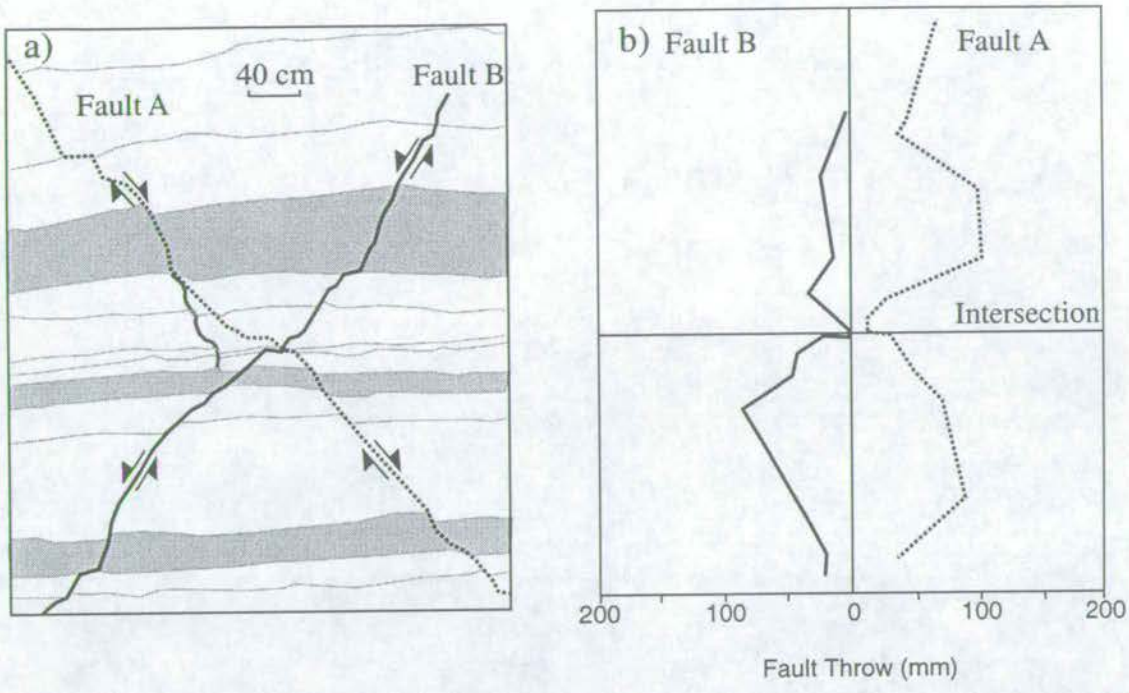

Figure 5.15. Example of conjugate faults in nature forming an X-shaped intersection. Reproduced from Watterson *et al.* (1998). a) Conjugate faults in chalks and marls. b) Throw profiles for Faults A and B.

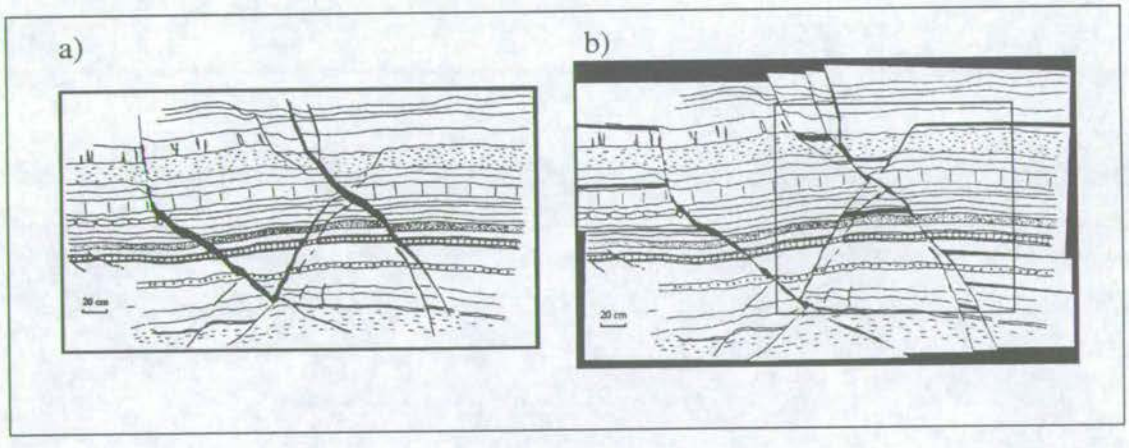

Figure 5.16. Restorations of an X-shaped intersection, after Odonne & Massonat (1992). a) Fault blocks assumed to be rigid. b) Fault blocks assumed to deform (Figure 5.17 zooms in on the structure within the box). Solid black areas areas indicate voids produced during restoration. Voids on a restored section indicate poor restoration or areas that experienced volume loss during deformation. Odonne & Massonat (1992) preferred restoration b) and the displacement field associated with this restoration is reproduced in Figure 5.18.

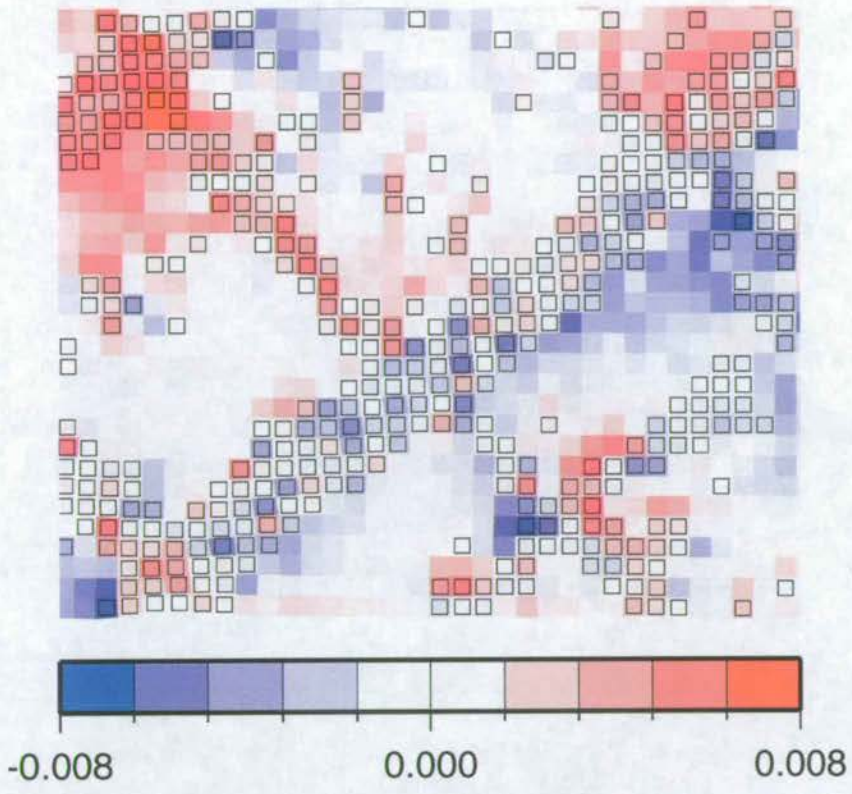

Figure 5.17. Volumetric strain in the blocks adjacent to an X-shaped fault intersection (snapshot from Experiment A at 1.6% total extension). Broken elements are outlined, blue elements are relatively compressed, red areas relatively dilated.

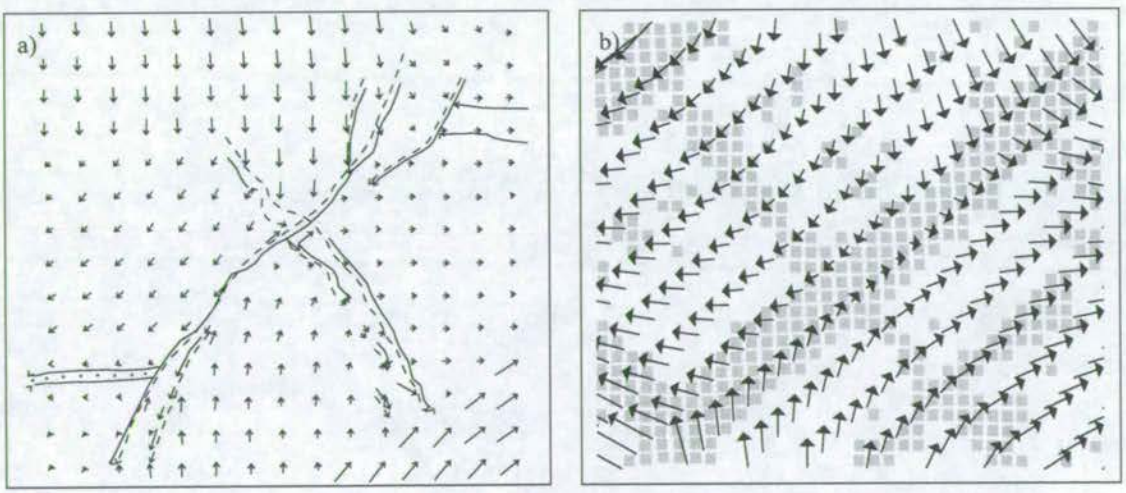

Figure 5.18. a) Displacement vectors of fault blocks near the natural X-shaped fault intersection shown in Figure 5.16. Displacements inferred from restoration b) in which fault blocks were not rigid. The final positions (continuous lines) and the reconstructed original positions (dashed lines) of the faults traces are also shown. Reproduced from Odonne & Massonat (1992), and reflected to aid comparison with b). b) Displacement from the undeformed state of mesh nodes near to the X-shaped intersection shown in Figure 5.17.

developed nearest to the wall. As deformation began to focus towards the moving wall, the faults in Experiment A had to rearrange to accommodate the non-rotation of the moving wall, but in Experiment B, no rearrangement was necessary.

5.2.5 Macroscopic stress-strain behaviour of Experiments A and B.

So far, we have looked in detail at the modes of fault growth and some quite specific fault geometries that spontaneously developed in ADELI simulations. Now, let us consider how the behaviour of the system as a whole changes during the faulting process.

The stress-strain response of a system depends not only on the mechanical behaviour of the material (softening or hardening) but also on the geometry of structures and on the boundary conditions of deformation. For example, Hobbs *et al.* (1990) present a numerical model of a material whose stress-strain behaviour is strain-softening in unconfined uniaxial compression but strain-hardening in constrained, constant volume compression. McKinnon & Garrido de la Barra (1998) coined the term "kinematic hardening" to describe the increase in the bulk strength of a system that results from interaction of fractures with restraining boundaries. The interaction of fractures themselves may also generate a form of kinematic hardening. For example, imagine a situation where extension is accommodated by conjugate faults. As time goes by, more energy is required to maintain the deformation rate not because the fault zone material is strain-hardening, but because more energy is needed to damage the rocks around the intersections as well as to produce slip on the faults. Wojtal & Mitra (1986) document a similar phenomenon in thrust belts, where the rocks in the fault zones themselves (foliated cataclasites) are softening, but the whole system is hardening because slip from flats onto ramps requires the internal deformation of the overriding thrust sheet.

Figure 5.19 presents the average extensional stress (σ_{11}, corrected for elastic stresses caused by the overburden) on the moving wall for Experiments A and B. As the material properties and boundary conditions are identical, differences in the mechanical response of the system must be due to the different pattern of faulting. The behaviour is identical in the two experiments until 0.8% extension. At this point, elements begin to fail and the material is no longer elastic. Stress continues to increase as the nucleation front spreads across the material until, at 1% extension, large faults begin to develop at the base of the model. In both runs the bulk stress decreases until 1.6% by which time the small structures are mostly inactive (Figure 5.3), nucleation has largely ceased (Figure 5.2) and strain is being accommodated by the larger structures. At 1.5% regional extension, the stress on the sidewall in Experiment A is lower than that in

Experiment B. This suggests that it is easier at this stage to accumulate displacement on the synthetic shears zones that have developed in A than the crossing conjugate shear zones in B. However, after 1.5% extension, both simulations show a renewed increase in strength (system hardening) because, in order to grow, the large faults must break all the elements adjacent to them; both weak and strong. The hardening is more pronounced in Experiment A as a result of the development of the new conjugate fault near to the moving wall.

5.2.6 Size cumulative frequency data

Figure 5.20 shows the fault size cumulative frequency data for the two simulations. The curves for both runs show many similarities, but there are also differences, which can be linked to fault behaviour. Dealing first with the similarities, at low strains, the majority of faults are active (Figure 5.21) and power laws characterise the size frequency distribution. In the 0.5% strain following the first appearance of faults, the power law exponent sharply decreases as strain increases (in A, $c = 1.25 \rightarrow 00.70$, in B $c = 1.24 \rightarrow 00.78$). This decrease results from localisation of strain onto the largest structures and also from the coalescence of structures, which increases the size of some structures while lowering the total number of faults (Figure 5.2). This trend agrees with the predictions of other numerical (Sornette & Davy 1991, Cowie *et al.* 1995) and geometrical (Cladouhos & Marrett 1996) models of fault growth and is consistent with the analogue modelling results of Sornette *et al.* (1993) and Ackermann *et al.* (2000).

At higher strains, for both experiments, the size distributions on log-log axes have three distinct segments: the smallest structures describe a straight line with a steep gradient, the intermediate structures possibly follow a straight line with a lower gradient and the very largest structures describe a convex-up curve. Note that both active and inactive structures contribute to the size frequency distribution of the whole population. In these experiments, I consider a structure to be active if the plastic strain has increased in any of its elements in the last time step. The transition from the simple power law distribution to the three segment distribution is not abrupt but gradual, though is clearly underway by 1.6% extension, when faults first span the entire thickness of the layer. By this time, most small faults have become inactive (Figures 5.3 and 5.22). The size distribution of these inactive faults hardly alters subsequently with time: changes only occur when small faults are removed from the population as they become part of a still-active, larger structure. Thus, the size frequency distribution of these faults retains a power law form, with a slope similar to that which described the whole population at the time when the smaller faults started to become inactive. By contrast, the distribution of the active structures makes a gradual transition from a power law form (straight line on log-log

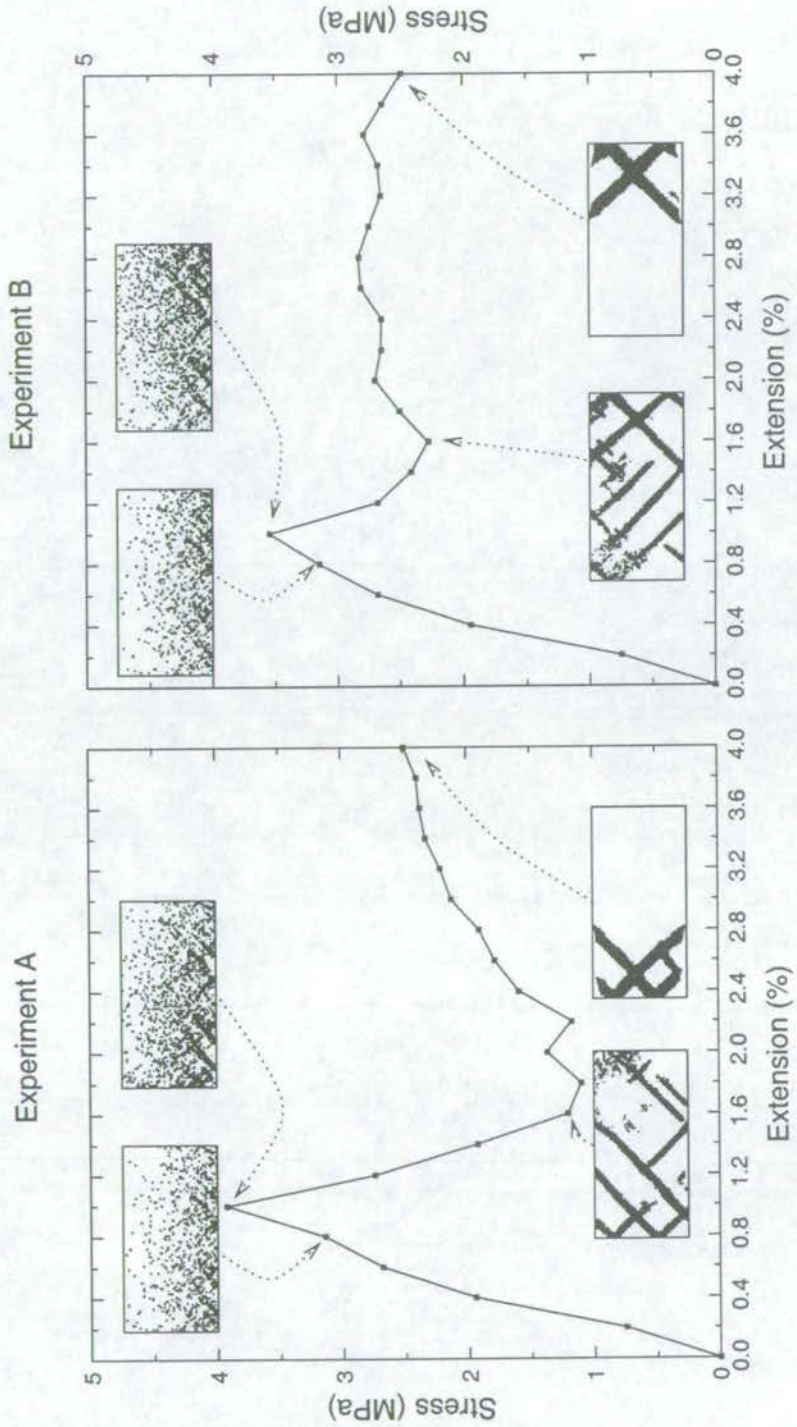

Figure 5.19. Mean extensional stress on the moving side wall (σ_{11}, corrected for elastic stresses induced by overburden) versus extension curves for Experiments A and B. Insets show the active elements at the times indicated.

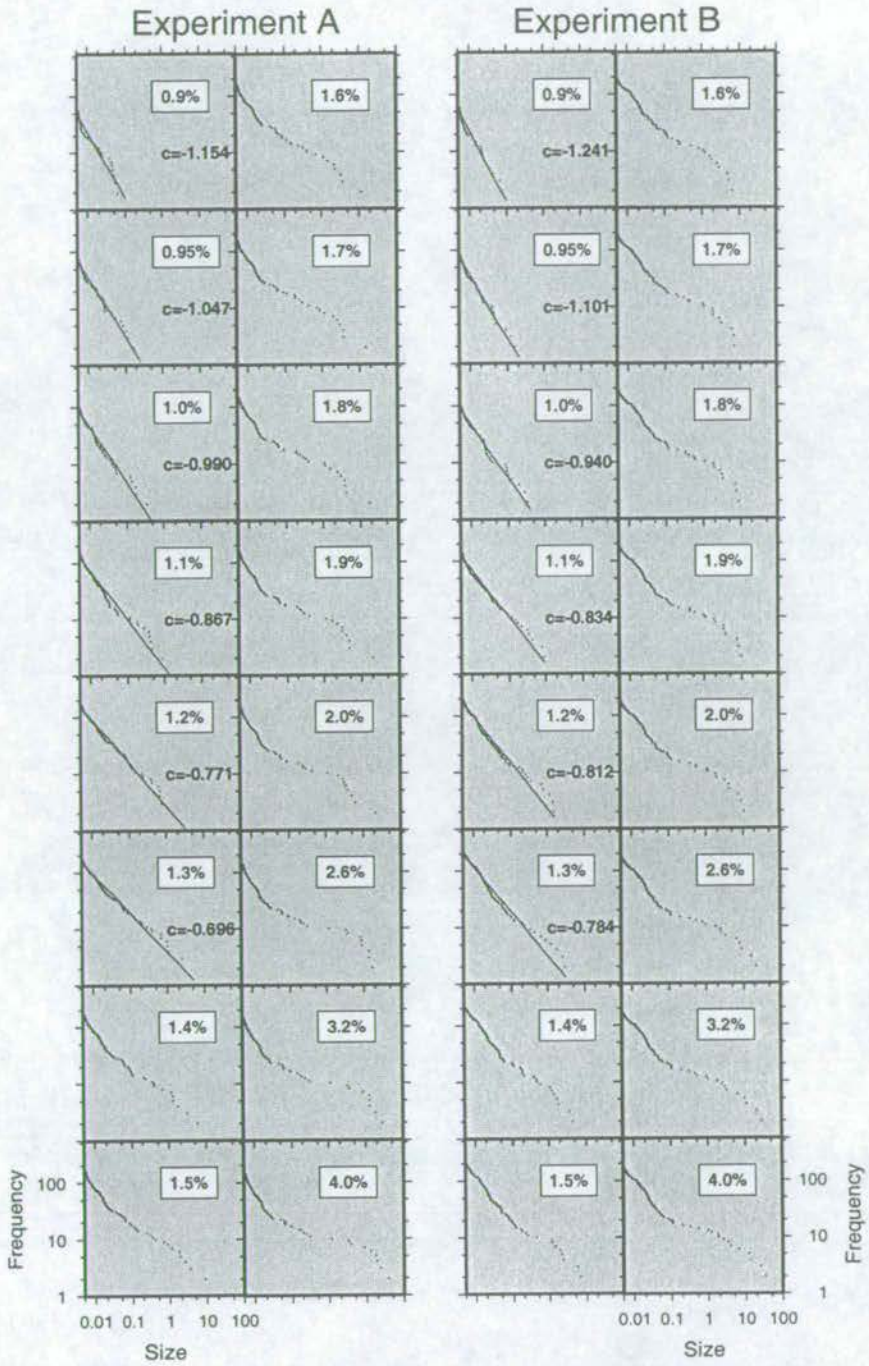

Figure 5.20. Size (total plastic strain - this measure of fault size is described in detail in Section 4.3) cumulative frequency distributions for the two model runs. Distributions from 0.9% to 4.0% regional extension are shown. Best-fitting power laws (straight lines - determined using linear regression, see Section 4.4) and power law exponents are shown on the first 6 plots. All graphs are plotted on axes of the same scale.

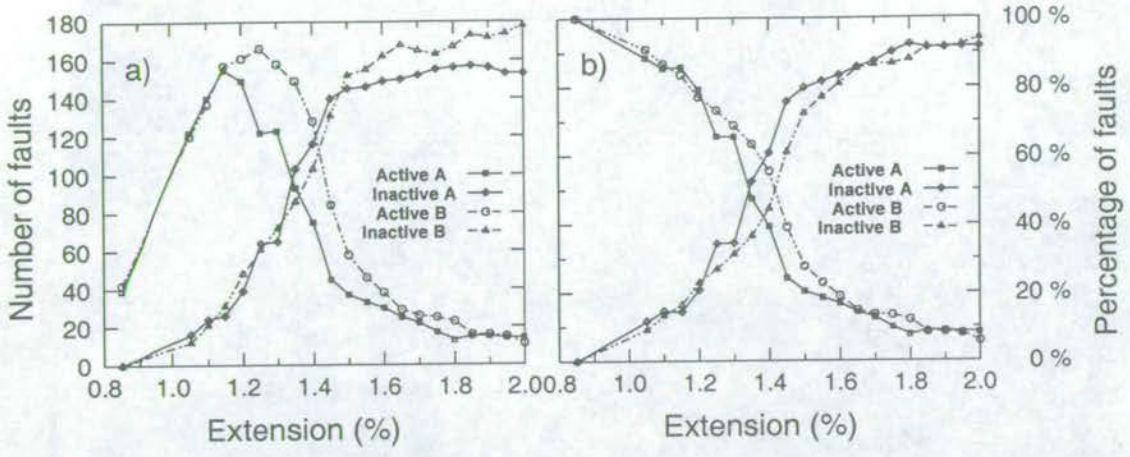

Figure 5.21. a) Number of structures and b) percentage of structures that are active and inactive in Experiments A and B. A structure is considered to be active if its total plastic strain has increased in the last 0.05% of regional extension.

axes, e.g. the populations at 1.4% regional extension on Figure 5.23 c and d) to exponential form (straight line on log-linear axes, e.g. the populations at 4.0% extension on Figure 5.23 a and b).

The two runs differ in the following ways. In the size distributions at the end of the two experiments (Figure 5.20), the small faults in Experiment A define a steeper gradient than those of Experiment B. This is a direct consequence of the spatial arrangement of the large faults, in place after only 1.2% extension in the two experiments. In Experiment B, major synthetic structures are evenly spaced across the model, with slightly larger fault blocks near to the moving wall. In Experiment A, the largest block occurs between two major synthetic structures near to the stationary wall. On the activity maps (Figure 5.3), after 1.2% extension, we see that activity is highest in the areas near to the moving wall. So, while the large fault blocks in Experiment A preserve a population of very small faults, the large blocks in Experiment B preserve a more evolved population with a wider range of sizes and lower slope on plots like Figure 5.20.

The size frequency distributions of intermediate and large-sized faults also show slight differences between the two experiments. A wider range of fault sizes defines the low-gradient segment of the size frequency distribution in Experiment A than in Experiment B and fewer faults define the curved distribution of the very largest faults. The behaviour of faults in the two experiments provides an explanation for these differences. In Experiment A, between 1.6% and 4% extension, the seven, large, interlocked segments adjacent to the moving wall rearranged themselves. No such rearrangement occurred in Experiment B and structures with

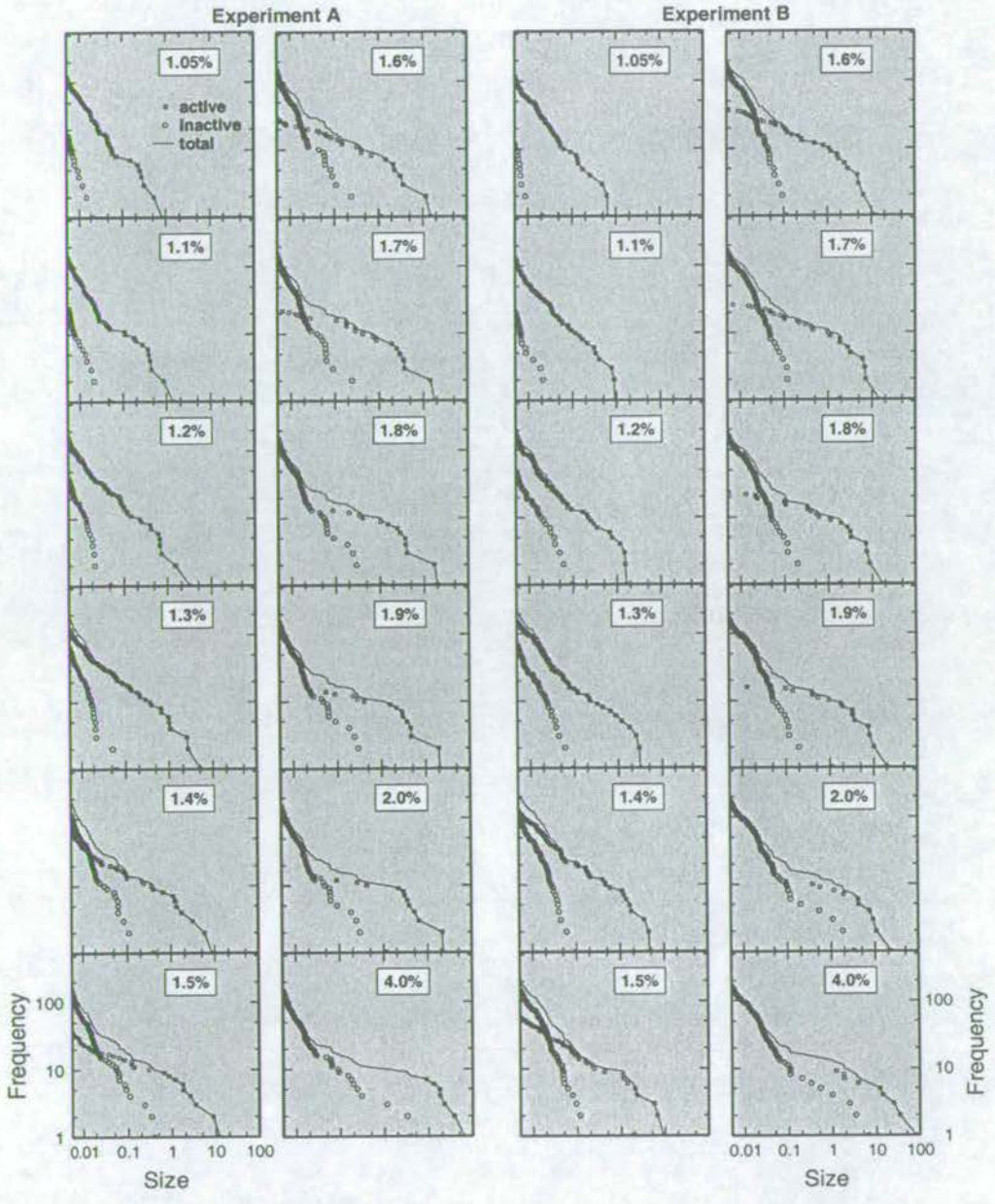

Figure 5.22. Size (total plastic strain) cumulative frequency distributions for the active and inactive populations in two model runs. All graphs are plotted on axes of the same scale.

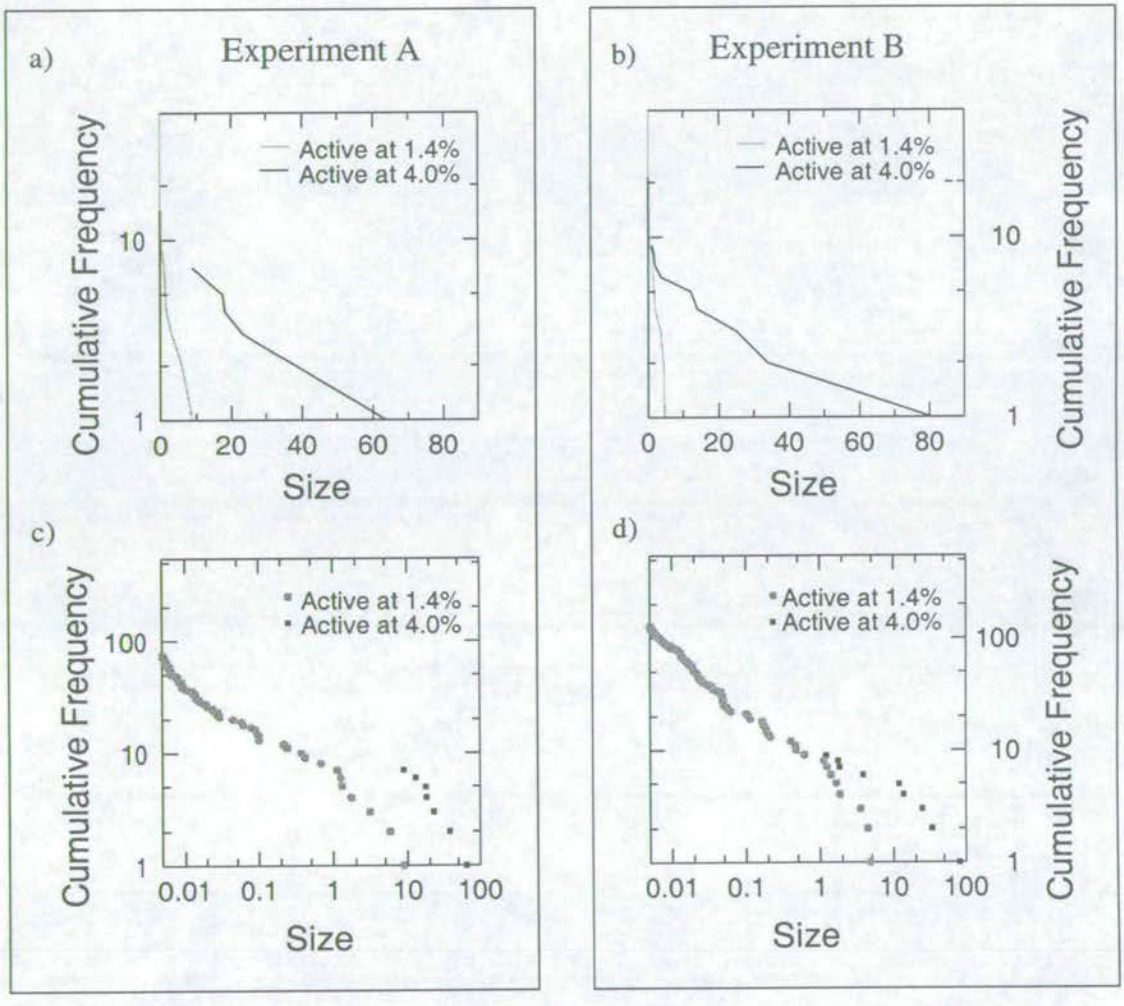

Figure 5.23. Size versus cumulative frequency for the active populations at 1.4% and 4.0% regional extension in a) Experiment A on log-linear axes, b) Experiment B on log-linear axes, c) Experiment A on log-log axes, d) Experiment B on log-log axes. Power laws plot as straight lines on log-log axes; exponential distributions plot as straight lines on log-linear axes.

a wider range of sizes continued to grow (this can be seen by comparing the active populations at 4% strain in the two experiments). In Experiment B, the size distribution shows the gradual localisation of strain onto the larger structures. The distribution for Experiment A reflects the channelling of almost all the available strain energy into growth of the new, conjugate fault (required by the irrotational boundary), leaving little to fuel the growth of other intermediate-sized faults.

5.3 Discussion of the Evolution of Modelled Structures

5.3.1 Comparisons with natural structures

It is fundamental to this study to assess which aspects of the modelled structures are realistic and which are not. This can only be done with reference to natural fault populations. However, it is often impossible to elucidate the evolution of a fault population by examining its present day appearance, so it is also important to compare the behaviour of this model with that of other physical and numerical models. ADELI is realistic in that features observed in nature such as horsts, grabens, and synthetic arrays or 'domino faults' all arise spontaneously in the model. It is also encouraging that modelled structures display a wide range of sizes and displacement profiles that resemble those found on faults in the field. Natural processes such as fault nucleation, growth, linkage, quiescence (inactivity) and fault-block rotation also feature in the model. ADELI is less realistic in that the dips of modelled faults are lower than typical values for natural, normal faults (45^o compared with 60^o). In ADELI, deformation initiates at the base of the deforming region. While some authors argue that failure is equally likely at all depth in the brittle crust (Cowie 1998a, Zoback & Healy 1984), others claim that faults nucleate at the free surface (Lin & Parmentier 1988) or at preferred depths (Scholz *et al.* 1993).

5.3.2 Dip direction of conjugate faults

There are two kinematically admissible modes of faulting by which a brittle layer can accommodate extension: domino style faulting and the formation of horst-graben features. Both styles of faulting have arisen in the simulations presented here, and both arise in nature. This prompts the question, what determines the style of faulting and, in the case of domino faulting, what determines the choice of dip direction? Suggested explanations can be divided into internal factors and external factors.

Dealing first with the internal factors: in an isotropic material at the point of failure, the two conjugate orientations for faulting are equally favourable, so we might expect equal numbers in each set. However, material heterogeneity or anisotropy might favour one over the other. Analogue experiments presented by Mandl (1993) p.117 support this argument. Where sand packs were built up from horizontal layers, no preferred fault orientation was observed. However, where the sediment was built up as dipping units, the resulting shear strength anisotropy favoured the development of faults synthetic with the dip of the sedimentary units. The geometry of the mesh is an internal factor in numerical experiments. The numerical simulations of McKinnon & Garrido de la Barra (1998) suggest that preferred fault orientations may be a mesh effect. In a regular, rectangular mesh, if one of the conjugate directions is closer to either of the grid axes, that conjugate set will be better developed. It is frequently cited (Barnichon & Charlier 1996, Belytschko *et al.* 1994) that the thickness of plastic shear bands is not determined physically, so shear zone thickness is inherently controlled by the mesh. The strain in a shear zone increases as its width decreases, so shear zones one element wide (the minimum possible) have the highest strain. Thus there is a biasing of the shear bands towards an alignment parallel to the grid axes, minimising width and maximising strain. In the ADELI experiments presented above, the grid orientation is unlikely to cause preferential development of one fault set, as the grid axes and the orientations of the principal stresses are coincident when failure first occurs. However, this effect could be significant for structures forming late in the simulation, when the grid is strongly deformed and the local stress field is often rotated (see Figure 5.10). Strong mechanical anisotropy is also an unlikely explanation for preferred dip directions in my experiments, as the material heterogeneity takes the form of random, uncorrelated noise.

Coming to the external factors, the analogue experiments of Freund (1974) suggest that it is the boundary conditions which produce domino-style faulting or horst-graben structures. When a block of clay was placed above an extending planar base, simultaneously-moving conjugate faults developed. He postulated that the planar shape of the extending base prevented "graben keels" from developing, frustrating domino-style faulting. The upper surface also influences fault development. Reches (1978) also emphasised the importance of boundary conditions. He showed from geometric and kinematic considerations that plane strain can be accommodated by just one fault set, but that irrotational plane strain requires two conjugate fault sets [Figure 7, (Reches 1978)]. His argument does not require equal numbers of faults with each dip direction, however, just that strain is equally partitioned between the two sets. Preferred fault dip can be caused by another external factor: non-uniform extension. Ishikawa & Otsuki (1995) found that asymmetry in their sand-box models of faults was strongly related to horizontal strain

gradients. They performed uniaxial extension experiments over a planar base and introduced horizontal strain gradients by placing the sandpile above a trapezoidal rubber sheet. They found a graben formed next to the moving wall, but faults synthetic to the extension direction developed elsewhere [a similar pattern to that which developed in Experiment B, above and in the experiments of Mansfield (Mansfield (1996), p.121)]. In experiments where both side-walls moved, they still report faults dipping towards the higher strain area (up the horizontal strain gradient).

In the experiments presented above, the distribution of variations in yield strength is the factor which most obviously determines whether a broken element will become a right-dipping or left-dipping structure. Thus if we look at the fault map at 1% extension, we see that very weak elements which form the nuclei of left-dipping structures in Experiment A also form the nuclei of left-dipping structures in Experiment B. The same is true of right dipping structures. However, as deformation proceeds, the number of elements in synthetic faults out-strips the number in antithetic structures. Strain gradients as postulated by Ishikawa & Otsuki (1995) seem to be a plausible explanation for this behaviour.

5.3.3 Fault activity and size distributions

It is often difficult and sometimes impossible to determine the pattern of activity in a fault population by looking at its present day expression. Numerical and physical models of fault growth are especially valuable in this regard, as they enable us to combine information on fault properties with information about growth histories. Of the existing models of fault growth in a brittle layer above a ductile substrate, few have examined the fault population statistics in cross-sectional view. The analogue modelling study of Fossen & Gabrielsen (1996) is one of these few. Figure 5.24 is a reproduction of Figure 7 from Fossen & Gabrielsen (1996), on which I have highlighted faults (identified by the authors) that have appeared (red), grown (green), linked (thick black) or become inactive (purple) since the last snapshot. Almost certainly there were faults in the plaster that are not marked on the figure (at several places marker horizons are displaced without a fault being marked). Despite such inaccuracies, it is clear that in this plaster model, as in my ADELI simulations, linkage of synthetic faults down-dip is not the dominant growth mechanism at any time (although Mansfield & Cartwright (1996) suggest that fault linkage down dip may be as common as linkage along strike). This plaster model and my ADELI simulations are also similar in that, in both models, faults can easily be divided into those contained within blocks and those that define blocks. In both models the largest structures are always active. However, there are also differences between the behaviour of faults

in the two models: for example in the plaster experiment, strain is not so strongly concentrated next to the moving wall and faults that have experienced a period of quiescence are sometimes reactivated. The size cumulative frequency distributions for faults in three plaster models are shown in Figure 5.25 (after Fossen & Gabrielsen (1996)). The distributions do not show the break in slope between small and large structures seen in my ADELI simulations. However, vertical lines of points (steps) and roll-overs at small fault sizes on Figure 5.25 indicate that small faults (perhaps as much as 3/4 of the total fault population) are poorly resolved. In common with my ADELI simulations, the large, layer-spanning faults describe a curve, not a straight line on log-log axes. This curve is most pronounced in Run 3, where metal plates at the interface of the plaster and barite layers localised the regional strain onto particular structures.

The numerical modelling study of Finch (1998) also presents fault growth in cross-section. However, for a number of reasons it is difficult to compare results from this model with those from ADELI. In Finch's (1998) code the brittle layer is made of discrete particles (with an average diameter of 1 km) connected by elastic bonds and faults are defined by lines of broken bonds (Figure 5.26). The 16 rows of elements in this model give a very coarse resolution for measuring fault lengths. Also, the scale of deformation in the simulations presented above (5 km x 10 km) is quite different to that used by Finch (1998) (35 km x 260 km). Conjugate structures arise in both models, but, in the discrete element model, small faults (lengths $< 25\%$ of the layer thickness) within fault-bounded blocks are rare. No mention is made of faults becoming permanently inactive by Finch (1998), although localisation of strain onto the largest faults is documented. The distribution of fault lengths in this model (Figure 5.27) shows a transition from power law to exponential form when faults begin to span the thickness of the layer, but no break in slope is evident.

The majority of analogue models that have studied fault activity and fault size frequency distribution have viewed the deforming region from above. This means that only structures that cut the upper surface of the layer can be studied. The population statistics, therefore, only reflect the behaviour of faults whose tiplines are not entirely surrounded by rock: small faults that are contained within the layer cannot feature in the population statistics. Three such analogue models are presented by Spyropoulos *et al.* (1999b), Ackermann *et al.* (2000) and Mansfield (1996). At 0.8 mm thick and > 10 cm long, the thickness (t) to length (l) ratio of the models presented by Spyropoulos *et al.* (1999b) is large at 1:125. Although still thin compared with this study that of Fossen & Gabrielsen (1996) (both have an initial t:l ratio of 1:2), the models presented by Ackermann *et al.* (2000) and Mansfield (1996) are considerably thicker: 1.8 cm or 3.6 cm thick and 12.5 cm long (t:l = 1:7 or 1:3.5) in Ackermann *et al.* (2000) and 4-5 cm thick and 14 cm long (t:l = 1:2.8-3.5) in Mansfield (1996). The layer

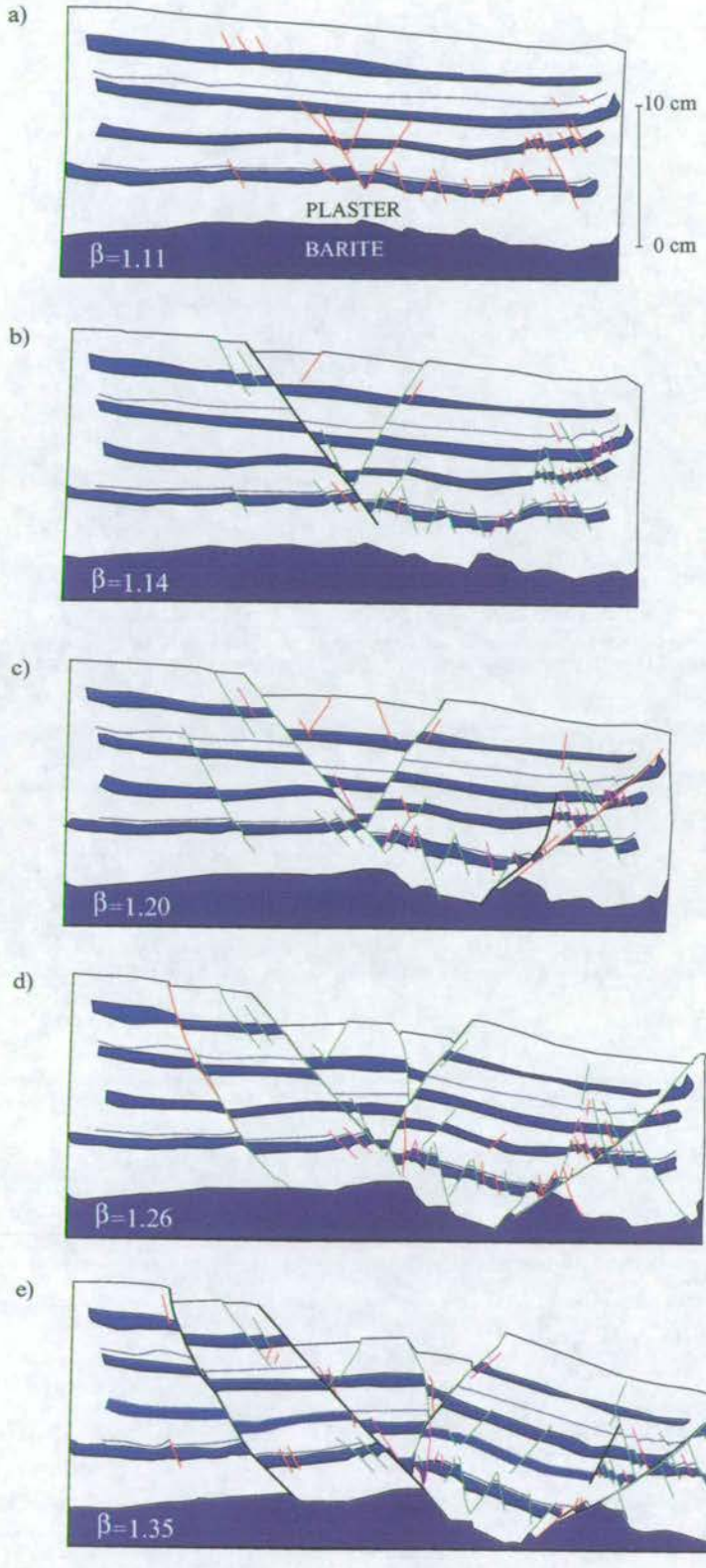

Figure 5.24. Wet plaster model of faults in cross-section, after Figure 7 of Fossen & Gabrielsen (1996). Faults are classified as having appeared (red), grown (green), linked (thick black line) or become inactive (purple) since the last snapshot. β = new length/original length of the model.

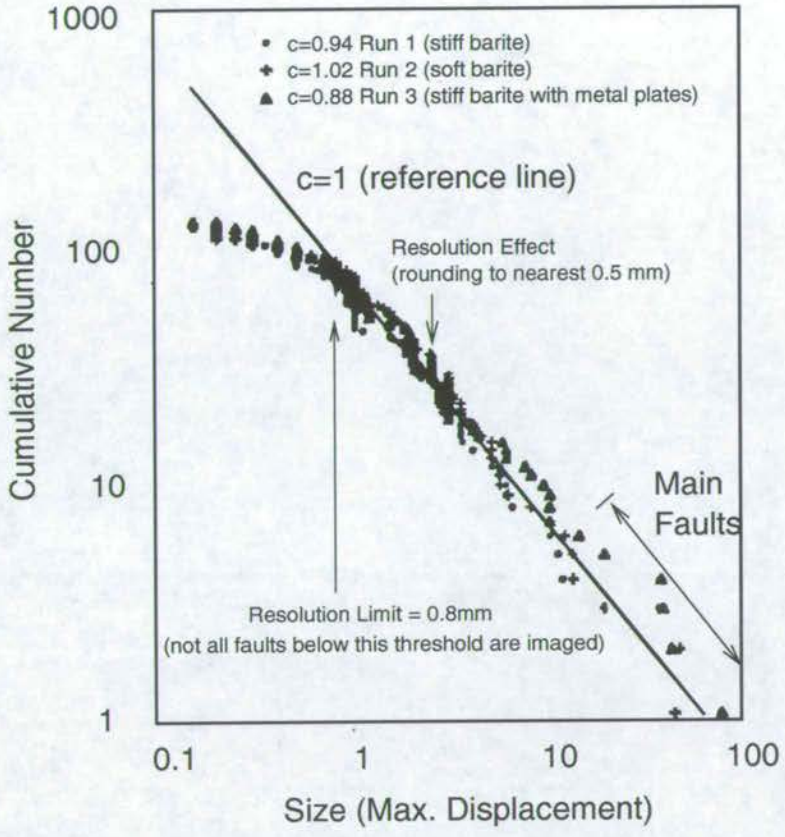

Figure 5.25. Size (displacement) frequency distributions from cross sections through wet-plaster models (after Figure 14 of Fossen & Gabrielsen (1996)). The faults generated in Run 2 is shown in Figure 5.24. The limited resolution of the measurement method causes a roll-over and steps in the distribution at small sizes.

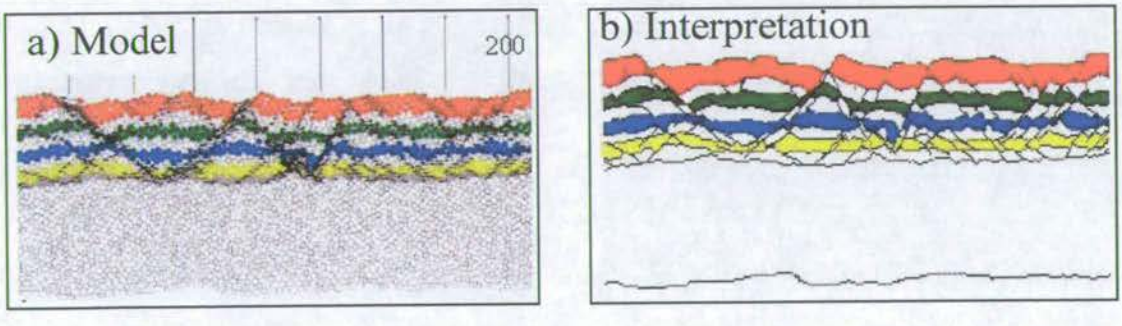

Figure 5.26. Discrete element model of faults in cross-section, after Finch (1998). Colours show elements that were initially in the same layer, black lines show broken bonds.

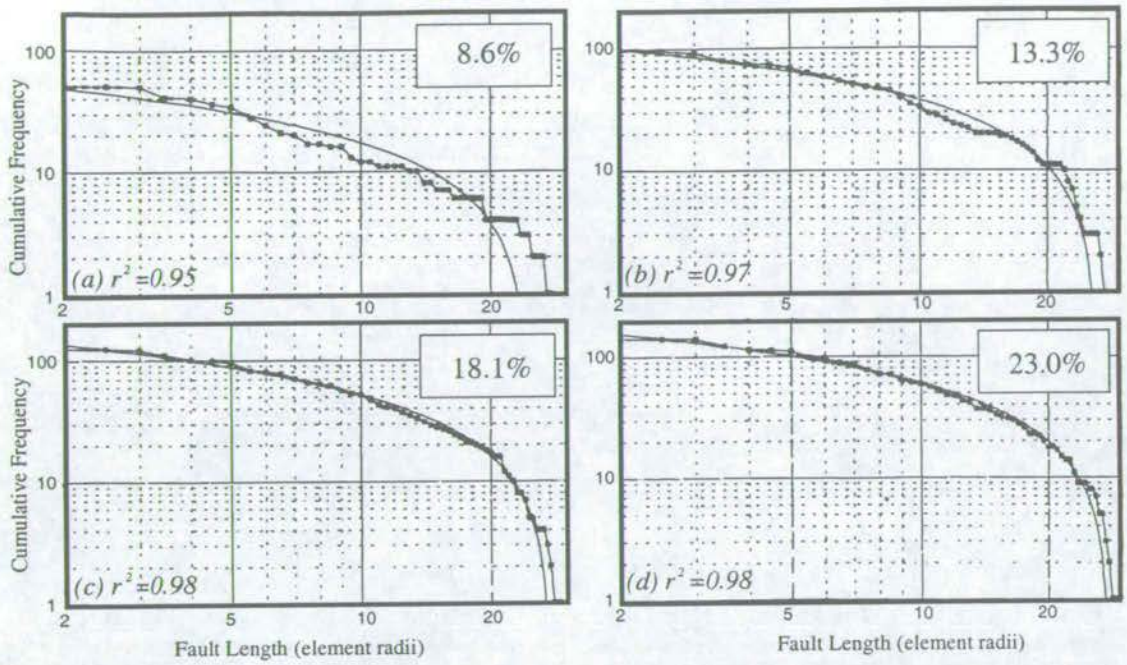

Figure 5.27. Length versus cumulative frequency distribution for faults in the discrete element model of Finch (1998) at 8.6, 13.3, 18.1 and 23.0% strain. There are clear discretisation effects (steps) and resolution effects (roll-over) at small length scales. Best-fitting exponential curves are also plotted. Increasing r^2 values indicate an improving fit.

used by Spyropoulos *et al.* (1999b) is so thin that even the smallest structures they could image (~2 mm) probably extended through the deforming layer. Both Ackermann *et al.* (2000) and Spyropoulos *et al.* (1999b) report a gradual transition from power law fault size frequency distributions to exponential fault size scaling. In Ackermann *et al.* (2000), the transition occurs when the length of the largest fault is comparable with the thickness of the layer and when faults start to coalesce. Spyropoulos *et al.* (1999b) also link the transition in scaling to a change in fault growth: it occurs as nucleation becomes rarer and coalescence becomes the dominant growth mechanism. In my simulations, it is only the largest, active structures that show the transition from power law to exponential scaling, whereas these authors claim that the entire population is exponentially distributed (although on Figure 4b of Spyropoulos *et al.* (1999b), faults in the smallest-sized bins follow a power law, not an exponential distribution). This apparent discrepancy might be explained by the fact that the inactive structures in my models - small faults and faults trapped within the layer - were not imaged in these experiments. This reasoning would also explain why Ackermann *et al.* (2000) see the emergence of exponential scaling when 80% of the faults are still active, compared with only 50% in my model: if small faults are removed from both active and inactive populations in an ADELI simulation, the percentage of active structures increases (Figure 5.28). Clifton *et al.* (2000) reports that the heaves on resolved faults accounted for as little as 30% of the imposed regional extension in their

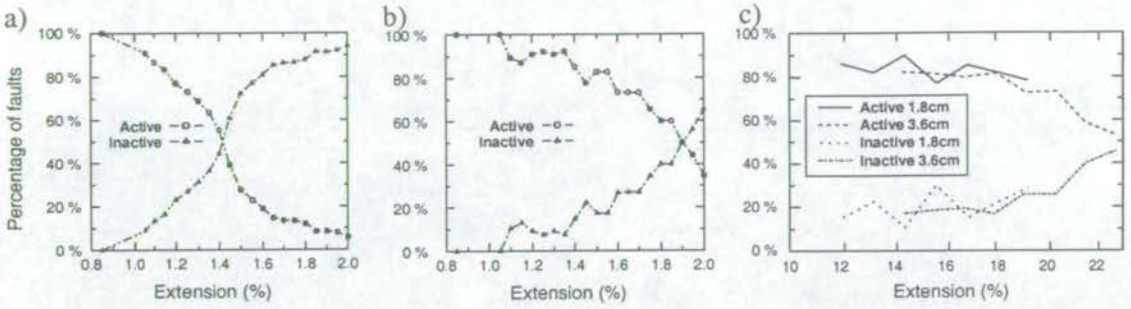

Figure 5.28. Proportion of active and inactive structures versus time for a) an ADELI run, b) an ADELI run where only large faults (total plastic strain > 0.05) are considered c) a wet plaster model, in which small faults contained within the layer are not imaged [after Ackermann *et al.* (2000)]. The relative number of active structures is increased at lower resolution.

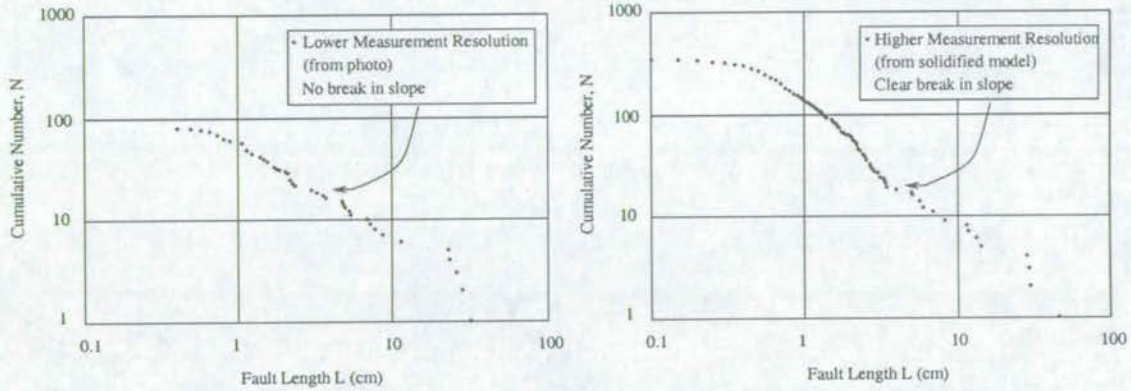

Figure 5.29. Measurement resolution effects in fault trace length cumulative frequency distributions, after Mansfield (1996). The higher-resolution method (right hand plot) shows a break in scaling between small and large faults not evident in the distribution generated by the lower-resolution method (left hand plot).

plaster models. The poor resolution and consequent paucity of small, intra-block faults in Finch (1998) might also explain why a fossil population of inactive, power law distributed faults is not evident in these simulations. The fault populations of Fossen & Gabrielsen (1996) (Figure 5.25) do not show exponential scaling at all, possibly because these population experienced a second phase of fault nucleation and small-fault activity associated with the internal deformation of rotating blocks. This large-strain phenomenon does not feature in the models of Finch (1998), Spyropoulos *et al.* (1999b) or Ackermann *et al.* (2000). Mansfield (1996), using experimental apparatus very similar to that of Fossen & Gabrielsen (1996), also found no transition to exponential length scaling. Mansfield (1996) measured fault trace lengths from photos of the upper surface of the model taken during the experiment [a measurement technique also used by Spyropoulos *et al.* (1999b) and Ackermann *et al.* (2000)] and also made higher resolution measurements of fault trace lengths on the upper surface directly after the model had solidified (Figure 5.29).

Fault size frequency distributions with "faceted" forms are a feature of both runs, and have been documented in natural fault systems by Wojtal (1994, 1996), Ackermann & Schlische (1997) and Fossen & Rørnes (1996). The distribution presented by Ackermann & Schlische (1997) has a "concave upward" form, with small faults defining a steep slope and the large structures a shallower slope. The distribution was generated by measuring trace lengths in map view [two-dimensional sampling, or $s = 2$ in the terminology of Marrett & Allmendinger (1991)]. The fault population itself consists of two sub-populations: master faults, which span but do not breach mechanical layers, and minor faults, which are contained within the layers and do not intersect the boundaries. The faults are small (most have lengths less than 1m) and normal. Ackermann & Schlische (1997) attribute the difference in power law exponent of the two sub-populations to the geometrical dimension (f) of the space they occupy: for master faults $f = 2$, whereas for small faults $f = 3$. Marrett & Allmendinger (1991) predict that the power law exponent for $f - s = 1$ (minor faults) will be one plus the power law exponent for $f - s = 0$ (major faults). However, Ackermann & Schlische (1997) concluded from the spatial distribution of the fractures that the minor faults are younger than the major faults. In this case another explanation presents itself: that the minor faults show a high exponent because they have had little time to link with each other.

The distributions presented by Wojtal (1994) have a "concave downward" form, with small faults defining a shallow slope and the large structures a steeper slope. These distributions were generated by measuring Dmax in map view. The faults in this study are large (displacements from centimetres to hundreds of metres) and form compressional duplex structures. Again, the faults used to compile these data fall into two sub-populations: large, block-defining faults and smaller faults within the thrust-bounded blocks. Wojtal (1994) states that the size distributions for the two sub-populations have different slopes because the faults behave differently through time. In Wojtal's (1994) model, strain is distributed among structures of all sizes while the duplex is forming, but after duplex formation, strain is focused onto the block-bounding faults. He argues that the slope of the size distribution for faults within the blocks decreases through time, because they continue to grow but few new faults form. By contrast the slope of the distribution for block-bounding faults increases through time, he argues, because these structures have slightly different displacements at the onset of duplex formation, but each accumulates displacement at the same rate once the duplex has formed.

The fault size cumulative frequency distributions presented by Fossen & Rørnes (1996) also show two distinct slopes on log-log axes. The distributions were generated by measuring the throw on several seismic lines and combining the data (Walsh *et al.* (1994) discuss this method in detail). Walsh *et al.* (1994) warn that faceted size frequency distributions can arise using

this method if there are two sets of faults with different strikes and sample lines are only perpendicular to one set. However, Fossen & Rørnes (1996) took profiles perpendicular to both the major N-S faults and the minor E-W faults, so under-sampling of faults oblique to the profile direction is not the cause of the break in slope reported in their study. Within a sub-region of their study area (a set of domino fault blocks), Fossen & Rørnes (1996) found that the break in slope on the size distribution coincided with the maximum throw observed on minor intra-block faults. Elsewhere, they found that, if faults were divided into sub-populations on the basis of their strike direction, the size cumulative frequency distributions for the sub-populations defined power laws with different exponents.

The various mechanisms for generating discontinuous size cumulative frequency distributions are presented in Figure 5.30. Do the explanations presented by previous workers account for the faceted size frequency distributions exhibited by structures in my models? Size is measured in ADELI simulations as the summed plastic strain for the whole structure, not the throw at the point where a profile crosses the fault, so the explanation given by Walsh *et al.* (1994) cannot apply. Although all structures in my models occupy two dimensions, Ackermann's (2000) argument based on dimensionality is still relevant in the sense that the growth of large faults in the model is restricted, unlike the growth of small faults. In my model, small faults can grow by breaking elements from beyond the tips (lengthening) or elements to either side of the failed zone (thickening), whereas faults that span the entire layer thickness or abut conjugate structures at both ends can only thicken with time. Wojtal's (1994) conceptual model of fault growth also linked different fault growth mechanisms with faults at different scales, and emphasised the idea that the different growth mechanism of large faults would localise strain on these structures. Strain localisation is clearly a feature of ADELI simulations too, though I would propose a further explanation. The key to understanding the faceted distributions of Figure 5.20 lies in the realisation that they consist of both active and inactive structures (Figure 5.22) and that the most common mode of growth (propagation of one tip, propagation of two tips, linkage/coalescence, increasing displacement without lengthening) changes through time. Different growth modes lead to different scaling properties, thus the size distribution of the largest (mostly active) faults is not continuous with the distribution of the smallest (mostly inactive) structures. While size frequency distributions like those of Figure 5.22 resemble those for cluster size in systems above the percolation threshold (see Stauffer & Aharony (1994), Figure 16, p.68), the observed transition is gradual, not abrupt, so it is difficult to classify this behaviour as a classic cross-over phenomenon in the terminology of percolation theory. Given a map of natural faults, one would not necessarily be able to identify those that were most recently active from those that switched off early in the deformation episode.

My findings suggest that it would be inadvisable to extrapolate scaling laws based on large, long-lived structures to small, possibly inactive structures nearby, even if they formed during the same extensional event.

5.4 Summary

In this chapter, I presented two experiments that had the same boundary conditions and the same material properties. Differences in the behaviour of the two experiments, and consequently the size frequency distributions, stemmed solely from the spatial arrangement of weaknesses within the mesh. Variations in yield strength determined where failure would initiate and, crucially for these two experiments, whether nearby elements would break to form synthetic or antithetic structures. The importance of the spatial arrangement of weaknesses is discussed further in Chapter 6.

The yield strength distribution in space had the greatest effect on the fault population at low strains, but the imposed irrotational boundary condition proved to be critical at higher strains. Where the major structures formed a conjugate set, the existing faults were able to accommodate the imposed boundary condition. This was not the case in the experiment where the major faults formed a domino array, and a new antithetic fault was forced to grow, resulting in strain-hardening of the whole system, despite the fact that individual elements were strain-softening.

Fault size cumulative frequency distributions changed from power law at low strains to a more complex forms at higher strains, with small faults defining steep slopes on log-log axes, intermediate-sized faults shallower slopes and large, layer-spanning faults defining curves. Small, intra-block faults that became inactive relatively early in the deformation explain the steeply-sloping section of each distribution. The relatively low slope of the intermediate-sized structures reflects the accelerated growth of larger structures due to strain localisation caused by softening. The curved size distribution of the largest faults can be fitted with an exponential relationship between size and cumulative number. The change in scaling from power law to exponential is related to the change in growth mechanism (from lengthening plus widening of the shear zone to widening alone) when the tips of large faults can no longer propagate due to interaction with other structures or with the edges of the deforming region.

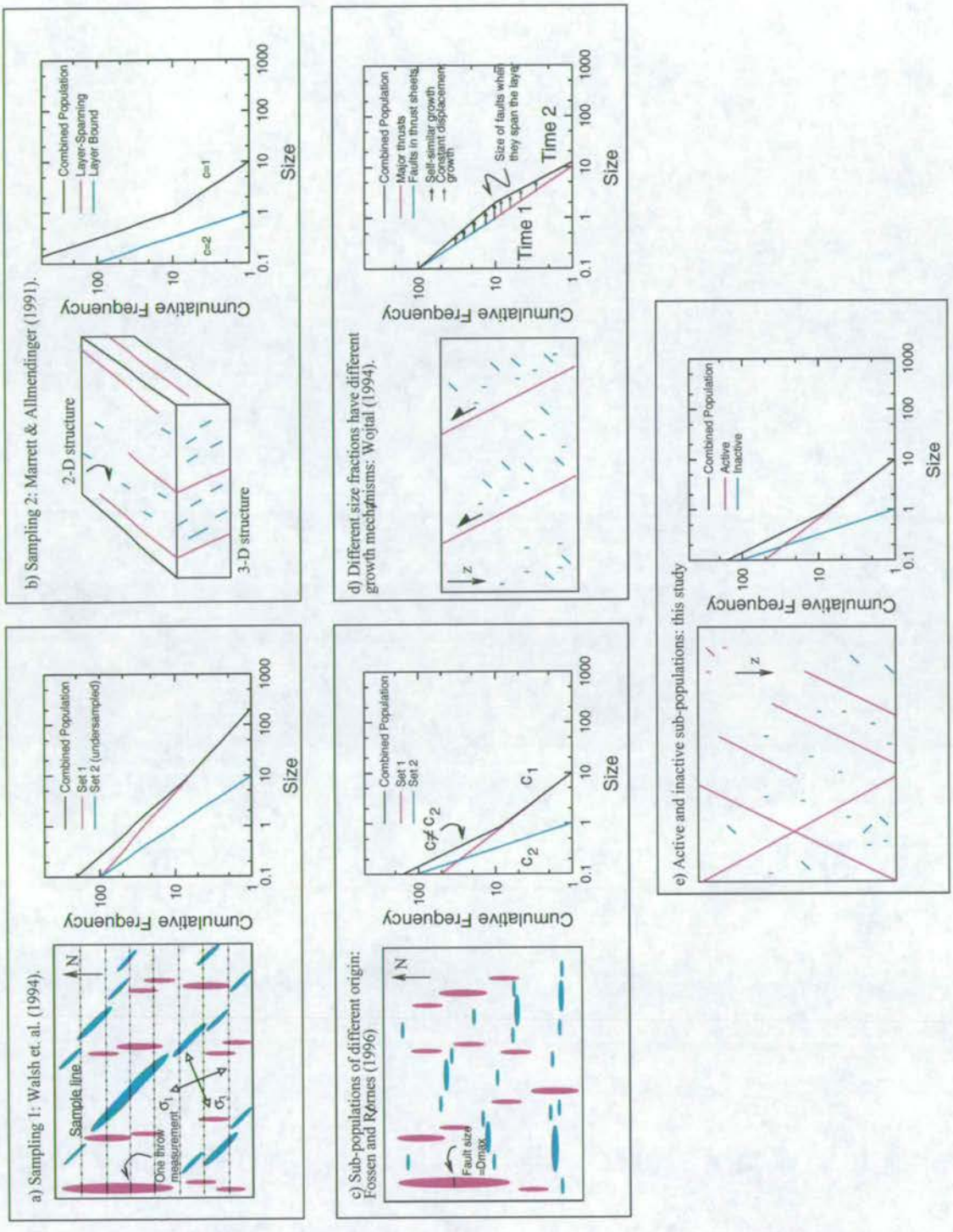

Figure 5.30. Summary of the different mechanisms for generating discontinuous size frequency distributions. Suggested explanations include sampling problems (a and b), combining faults from different tectonic episodes (c) and combining faults with different growth mechanisms (d). This study suggests that combining the active and inactive fault population might be another cause of discontinuous size cumulative frequency distributions (e).

Chapter 6

Experiments Varying Internal Fabric

The aim of this chapter is to investigate how the internal fabric influences fault growth and consequently fault scaling properties. The internal fabric of a deforming material is defined by the rheology and the heterogeneity. I show that different behaviour (e.g. growth by coalescence, deactivation of small faults, localisation of strain onto the largest structures) can be favoured by varying the distribution of yield strength and the amount of softening. I also present experiments in which different fault patterns and size frequency distributions arise from the deformation of samples with statistically identical material properties

6.1 Outline of the Experiments.

The pattern of fault growth is affected by the internal fabric (rheology plus heterogeneity) of the deforming material. In the case of a Von Mises material the rheology can be specified by two elastic parameters (Young's modulus and Poisson's ratio) and three plastic parameters, namely the yield strength, the strength loss on failure and the strain over which that strength loss is accomplished. In a heterogeneous medium, the rheological parameters are not the same throughout the mesh, they vary from element to element. Heterogeneity can be described in terms of a frequency distribution which shows how many elements there are with the highest, mean and lowest values of the varying parameter. The experiments presented here investigate

the effect of varying heterogeneity in two plastic parameters: the yield strength and the stress drop on failure.

The results of a particular model depend on the frequency distribution of the strengths, the strength loss on failure and the spatial distribution of material properties (where exactly the strongest and weakest elements in the mesh are). To eliminate differences due to boundary conditions, all the runs presented in this chapter used the standard model set up with isostasy at the base of the model and just one moving wall. In the first set of experiments, the spatial arrangement of strengths was varied. In the second set, the amplitude of the heterogeneity (the range of strengths present in the model) was varied between the runs. In the third set of experiments, a single mesh with heterogeneous yield strengths was deformed, but the strength loss experienced by every element in the mesh upon failure was varied from run to run.

6.2 Varying the Spatial Arrangement of Heterogeneity

Four meshes were created by using different seeds (4067, 6007, 7177, 7817) in the random number generator. Each of these was reflected about its centre along a vertical axis, to generate a further four meshes. As the applied boundary conditions are asymmetric, deformations of a mesh and its mirror-image are not equivalent. The same strength distribution was used in each of the eight experiments: the mean strength was 275 MPa, the standard deviation 25MPa and the strengths followed a normal distribution over 3 standard deviations. Size frequency distributions were calculated (using total plastic strain as a measure of size, see Section 4.3) for all eight runs at write times 6-10, which correspond to 1%, 1.2%, 1.4%, 1.6% and 1.8% extension. This time interval covers the evolution of the population from first nucleation to the point where faults are beginning to span the full layer thickness. Power laws were fitted using linear regression (Section 4.4) in log-log space over the straight line section defined by the small to intermediate-sized faults.

Figure 6.1 shows the size cumulative frequency distributions resulting from these experiments. Some features are common to all runs, for example in each run there is generally a decrease in fitted c through time. Also, during the course of each run, size frequency distributions show a transition from a straight line in log-log space to a more complex form with one or more inflection points. However, there are also differences in the distributions produced by the different runs. For example, at any time, there is a range in the power law exponent shown by the distributions. The positions of inflection points also vary. Distributions from meshes

which are mirror images (for example n4067 and m4067 - mirror pairs have the same shading on Figure 6.1) are as different as distributions from meshes produced by different seeds: just by looking at the distributions, one could not identify those belonging to mirror pairs. For example, at time 8 model m7817 has the highest value of c of all eight runs (0.975 ± 0.0128) but its mirror mesh, n7817, has next to the lowest value (0.7518 ± 0.0096).

Figure 6.2 illustrates the pattern of broken elements within each simulation. In all runs, faults develop in the same way as in the two runs studied in detail in the previous chapter. That is, nucleation initiates at the base of the model, faults grow upwards by breaking the elements ahead of their tips or by coalescing with pre-existing structures and, with time, strain localises in the area closest to the moving wall. In all of the runs with different seeds, major structures have similar thicknesses and are spaced at preferred distances throughout the mesh. The failure patterns in the eight runs differ in terms of the relative numbers of major synthetic and antithetic faults and the precise spatial arrangement of the major structures. As discussed in Section 5.2.3, size frequency distributions are affected by the size of fault-bounded blocks and the spatial arrangement of the large structures. Large blocks containing many small structures can be seen towards the left hand side of model runs n4067 and n6007. Structures within fault-bounded blocks are largely isolated from the active fault population. The presence of such sub-populations within large blocks results in a break in slope between the small and intermediate-sized structures on Figure 6.1. This was discussed further in Section 5.2.3.

In runs m6007 and m7817, several large and intermediate-sized structures occur near to the moving wall, whereas in runs m4067, n4067 and n6007 only a few large faults are present in this area. As activity is concentrated near to the moving wall during extension, the accelerated growth of the very largest structures in runs m6007 and m7817 produces a break in slope between the intermediate-sized and large structures on Figure 6.1. In runs m4067, n4067 and n6007 a wider size-range of structures continues to be active and no such break in the size frequency distribution appears.

Other modellers of fault populations (Spyropoulos *et al.* 1999b, Cox & Paterson 1990) commonly combine the distributions resulting from several runs to create a larger population and make predictions about "average behaviour". Pickering *et al.* (1995) warn against this approach, as it increases the total number of faults (the size range) without increasing the size of the largest structure (the scale range), and so can give artificially high values of the power law exponent c. However, for comparison with the aforementioned studies, I also tried this approach. The combined size frequency distributions at times 6-10 are show in Figure 6.3. Even at time 6, the combined distribution does not show a simple power law over the full size

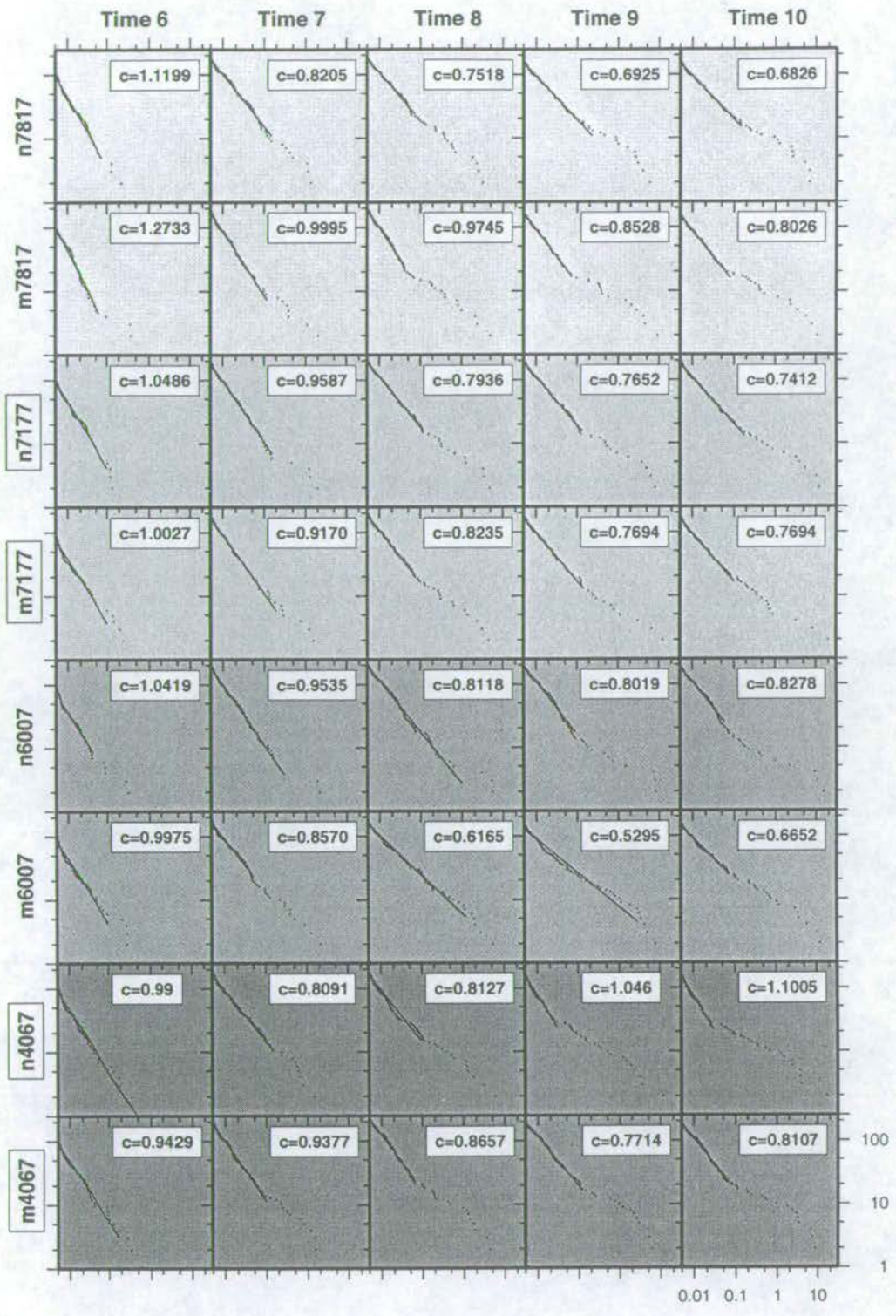

Figure 6.1. Total plastic strain - cumulative frequency plots from experiments varying seed for heterogeneity. For each seed (4067, 6007, 7177 and 7817), the normal mesh and its mirror image have the same background shade. All graphs have the same axes as the annotated plot at the bottom right of the figure. Best-fitting power laws, with exponents, c, are plotted over the interval used in linear regression. Estimated errors on c are typically less than 0.02.

Figure 6.2. Broken elements maps for runs varying the seed for heterogeneity.

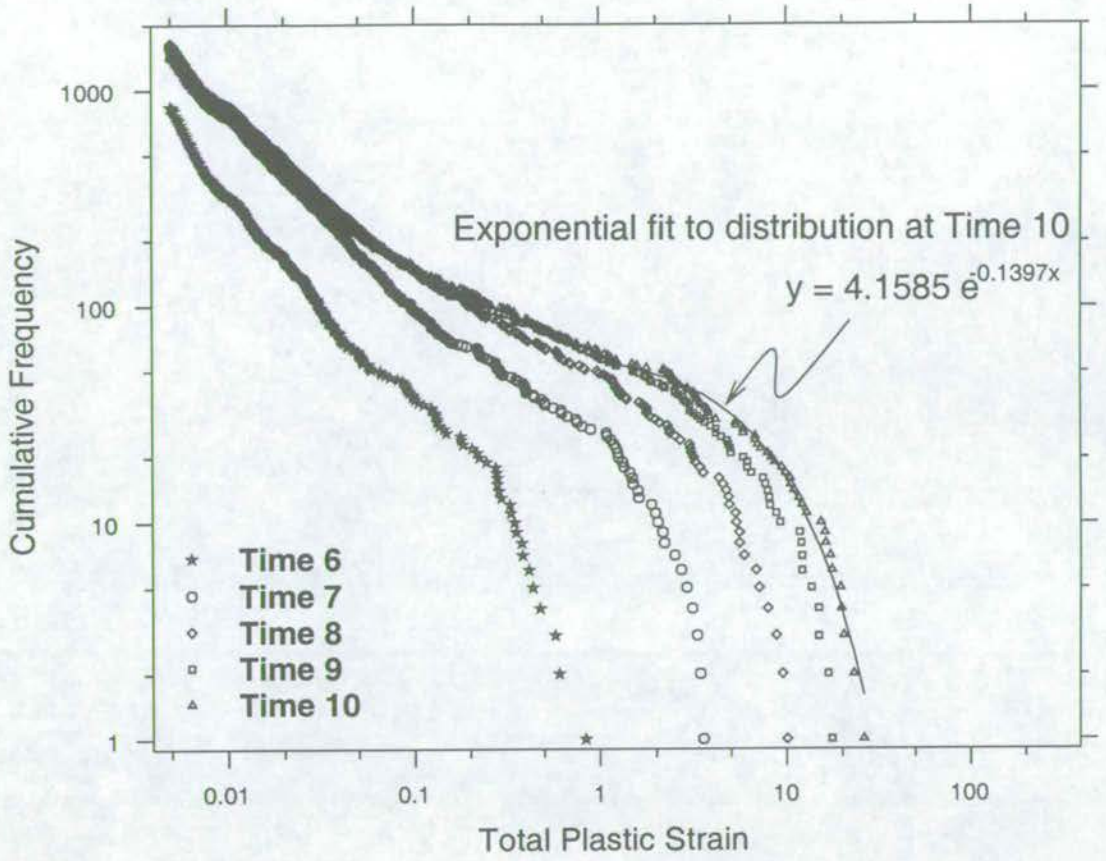

Figure 6.3. Total plastic strain - cumulative frequency plots for the combined datasets.

range, although small faults do follow a power law. The exponents of power-laws that best-fit these small faults are plotted in Figure 6.4 Extrapolating the trend of the large or intermediate-sized faults would over-estimate or under-estimate, respectively, the number of small faults. The slope of the mid-section of the distribution decreases dramatically through time, but the slope defined by the smallest faults is higher and barely changes whilst the distribution of the largest faults evolves from a straight line, which can be fitted with a power law, to a curve that is best fitted with an exponential law. Figure 6.4 shows the power law exponent of the combined dataset, together with the values of c fitted to the individual datasets, versus time. Note that the change in $c_{combined}$ as strain increases is less than the range of c produced by varying the seed.

The value of c obtained for a fault population depends in part on the method used to fit a power law to the distribution (see Section 4.4). For this reason, the above analysis was repeated using the log-interval distribution. A log interval width of 0.1 was used and the power law was fitted over the portion of the distribution between the y-axis and the first empty bin. In the absence of an empty bin, the power law was fitted up to the point where two adjacent bins

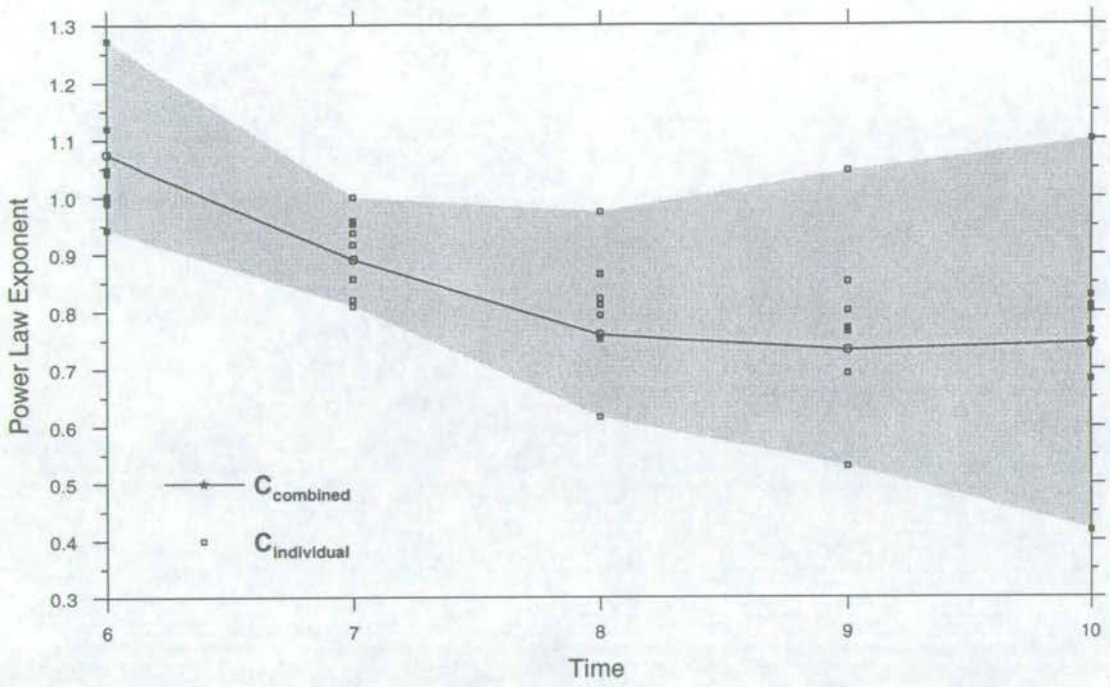

Figure 6.4. c values for the combined datasets compared with those of the individual datasets. Values of c are calculated using the size-cumulative frequency distributions presented in Figures 6.1 and 6.3.

contained the same number of structures. The results are presented in Figures 6.5, 6.6 and 6.7. Estimates of c from the log-interval distributions are typically higher than those for the cumulative distributions, though they agree within 95% confidence limits. The log interval distributions also yield larger uncertainties on c (right column, Figure 6.5). The eight runs show no common trend in how c changes with increasing strain. For distributions from any particular run and even for all the runs combined, the change in c with increasing strain is no bigger than the typical uncertainty on c (see Figure 6.5) and less than the variation in c caused by varying the seed (see Figure 6.7).

6.3 Varying the Strength Distribution

In this study, heterogeneity takes the form of a normal distribution of yield strengths. By increasing the standard deviation of the distribution I increase the amplitude of the heterogeneity. To investigate the effect of changing the amplitude of the heterogeneity, I used the standard mesh (random heterogeneity with 4067 as the seed in the random number generator) for the spatial distribution and Gaussian yield strength distributions with standard deviations of 0, 7.5, 15 and 25 MPa. As discussed in Section 3.5.2, the simulation with

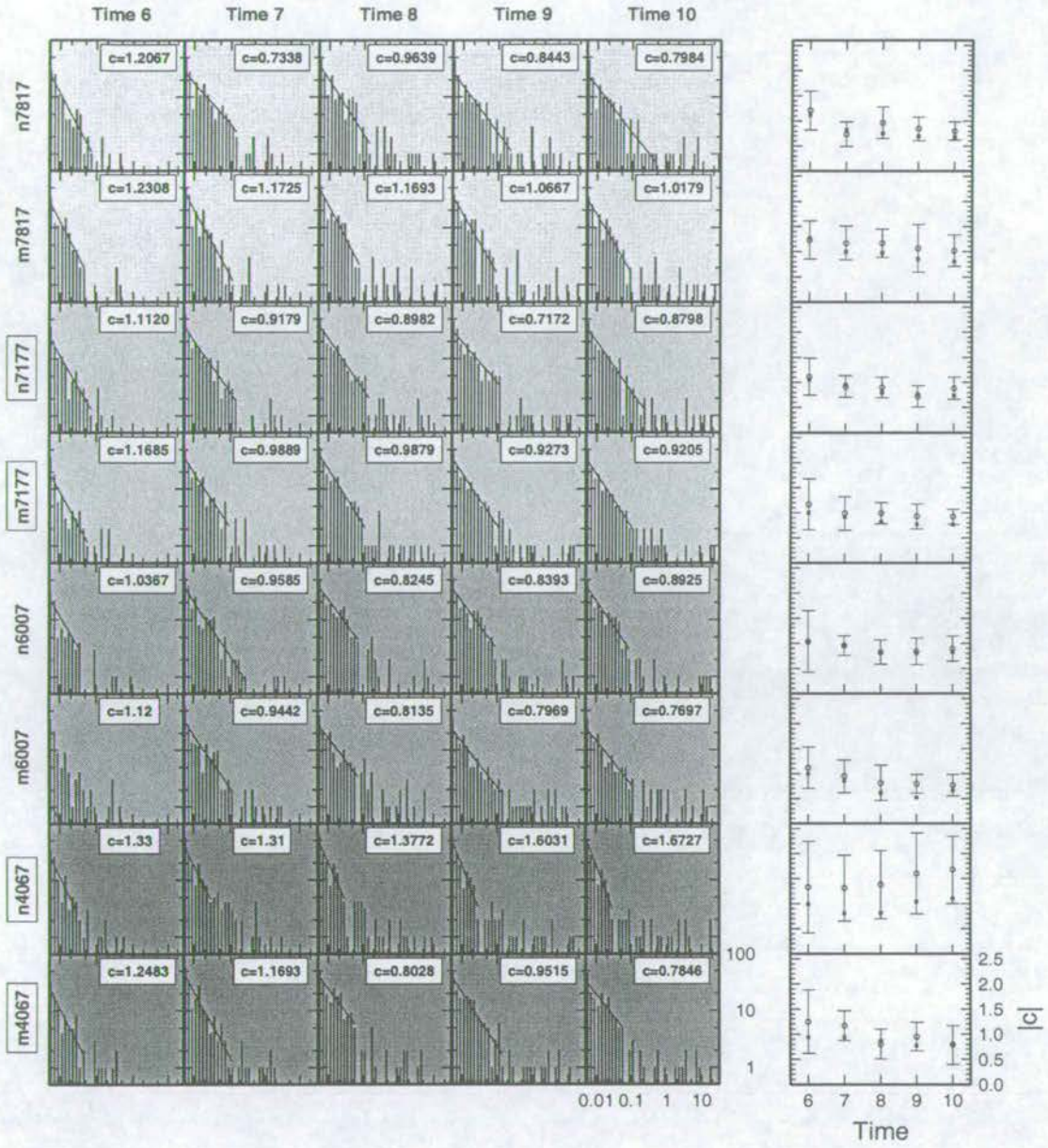

Figure 6.5. Total plastic strain in log-intervals versus discrete frequency for experiments varying the heterogeneity seed. All graphs have the same axes as the annotated plot at the bottom right of the figure. Power laws fits are plotted over the interval covered by the data used in linear regression. The right hand column shows best fitting power law exponents, c, and 95% confidence limits determined for the log-interval (circles) and cumulative (square) frequency datasets. Error bars for the cumulative frequency datasets are smaller than the diameter of the square symbol.

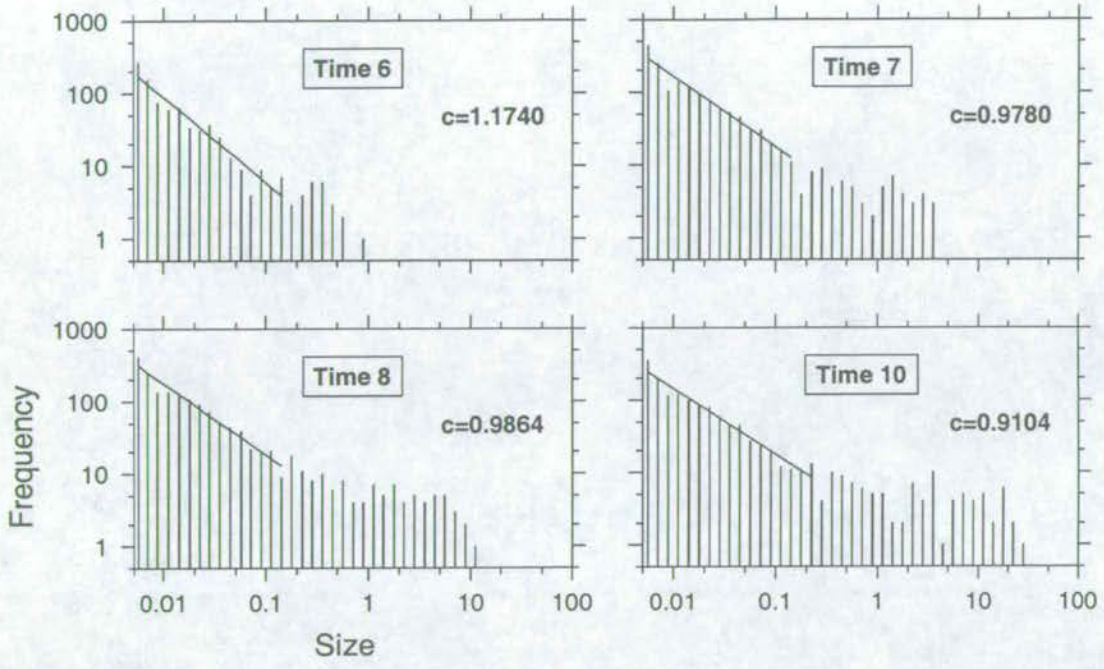

Figure 6.6. Total plastic strain in log-intervals versus frequency plots for the combined datasets.

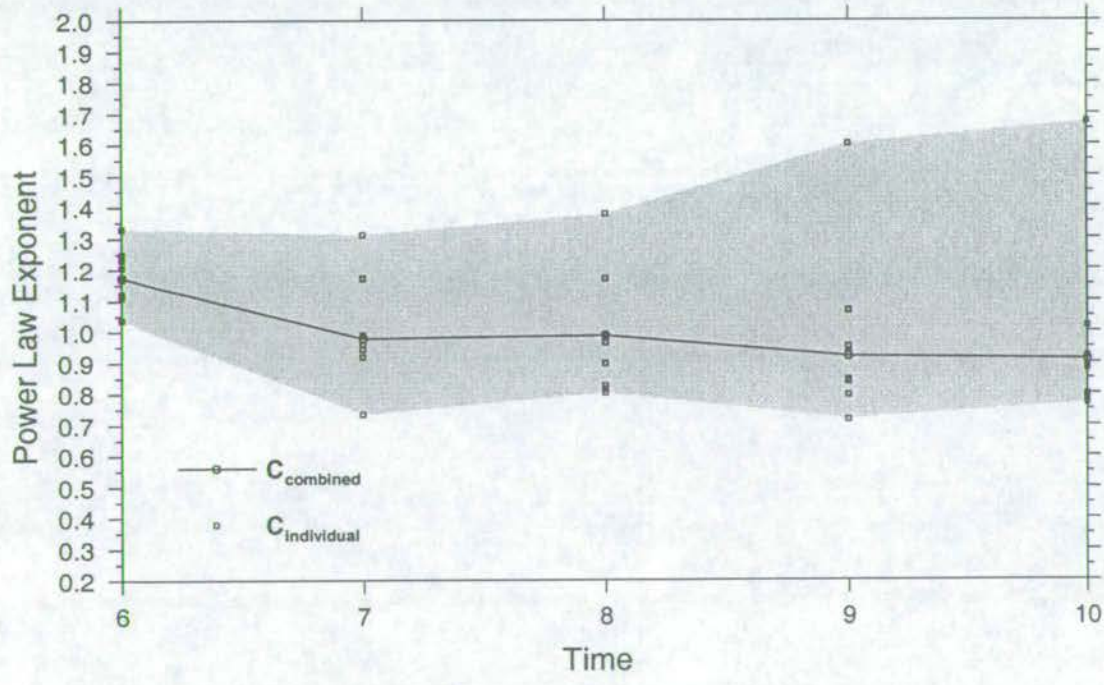

Figure 6.7. c values determined using the log-interval distribution for the combined datasets (Figure 6.6) compared with those of the individual datasets (Figure 6.5).

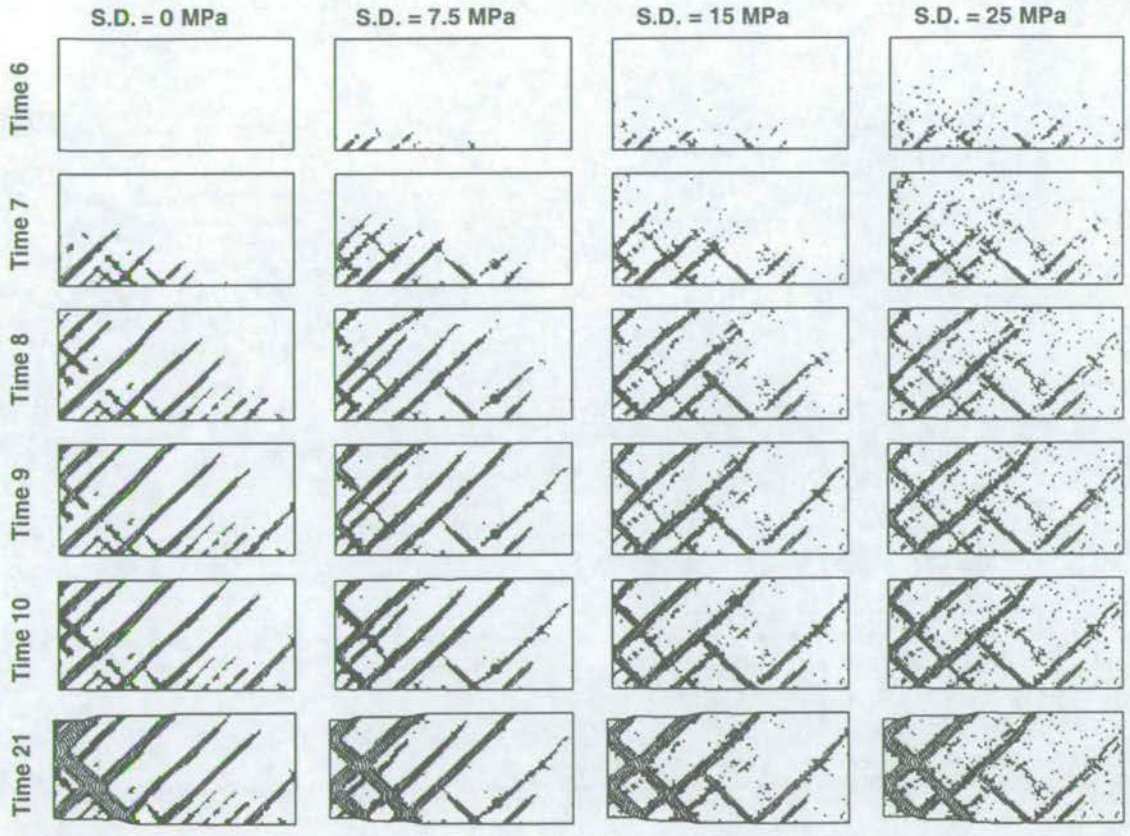

Figure 6.8. Broken element maps for runs with different amplitudes of heterogeneity. Values at the top of each column correspond to the standard deviation of the yield strength distribution.

homogeneous material properties was particularly sensitive to the order in which the calculation was performed. All the simulations presented in this section have the moving wall on the left-hand-side.

Figure 6.8 shows the patterns of broken elements in each simulation. In the homogeneous model, evenly spaced, predominantly synthetic (left-dipping) shear zones formed at first. The imposed boundary conditions prevented the moving wall from rotating and so forced the development of antithetic (right-dipping) structures by time 21. Synthetic structures dominated the heterogeneous runs too. However, as the amplitude of heterogeneity was increased the fault patterns showed less similarity with the homogeneous case. In terms of the fault maps, increasing the amplitude of heterogeneity caused more elements within fault-bounded blocks to fail. Also, as the amplitude of heterogeneity was increased, elements failed earlier in the simulation.

These differences in behaviour were also reflected in the size frequency distributions (Figure 6.10). Runs with stronger heterogeneity had a greater proportion of small structures and

more structures in total (Figure 6.9) at any particular strain. In the homogeneous model, the total number of faults increased to a maximum and then remained constant, whereas in the heterogeneous runs, the total number of faults reached a peak and then fell. The only process that can reduce the total number of faults is coalescence, so greater heterogeneity leads to increased coalescence. At low strains, power laws could be fitted to the whole range of fault sizes. The power law exponent for intermediate-sized faults was generally larger for runs with stronger heterogeneity (only the homogeneous run does not follow this pattern), even though there was more coalescence or linkage in these runs. At higher strains, the more heterogeneous runs displayed "faceted" distributions, with small faults defining a steeply-sloping line in log-log space and intermediate-sized structures a much flatter line. This also is related to changes in the fault pattern associated with increasing the heterogeneity. In the homogeneous run, almost all of the faults are of the block-defining type: growing upward from the base of the model, or away from the moving wall, by propagating one free tip. With increasing heterogeneity, the number of block-defining faults changes little, but the number of intra-block structures increases. Faults in this second population are generally small, become inactive at relatively low strain and are free to propagate upwards, downwards or break elements to either side. The contribution this second populations makes to the shape of the overall size cumulative frequency distribution is apparent by considering the active and inactive structures in the four models at Time 10 (highlighted on Figure 6.10).

6.4 Varying the Amount of Softening

Elements can fail simply in response to the loading at the boundary. However, points in the mesh are also loaded when the stress drops in a nearby element as it breaks (Figure 5.10). Although this additional load is transient, depending on the magnitude of the stress drop, it can also trigger failure. As there is no healing in ADELI simulations, strength lost at failure cannot be recovered and so softening is permanent. Thus, within the process of failure we have mechanisms both for creating diffuse patches of broken elements and localising strain onto the very weakest elements. The aim of these experiments was to determine which of these mechanisms dominates in ADELI simulations.

The effect of softening (the loss of strength and drop in stress as the material yields) was investigated in the following way. I used the standard mesh (random heterogeneity with 4067

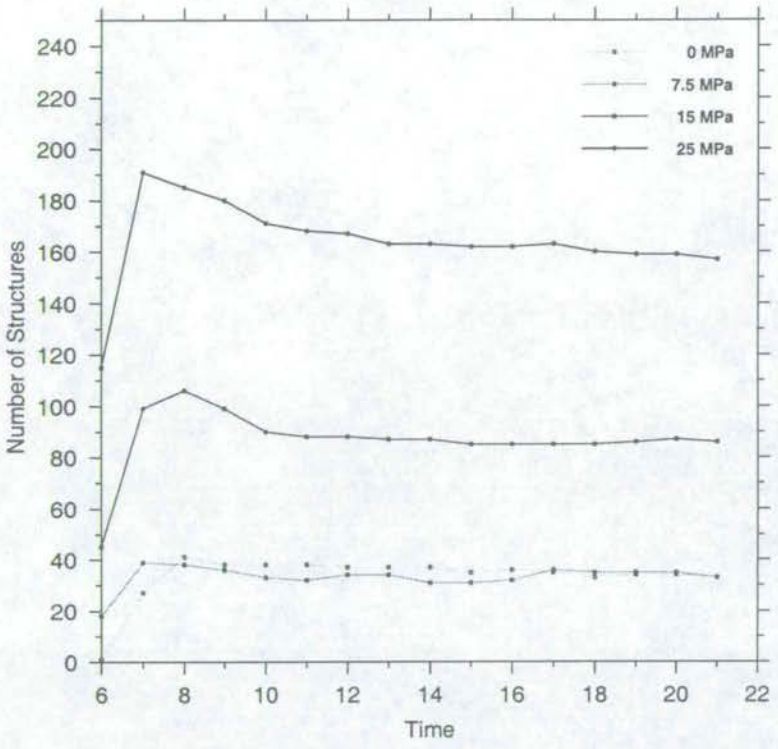

Figure 6.9. Total number of faults versus time in four runs with different amplitudes of heterogeneity.

in the random number generator) for the spatial distribution, a Gaussian frequency distribution of yield strengths (mean 275MPa, standard deviation 25MPa) and a stress drop on failure that was homogeneous in any one run, but took values 75MPa (standard model), 30MPa, 15MPa 7.5MPa and 0MPa (no softening) in different runs. All models were extended by moving the left-hand wall.

Figure 6.11 illustrates the pattern of broken elements in four of the simulations. The first thing to notice is that localisation occurs even in the run with no softening. Softening is not necessary for localised failure, but it does affect the pattern of failure in space. For example, at time 6, the area containing broken elements is largest in the run with the most softening. Larger stress drops trigger the failure of elements further from the locus of fault nucleation (the bottom left corner of the model). Runs with more softening have thinner clusters, fewer broken elements within fault blocks and fewer broken elements in total. For the experiments with stress drops of 15 and 0MPa, the pattern of faulting at the end of the experiment (time 21) is similar: they both show one X-shaped feature near to the moving wall and another closer to the centre of the model. In the experiment with the highest stress drop (75MPa), the central "X" is absent and in its place there is a large synthetic fault and smaller V-shaped conjugate set. The pattern of broken elements is transitional between these two forms when the strength loss is 30MPa.

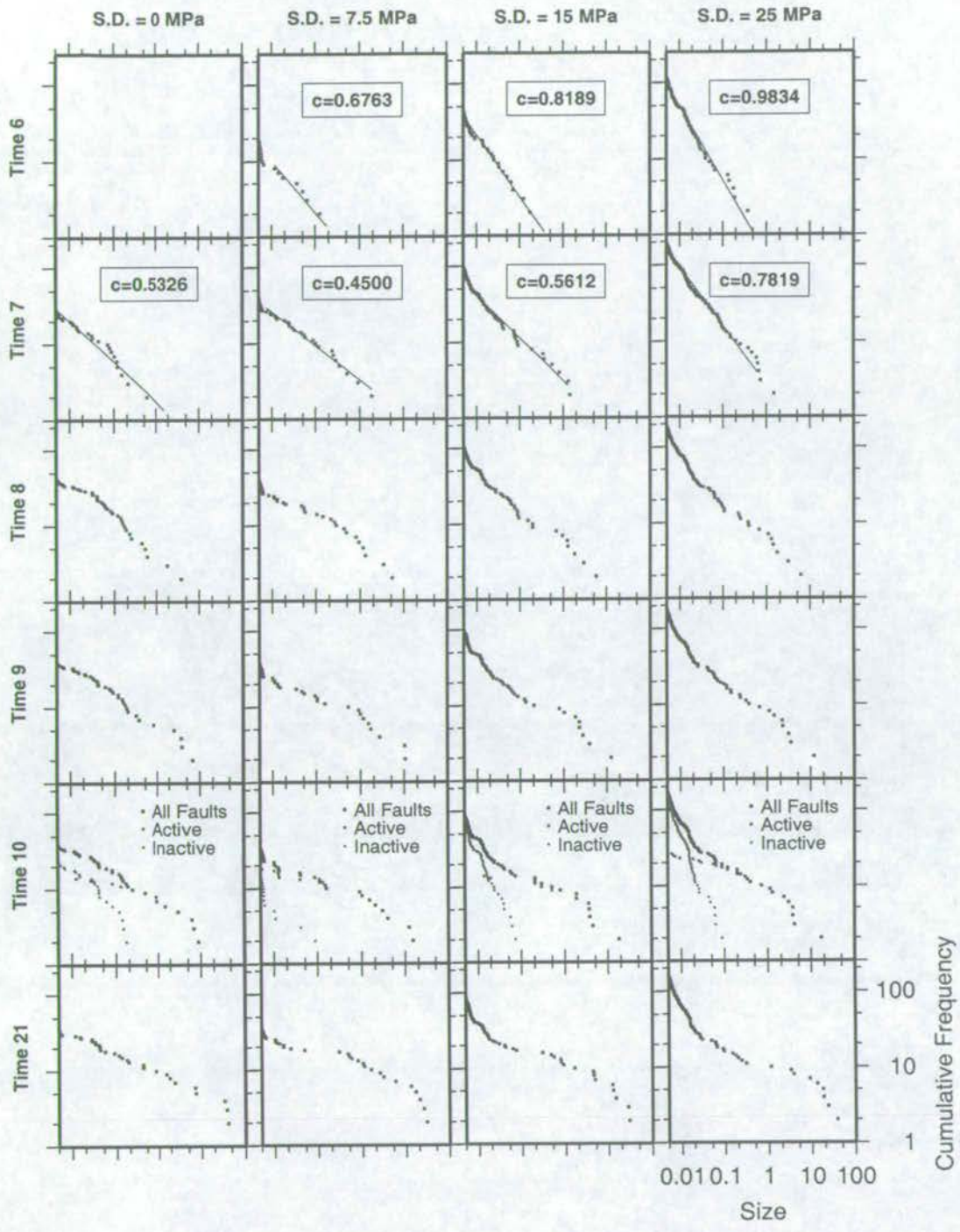

Figure 6.10. Fault size (measured as total plastic strain) versus cumulative frequency for runs with different amplitudes of heterogeneity. All graphs have the same axes as the annotated plot at the bottom right of the figure. Values at the top of each column correspond to the standard deviation of the yield strength distribution. Best fit power laws are plotted in the interval over which they were calculated. Active and inactive populations are plotted separately at Time 10, to highlight the contribution of small, intra-block faults, which are inactive by this point and more numerous in the more heterogeneous runs.

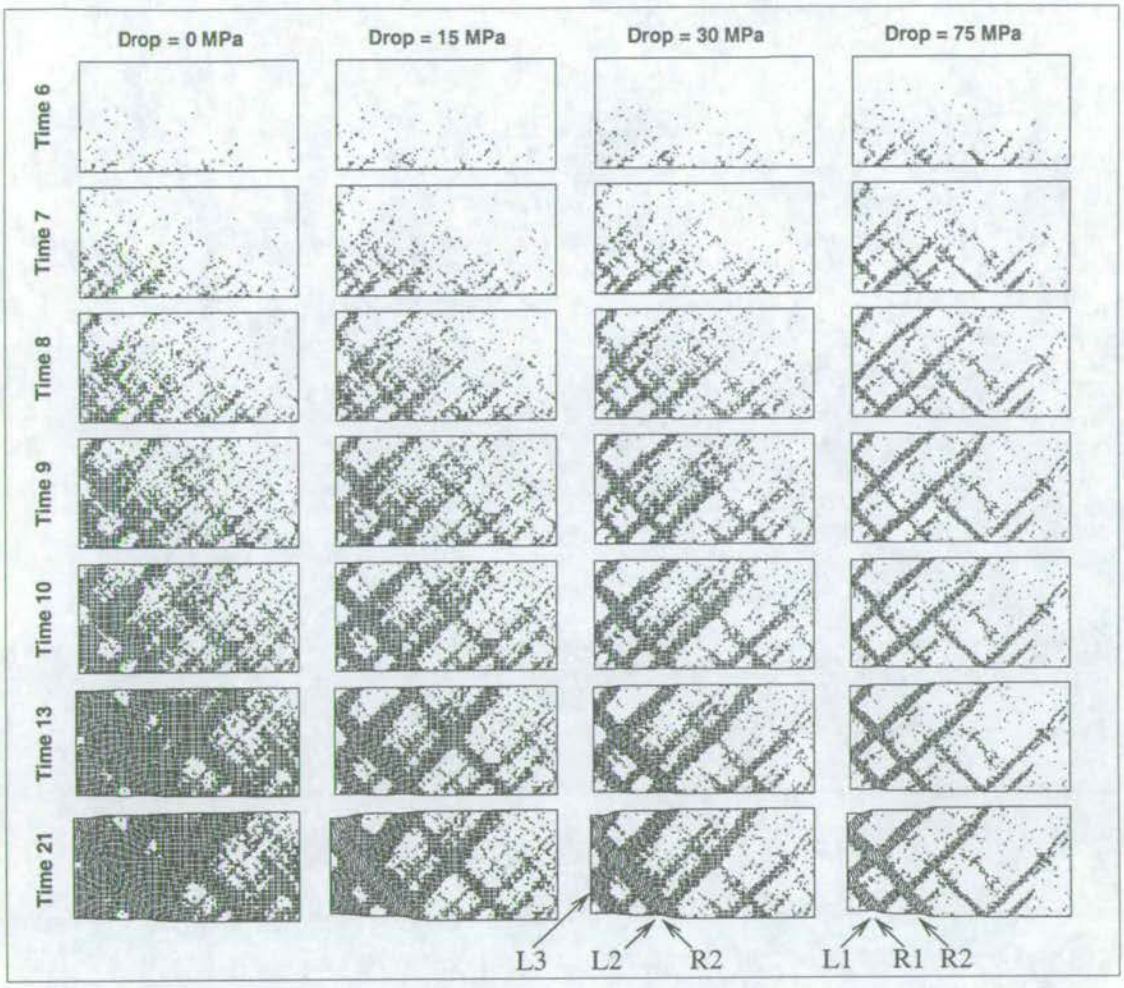

Figure 6.11. Broken element maps for runs with different amplitudes of post-yield stress drop.

The stress drop on failure has such a strong influence on the fault pattern in these experiments because it determines the extent to which strain is localised on the largest faults. In the run with the high stress drop, the major fault R1 (see Figure 6.11) has much more displacement than the fault above it, R2. This is because it has been growing longer (being nearer to the base of the model) and, crucially, is much weaker because of the large post-yield strength loss. When a structure intersects with the boundary, it promotes the growth of a conjugate structure at the intersection. In the high stress drop model, because R1 has initially more displacement than R2, the reflection of R1 at the base (the fault L1) is dominant over the reflection of R2 (the fault L2). In the lower stress drop runs, R1 is less soft and has accumulated less displacement than in the higher stress drop runs and so it is the reflection of R2 that comes to dominate. A similar argument regarding the size of L3 and its reflection from the upper boundary can be used to explain the presence of the right-dipping limb of the central X in the low strength loss models, and its absence in the high strength loss runs.

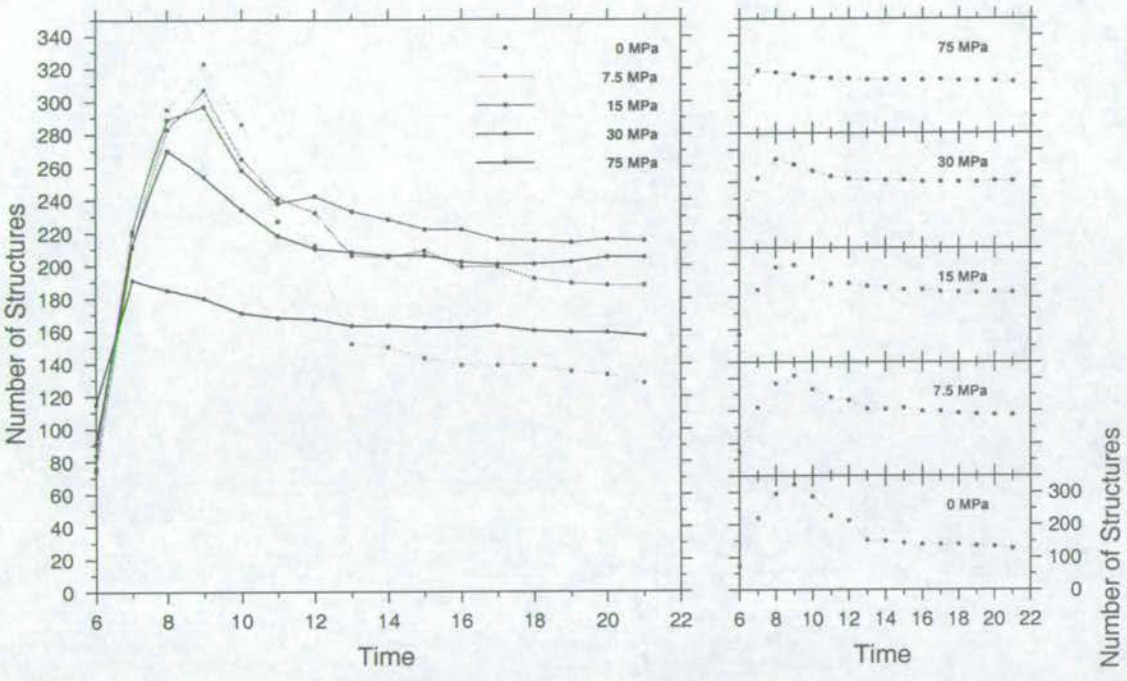

Figure 6.12. Total number of faults versus time in runs with different amounts of strength loss on failure.

Figure 6.12 shows the total number of structures in each model through time. In all models the total number of faults increases, reaches a maximum and then decreases, at first sharply and then more gradually. As softening is increased, the peak occurs earlier and the drop in the number of faults is smaller. This again relates to the fault pattern: in the runs with the least softening, because so many elements are broken early on, many small structures are assimilated by the largest structures as they grow. In contrast, because the deformation is more localised in the runs with more softening, growing structures are less likely to encounter a previously broken element and assimilation is less common.

It is clear from the patterns of broken elements that the stress drop on failure influences how strain is localised in space and time. Figure 6.13 emphasises this point - in the lower stress-drop runs, elements across the mesh are still actively accumulating strain between times 9 and 10, whereas in the higher stress drop runs, only those elements in the major shear zones are still active. Patterns of localisation and activity control parameters like the size of the largest structure and the number of linkage opportunities, therefore it is unsurprising that experiments with different stress drops have dramatically different size frequency distributions (Figure 6.14). The effect of assimilation is most obvious in the 0MPa strength loss run, where it is manifest as a decrease in the number of the small faults in particular through time, producing a "roll-over" in the small size range. The 75MPa run shows the clearest evidence for localisation: from time

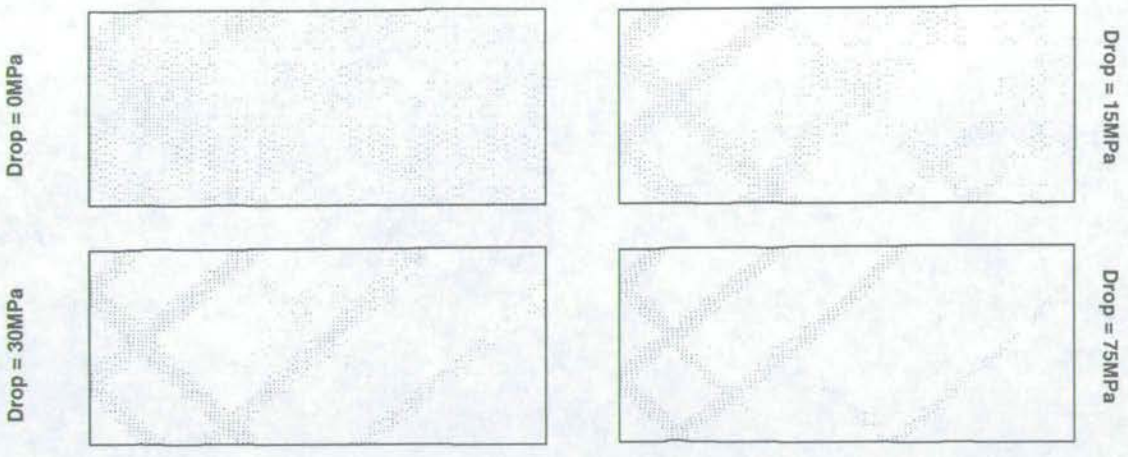

Figure 6.13. Maps showing the change in plastic strain in each element between times 9 and 10. All four plots use the same palette: white elements are inactive, black the most active.

8 onwards there is a bulge in the size cumulative frequency distribution in the larger size range, reflecting the accelerated growth of the largest structures due to strain localisation. Although both localisation and assimilation feature in the 15MPa run, the size frequency distribution shows neither a roll-over nor a bulge. The two processes are balanced in this run and structures across the full range of sizes continue to be involved in the population evolution throughout the experiment, resulting in a distribution that describes a straight line in log-log space at all times.

6.5 Discussion

The fall in c with increasing strain observed in the first set of experiments is consistent with the results of other numerical (Cowie *et al.* 1993) and analogue (Ackermann *et al.* 1997) models. Changes in scaling when faults penetrate the entire layer thickness has also been observed by Ackermann *et al.* (1997) and Spyropoulos *et al.* (1999). The physical reasons behind these observations were explained in Chapter 5. However, in addition to variation in c due to increased strain, two other factors affect the power law exponent in these experiments. Firstly, there is a statistical uncertainty on the value of c. This is higher when the power law is fitted to a log-interval size frequency distribution rather than a cumulative distribution, and decreases as the number of data points included in the fitting algorithm is increased. The value of c also varies depending on the seed used. At the same strain, materials with statistically identical properties have significantly different size frequency distributions. This suggests that extrapolating information about fault size scaling from one area to another (e.g. from an

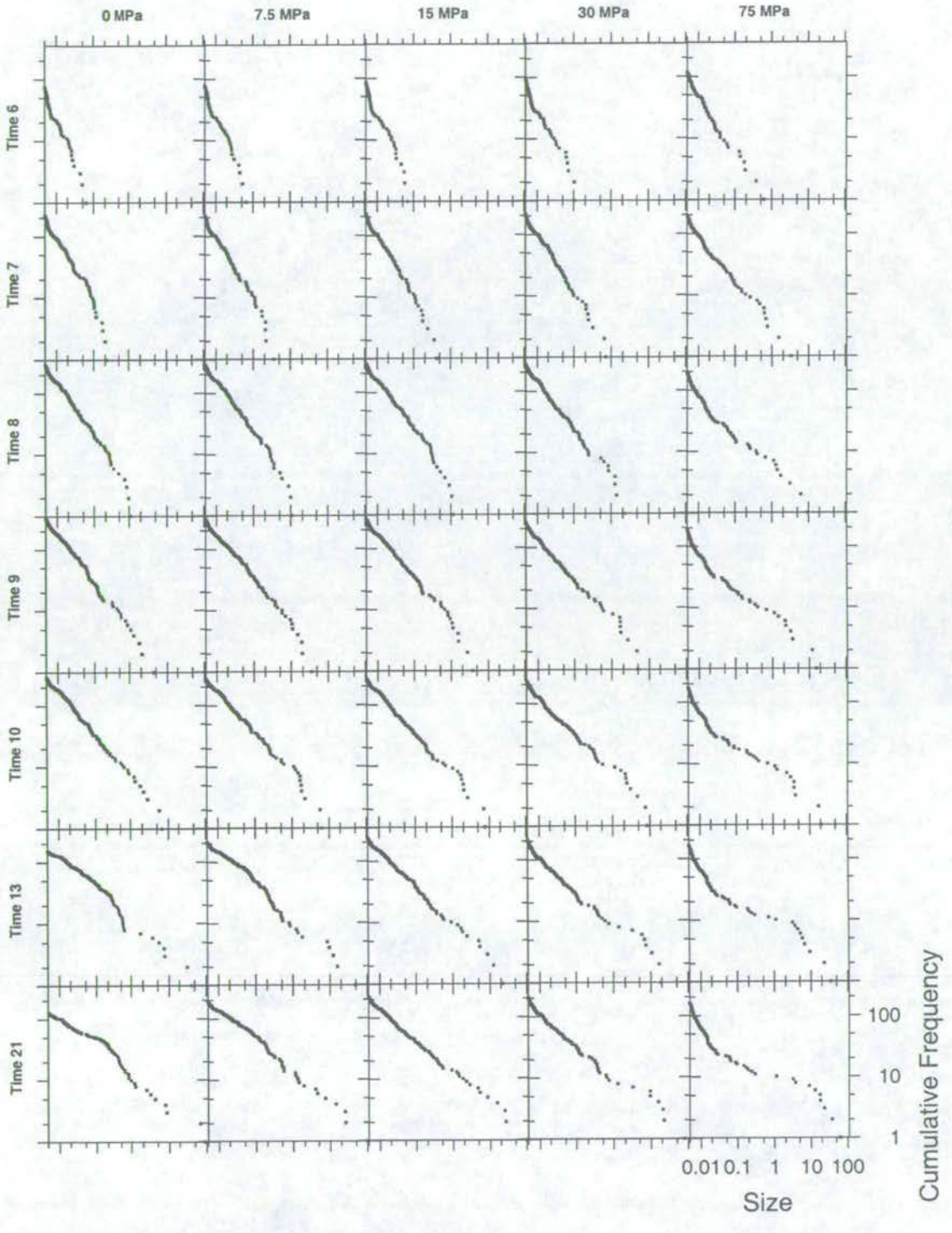

Figure 6.14. Fault size (measured as total plastic strain) versus cumulative frequency for runs with different stress drops on failure. All graphs have the same axes as the annotated plot at the bottom right of the figure.

area with with high resolution 3D seismic to a poorly-imaged, adjacent area) should be done cautiously, even if the areas have the same lithologies and tectonic histories.

Figure 7 of Cladouhos & Marrett (1996) shows values of c and strain calculated for eight fault populations in several of lithologies, with c between 0.67 and 2.07 and strains covering 1.5 orders of magnitude. No error estimates are reported for either c or strain. In light of the first set of experiments presented in this chapter, it is perhaps unsurprising that Cladouhos & Marrett (1996) found no relationship between c and strain in real datasets. Previous numerical modellers of fault population statistics have considered the data from different runs as a single population and focussed on the "average behaviour" of the system. For a geologist working with a single population of typically a few hundred faults, the average behaviour is perhaps not so important as the range of likely behaviour, particularly if extrapolating to either smaller length scales or adjacent areas.

Several previous studies of faulting have incorporated heterogeneous strengths in numerical models (McKinnon & Garrido de la Barra 1998, Cowie *et al.* 1993, Cox & Paterson 1990). Cowie *et al.* (1993) state that the percentage disorder (width of the strength distribution) does not affect their results: in all their experiments they observe spatio-temporal clustering of activity, self-organisation and the emergence of power law size scaling. I also observed these phenomena in all of the experiments, regardless of the width of the strength distribution. However, some phenomena are sensitive to the width of the strength distribution. In this regard, my results are basically compatible with those of Cox & Paterson (1990), who also saw that widening the strength distribution increases the proportion of elements that have failed at a particular time and advances the onset of failure. Spyropoulos *et al.* (1999) present a graph of crack density versus time that is strikingly similar to Figure 6.9. As their model has periodic boundaries, crack density is directly equivalent to the total number of structures in my study. With increasing heterogeneity, they too observe higher peak crack densities and larger falls in crack density after the peak.

The models presented by Spyropoulos *et al.* (1999) and Cox & Paterson (1990) include some form of material weakening combined with stress drop at failure, and in this sense are similar to ADELI. In contrast, in the model presented by Cowie *et al.* (1993) and Cowie *et al.* (1995), elements undergo a stress drop on failure but regain their pre-failure strength instantaneously. This difference may account for the different localisation behaviour seen in the models. In ADELI, higher stress drop runs create wider areas of yielding initially, as breaking elements load other elements nearby. However, strain quickly localises onto the first-broken elements because these elements are so much weaker than unbroken elements in the rest of the mesh.

Cowie *et al.* (1995) also describe runs in which the stress drop was large compared with the range of strengths, but in their model, such runs produce a wide zone of diffuse rupture activity and strain does not localise onto a well-defined fault trace.

The runs with very little softening produce broad bands of shearing that do not particularly resemble faults in nature. However, I propose that these experiments are still useful for illustrating the effects of fault growth processes on fault size frequency populations. All the experiments show a decrease in the slope of the distribution in log-log space through time. In the runs with little softening, the decrease was accomplished by coalescence/linkage/assimilation, reducing the number of small faults and increasing the size of the large ones. In the runs with pronounced softening, the slope decreases through time by retarding the growth of small and intermediate-sized faults, or even deactivating them entirely, and accelerating the growth of the very largest structures.

Chapter 7

Experiments Varying External Properties

The purpose of this chapter is to describe how the pattern of fault evolution described in Chapter 5 is affected by changing the external properties of the system. Just as the rheology and heterogeneity define the internal properties of the modelled system, the size and shape of the deforming region and the boundary conditions define the external properties. I show that different fault patterns emerge in models overlying an inviscid fluid substrate compared to models on a rigid base. I explain the differences in terms of the overall kinematics imposed by the boundary conditions and go on to show how the different growth histories are reflected in fault size cumulative frequency distributions. I also present simulations with varying layer thicknesses, and show how the thickness and aspect ratio of the layer affects the pattern of activity and localisation of strain through time. Differences in the number of active faults and the partitioning of strain between faults of various sizes are manifest in the fault size cumulative frequency distribution. I observe that parameters such as the percentage of elements that are broken, the size of the largest structure and the time at which faults span the layer correlate with layer thickness.

7.1 Fixed or Isostatic Lower Boundary

7.1.1 Motivation

The experiments presented in Chapters 5 and 6 all featured a deforming layer lying above a fluid, so the boundary condition at the base of these models was isostatic. Although this situation exists in nature where faulting occurs in a brittle layer above a thick salt or mobile shale unit (the faults in Canyonlands National Park, Utah (Cartwright *et al.* 1995, Mansfield 1996, McGill & Stromquist 1979) are a good example of this scenario), this situation is rare. Faults in sedimentary sequences that over-lie rigid basement are more common in nature, and are certainly the focus of more fault population studies [e.g. Fossen & Hesthammer (2000), Fossen & Rørnes (1996), Walsh *et al.* (1994), Gauthier & Lake (1993), Childs *et al.* (1990)]. The first reason, then, for performing experiments with both isostatic and rigid boundary conditions is to simulate a wider range of natural scenarios and thus enable direct comparison with more fault populations studies. Experiments using analogue models also feature deforming layers above viscous fluids such as honey (Davy *et al.* 1995), molten wax (Brune & Ellis 1997) and barite mud (Fossen & Gabrielsen 1996, Mansfield 1996) as well as above rigid bases (Ackermann *et al.* 2000, Spyropoulos *et al.* 1999b). Conclusions drawn from both rigid-based or isostatic-based analogues have been applied indiscriminantly. A second reason for performing ADELI experiments with both basal boundary conditions is to assess the validity of such extrapolations and determine whether isostatic and rigid systems are so different that we must compare like-with-like or whether insights gained from one system can be applied to both.

7.1.2 Approach

The models presented in Section 5.1 as Experiments A and B were re-run, replacing the isostatic basal boundary condition with one of frictionless sliding. The re-run models (hereafter referred to as Rigid A and Rigid B) were identical to Section 5.1's Experiments A and B (hereafter referred to as Isostatic A and Isostatic B) in all other respects, such as internal fabric and strain rate. In Rigid A and Isostatic A, deformation was accomplished by moving the left hand wall. In Rigid B and Isostatic B, the right hand wall was moved.

7.1.3 Fault patterns in space and time

Isostasy at the base of a thinning and extending layer requires that material displaced downward from the top of the model be balanced by material displaced upwards at the base. This condition does not apply in layers deforming above a rigid layer, and so the bulk displacement fields in models with isostatic and rigid basal boundary conditions are quite different (Figure 7.1 a and d). Different displacement fields imposed by the boundary conditions lead to the following differences in the pattern of faulting in cross-section (Figure 7.1). In Isostatic A and Isostatic B, conjugate faults intersect midway through the layer, forming X-shapes. This geometry is compatible with the imposed isostatic condition. In Rigid A and Rigid B, conjugate faults more commonly intersect at the base of the layer. In Rigid B, the two largest faults are similarly-sized conjugates and a simple graben develops. In Rigid A, faults synthetic to the overall thinning of the model dominate, and a series of half-grabens results. The fault patterns in Isostatic A and Isostatic B are qualitatively very similar, although they differ in detail. The patterns in Rigid A and Rigid B are markedly different, despite the fact that the same heterogeneous block was deformed in all four experiments. In the isostatic simulations, strain is concentrated near to the moving wall as time progresses, whereas in the simulations with a rigid base, some of the most active elements are far from the moving wall at 1.7% extension (next to bottom row of Figure 7.2). The activity patterns in the two isostatic simulations are more similar to each other than those in the rigid-based simulations: in both isostatic simulations several large and intermediate-sized faults are still active at 2.0% extension; this is also the case in Rigid A, but in Rigid B activity is limited to the three largest structures at this stage.

7.1.4 Fault population statistics

The maximum number of faults in each rigid run (180 in Rigid A, 210 in Rigid B) is lower than in the equivalent isostatic run (196 in Isostatic A, 235 in Isostatic B) but the total number of faults versus time changes in the same way in all four experiments (Figure 7.3). In all four simulations, the proportion of the total plastic strain (summed across the whole mesh) taken up by the five largest faults increases through time (Figure 7.4), but localisation is faster in the rigid-based models. In all four simulations, the slope of the size cumulative frequency distributions decreases as the region extends (Figure 7.5). The distributions for the isostatic models are more similar to each other than the distributions for the rigid-based models. This is because fault activity patterns in the isostatic runs are very similar, but very different in the rigid-based runs (see Figure 7.2). In contrast, strain is more localised onto the three largest

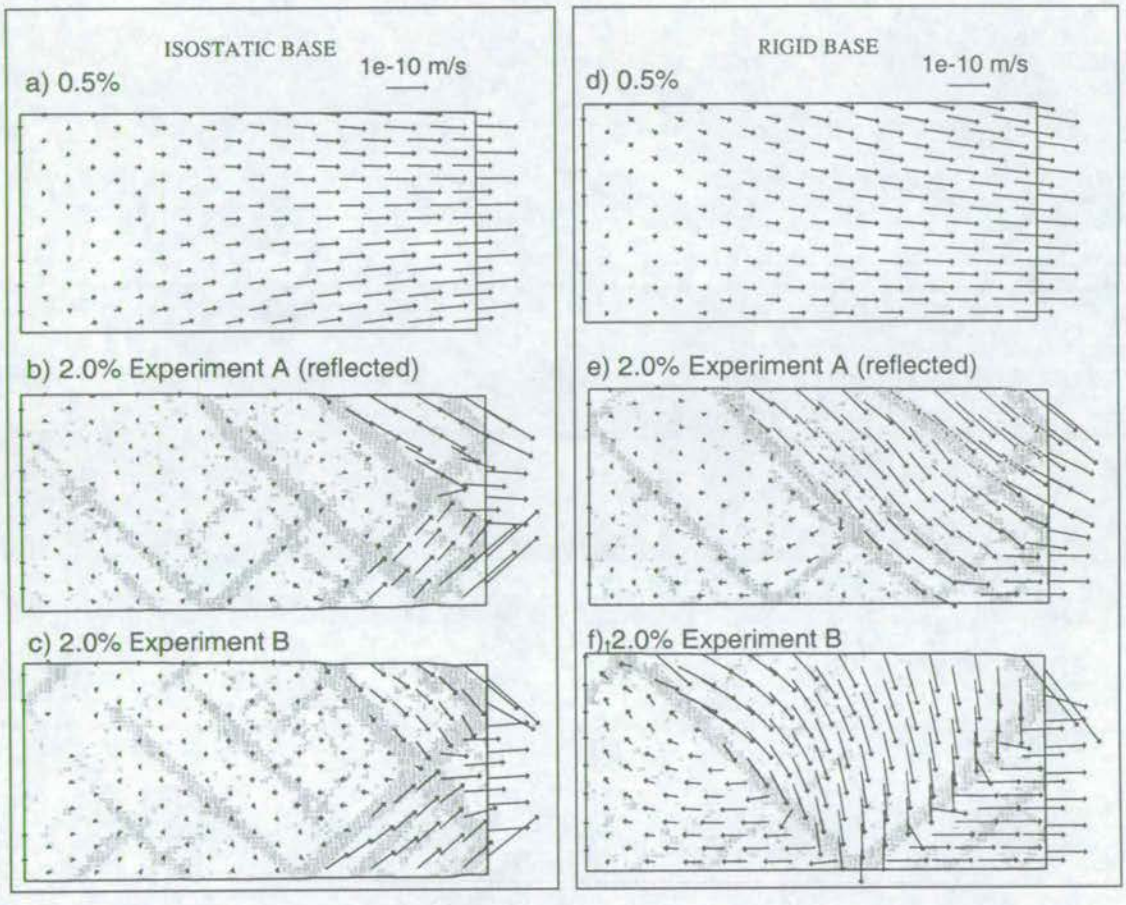

Figure 7.1. Bulk kinematics imposed by a) isostatic and d) rigid basal boundary conditions. Faults pattern and instantaneous velocity vectors at 2.0% regional extension in b) Isostatic A, c) Isostatic B, e) Rigid A and f) Rigid B.

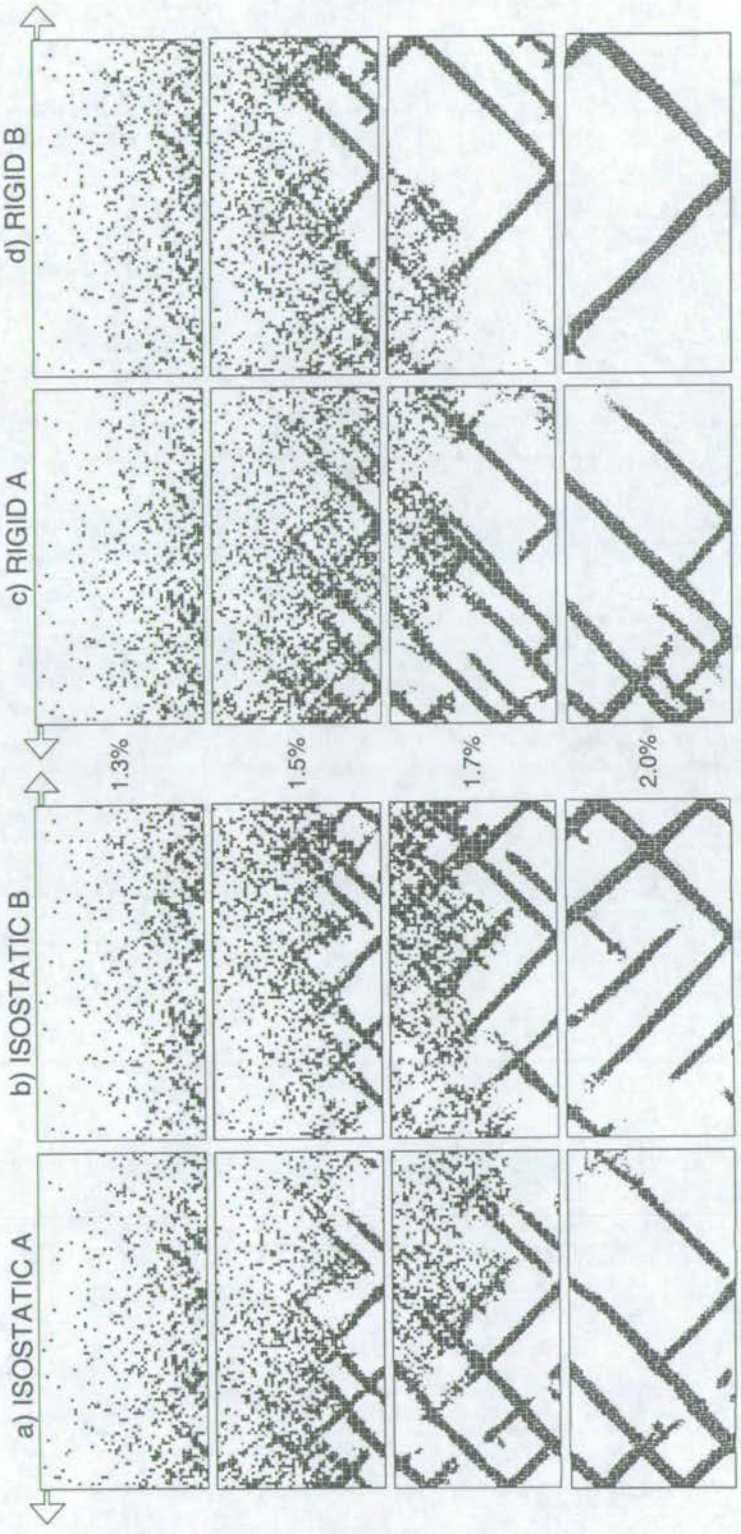

Figure 7.2. Maps of elements whose plastic strain has increased in the last 0.1% strain i.e. those that are active. a) Isostatic A, b) Isostatic B, c) Rigid A and d) Rigid B. Arrows indicate which sidewall is moving. Numbers in the central column are regional extension at the time of each snapshot.

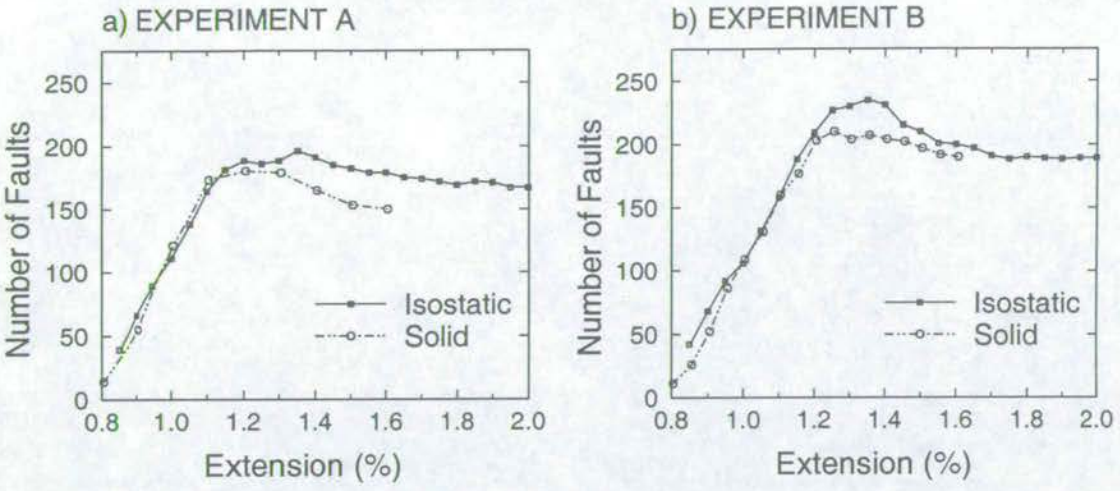

Figure 7.3. Number of faults (both active and inactive) versus regional extension in rigid- and isostatic-based simulations. a) Experiments in which the left wall was moved. b) Experiments in which the right wall was moved.

structures in Rigid B than A, resulting in more small faults becoming inactive earlier in Rigid B than Rigid A. This is shown in Figure 7.6, where the percentage of inactive faults in the total population is plotted as a function of strain. Note that the curve for Rigid B on the upper figure, is at all times above that of Rigid A.

7.1.5 Discussion

These experiments suggest that fault development is more consistent in simulations using isostatic rather than rigid-based models. The isostatic basal boundary condition leads to stronger strain concentration close to the moving wall. The development of faults is thus more constrained in isostatic compared to rigid-based models. Fault populations in rigid-based models have more degrees of freedom, and so wider variations in fault patterns can develop. However, only tentative conclusions can be made on the basis of only four simulations.

Taking a broader view, the difference between rigid and isostatic fault maps and size-frequency distributions are no greater than the differences observed in the isostatic runs with different heterogeneous seeds (Section 6.2). Most workers in the field of fault population studies would be wary about combining ideas resulting from experiments with different boundary conditions, but combining insights from fault populations in different materials is generally accepted. This suggests that both of these practices are equally valid or invalid. The processes controlling fault development are not fundamentally different in the different systems - but the specifics of

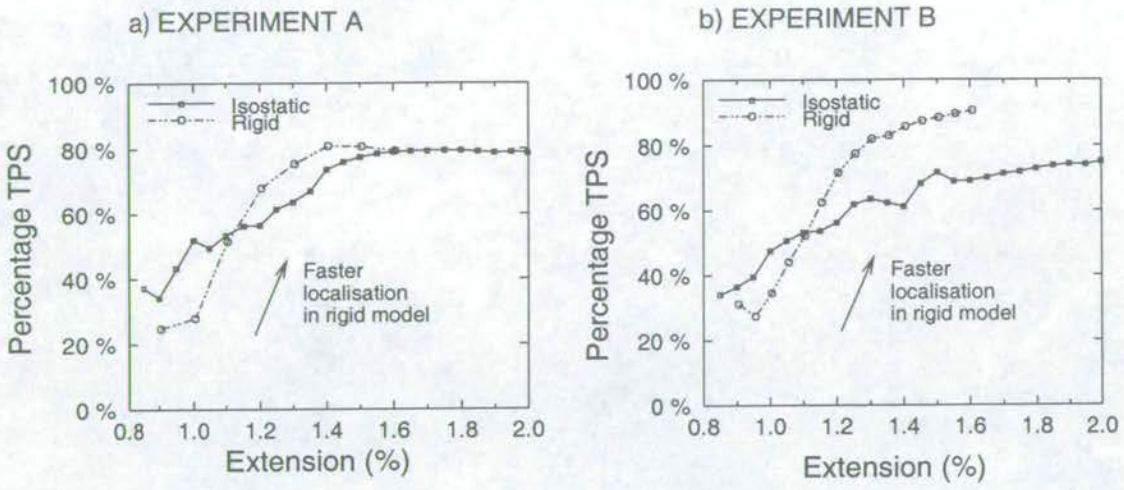

Figure 7.4. Percentage of total plastic strain summed over the whole mesh that is accounted for by the five largest faults. Points are only plotted if the entire fault population contains more than 50 structures.

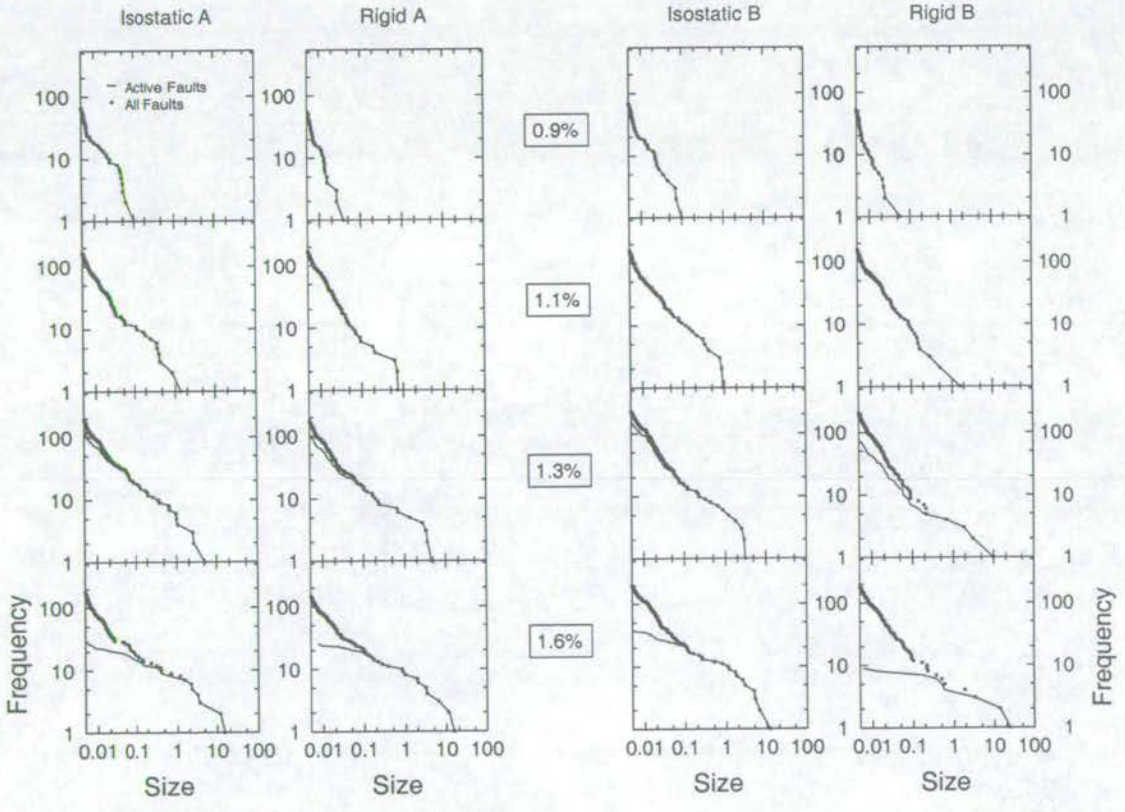

Figure 7.5. Size (total plastic strain) cumulative frequency distributions for faults produced in simulations with rigid and isostatic basal boundary conditions. Dots indicate the total fault populations, the active populations are shown by the solid lines.

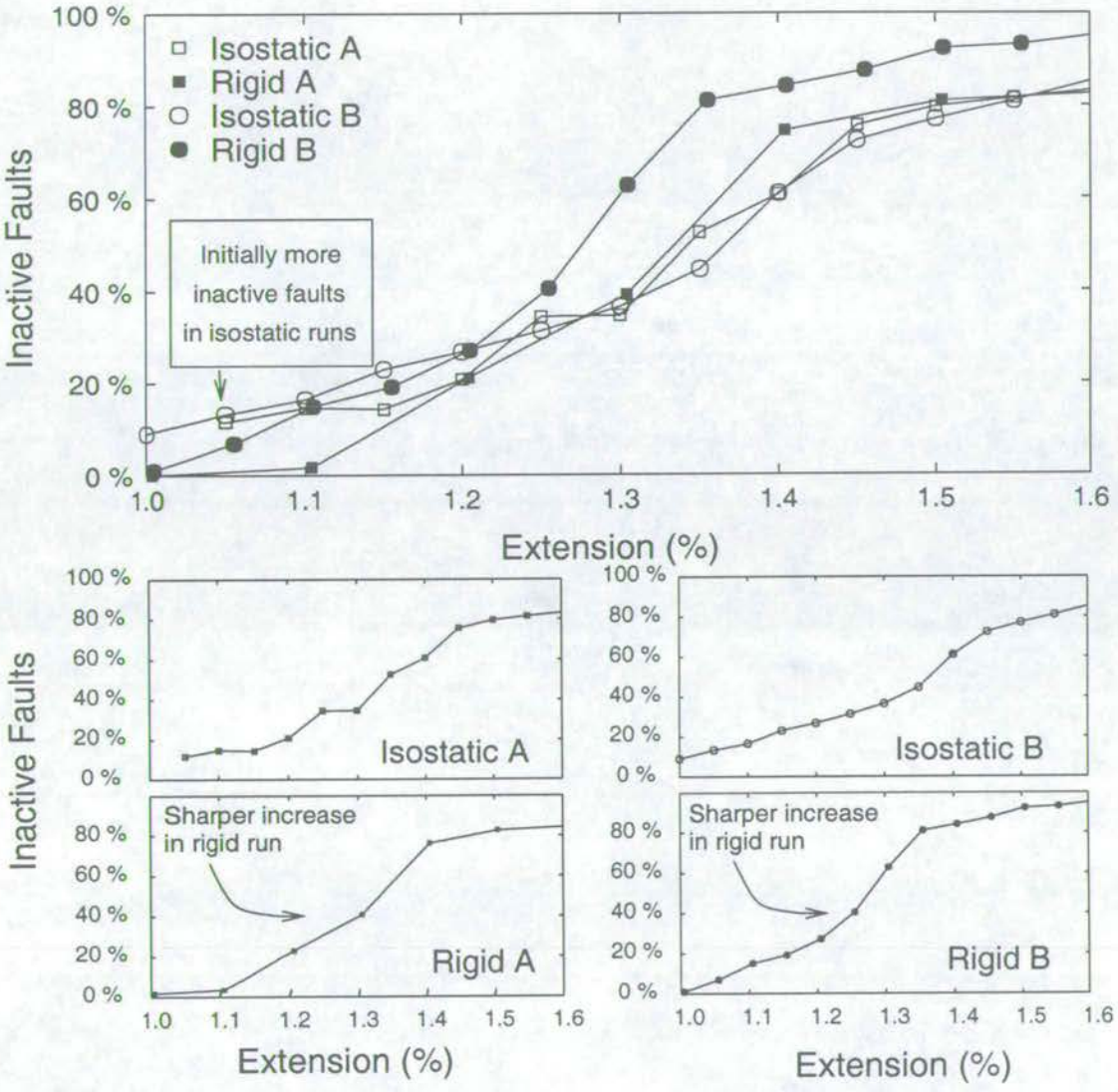

Figure 7.6. Percentage of inactive structures in isostatic and rigid-based simulations.

a particular system (rock properties, boundary conditions and so on) do determine the relative importance of each of these processes in time and space.

7.2 Thickness of the Deforming Layer

7.2.1 Motivation

It has been proposed that the thickness of the upper brittle crust has a direct effect on fault development in extending tectonic terranes (Jackson & White 1989, Contreras, Anders & Scholz 2000). Also, studies of fault development using analogue (Ackermann *et al.* 2000) and numerical (Finch 1998) models link changes in fault scaling to faults first breaching the mechanical layer. In Section 5.2.6 I observed that the transition from power law fault size cumulative frequency distributions to distributions with a break in scaling occurred as faults began to span the entire layer thickness. The reasons for performing experiments with different layer thicknesses are then two-fold: to assess whether faults breaching the layer caused the transition observed in Section 5.2.6, or whether the two events were unrelated but coincided by chance in this experiment; to establish whether those parameters of fault populations that have been found to be layer thickness-dependent in other analogue and numerical models [parameters such as the maximum fault size and number of structures (Ackermann *et al.* 2000)] also vary with layer thickness in ADELI simulations.

7.2.2 Approach

To create meshes of different thicknesses, rows of elements were removed from the top of the mesh that was presented in Section 5.1 as Experiment B. Faults in ADELI experiments primarily grow upwards from the base of the model, so by reducing the thickness in this way, the pattern of material heterogeneity encountered by growing faults did not change between experiments. Reducing the thickness without changing the length of the model changes the aspect ratio and also the total number of elements in the simulation, which is unfortunate. However, Ackermann *et al.* (2000) and Finch (1998) adopt the same approach in their experiments with varying initial layer thickness and other approaches (e.g. maintaining aspect ratio and/or number of elements) have comparable drawbacks (e.g. they require a change in the shape and size of the elements, and thus, changes in the spatial arrangement of material heterogeneity).

7.2.3 The mechanical effect of changing layer thickness

I have previously shown (Section 5.2) that failure of elements in the ADELI model used here depends only on deviatoric stress, and that while the material is being deformed elastically, deviatoric stress increases towards the moving wall and with depth. The deviatoric stress in each element also increases with time as the material continues to extend. Consequently, at a particular time, the deviatoric stress in equivalent elements (e.g. the element in the centre of the bottom row in each model) will be higher in a model 50 elements deep rather than 25 (Figure 7.7). Note that the pattern of deviatoric stress in the 2.5 km thick model is not quite the same as that in the upper half of the 5.0 km thick model. This results from the isostatic forces at the base of the model (the neutral plane in the thinnest model is 1.25 km below the surface, compared with 2.5 km in the thickest model).

7.2.4 Fault patterns in space and time

Initial failure occurs slightly sooner in the thicker model because of the larger overburden and consequently larger deviatoric stresses in the elements at the base of the model. However, because the time interval between snapshots is larger than time separating initial failure in the three models, we see that broken elements first appear in the same snapshot in all three models (0.85% regional extension - top plot on Figure 7.8). The failure is more widespread in the thicker model, however, reflecting the fact that elements have been failing for longer in this model.

In Section 5.2 I noted that deformation in the standard model (in which the right wall was moved) took the form of a "failure front" moving from bottom-right to top-left across the model. In addition to delaying the onset of failure, thinning the deforming layer changes the speed at which the failure front moves. Figure 7.9 shows the times at which the failure front first reaches elements on the upper surface and left hand wall in the three experiments. The time taken for the deformation front to traverse the layer from bottom to top scales with layer thickness, suggesting that the front moves upwards at the same rate regardless of the layer thickness. However, the deformation front moves more quickly from right to left in the thicker model. This is because, in the pre-failure regime as illustrated on Figure 7.8, elements far from the moving wall have a higher deviatoric stress in the thicker model than in the thinner model. Consequently, elements in the thicker model are closer to failure than their equivalents in the thinner model, and so are more susceptible to triggering by the failure of neighbouring

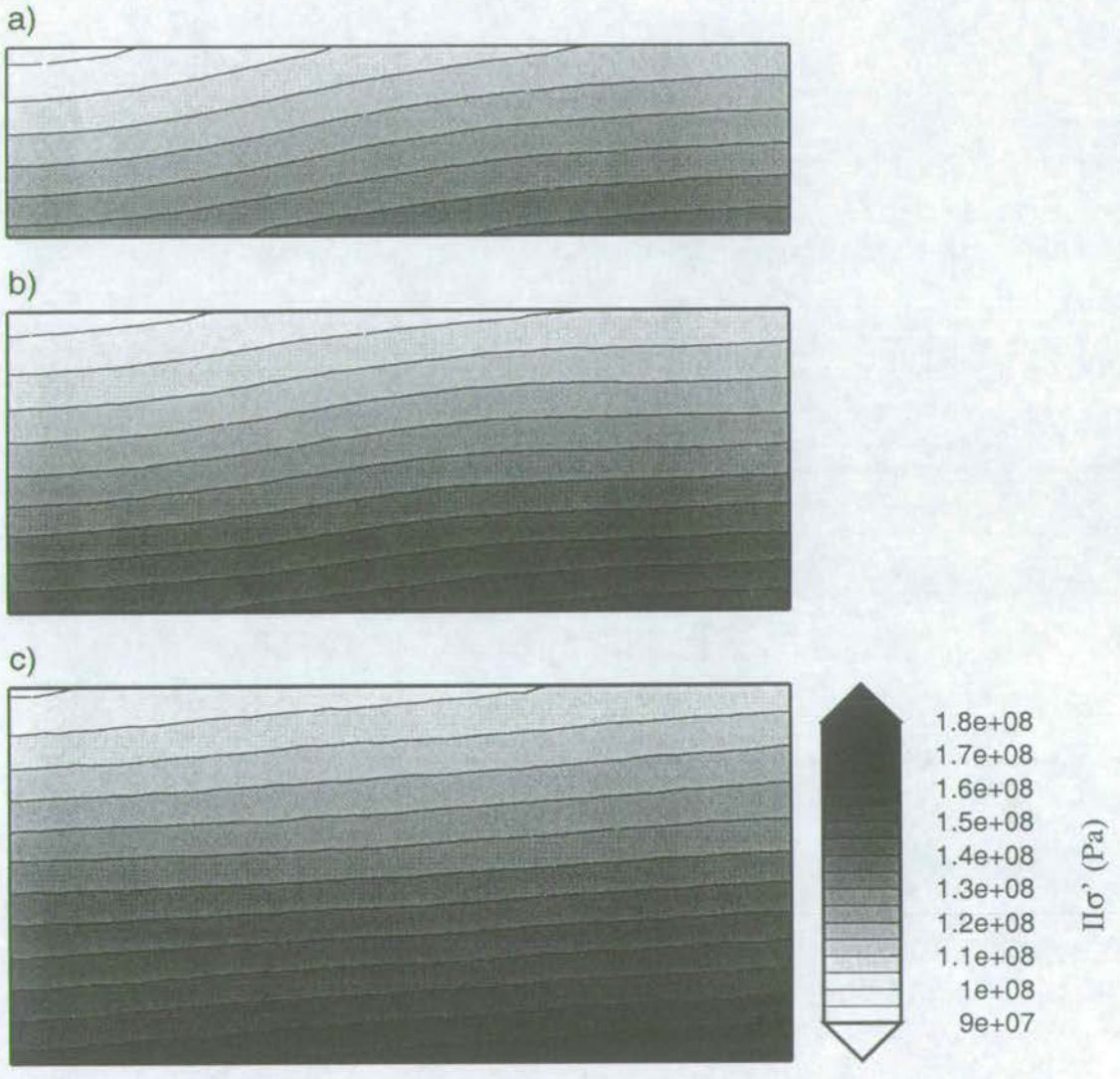

Figure 7.7. Second invariant of the deviatoric stress tensor at 0.5% extension in models a) 2.5 km, b) 4.0 km and c) 5.0 km thick.

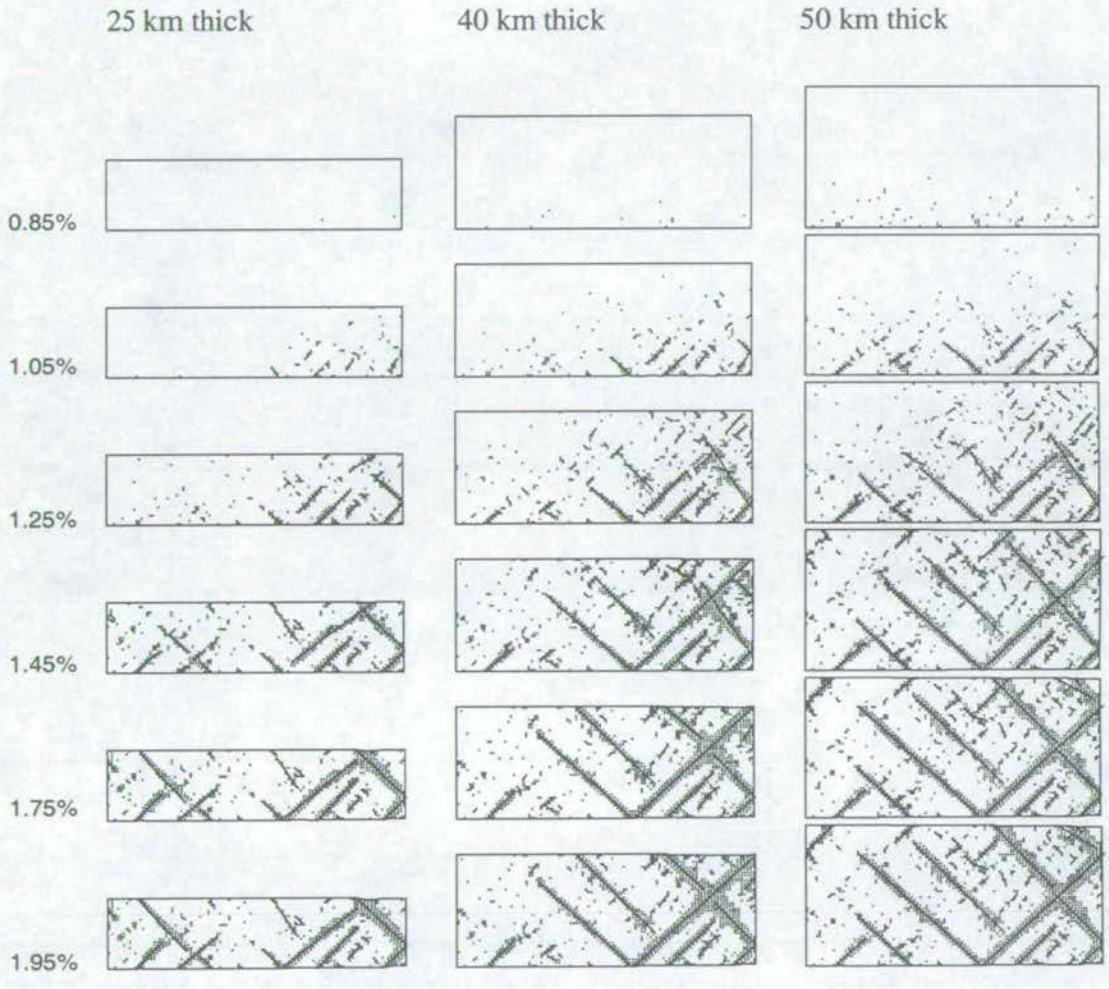

Figure 7.8. Maps of broken elements in models of different thicknesses. Regional extension at the time of each snapshot is shown on the left.

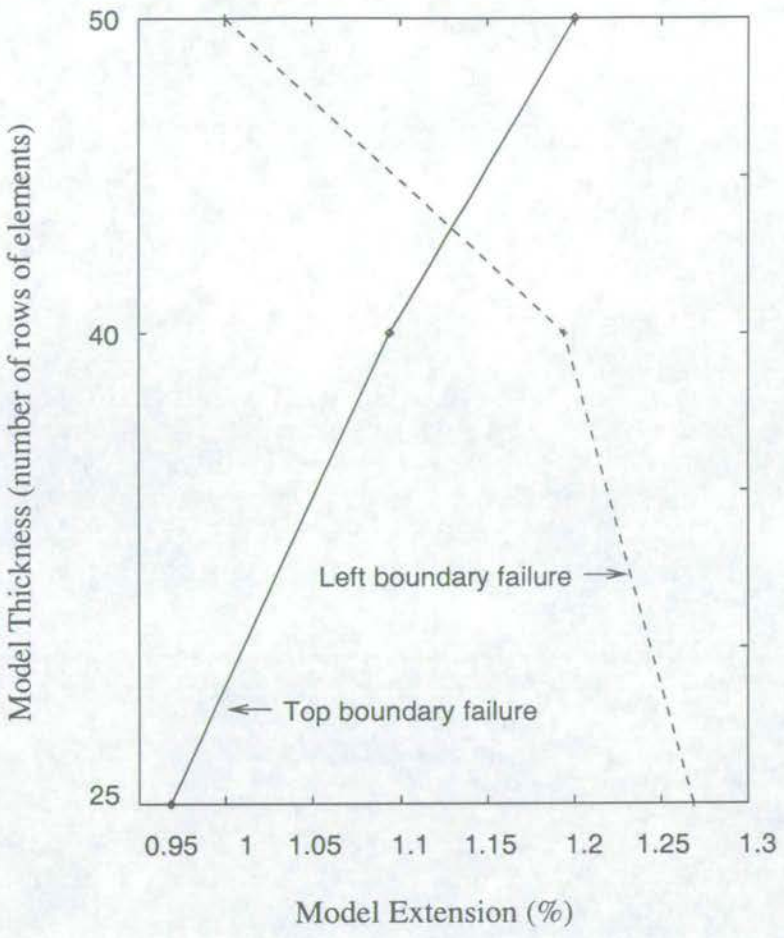

Figure 7.9. Failure times of the first perimeter elements to break versus model thickness. The failure front moves more quickly right-to-left as thickness increases. The failure front moves upwards at about the same speed in all three models (see Figure 7.8) but reaches the upper boundary later in the thickest model because it has to traverse a greater distance.

elements. The movement of the deformation front can also be seen on Figure 7.10, as can localisation of plastic strain in space for the three different layer thicknesses.

7.2.5 Fault population statistics

The percentage of elements that have broken, the size of the largest structure and the total number of structures all vary systematically with layer thickness. At any particular time/amount of regional extension, the percentage of broken elements increases as layer thickness increases (Figure 7.11). This again relates to the stress state prior to initial failure in each of the models. High deviatoric stresses persist further from the moving wall in the thicker model, meaning that more elements are closer to failure and therefore susceptible to triggering by plastic deformation in neighbouring elements, resulting in a higher proportion of failed

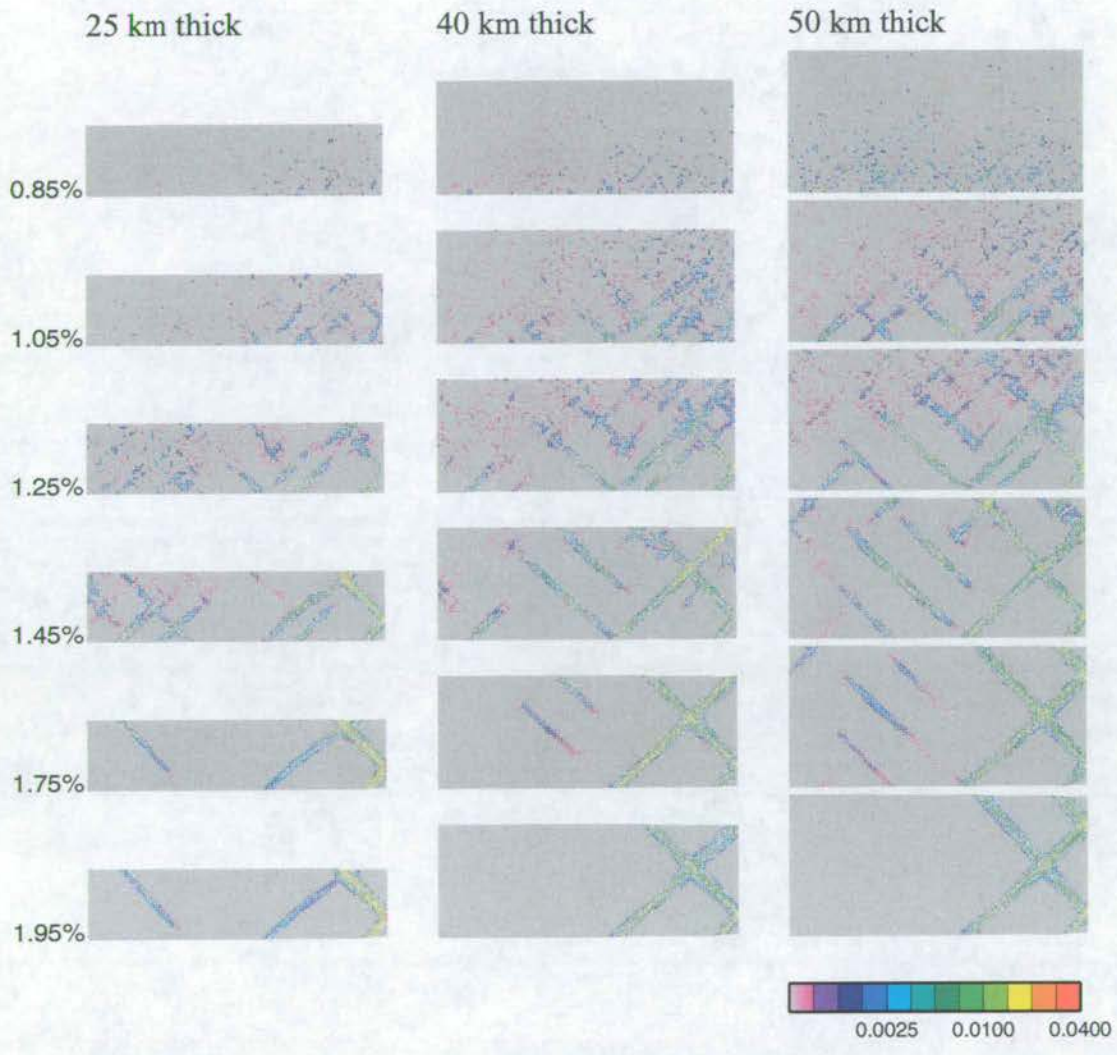

Figure 7.10. Maps of active elements in models of different thicknesses. Elements are colour-coded by how much plastic strain they have accumulated in the last 0.05% regional extension. The regional extension at the time of each snapshot is shown on the left.

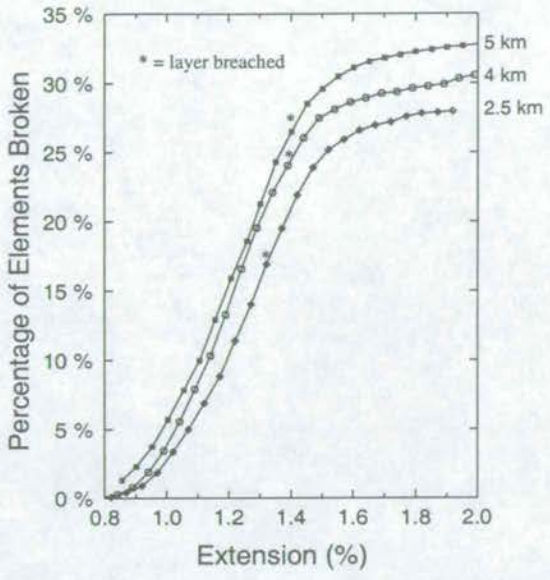

Figure 7.11. Regional extension versus the percentage of elements that have failed in simulations 2.5, 4.0 and 5.0 km thick. The time at which the layer is breached (when the top and bottom of the layer are connected by a continuous path of broken elements) is highlighted. All three curves show the same form, but proportionally more elements have failed in the thicker model at any given time. This is a function of the stress state when initial failure occurs - see text.

elements at any given time. The size of the largest fault (measured as the sum of the plastic strains in the elements belonging to the structure) increases, but does not scale linearly, with layer thickness (Figure 7.12a). The largest fault in the 5.0 km thick model is at all times more than twice as large as the largest fault in the 2.5 km thick model. The largest faults contribute proportionally less to the total strain as layer thickness increases (Figure 7.12b): strain is more localised into large structures in the thinner model. Figure 7.13 shows that, at a particular regional extension, thicker models have more faults. This figure also shows that the number of faults increases faster and peaks sooner in thicker models. As proportionally more elements break in the nucleation phase in thicker models, there are more opportunities for linkage in thicker models. Consequently, when the system moves from the nucleation-dominant to the growth/coalescence-dominant phase, the total number of faults decreases more dramatically in the thicker models. Up to about 1.5% regional extension, a lower proportion of faults are active in the thicker model (Figure 7.14).

Fault size cumulative frequency distributions for models of all thicknesses show the transition from simple power laws to more complex forms (Figure 7.16) as observed in Section 5.2.6. Before the transition, the power law exponent at a particular time is lower in the thicker model (Figure 7.15), as deformation begins earlier and progresses more rapidly as thickness increases. After the transition, the active population gives a poorer fit to a power law, so by tracking the

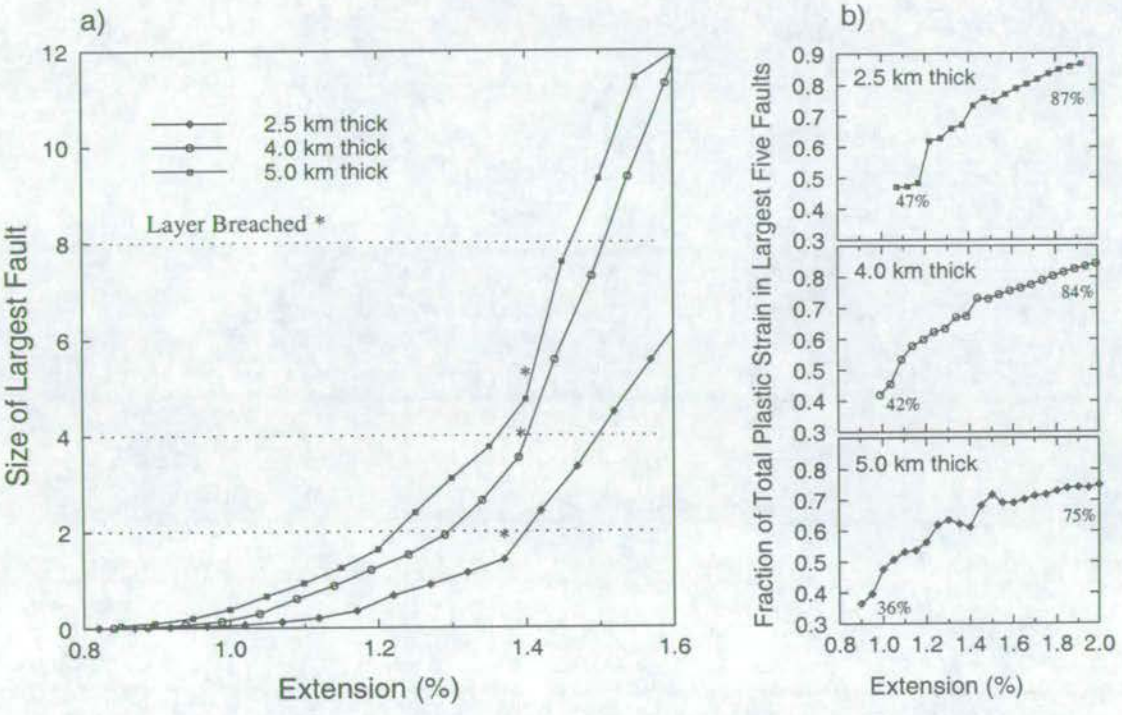

Figure 7.12. Regional extension versus a) the size of the largest fault (Smax) in the 2.5, 4.0 and 5.0 km thick models b) the percentage of the total plastic strain (summed over all elements in the mesh) in elements belonging to the five largest structures (curves shown once the total number of faults exceeds 50). Using the dotted lines as a guide, we see that Smax in the 5.0 km model is more than double Smax in the 2.5 km model, so scaling is not linear. As layer thickness increases less of the total strain is accommodated by the largest faults.

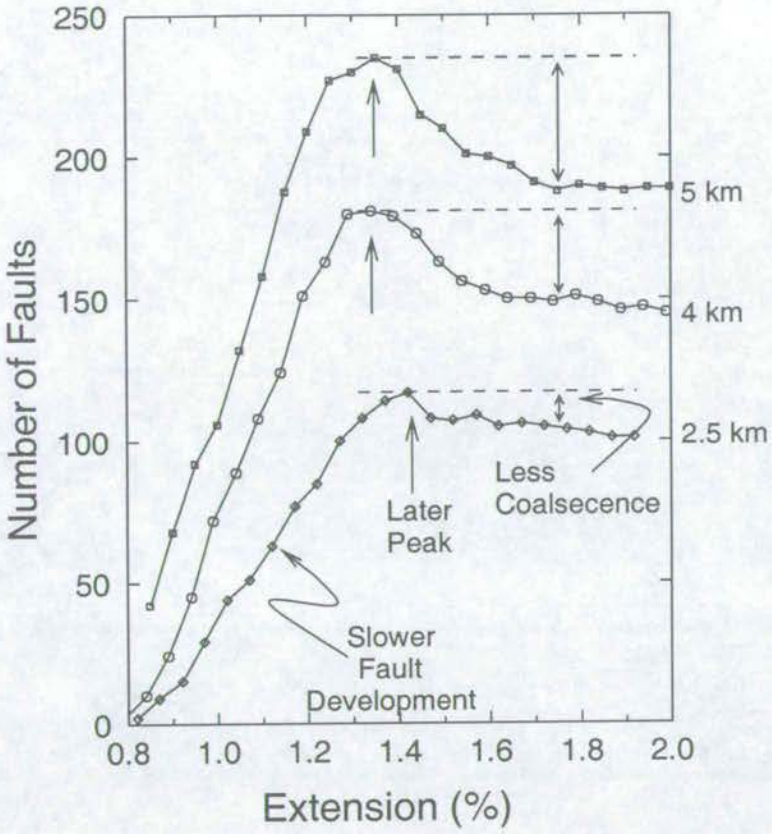

Figure 7.13. Regional extension versus the number of faults in models 2.5, 4.0 and 5.0 km thick.

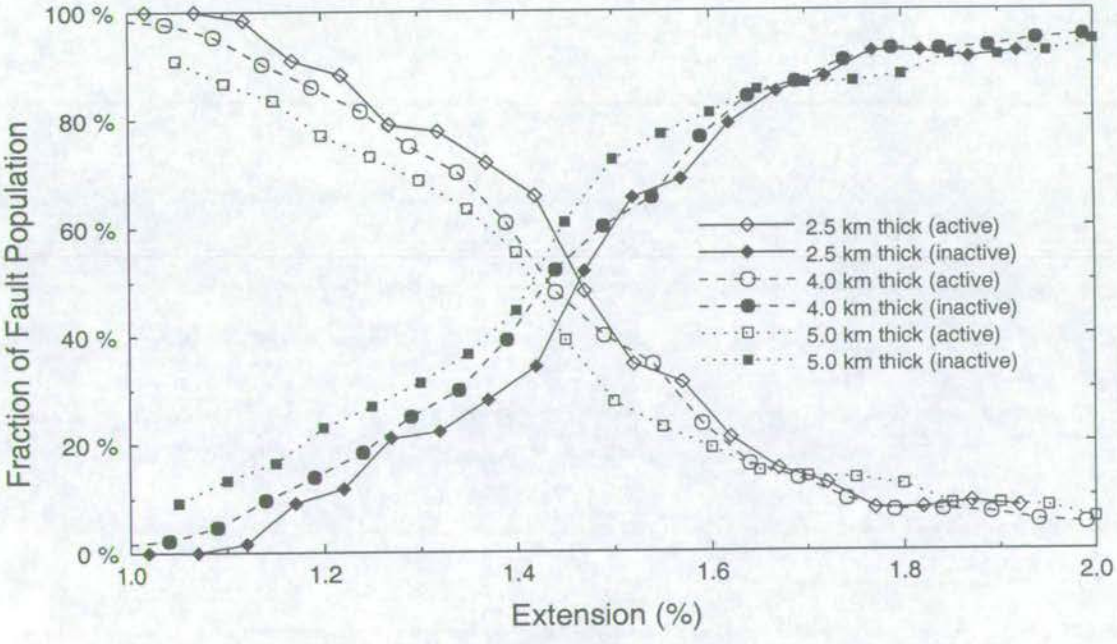

Figure 7.14. Regional extension versus the percentage of faults that are active/inactive in models 2.5, 4.0 and 5.0 km thick.

R^2 regression statistic through time, we can objectively time the crossover (Figure 7.17). The transition is gradual and occurs around the same time in the three models presented here, even though breaching of the layer occurs earlier in thinner models (Figure 7.11). Arguably, the transition occurs slightly earlier in the 4.0 km model than the 5.0 km model, but the 2.5 km model does not follow this trend. I propose that the time of the transition from power law to a more complex distribution is not solely dependent on layer thickness. As noted previously, changes in the form of the fault size frequency distribution stem from changes in the relative importance of different fault growth processes (nucleation, tip propagation and coalescence). The distributions in Figure 7.16 acquire the more complex (i.e. non-power law) shape when growth of the largest faults outstrips growth of intermediate-sized faults and nucleation of new faults. Which growth process dominates in a particular area at a particular time depends on the position of the deformation front, which in turn depends on the pre-failure stress pattern, which itself depends on the size and shape of the deforming region and the boundary conditions. In the 5.0 km model, the deformation front has traversed the model right-to-left and bottom-to-top when strain localises onto the large faults near the moving wall, producing the change in shape in the fault size distribution (around 1.4% regional extension). At this point in the 2.5 km model, the deformation front has traversed the model bottom-to-top but has yet to reach the left wall. Consequently, in the right half of the region strain is localising onto large faults, but in the left half intermediate-sized faults are still growing and faults are still nucleating. The localisation in the right half is balanced by the continued growth in the left half, and so the transition in the 2.5 km model is delayed.

7.2.6 Discussion

Several features of fault populations have been directly related to the thickness of the deforming layer by other workers. In the discrete element model of Finch (1998) (described in more detail in Section 5.3.3), layer thicknesses of 15.75, 14.0 and 12.25 km were modelled. Finch (1998) found that the thinner models had fewer broken bonds than the thicker model and fewer faults at any given time. As layer thickness decreased, the exponent of the best-fitting power law for the length cumulative frequency distribution also decreased. These observations agree with my observations of faults in cross-section, presented above.

The results of Ackermann *et al.* (2000) are not entirely consistent with my results or those of Finch (1998). Ackermann *et al.* (2000) presents two wet plaster models, with layer thicknesses of 1.8cm and 3.6cm. Firstly, they state that failure occurs much earlier in the thin model. However, because of the experimental set-up used, they can measure only those faults that

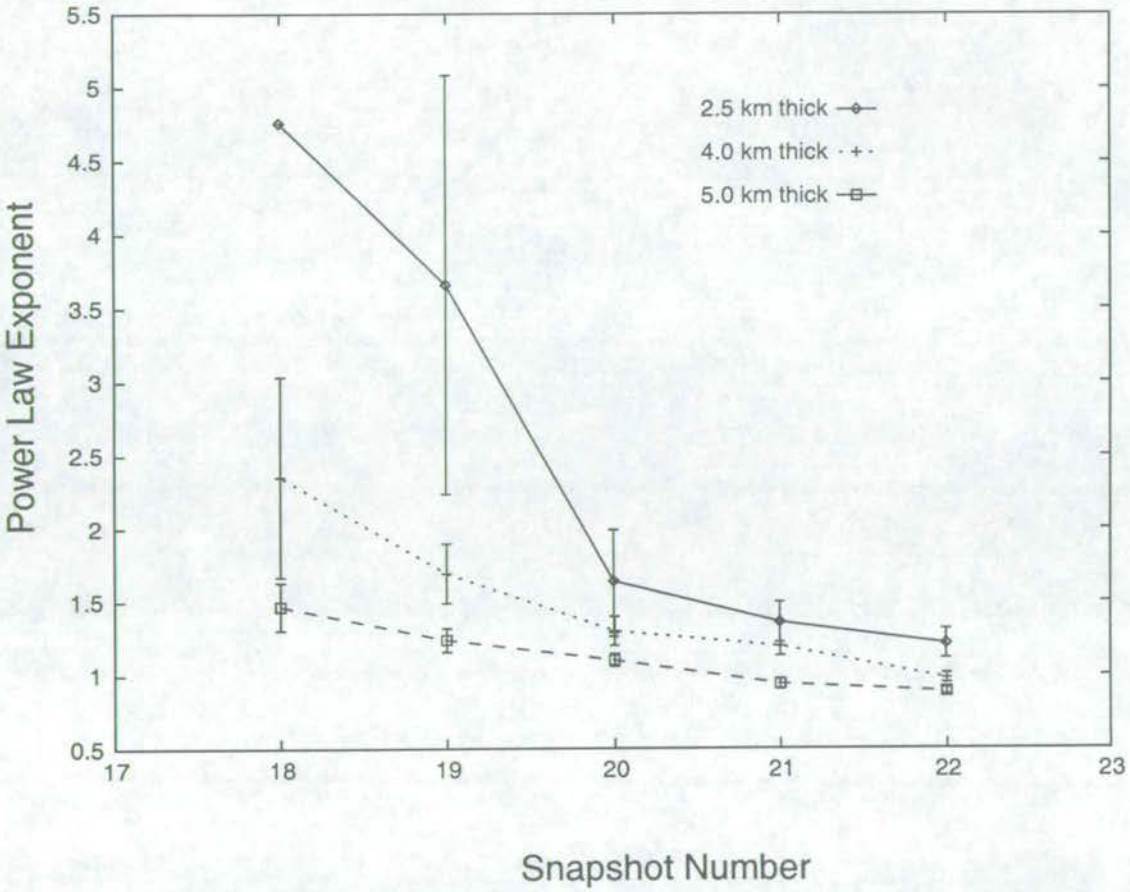

Figure 7.15. Snapshot number versus power law exponent (plus 99% confidence limits) of the whole fault population in models 2.5, 4.0 and 5.0 km thick. Each power law was fitted using linear regression after taking logs of the cumulative frequency distribution. In the power law regime (up to time 22 or 1.5% extension), thicker models have lower exponents, reflecting the fact that deformation begins earlier and progresses more rapidly as thickness increases.

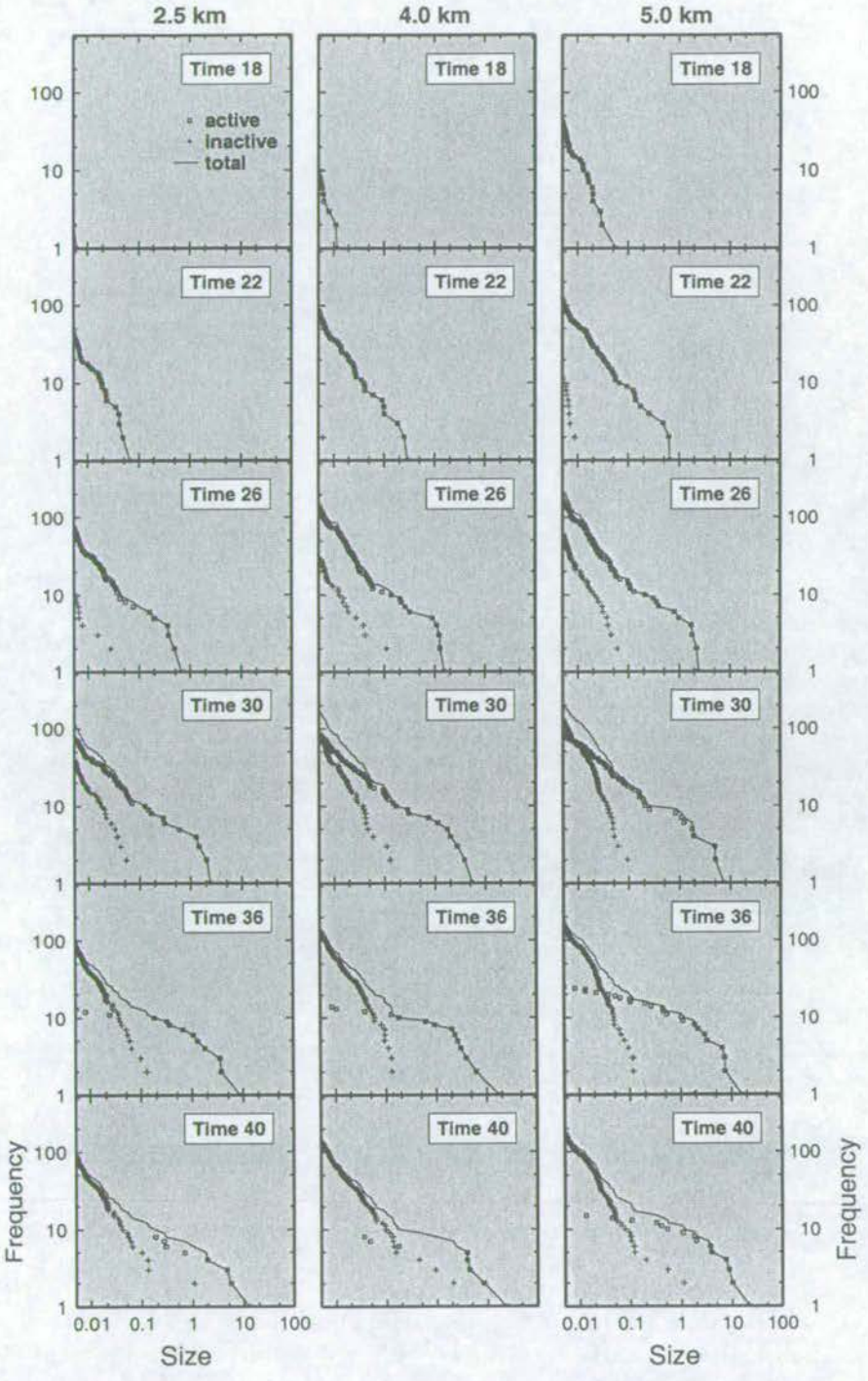

Figure 7.16. Fault size (total plastic strain) versus cumulative frequency for models 2.5, 4.0 and 5.0 km thick. Statistics for the active, inactive and whole population are plotted (see key, top left plot), the same axes are used throughout. The times on each plot refer to the snapshot number (Time 40 corresponds to 1.95% strain). In all three models, the distribution of the whole population is no longer power law by Time 26.

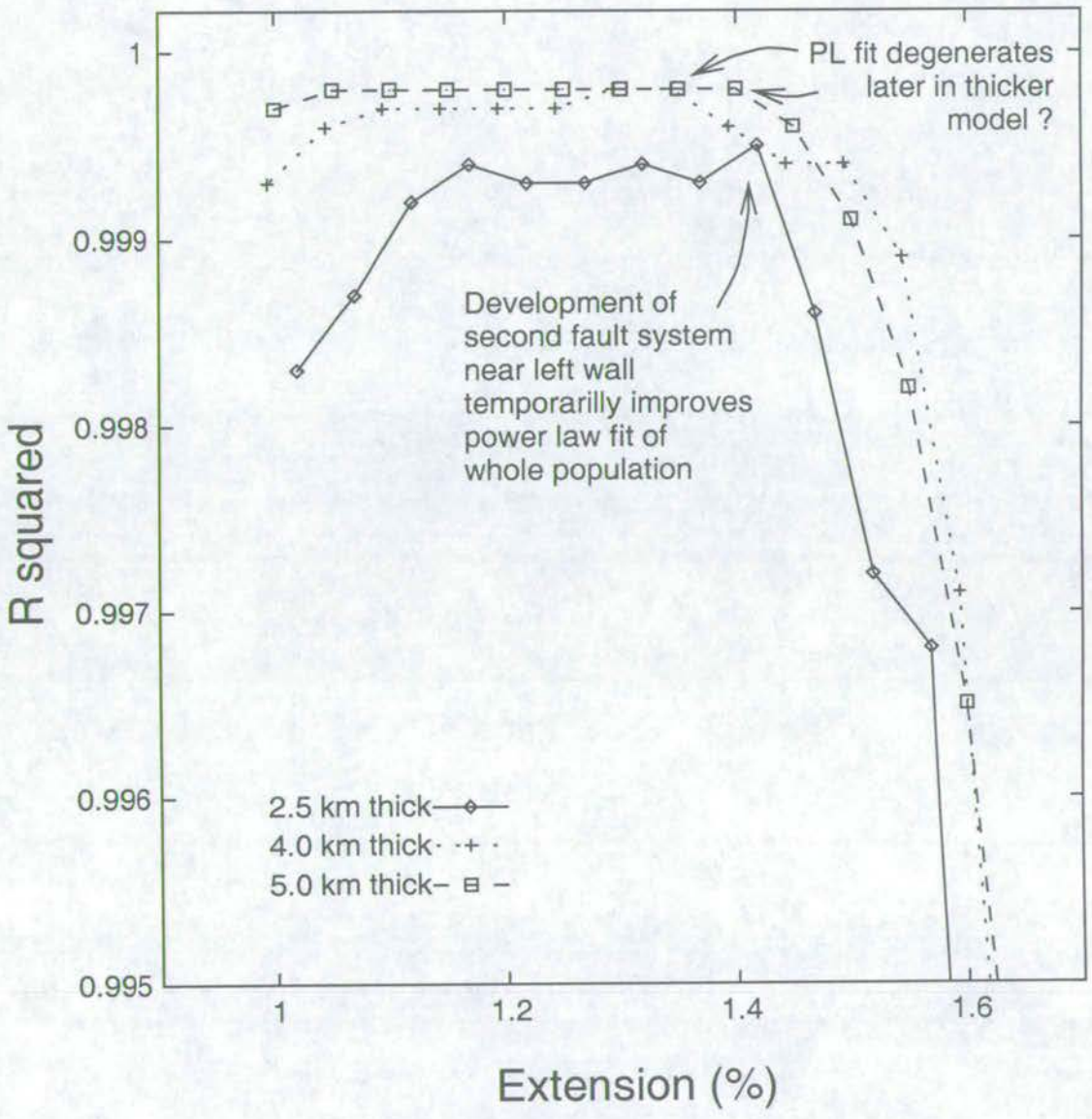

Figure 7.17. Regional extension versus the R^2 statistic for linear regression of $\log(size)$ with $\log(cumulative frequency)$ in the active population. Poorer power law fits result in a sharp decrease in R^2.

cut the top surface of the clay layer. Ackermann *et al.* (2000) make no claim that all faults initiate at the top surface and propagate downwards, so it is perhaps wiser to say that they observe that faults cut the top surface sooner in the thin model. This *is* consistent with my observations: although failure initiates later in the thinner model, faults reach the upper surface sooner because they have to propagate over a shorter distance than in the thick model. As layer thickness decreases, Ackermann *et al.* (2000) observe that the following parameters, measured at a given strain, all increase: total fault length (analogous to the number of broken elements in my simulations), maximum fault length and the number of faults. These observations are inconsistent with the results above and those of Finch (1998) and again might reflect the fact that, in the thin experiment, more faults penetrate the upper surface of the model sooner. In contrast with this study and that of Finch (1998), Ackermann *et al.* (2000) observe that the power law exponent is lower in the thicker model. This discrepancy, too, may be attributed to sampling. If faults nucleate within the deforming layer, and not at the upper surface, we would expect a lower proportion of small faults to cut the upper surface in the thicker experiment. Under-sampling the number of small faults in the system would produce a lower slope on a fault size cumulative frequency diagram on log-log axes, and so a lower power law exponent *c*. Finch (1998) and Ackermann *et al.* (2000) observe that power law size scaling breaks down later in their thicker models. My study suggests that layer thickness is only half of the story: the time taken for deformation to spread right across the model is as important in determining the time of the transition from power law to non-power law scaling as the time taken for faults to span the layer and become the main sink for additional strain.

7.3 Summary

In this chapter two external properties of the deforming region were varied: the basal boundary condition (whether isostatic or rigid) and the thickness of the layer. Changing the basal boundary condition changed the bulk kinematics imposed on the system and consequently the pattern and rate of strain localisation in space. The isostatic basal boundary condition constrained fault development more than the rigid basal boundary condition, resulting in fault patterns and size frequency distributions that were quite similar in the isostatic runs but much more variable in the rigid runs.

The stress states in the models prior to failure were different in the models with different layer thicknesses. This not only altered the pattern of nucleation but also the rate at which deformation progressed through the model. Consequently every single parameter used to

describe fault populations (percentage of broken elements, number of faults, size of the largest fault, percentage of structures that are active/inactive, power law exponent of the size frequency distribution) was found to vary systematically with layer thickness. The fault size frequency distributions lost their power law form when the growth of the largest faults outstripped the growth of intermediate-sized faults and nucleation of new faults. The processes controlling fault development are not fundamentally different in different systems but which growth process dominates in a particular area at a particular time depends on the position of the deformation front, which in turn depends on the pre-failure stress pattern, which itself depends on the deforming material, the size and shape of the deforming region and the boundary conditions.

Chapter 8

Synthesis and Conclusions

In the foregoing chapters, results and ideas generated during fieldwork and numerical modelling were accompanied by short discussions. The purpose of this chapter is to summarise my results and conclusions and put the ideas in a broader context.

8.1 The Problem of Interpreting Fault Scaling

When this project was initiated, previous work using theoretical arguments, numerical modelling and field observations did not give a consistent picture of fault size scaling. Theoretical arguments suggested that fault size frequency distributions should be power law with a universal value of c (Sornette & Davy 1991, Scholz 1997). However, observations of natural faults included power law size cumulative frequency distributions with a wide range of c values (Yielding *et al.* 1992) and some non-power law distributions too [e.g. Bohnenstiehl & Klienrock (1999)]. The early numerical models that were used to investigate fault scaling were either limited to very small percentage strains (Cowie *et al.* 1993) or had periodic boundary conditions and simple homogeneous material properties (Poliakov *et al.* 1994). In these models, linkage was identified as a growth process leading to lowering c values with increasing deformation (Cowie *et al.* 1993). Other geometrical models also suggested that c should relate to total strain (Cladouhos & Marrett 1996). However, attempts to interpret the power law exponents of real populations in terms of the total strain experienced by the faulted region had limited success (Cladouhos & Marrett 1996). The aim of this project was to attempt to resolve this confusion, by considering other potential controls on fault size scaling as well as growth processes such as linkage.

The first step was to gain evidence that factors other than the mode of fault growth (nucleation, isolated growth, linkage) influence size frequency distributions. This evidence came from the Chimney Rock Fault Array, Utah, where the fault size cumulative frequency distribution follows a power law with a low exponent, c, even though the orthorhombic geometry of the faults inhibits growth by linkage (Section 2.7.4). However, studies of two other orthorhombic arrays revealed that low exponent power law distributions do not characterise all such arrays. In Section 5.3.3, I presented further examples of low exponent, power law fault size distributions from published analogue and numerical simulations where fault growth by linkage was only a minor growth mechanism. The second step was to generate populations of faults in a 2D numerical model with heterogeneous material properties, under a range of initial and boundary conditions. The aim was to provide alternative explanations for the observed variation in natural fault size frequency distributions.

8.2 The Significance of c

Fault populations generated in the numerical simulations showed both power law and non-power law distribution types, and the power law distributions showed a range of values of c. No evidence was found to support the idea of an attracting or universal value of c. In each simulation, the exponent c of the fault size cumulative frequency distribution was observed to decrease with increasing extension; this was partly due to coalescence, but also because larger faults grew disproportionately faster than smaller ones. This is the first time that activity and growth rates rather than a specific growth mechanism has been invoked as the cause of low exponent power law size frequency distributions.

The dependence of c on total strain was weak and easily masked by other contributing factors. I found that the exponent c varied systematically with material properties: c decreased as heterogeneity decreased and strength loss on failure increased (Figures 6.10 and 6.14). By decreasing the strength range from 0 to 75 MPa, exponents ranging from 0.5326 ± 0.045 to 0.7819 ± 0.015 at the same amount of total strain were generated. Simulations with statistically identical material properties but different random heterogeneity in space gave power law distributions with significantly different values of c (Figure 6.1). At low strains in the models with different spatial heterogeneity, c ranged from 0.9429 to 1.273 (errors on these values were typically < 0.05). At higher strains, the exponents of the distributions varied from 0.6652 to 1.1005 (with similar typical errors). In comparison, within a single simulation, c typically changed by only 0.25 as regional strain increased. Assuming that the natural system

is similarly sensitive to the spatial arrangement of weaknesses, it is unsurprising that attempts to relate the power law exponent of real populations to the total strain have had little success. This result further implies that extrapolating a scaling law derived in one area into an adjacent area is inadvisable, even if the rock types and deformation histories in the two areas are the same.

8.3 Breaks in Power Law Scaling

In all simulations presented in this study, as strain increased, a larger proportion of small faults became inactive and more faults became constrained as their tips abutted other structures or intersected with the perimeter of the model. Unconstrained, small faults in this model grow by lengthening and widening, whereas the constrained faults can only grow by widening, so as strain increased, faults of different sizes grew by different mechanisms. As a result, small and large faults no longer described a single power law for fault sizes. At higher strains, the size distribution of large, active faults was better fitted by an exponential, rather than power law, relationship. The initial conditions (e.g. rheology) and the boundary conditions (e.g. whether the base is rigid or isostatically compensated) controlled how fast strain localised onto the large structures (Section 7.1) and the size and shape of the deforming region influenced when the major faults became constrained (Section 7.2).

Analogue modellers (Ackermann *et al.* 2000, Clifton *et al.* 2000) and some workers in the field (Ackermann & Schlische 1997) link breaks in scaling to faults first spanning the mechanical layer in which they form. This thesis is the first study to document scaling breakdown due instead to the focusing of strain onto faults of certain sizes, or in certain locations, in response to the rheology of the deforming material and the boundary conditions, not simply layer thickness alone. The breakdown in scaling occurs at larger strains, suggesting that extrapolating scaling relationships beyond the range of observation is more likely to give incorrect estimates in higher strain regions.

Although breaks in scaling have been reported frequently in physical analogue models, few studies document their existence in natural fault populations. Layering is a key difference between models in which breaks in scaling have been observed and nature: the model used in this study and the plaster models of Ackermann *et al.* (2000), Clifton *et al.* (2000) and Spyropoulos *et al.* (1999b) contain one isotropic layer, whereas in reality, as faults grow they encounter and breach multiple mechanical layers. Consequently, they may go through several

phases of being constrained and unconstrained with respect to different layers and phases of being relatively weak or strong, if the layers have significantly different strengths. Fault size frequency distributions even more complicated than the disjointed distributions observed in this study would surely result. Fitting a single power law exponent to such a distribution would be of questionable value.

8.4 Further Work

Clearly not all possible controls on faulting have been investigated in this study. Some controls cannot be investigated using the current implementation of ADELI. These include the influence of fluids on faulting, how temperature variation in the crust affects rheology (and so faulting) and the three dimensional nature of faults. However, other factors that might influence faulting could be usefully investigated using this model:

- The amplitude of the heterogeneity (the standard deviation of the normal distribution of strengths) and the stress drop on failure were internal properties investigated in this study found to affect fault population development. It would be useful to quantify the effect of other parameters, such as the mean of the normal distribution and to use other forms for the frequency distribution.
- In this study, heterogeneity of material properties always took the form of random, uncorrelated noise. It might be geologically more realistic to include layering or other forms of correlated variation in material properties.
- At present, both the boundary conditions and the micro-rheology (constitutive law for each element) favour localisation of strain onto preferred faults. Faults are thought to recover some strength after failing (Cowie *et al.* 1993), so how would a healing micro-rheology influence fault growth and size frequency statistics?
- The yield criterion used in this study (Von Mises) is clearly unrealistic in that it takes no account of mean stress (pressure). It would be useful to perform a similar study incorporating a pressure sensitive yield criterion; for example using the Drucker Prager criterion with variation in cohesion rather than friction angle to provide yield strength heterogeneity without variable post-yield behaviour.

Work on fault populations to date has been frustrated by the difference in the dimensionality of the faulting phenomenon (4D - three spatial dimensions plus time) and the dimensionality

of observations and simulation methods. In many analogue models only faults that cut the top surface can be monitored through time, fault size can only be measured using proxies like trace length or maximum displacement and faults within the layer and only be examined by cutting the model into a series of cross-sections at the end of the experiment. By using the innovative X-ray tomography techniques pioneered by Colletta *et al.* (1991), analogue modellers can now make better measurements of fault size, like displacement integrated over the fault surface. They can also image faults enclosed within the layer and study the development of all faults through time. However, even these sophisticated models suffer the problems all physical analogue models face: difficulties characterising the rheology and heterogeneity of the modelling material and also reproducibility. Some fully three-dimensional numerical codes, without periodic boundary conditions, have recently been developed [e.g. Finch (2000), Tuckwell (2000*b*) and Niño (2000)] which will enable the measurements described above to be interpreted in terms of stress. The present study incorporates only one isotropic, if heterogeneous, layer. With a 3D model, we could answer the question " When fault tip lines encounter multiple layers, and limited horizontal as well as vertical dimensions of the deforming region, how do fault population statistics respond?" Also, a 3D model would allow us to study for the first time the development of orthorhombic fault populations and their size distributions.

References

Ackermann, R. & Schlische, R. (1997), 'Anticlustering of normal faults around larger faults', *Geology* **25**(12), 1127–1130.

Ackermann, R. & Schlische, R. (1999), Uh oh! $n < 1$: Dynamic length-displacement scaling, *in* 'AGU Spring Meeting Abstracts, supplement to Eos vol88, number 17', p. S328.

Ackermann, R., Schlische, R. & Withjack, M. (1997), Systematics of an evolving population of normal faults in scaled physical models., *in* 'Abstracts with Program, Annual Meeting', Geological Society of America.

Ackermann, R., Withjack, M. & Schlische, R. (2000), 'The geometric and statistical evolution of normal fault systems: An experimental study of the effects of mechanical layer thickness on scaling laws.', *Journal of Structural Geology (in press)* **0**(0), 0–35.

Aharonov, E. (1999), On phase transitions and liquefaction in fault gouge., *in* 'AGU Spring Meeting Abstracts, supplement to Eos Volume 80, Number 17', American Geophysical Union., p. S329.

Anderson, E. (1951), *The Dynamics of Faulting.*, Oliver and Boyd., London.

Aydin, A. & Johnson, A. (1978), 'Development of faults as zones of deformation bands and slip surfaces in sandstone.', *Pure and applied geophysics* **116**, 931–942.

Aydin, A. & Reches, Z. (1982), 'Number and orientation of fault sets in the field and in experiments.', *Geology* **10**, 107–112.

Baidyuk, B. (1967), *Mechanical properties of rocks.*, Consultants Bureau, New York.

Ball, P. (1993), *The self-made tapestry.*, Oxford University Press, Oxford.

Barnett, J., Mortimer, J., Rippon, J., Walsh, J. & Watterson, J. (1987), 'Displacement geometry in the volume containing a single normal fault.', *Bulletin of The American Association of Petroleum Geologists* **71**, 925–937.

Barnichon, J. D. & Charlier, R. (1996), Finite element modelling of the competition between shear bands in the early stages of thrusting: Strain localization analysis and constitutive law influence., *in* P. G. Buchanan & D. A. Nieuwland, eds, 'Modern developments in structural interpretation, validation and modelling.', number 99 *in* 'Special Publications', Geological Society of London., pp. 235–250.

Barton, C. & Zoback, M. (1992), 'Self-similar distribution and properties of macroscopic fractures at depth in crystalline rock in the Cajon Pass scientific drillhole.', *Journal of Geophysical Research* **97**(B4), 5181–5200.

Bath, M. (1981), 'Earthquake magnitude - recent research and current trends.', *Earth Science Review* **17**, 315–398.

Belytschko, T., Chiang, H.-Y. & Plaskacz, E. (1994), 'High resolution two-dimensional shear band computations: imperfections and mesh dependence.', *Computer Methods in Applied Mechanics and Engineering.* **119**, 1–15.

Berkowitz, B. & Adler, P. (1998), 'Stereological analysis of fracture network structure in geological formations.', *Journal of Geophysical Research.* **103**(B7), 15339–15360.

Blackstone, D. (1988), 'Travellers guide to the geology of Wyoming.', *Bulletin of the Geological Survey of Wyoming* **67**, All pages.

Bohnenstiehl, D. & Klienrock, M. (1999), 'Faulting and fault scaling on the median valley floor of the trans-Atlantic geotraverse (TAG) segment, 26°N on the Mid-Atlantic Ridge', *Journal of Geophysical Research* **104**(B12), 29,351–29,364.

Borgos, H., Cowie, P. & Dawers, N. (2000), 'Practicalities of extrapolating 1D fault and fracture size-frequency distributions to higher dimensional samples.', *Journal of Geophysical Research (in press).*

Brace, W., Paulding, B. & Scholz, C. (1966), 'Dilatancy in the fracture of crystalline rocks.', *Journal of Geophysical Research* **71**, 3939–3953.

Bruhn, R. & Pavlis, T. (1981), 'Late Cenozoic deformation in the Matanuska Valley, Alaska: Three-dimensional strain in a fore-arc region.', *Geological Society of America Bulletin* **92**(1), 282–293.

Brune, J. & Ellis, M. (1997), 'Structural features in a brittle-ductile wax model of continental extension.', *Nature* **387**, 69–70.

Bürgmann, R., Pollard, D. & Martel, S. (1994), 'Slip distributions on faults: Effects of stress gradients, inelastic deformation, heterogeneous host-rock stiffness, and fault interaction.', *Journal of Structural Geology* **16**, 1675–1690.

Carbotte, S. & Macdonald, K. (1994), 'Comparison of seafloor tectonic fabric at intermediate, fast and super fast spreading ridges: Influence of spreading rate, plate motions and ridge segmentation on fault patterns', *Journal of Geophysical Research* **99**(B7), 13,609–13,631.

Cartwright, J., Trudgill, B. & Mansfield, C. (1995), 'Fault growth by segment linkage: an explanation for scatter in maximum displacement and trace length data from the Canyonlands Grabens of SE Utah.', *Journal of Structural Geology* **17**(9), 1319–1326.

Castaing, C., Halawani, M., Gervais, F., Chilés, J., Genter, A., Bourgine, B., Ouillon, G., Brosse, J., Martin, P., Genna, A. & Janjou, D. (1996), 'Scaling relationships in intraplate fracture systems related to Red Sea rifting', *Tectonophysics* **261**, 291–314.

Childs, C., Nicol, A., Walsh, J. J. & Watterson, J. (1996), 'Growth of vertically segmented normal faults', *Journal of Structural Geology* **18**(12), 1389–1397.

Childs, C., Walsh, J. & Watterson, J. (1990), A method for estimation of the density of fault displacements below the limits of seismic resolution, *in* A. Buller, ed., 'North Sea Oil and Gas Reservoirs II', Norwegian Institute of Technology.

Childs, C., Walsh, J. J. & Watterson, J. (1995), 'Fault overlap zones within developing normal fault systems.', *Journal of Structural Geology* **152**(12), 535–549.

Cladouhos, T. & Marrett, R. (1996), 'Are fault growth and linkage models consistent with power-law distributions of fault lengths?', *Journal of Structural Geology* **18**(2/3), 281–293.

Clarke, R., Cox, S. & Laslett, G. (1999), 'Generalizations of power-law distributions applicable to sampled fault-trace lengths: model choice, parameter estimation and caveats.', *Geophysical Journal International* **136**, 357–372.

Clifton, A. & Schlische, R. (1997), Using scaled physical models of oblique deformation to analyze the spatial and temporal evolution of fault systems., *in* 'Abstracts with Program, Annual Meeting', Vol. 29/6, Geological Society of America, pp. A–258.

Clifton, A., Schlische, R., Withjack, M. & Ackermann, R. (2000), 'Influence of rift obliquity on fault-population systematics: results of experimental clay models.', *Journal of Structural Geology* **22**, 1491–1509.

Colletta, B., Letouzey, J., Pinedo, R., Ballard, J. & Bale, P. (1991), 'Computerized x-ray tomography analysis of sandbox models - examples of thin-skinned thrust systems', *Geology* **19**(11), 1063–1067.

Contreras, J., Anders, M. & Scholz, C. (2000), 'Growth of a normal fault system: observations form the Lake Malawi basin of the east African rift', *Journal of Structural Geology* **22**(1), 159–168.

Cowie, P. (1998a), Normal fault growth in three-dimensions in continental and oceanic crust., *in* R. Buck, P. Delaney, J. Karsen & Y. Lagabrielle, eds, 'Faulting and magmatism at mid-ocean ridges.', number 106 *in* 'Geophysical monograph series', American Geophysical Union, pp. 325–347.

Cowie, P. (1998b), 'A healing-reloading feedback control on the growth rate of seismogenic faults.', *Journal of Structural Geology* **20**, 1075–1087.

Cowie, P. & Scholz, C. (1992*a*), 'Displacement-length scaling relationship for faults: data synthesis and discussion.', *Journal of Structural Geology* **14**, 1149–1156.

Cowie, P. & Scholz, C. (1992*b*), 'Physical explanation for displacement-length scaling relationship of faults using a post-yield fracture mechanics model.', *Journal of Structural Geology* **14**, 1133–1148.

Cowie, P. & Shipton, Z. (1998), 'Fault displacement gradients and process zone dimensions.', *Journal of Structural Geology* **20**, 983–997.

Cowie, P., Malinverno, A., Ryan, W. & Edwards, M. (1994), 'Quantitative fault studies on the East Pacific Rise: A comparison of sonar imaging techniques.', *Journal of Geophysical Research* **99**, 15,205–15,218.

Cowie, P., Sornette, D. & Vanneste, C. (1995), 'Multifractal scaling properties of a growing fault population.', *Geophysical Journal International.* **122**, 457–469.

Cowie, P., Vanneste, C. & Sornette, D. (1993), 'Statistical physics model for the spatiotemporal evolution of faults.', *Journal of Geophysical Research* **98**(B12), 21809–21821.

Cox, S. & Paterson, L. (1989), 'Tensile failure of heterogeneous solids with distributed breaking strengths.', *Physical Review B* **40**(7), 4690–4695.

Cox, S. & Paterson, L. (1990), Damage development during rupture of heterogeneous brittle materials: a numerical study., *in* R. Knipe & E. Rutter, eds, 'Deformation mechanisms, rheology and tectonics.', number 54 *in* 'Special Publications', Geological Society of London, pp. 57–62.

Crider, J. & Pollard, D. (1996a), Breached normal fault relays and the generation of fault patterns: results from 3D numerical models and field observation, *in* 'Abstracts with Program, Annual Meeting', Vol. 28, Geological Society of America, p. 242.

Crider, J. & Pollard, D. (1996b), Anatomy and evolution of a normal fault relay ramp, *in* 'AGU Fall Meeting Abstracts, supplement to Eos Vol. 77, number 46', p. 643.

Cundall, P. (1989), 'Numerical experiments on localization in frictional materials.', *Ingenieur Archives* **58**, 148–159.

Cundall, P. & Board, M. (1988), 'A microcomputer program for modelling large strain plasticity problems.', *Numerical Methods in Geomechanics.*

Davis, G. (1978), 'Monocline fold patterns of the Colorado Plateau.', *Geological Society of America Memoir* **151**, 215.

Davis, J. (1986), *Statistics and Data Analysis in Geology*, John Wiley and Sons, Inc., New York.

Davis, R. & Fletcher, R. (1990), Shear bands in a plastic layer at yield under combined shortening and shear: a model for the fault array in a duplex., *in* R. Knipe & E. Rutter, eds, 'Deformation mechanisms, rheology and tectonics.', number 54 *in* 'Special Publications', Geological Society of London, pp. 123–131.

Davy, P. (1993), 'On the frequency-length distribution of the San Andreas fault system', *Journal of Geophysical Research Solid Earth* **98**(B7), 12141–12151.

Davy, P., Hansen, A., Bonnet, E. & Zhang, S.-H. (1995), 'Localization and fault growth in layered brittle-ductile systems: Implications for deformations of the lithosphere.', *Journal of Geophysical Research* **100**(B4), 6281–6294.

Dawers, N. & Anders, M. (1995), 'Displacement-length scaling and fault linkage', *Journal of Structural Geology* **17**, 607–614.

Dawers, N., Anders, M. & Scholz, C. (1993), 'Growth of normal faults: Displacement-length scaling', *Geology* **21**, 1107–1110.

Donath, F. (1962), 'Analysis of Basin and Range structure South Central Oregon.', *Geological Society of America Bulletin* **73**, 1–16.

Dresden, G., Gwildis, U. & Kluegel, T. (1991), Numerical and analogue modelling of normal fault geometry., *in* A. Roberts, G. Yielding & B. Freeman, eds, 'The geometry of normal faults.', number 56 *in* 'Special Publications', Geological Society of London, pp. 207–217.

Drucker, D. & Prager, W. (1952), 'Soil mechanics and plastic analysis of limit design.', *Quarterly Journal of Applied Mathematics* **10**, 157–165.

Finch, E. (1998), A crustal lattice solid model: The evolution geometry and scaling of tectonic extension., Phd, University of Ulster.

Finch, E. (2000), Personal web page, www.man.ac.uk/Geology/research /BSG/efinch.html.

Fossen, H. & Gabrielsen, R. (1996), 'Experimental modelling of extensional fault systems by use of plaster.', *Journal of Structural Geology* **18**(5), 673–687.

Fossen, H. & Hesthammer, J. (1997), 'Small faults and their significance in porous sandstone reservoirs.', *First Break*.

Fossen, H. & Hesthammer, J. (2000), 'Possible absence of small faults in the Gullfaks Field, northern North Sea: implications for downscaling of faults in some porous sandstones.', *Journal of Structural Geology* **22**, 851–863.

Fossen, H. & Rørnes, A. (1996), 'Properties of fault populations in the Gullfaks Field, northern North Sea.', *Journal of Structural Geology* **18**(2/3), 179–190.

Freund, R. (1974), 'Kinematics of transform and transcurrent faults.', *Tectonophysics* **21**, 93–134.

Gabrielsen, R. & Koestler, A. (1987), Description and structural implications of fractures in late Jurassic sandstones of the Troll Field, northern North Sea, *in* Koestler & Olaussen, eds, 'Tectonics and deposition in sedimentary basins.', number 67 *in* 'Proceedings of the 4th TSGS Conference, Stavanger 1986', Norsk Geologisk Tindskrift, pp. 371–382.

Gauthier, B. & Lake, S. (1993), 'Probabilistic modelling of faults below the limit of seismic resolution in Pelican Field, North Sea, offshore United Kingdom.', *The American Association of Petroleum Geologists Bulletin.* **77**(5), 761–777.

Gerbault, M., Poliakov, A. & Daignieres, M. (1998), 'Prediction of faulting from the theories of elasticity and plasticity: What are the limits?', *Journal of Structural Geology* **20**(2/3), 301–320.

Gillespie, P., Walsh, J. & Watterson, J. (1992), 'Limitations of dimension and displacement data from single faults and the consequences for data analysis and interpretation.', *Journal of Structural Geology* **14**(10), 1157–1172.

Golombek, M., Banerdt, W., Tanaka, K. & Tralli, D. (1992), 'A prediction of Mars seismicity from surface faulting.', *Science* **258**, 979–981.

Gross, M., Gutierrez-Alonso, G., Bai, T., Wacker, M., Collinsworth, K. & Behl, R. (1997), 'Influence of mechanical stratigraphy and kinematics on fault scaling relations', *Journal of Structural Geology* **19**(2), 171–183.

Gross, S. (1999), Appropriate statistics for stress triggering, *in* 'AGU Spring Meeting Abstracts, supplement to Eos Vol.80, number 17', p. S324.

Gudmundsson, A. (1987), 'Geometry, formation and development of tectonic fractures on the Rekjanes Peninsula, southwest Iceland', *Tectonophysics* **139**, 295–308.

Gudmundsson, A. (2000), 'Fracture dimensions, displacements and fluid transport', *Journal of Structural Geology* **22**, 1221–1231.

Gupta, S., Underhill, J., Sharp, I. & Gawthorpe, R. (1999), 'Role of fault interactions in controlling synrift sediment dispersal patterns: Miocene, Abu Alaqa Group, Suez Rift Sinai, Egypt.', *Basin Research* **11**, 167–189.

Handge, U. A., Sokolov, I. M. & Blumen, A. (1997), 'Fragmentation of viscoelastic surface layers.', *Europhys. Lett.* **40**, 275–280.

Harris, R. (1998), 'Introduction to special section: Stress triggers, stress shadows and implication for seismic hazard.', *Journal of Geophysical Research* **103**(B10), 24,374–24,358.

Hassani, R. (1994), Modélisation numérique de la déformation des systèmes géologiques., Thèse de Doctorat, Universite de Montpellier II.

Hassani, R. & Chéry, J. (1996), 'Anelasticity explains topography associated with Basin and Range normal faulting.', *Geology* **24**(12), 1095–1098.

Hassani, R., Jongmans, D. & Chéry, J. (1997), 'Study of plate deformation and stress in subduction processes using two-dimensional numerical models.', *Journal of Geophysical Research* **102**(B8), 17,951–17,965.

Hatton, C., Main, I. & Meredith, P. (1994), 'Non-universal scaling of fracture length and opening displacement.', *Nature* **367**, 160–162.

Heimpel, M. & Olson, P. (1996), 'A seismodynamical model of lithosphere deformation: Development of continental and oceanic rift networks.', *Journal of Geophysical Research* **101**(B7), 16155–16176.

Higgins, R. & Harris, L. (1997), 'The effect of cover composition on extensional faulting above re-activated basement fault: results from analogue modelling', *Journal of Structural Geology* **19**(1), 89–98.

Hill, R. (1950), *The Mathematical Theory of Plasticity*, University Press, Oxford.

Hobbs, B., Mülhaus, H. & Ord, A. (1990), Instability, softening and localization of deformation., *in* R. Knipe & E. Rutter, eds, 'Deformation mechanisms, rheology and tectonics.', number 54 *in* 'Special Publications', Geological Society of London, pp. 143–165.

Homberg, C., Hu, J., Angelier, J., Bergerat, F. & Lacombe, O. (1997), 'Characterisation of stress perturbations near major fault zones: insights from 2-d distinct element numerical modelling and field studies.', *Journal of Structural Geology* **19**(5), 703–718.

Horsfield, W. (1980), 'Contemporaneous movement along crossing conjugate normal faults.', *Journal of Structural Geology* **2**(3), 305–310.

Huc, M., Hassani, R. & Chéry, J. (1998), 'Large earthquake nucleation associated with stress exchange between middle and upper crust.', *Geophysical Research Letters* **25**(4), 551–554.

Illies, J. (1977), Ancient and recent rifting in the Rhinegraben, *in* 'Fault tectonics in N.W. Europe.', number 56 *in* 'Geologie en Mijnbouw', pp. 329–350.

Ishikawa, M. & Otsuki, K. (1995), 'Effects of strain gradients on asymmetry of experimental normal fault systems.', *Journal of Structural Geology* **17**(7), 1047–1053.

Jackson, J. & Leeder, M. (1994), 'Drainage systems and the development of normal faults: an example from Pleasant Valley, Nevada.', *Journal of Structural Geology* **16**, 1041–1059.

Jackson, J. & McKenzie, D. (1983), 'The geometrical evolution of normal fault systems.', *Journal of Structural Geology* **5**(5), 471–482.

Jackson, J. & White, N. (1989), 'Normal faulting in the upper continental crust: observations from regions of active extension.', *Journal of Structural Geology* **11**, 15–36.

Jaeger, J. & Cook, N. (1968), *Fundamentals of Rock Mechanics.*, Methuen, London.

Jones, C. & Murrell, S. (1989), *Rock at great depth.*, Rotterdam, pp. 241–247.

Kakimi, T. (1980), 'Magnitude-frequency relation for displacement of minor faults and its significance in crustal deformation.', *Bulletin of the Geological Society of Japan* **31**, 467–487.

Katz, O., Reches, A., Lyakovsky, V. & Baer, G. (1999), Rock damage at the proximity of small faults: Field measurements of elastic wave velocity and elastic rebound., *in* 'AGU Spring Meeting Abstracts, supplement to Eos Vol.80, number 17', p. S335.

Kautz, S. & Sclater, J. (1988), 'Internal deformation in clay models of extension by block faulting', *Tectonics* **7**(4), 823–832.

Kelley, V. (1955), 'Monoclines of the Colorado Plateau.', *Geological Society of America Bulletin* **66**, 789–804.

Kelley, V. (1979), Tectonics, Middle Rio Grande Rift, New Mexico., *in* R. Riecker, ed., 'Rio Grande Rift: Tectonics and Magmatism', American Geophysical Union, Washington, D.C., pp. 57–70.

King, G. (1983), 'The accommodation of large strains in the upper lithosphere and other solids: the geometrical origin of the seismic b-value', *Pure and Applied Geophysics* **121**, 761–816.

Knipe, R., Jones, G. & Fisher, Q. (1998), Faulting, fault sealing and fluid flow in hydrocarbon reservoirs: an introduction., *in* G. Jones, Q. Fisher & R. Knipe, eds, 'Faulting, Fault Sealing and Fluid Flow in Hydrocarbon Reservoirs', number 147 *in* 'Special Publications', The Geological Society of London, pp. vii–xxi.

Koestler, A. (1994), Scaling properties of extensional fault populations: the natural gap at the medium scale., *in* 'Tectonic Studies Group of the Geological Society of London. Abstract with Program for Edinburgh Fault Populations Meeting', pp. 21–23.

Koestler, A. & Ehrmann, W. (1991), Description of brittle extensional features in chalk on the crest of a salt ridge (NW Germany)., *in* A. Roberts, G. Yielding & B. Freeman, eds, 'The geometry of normal faults.', number 56 *in* 'Special Publications', Geological Society of London, pp. 113–123.

Krantz, R. (1986), The odd-axis model: orthorhombic fault patterns and three-dimensional strain fields, PhD thesis, University Tucson, Arizona.

Krantz, R. (1988), 'Multiple fault sets and 3d strain: theory and application.', *Journal of Structural Geology* **10**, 225–237.

Krantz, R. (1989), 'Orthorhombic fault patterns: the odd axis model and slip vector orientations.', *Tectonics* **8**(3), 483–495.

Kreysig, E. (1993), *Advanced Engineering Mathematics*, 7th edn, John Wiley and Sons, Inc., Singapore.

Kusky, T., Bradley, D. & Haeussler, P. (1997), 'Progressive deformation of the Chugach accretionary complex, Alaska, during a Paleogene ridge-trench encounter.', *Journal of Structural Geology* **19**(2), 139–157.

Leeder, M. & Jackson, J. (1993), 'The interaction between normal faulting and drainage in active extensional basins, with examples form the western United States and central Greece.', *Basin Research* **5**, 79–102.

Leroy, Y. & Ortiz, M. (1989), 'Finite element analysis of strain localization in frictional materials.', *Int. Jour. Num. Anal. Meth. Geomech.* **13**, 53–74.

Lin, J. & Parmentier, E. (1988), 'Quasistatic propagation of a normal fault: a fracture mechanics model.', *Journal of Structural Geology* **10**, 249–262.

Maerten, L., Willemse, E., Pollard, D. & Rawnsley, K. (1999), 'Slip distributions on intersecting normal faults.', *Journal of Structural Geology* **21**(1), 259–271.

Maillot, B., Cowie, P. & Lague, D. (1998), Simulating polyphase faulting with a tensorial 3d model of fault growth, *in* G. Jones, Q. Fisher & R. Knipe, eds, 'Faulting, Fault Sealing and Fluid Flow in Hydrocarbon Reservoirs', number 147 *in* 'Special Publications', The Geological Society of London, pp. 209–216.

Main, I., Meredith, P., Sammonds, P. & Jones, C. (1990), Influence of fractal flaw distributions on rock deformation in the brittle field., *in* R. Knipe & E. Rutter, eds, 'Deformation mechanisms, rheology and tectonics', number 54 *in* 'Special Publications', Geological Society of London.

Mair, K. (1997), Experimental studies of fault zone development in a porous sandstone, PhD thesis, University of Edinburgh.

Mair, K., Main, I. & Elphick, S. (2000), 'Sequential growth of deformation bands in the laboratory.', *Journal of Structural Geology* **22**, 25–42.

Malone, S., Rothe, G. & Smith, S. (1975), 'Details of microearthquake swarms in the Columbia Basin, Washington.', *Seismological Society of America Bulletin* **65**, 855–864.

Mandl, G. (1993), *Mechanics of Tectonic Faulting*, Developments in Structural Geology, 2nd edn, Elsevier.

Mansfield, C. (1996), Fault growth by segment linkage., Ph.d., University of London.

Mansfield, C. & Cartwright, J. (1996), 'High resolution fault displacement mapping from three-dimensional seismic data: evidence for dip linkage during fault growth.', *Journal of Structural Geology* **18**(2/3), 249–263.

Marchal, D., Guiraud, M., Rives, T. & van den Driessche, J. (1998), Space and time propagation processes of normal faults., *in* G. Jones, Q. Fisher & R. Knipe, eds, 'Faulting, fault sealing and fluid flow in hydrocarbon reservoirs.', number 147 *in* 'Special Publications', Geological Society of London., pp. 51–71.

Marrett, R. (1999), 'Extent of power law scaling for natural fractures in rock.', *Geology* **27**(9), 799–802.

Marrett, R. & Allmendinger, R. (1991), 'Estimates of strain due to brittle faulting: sampling of fault populations.', *Journal of Structural Geology* **13**(6), 735–738.

Marrett, R. & Allmendinger, R. (1992), 'Amount of extension on "small" faults: an example from the Viking Graben.', *Geology* **20**, 47–50.

Martel, S. (1997), 'Effects of cohesive zones on small faults and implications for secondary fracturing and fault trace geometry.', *Journal of Structural Geology* **19**(6), 835–847.

Martel, S. (1999), 'Mechanical controls on fault geometry', *Journal of Structural Geology* **21**, 585–596.

McClay, K. (1990), Deformation mechanics in analogue models of extensional fault systems., *in* R. Knipe & E. Rutter, eds, 'Deformation mechanisms, rheology and tectonics.', number 54 *in* 'Special Publications', Geological Society of London, pp. 445–453.

McGill, G. & Stromquist, A. (1979), 'The grabens of Canyonlands National Park, Utah: geometry, mechanics and kinematics.', *Journal of Geophysical Research* **84**, 4547–4563.

McKinnon, S. & Garrido de la Barra, I. (1998), 'Fracture initiation, growth and effect on stress field: a numerical investigation.', *Journal of Structural Geology* **20**(12), 1673–1689.

Mestat, P. (1993), *Lois de comportementes géomatériaux et modélisation par la méthode des éléments finis.*, LCPC, Paris.

Morewood, N. & Roberts, G. (1999), 'Lateral propagation of the surface trace of the South Alkyonides normal fault segment, central Greece: its impact on models of fault growth and displacement-length relationships', *Journal of Structural Geology* **21**, 635–652.

Muraoka, H. & Kamata, H. (1983), 'Displacement distribution along minor fault traces.', *Journal of Structural Geology* **5**(5), 483–495.

Needham, T., Yielding, G. & Fox, R. (1996), 'Fault population description and prediction using examples from the offshore UK', *Journal of Structural Geology* **18**(2/3), 155–168.

Niño, F. (1997), Modélisation numérique de la déformation de la déformation localisée et de l'activité tectonique des failles., Thèse de Doctorat, Universite de Montpellier II.

Niño, F. (2000), Personal web page, www.glg.ed.ac.uk/home/Fernando.Nino/.

Niño, F., Chéry, J. & Gratier, J.-P. (1998), 'Mechanical modelling of compressional basins: Origin and interaction of faults, erosion and subsidence in the Ventura Basin, California', *Tectonics* **17**(6), 955–972.

Niño, F., Philip, H. & Chéry, J. (1998), 'The role of bed-parallel slip in the formation of blind thrust faults', *Journal of Structural Geology* **20**(5), 503–516.

Nicol, A., Walsh, J., Watterson, J. & Bretan, P. (1995), 'Three-dimensional geometry and growth of conjugate normal faults.', *Journal of Structural Geology* **17**(63), 847–862.

Nicol, A., Walsh, J., Watterson, J. & Gillespie, P. (1996), 'Fault size distributions: are they really power law?', *Journal of Structural Geology* **18**(2/3), 191–197.

Nicol, A., Walsh, J., Watterson, J. & Underhill, J. (1997), 'Displacement rates of normal faults.', *Nature* **390**(6656), 157–159.

Odé, H. (1960), Faulting as a velocity discontinuity in plastic deformation., *in* D. Griggs & J. Handin, eds, 'Rock Deformation', Vol. 79 of *Geological Society of America Memoir*, Geological Society of America, pp. 293–321.

Odling, N. (1997), 'Scaling and connectivity of joint systems in sandstones from Western Norway.', *Journal of Structural Geology* **19**(10), 1257–1271.

Odling, N., Gillespie, P., Bourgine, B., Castaing, C., Chilés, J., Christensen, N., Fillion, E., Genter, A., Olsen, C., Thrane, L., Trice, R., Aarseth, E., Walsh, J. & Watterson, J. (1999), 'Variations in fracture system geometry and their implications for fluid flow in fractured hydrocarbon reservoirs.', *Petroleum Geoscience* **5**, 373–384.

Odonne, F. & Massonat, G. (1992), 'Volume loss and deformation around conjugate fracture: comparison between a natural example and analogue experiments.', *Journal of Structural Geology* **14**(8/9), 963–972.

Oertel, G. (1965), 'The mechanism of faulting in clay experiments.', *Tectonophysics* **92**, 343–393.

Ord, A. (1990), Mechanical controls on dilatant shear zones., *in* R. Knipe & E. Rutter, eds, 'Deformation mechanisms, rheology and tectonics.', number 54 *in* 'Special Publications', Geological Society of London, pp. 183–192.

Ortega, O. & Marrett, R. (2000), 'Prediction of macrofracture properties using microfracture information, Mesaverde Group sandstones, San Juan basin, New Mexico.', *Journal of Structural Geology* **22**, 571–588.

Ouillon, G., Castaing, C. & Sornette, D. (1996), 'Hierarchical geometry of faulting', *Geophysical Research Letters* **101**(B3), 5477–5487.

Pacheco, J., Scholz, C. & Sykes, L. (1992), 'Changes in frequency-size relationship from small to large earthquakes.', *Nature* **355**, 71–73.

Peacock, D. & Sanderson, D. (1991), 'Displacements, segment linkage and relay ramps in normal fault zones.', *Journal of Structural Geology* **13**, 721–733.

Pickering, G., Bull, J. & Sanderson, D. (1995), 'Sampling power-law distributions.', *Tectonophysics* **248**, 1–20.

Pickering, G., Peacock, D., Sanderson, D. & Bull, J. (1997), 'Modelling tip zones to predict the throw and length characteristics of faults', *American Association of Petroleum Geologists Bulletin* **81**, 82–99.

Poliakov, A. & Hermann, H. (1994), 'Self-organised criticality of plastic shear bands in rocks.', *Geophysical Research Letters* **21**(19), 2143–2146.

Poliakov, A., Herrman, H., Podlachikov, Y. & Roux, S. (1994), 'Fractal plastic shear bands', *Fractals* **2**, 567–581.

Pollard, D., Saltzer, S. & Rubin, A. (1993), 'Stress inversion methods; are they based on faulty assumptions?', *Journal of Structural Geology* **15**, 1045–1054.

Poulimenos, G. (2000), 'Scaling problems of normal fault populations in the western Corinth Graben, Greece: implications for fault growth in large strain settings.', *Journal of Structural Geology* **22**, 307–322.

Prandtl, L. (1920), 'Ueber die haerte plasticher koerper.', *Goettinger Nachr. Maths-physics. Kl.* pp. 674–685.

Press, W., Teukolsky, S., Vetterling, W. & Flannery, B. (1996), *Numerical recipes in Fortran*, 2nd edn, Cambridge University Press.

Reches, Z. (1978), 'Analysis of faulting in three-dimensional strain field.', *Tectonophysics* **47**, 109–129.

Reches, Z. & Deitrich, J. (1983), 'Faulting of rocks in three-dimensional stress fields.I. Failure of rocks in servo-control experiments.', *Tectonophysics* **95**, 111–132.

Rives, T., Razack, M., Petit, J.-P. & Rawnsley, K. (1992), 'Joint spacing: analogue and numerical simulations.', *Journal of Structural Geology.* **14**, 925–937.

Rosendahl, B. (1975), 'Architecture of continental rifts with special reference to East Africa.', *J. Mech. Phys. Solids* **23**, 371–394.

Rudnicki, J. (1977), 'The inception of faulting in a rock mass with a weakened zone.', *Journal of Geophysical Research* **82**(5), 844–854.

Rudnicki, J. & Rice, J. (1975), 'Conditions for the localisation of deformation in pressure sensitive dilatant materials', *Journal of the Mechanics and Physics of Solids* **23**, 371–394.

Schlische, R., Young, S., Ackermann, R. & Gupta, A. (1996), 'Geometry and scaling relations of a populations of very small rift-related normal faults.', *Geology* **24**, 683–686.

Scholz, C. (1995), Fractal transitions on geological surfaces., *in* P. G. Buchanan & D. A. Nieuwland, eds, 'Fractals in the Earth Sciences.', Barton, C.C. and La Pointe, P.R., Plenum, New York., pp. 131–140.

Scholz, C. (1997), 'Earthquake and fault populations and the calculation of brittle strain', *Geoweissenschaften* **15**, 124–129.

Scholz, C. & Cowie, P. (1990), 'Determination of total strain from faulting using slip measurements.', *Nature* **346**, 837–838.

Scholz, C., Dawers, N., Yu, J.-Z., Anders, M. & Cowie, P. (1993), 'Fault growth and fault scaling laws: preliminary results.', *Journal of Geophysical Research* **98**(B12), 21951 – 21961.

Schultz-Ela, D. & Jackson, M. (1996), 'Relation of subsalt structures to suprasalt structures during extension', *American Association of Petroleum Geologists Bulletin* **80**(12), 1896–1924.

Schultz, R. & Fori, A. (1996), 'Fault length statistics and implications of graben sets at Candor Mensa, Mars', *Journal of Structural Geology* **18**(2/3), 373–383.

Scott, R. & Castellanos, M. (1984), Stratigraphic and structural relations of volcanic rocks in drillholes USW GU-3 and USW G-3, Yucca Mountain, Nye County, Nevada., Technical report, U.S. Geological Survey, open file report.

Scotti, O., Nur, A. & Estevez, R. (1991), 'Distributed deformation and block rotation in three dimensions', *Journal of Geophysical Research* **96**(B7), 12225–12243.

Seagall, P. & Pollard, D. (1980), 'Mechanics of discontinuous faults.', *Journal of Geophysical Research* **85**, 4337–4350.

Shipton, Z. (1999), Fault displacement profiles and off-fault deformation: interpreting the record of fault growth at the Chimney Rock Fault Array, Utah, USA., PhD thesis, Edinburgh University.

Sornette, A., Davy, P. & Sornette, D. (1990*a*), 'Growth of fractal fault patterns.', *Physics Review Letters* **65**(18), 2266–2269.

Sornette, A., Davy, P. & Sornette, D. (1993), 'Fault growth in brittle-ductile experiments and the mechanics of continental collisions.', *Journal of Geophysical Research* **98**, 12,111–12,139.

Sornette, D. & Davy, P. (1991), 'Fault growth and the universal fault length distribution', *Geophysics Research Letters* **18**, 1097–1081.

Sornette, D., Davy, P. & Sornette, A. (1990*b*), 'Structuration of the lithosphere as a self-organised critical phenomenon.', *Journal of Geophysical Research* **95**, 17353–17361.

Spyropoulos, C. E., Scholz, C. & Shaw, B. (1999), 'Transition regimes for growing crack populations.', *Journal of Structural Geology (in print)* **00**(00), 00–00.

Spyropoulos, C., Griffith, W., Scholz, C. & Shaw, B. (1999b), 'Experimental evidence for different strain regimes of crack populations in a clay model.', *Geophysical Research Letters* **26**, 1081–1084.

Stauffer, D. & Aharony, A. (1994), *Introduction to percolation theory*, 2nd edn, Taylor and Francis.

Steen, O. & Andresen, A. (1999), 'Effect of lithology on geometry and scaling of small faults in Triassic sandstones, East Greenland.', *Journal of Structural Geology* **21**(10), 1351–1368.

Stewart, J. (1980), Geology of Nevada, Special publication., Nevada Bureau of Mines and Geology.

Stewart, S. & Argent, J. (2000), 'Relationship between polarity of extensional fault arrays and presence of detachments.', *Journal of Structural Geology* **22**, 693–711.

Suppe, J., Chou, G. & Hook, S. (1992), Rates of folding and faulting determined from growth strata., *in* K. McClay, ed., 'Thrust Tectonics', Chapman and Hall, London, pp. 105–122.

Thompson, G. & Burke, D. (1973), 'Rate and direction of spreading in Dixie Valley, Basin and Range Province, Nevada.', *Bulletin of the Geological Society of America* **84**, 627–632.

Tibaldi, A. (1988), 'The Pleistocene fault pattern in Northern Michoacan, Mexico: an example of three-dimensional strain.', *Annales Tectonicae* **111**(1), 34–43.

Tibaldi, A. & Grazioto, E. (1997), 'Three-dimensional compression deformations in the Zailiski Alatau Mountains, Kazakstan.', *Geodynamica Acta* **10**(5), 239–249.

Touloukian, Y., Judd, W. & Roy, R. (1981), *Physical properties of rocks and minerals.*, MacGraw-Hill, New York.

Trudgill, B. & Cartwright, J. (1994), 'Relay-ramp forms and normal fault linkages, Canyonlands National Park, Utah.', *Geological Society of America Bulletin* **106**, 1143–1157.

Tuckwell, G. (2000*a*), Heterogeneity and boundary conditions: fundamental controls on the geometry and distribution of brittle deformation., *in* 'Abstracts with Program, Geoscience 2000, Joint meeting of The Geological Society of London, British Geophysical Association, Mineralogical Society and the Palaeontological Association', p. 136.

Tuckwell, G. (2000*b*), Personal web page, http://pangaea.esci.keele.ac.uk/geophysics /html/brittle_deformation.html.

Twiss, R. & Moores, E. (1992), *Structural Geology*, W.H. Freeman and Company, New York.

Van Eekelen, H. (1980), 'Isotropic yield surfaces in three dimensions for use in soil mechanics.', *International Journal for Numerical and Analytical Methods in Geomechanics* **4**, 98–101.

Villemin, T. & Sunwoo, C. (1987), 'Distribution logarithmique des rejets et longeurs de failles: Examples du Bassin Houiller, Lorraine', *C. R. Acad. Sci. Paris* **305**, 1309–1312.

Walsch, J. (1966), 'Geologic map of the Eldawa-Ravine-Kabernet area, Kenya.', Kenya Ministry of Natural Resources and Wildlife, Mines and Geological Department, Scale 1:125 000.

Walsh, J. & Watterson, J. (1988), 'Analysis of the relationship between displacements and dimensions of faults.', *Journal of Structural Geology* **10**(3), 239–247.

Walsh, J. & Watterson, J. (1992), 'Populations of faults and fault displacements and their effects on estimates of fault related regional extension.', *Journal of Structural Geology* **14**, 701–712.

Walsh, J., Watterson, J. & Yielding, G. (1991), 'The importance of small-scale faulting in regional extension.', *Nature* **351**, 391–393.

Walsh, J., Watterson, J. & Yielding, G. (1994), Determination and interpretation of fault size populations: procedures and problems, *in* J. Aasen, E. Berg, A. Buller, O. Hjelmeland, R. Holt, J. Kleppe & O. Torsaeter, eds, 'North Sea Oil and Gas Reservoirs III', Vol. 10, Graham and Trotman, London, pp. 141–145.

Watterson, J., Nicol, A., Walsh, J. J. & Meier, D. (1998), 'Strains at the intersections of synchronous conjugate normal faults.', *Journal of Structural Geology* **20**(4), 363–379.

Wessel, P. & Smith, W. (1998), 'New, improved version of the generic mapping tools released.', *Eos, Transactions of the American Geophysical Union* **79**, 579.

Westaway, R. (1994), 'Quantitative analysis of populations of small faults.', *Journal of Structural Geology* **16**, 1259–1273.

Willemse, E. (1997), 'Segmented normal faults: correspondence between three-dimensional mechanical models and field data.', *Journal of Geophysical Research* **102**, 675–692.

Willemse, E., Pollard, D. & Aydin, A. (1996), 'Three-dimensional analyses of slip distributions on normal fault arrays with consequences for fault scaling.', *Journal of Structural Geology* **18**(2/3), 295–309.

Wilson, S., Henderson, J. & Main, I. (1996), 'A cellular automaton model: the influence of heterogeneity in the failure process.', *Journal of Structural Geology* **18**(2/3), 343–348.

Withjack, M. & Scheiner, C. (1982), 'Fault patterns associated with domes - an experimental and analytical study.', *Bulletin of the American Association of Petroleum Geologists.* **66**(3), 302–316.

Wojtal, S. (1994), 'Fault scaling laws and temporal evolution of fault systems.', *Journal of Structural Geology* **16**(4), 603–612.

Wojtal, S. (1996), 'Changes in fault displacement populations correlated to linkage between faults.', *Journal of Structural Geology* **18**(2/3), 265–279.

Wojtal, S. & Mitra, G. (1986), 'Strain hardening and strain softening in fault zones from foreland thrusts.', *Geological Society of America Bulletin* **97**, 674–687.

Wu, D. & Brun, R. (1994), 'Geometry and kinematics of active normal faults, South Oquirrh Mountains, Utah: implications for fault growth.', *Journal of Structural Geology* **16**, 1061–1075.

Wu, H. & Pollard, D. (1995), 'An experimental study of the relationship between joint spacing and layer thickness.', *Journal of Structural Geology* **17**, 887–905.

Yates, R. & Thompson, G. (1959), 'Geology and quicksilver deposits of the Terlinua district, Texas.', *U.S. Geological Survey Professional Paper.*

Yielding, G., Needham, T. & Jones, H. (1996), 'Sampling of fault populations using sub-surface data: a review', *Journal of Structural Geology* **18**(2/3), 135–146.

Yielding, G., Walsh, J. & Watterson, J. (1992), 'The prediction of small-scale faulting in reservoirs', *First Break* **10**, 449–460.

Zienkiewickz, O. (1977), *The finite element method*, McGraw-Hill, London.

Zoback, M. & Healy, J. (1984), 'Friction, faulting and in situ stress', *Annales Geophysicae* **2**(6), 689–698.